Phoolendra K. Mishra
Kristopher L. Kuhlman *Editors*

Advances in Hydrogeology

Springer

Advances in Hydrogeology

Phoolendra K. Mishra • Kristopher L. Kuhlman
Editors

Advances in Hydrogeology

Springer

Editors
Phoolendra K. Mishra
Civil & Environmental Engineering
California State University
Fullerton, California, USA

Kristopher L. Kuhlman
Repository Performance Department
Sandia National Laboratories
Carlsbad, New Mexico, USA

ISBN 978-1-4614-6478-5 ISBN 978-1-4614-6479-2 (eBook)
DOI 10.1007/978-1-4614-6479-2
Springer New York Heidelberg Dordrecht London

Library of Congress Control Number: 2013933366

© Springer Science+Business Media New York 2013
This work is subject to copyright. All rights are reserved by the Publisher, whether the whole or part of the material is concerned, specifically the rights of translation, reprinting, reuse of illustrations, recitation, broadcasting, reproduction on microfilms or in any other physical way, and transmission or information storage and retrieval, electronic adaptation, computer software, or by similar or dissimilar methodology now known or hereafter developed. Exempted from this legal reservation are brief excerpts in connection with reviews or scholarly analysis or material supplied specifically for the purpose of being entered and executed on a computer system, for exclusive use by the purchaser of the work. Duplication of this publication or parts thereof is permitted only under the provisions of the Copyright Law of the Publisher's location, in its current version, and permission for use must always be obtained from Springer. Permissions for use may be obtained through RightsLink at the Copyright Clearance Center. Violations are liable to prosecution under the respective Copyright Law.
The use of general descriptive names, registered names, trademarks, service marks, etc. in this publication does not imply, even in the absence of a specific statement, that such names are exempt from the relevant protective laws and regulations and therefore free for general use.
While the advice and information in this book are believed to be true and accurate at the date of publication, neither the authors nor the editors nor the publisher can accept any legal responsibility for any errors or omissions that may be made. The publisher makes no warranty, express or implied, with respect to the material contained herein.

Printed on acid-free paper

Springer is part of Springer Science+Business Media (www.springer.com)

Contents

1 Recent Advances in Statistical and Scaling Analysis of Earth and Environmental Variables 1
Shlomo P. Neuman, Alberto Guadagnini, Monica Riva, and Martina Siena

2 An Advanced Constitutive Law in Multiphase Flow Model for Simulations in Compressible Media 27
C.H. Tsai and G.T. Yeh

3 Fluid Pressure Redistribution Events Within a Fault: Impact of Material Property Correlation 57
Sean A. McKenna and Darin Q. Pike

4 Sparsity-Promoting Solution of Subsurface Flow Model Calibration Inverse Problems 73
Behnam Jafarpour

5 Analytic Modeling of Transient Multilayer Flow 95
Mark Bakker

6 Tortuosity and Archie's Law 115
Yuan Liu and Peter K. Kitanidis

7 Measurement of Streaming Potentials Generated During Laboratory Simulations of Unconfined Aquifer Pumping Tests 127
Bwalya Malama

8 Description, Analysis, and Interpretation of an Infiltration Experiment in a Semiarid Deep Vadose Zone 159
Marcel G. Schaap

9 Unconfined Aquifer Flow Theory: From Dupuit to Present 185
Phoolendra K. Mishra and Kristopher L. Kuhlman

Index 203

Contributors

Mark Bakker Delft University of Technology, Faculty of Civil Engineering and Geosciences, Delft, The Netherlands

Alberto Guadagnini Dipartimento di Ingegneria Idraulica, Ambientale, Infrastrutture Viarie e Rilevamento, Politecnico di Milano, Milano, Italy

Behnam Jafarpour Department of Chemical Engineering and Materials Science, University of Southern California, Los Angeles, CA, USA

Peter K. Kitanidis Yang & Yamazaki Environment & Energy Building - MC 4020, Stanford University, Stanford, CA, USA

Kristopher L. Kuhlman Sandia National Laboratories, Carlsbad, NM, USA

Yuan Liu Yang & Yamazaki Environment & Energy Building - MC 4020, Stanford University, Stanford, CA, USA

Bwalya Malama Sandia National Laboratories, Carlsbad, NM, USA

Sean A. McKenna IBM Research Center, IBM Smarter Cities Technology Centre, Dublin, Ireland

Phoolendra K. Mishra Civil & Environmental Engineering, California State University, Fullerton, CA, USA

Shlomo P. Neuman Hydrology and Water Resources, University of Arizona, Tucson, AZ, USA

Darin Q. Pike Sandia National Laboratories, Albuquerque, NM, USA

Monica Riva Dipartimento di Ingegneria Idraulica, Ambientale, Infrastrutture Viarie e Rilevamento, Politecnico di Milano, Milano, Italy

Marcel G. Schaap Department of Soil water and Environmental Science, University of Arizona, Tucson AZ, USA

Martina Siena Dipartimento di Ingegneria Idraulica, Ambientale, Infrastrutture Viarie e Rilevamento, Politecnico di Milano, Milano, Italy

Chia-Hsing Tsai Taiwan National Central University, Taiwan, China

Gour-Tsyh Yeh University of Central Florida and NSC Endowed Professor, Taiwan University of Central Florida, Orlando, FL, USA

Chapter 1
Recent Advances in Statistical and Scaling Analysis of Earth and Environmental Variables

Shlomo P. Neuman, Alberto Guadagnini, Monica Riva, and Martina Siena

Abstract Many earth and environmental variables appear to be self-affine (monofractal) or multifractal with Gaussian or heavy-tailed distributions. The literature considers self-affine and multifractal types of scaling to be fundamentally different, the first arising from additive and the second from multiplicative random fields or processes. Recent work by the authors demonstrates theoretically and numerically that square or absolute increments of samples from truncated fractional Brownian motion (tfBm) exhibit apparent multifractality at intermediate ranges of separation lags, with breakdown in power-law scaling at small and large lags as is commonly exhibited by data. The same is true of samples from sub-Gaussian processes subordinated to tfBm with heavy-tailed subordinators such as lognormal or Lévy, the latter leading to spurious behavior. It has been established empirically that, in numerous cases, the range of lags exhibiting power-law scaling can be enlarged significantly, at both ends of the spectrum, via a procedure known as extended self-similarity (ESS). No theoretical model of the ESS phenomenon has previously been proposed outside the domain of Burger's equation. Our work

---

S.P. Neuman (✉)
Department of Hydrology and Water Resources, University of Arizona, Tucson,
AZ 85721, USA
e-mail: neuman@hwr.arizona.edu

A. Guadagnini • M. Riva
Dipartimento di Ingegneria Civile e Ambientale, Politecnico di Milano, Piazza L. Da Vinci 32,
20133 Milano, Italy
e-mail: alberto.guadagnini@polimi.it; monica.riva@polimi.it

M. Siena
Dipartimento di Ingegneria Civile e Ambientale, Politecnico di Milano, Piazza L. Da Vinci 32,
20133 Milano, Italy

Dipartimento di Matematica e Informatica, Università di Trieste, Piazzale Europa 1,
34127 Trieste, Italy
e-mail: martina.siena@phd.units.it

P.K. Mishra and K.L. Kuhlman (eds.), *Advances in Hydrogeology*,
DOI 10.1007/978-1-4614-6479-2_1,

© Springer Science+Business Media New York 2013

demonstrates that ESS is consistent, at all separation scales, with sub-Gaussian processes subordinated to tfBm. This makes it possible to identify the functional form and estimate all parameters of corresponding models based solely on sample structure functions of the first and second orders. The authors' recent work also elucidates the well-documented but heretofore little-noticed and unexplained phenomenon that whereas the frequency distribution of log permeability data often seems to be Gaussian (or nearly so), that of corresponding increments (as well as those of many other earth and environmental variables) tends to exhibit heavy tails, which sometimes narrow down with increasing separation distance or lag.

1.1 Introduction

The literature indicates (Neuman and Di Federico 2003 and references therein) that hydrogeologic variables exhibit isotropic and directional dependencies on scales of measurement (data support), observation (extent of phenomena such as a dispersing plume), sampling window (domain of investigation), spatial correlation (structural coherence), and spatial resolution (descriptive detail). Attempts to explain such scale dependencies have focused in part on observed and/or hypothesized power-law behaviors of structure functions of variables such as permeability or log permeability (e.g., Neuman 1990, 1994; Painter 1996; Liu and Molz 1997a, 1997b; Tennekoon et al. 2003); space-time infiltration (Meng et al. 2006); river runoff (Koscielny-Bunde et al. 2006) and streamflows (Movahed and Hermanis 2007; Zhang et al. 2008, 2009); raindrop sizes and positions (Lilley et al. 2006); soil properties (Caniego et al. 2005; Zeleke and Si 2006, 2007); electrical resistance, natural gamma ray, and spontaneous potential (Yang et al. 2009); sediment transport (Ganti et al. 2009; Singh et al. 2011); and precipitation (Paschalis et al. 2012). Let

$$S_N^q(s) = \frac{1}{N(s)} \sum_{n=1}^{N(s)} |\Delta Y_n(s)|^q \tag{1.1}$$

be an order q sample structure function of a random function $Y(x)$ defined on a continuum of points x in space or time (for simplicity, we limit our discussion here to one dimension) where $\Delta Y_n(s) = Y(x_n + s) - Y(x_n)$ is a sampled increment of the function over a separation distance (lag) s between two points on the x axis and $N(s)$ the number of measured increments. Then $Y(x)$ is said to exhibit power-law scaling if

$$S_N^q(s) \propto s^{\xi(q)}, \tag{1.2}$$

where the power or scaling exponent, $\xi(q)$, depends solely on the order q. When the scaling exponent is linearly proportional to q, $\xi(q) = Hq$, $Y(x)$ is said to form a self-affine (monofractal) random field (or process) with Hurst exponent H; when $\xi(q)$ is a nonlinear function of q, $Y(x)$ has traditionally been taken to be multifractal (Frisch 1995; Turcotte 1997; Rodriguez-Iturbe and Rinaldo 1997; Mandelbrot and Hudson 2004; Molz et al. 2003).

The literature considers self-affine and multifractal modes of scaling to be fundamentally different, the first arising from additive and the second from multiplicative random fields or processes. However, there is no known universally valid expression for $\xi(q)$ in the multifractal context (Monin and Yaglom 1975; Lovejoy and Schertzer 1995; Qian 2000; Nikora 2005; Veneziano et al. 2006; Fraysse 2007). Analogy to Richardson's (1922) concept of multiplicative energy cascades in turbulence (Frisch 1995) has led Schertzer and Lovejoy (1987) to write $\xi(q) = qH - K(q)$ and express $K(q)$ explicitly in terms of H, a Lévy index α and a "codimension" proportional to the variance of the normal distribution when $\alpha = 2$ and to the width of the zero-mean symmetric Lévy stable distribution when $0 < \alpha < 2$. Their multiplicative cascade model, termed universal by the authors, suggests that $H = \xi(1)$; others approximate H by $d\xi/dq$ near $q = 0$. Nonlinear variation of $\xi(q)$ with q is also reproduced by a model of fractional Laplace motions due to Meerschaert et al. (2004; see Kozubowski et al. 2006, and Ganti et al. 2009).

Power-law scaling is typically inferred from measurements by the method of moments. This consists of calculating sample structure functions (1.1) for a finite sequence, q_1, q_2,…, q_n, of q values and for various separation lags. For each order q_i, the logarithm of $S_N^{q_i}$ is related to log s by linear regression and the power $\xi(q_i)$ set equal to the slope of the regression line. Linear or near-linear variation of log $S_N^{q_i}$ with log s is typically limited to intermediate ranges of separation scales, $s_I < s < s_{II}$, where s_I and s_{II} are theoretical or empirical lower and upper limits, respectively (Stumpf and Porter 2012). Breakdown in power-law scaling is attributed in the literature to noise at lags smaller than s_I and to undersampling at lags larger than s_{II} (Tessier et al. 1993). Benzi et al. (1993a, 1993b) discovered empirically that the range $s_I < s < s_{II}$ of separation scales over which velocities in fully developed turbulence (where Kolmogorov's dissipation scale is assumed to control s_I) scale according to (1.2) can be enlarged significantly, at both small and large lags, through a procedure they called extended self-similarity (ESS). ESS arises from the observation that structure functions of different orders, q and p, computed for the same separation lag are related by

$$S_N^q(s) \propto S_N^p(s)^{\beta(q,p)}, \tag{1.3}$$

where $\beta(q,p) = \xi(q)/\xi(p)$ is a ratio of scaling exponents. Benzi et al. (1996) introduced, and Nikora and Goring (2001) employed, a modified version of the same. Chakraborty et al. (2010) cite the success of ESS in extending observed scaling ranges, and thus allowing more accurate empirical determinations of the functional exponent $\xi(q)$ for turbulent velocities. ESS has been reported to achieve similar results for diffusion-limited aggregates, natural images, kinetic surface roughening, fluvial turbulence, sand wave dynamics, Martian topography, river morphometry, gravel-bed mobility and atmospheric barometric pressure, low-energy cosmic rays, cosmic microwave background radiation, metal-insulator transition, irregularities in human heartbeat time series, turbulence in edge magnetized plasma of fusion devices, and turbulent boundary layers of the Earth's magnetosphere (see Guadagnini and Neuman 2011 and references therein).

In almost all cases where sufficient data are available to compute sample structure functions of several orders in excess of 2, whether by the method of moments or ESS, $\xi(q)$ has been found to vary in a nonlinear fashion with q. The literature has interpreted this to imply that the corresponding data represent multifractals or, in a few cases, fractional Laplace motions. We note, however, that neither of these mathematical constructs (a) reproduces the ubiquitous breakdown in power-law scaling at small and large lags observed on the majority of data that exhibit power-law scaling, regardless of disciplinary origin, or (b) provides a rationale for the ability of ESS to extend power-law scaling to such lags.

Spatial and/or temporal increments of earth and environmental data often exhibit sample frequency distributions that are heavy tailed (Kumar and Foufoula-Georgiou 1993; Painter 1996; Yang et al. 2009). In some cases, these distributions transition from heavy tailed at small lags (separation distances or scales) to near-Gaussian at larger lags (Liu and Molz 1997a; Painter 2001; Ganti et al. 2009; Riva et al. 2013), a phenomenon also observed in fully developed turbulence (Boffetta et al. 2008). Liu and Molz (1997b) analyzed spatial increments of log hydraulic conductivities measured with a borehole flowmeter at Columbus Air Force Base, Mississippi. They considered the increments to have a Lévy- or α-stable distribution and used the quantile method of Fama and Roll (1971), as well as characteristic function-based methods (Press 1972), to estimate their Lévy or stability index, α. Regardless of which estimation method they had used, the authors found α to increase monotonically with lag toward an asymptotic value close to 2, the Gaussian distribution being characterized by $\alpha = 2$. Higher moment analyses of the same data and of incremental log mini-air permeability data from a vertical Berea sandstone core due to Goggin et al. 1989), conducted by Lu and Molz (2001), showed power-law tails with indices $\alpha > 2$ that did not vary significantly with lag.

Painter (2001) analyzed incremental log electrical resistivity data from an Alaskan petroleum reservoir and permeability data from the Kuparuk River field in Alaska Gaynor et al. (2000), the Hawkesbury sandstone in Australia (Liu et al. 1996), and the Page formation in Utah (Goggin et al. 1992). The Kuparuk River data include minipermeameter and plug measurements on a single core, the Hawkesbury sandstone data consist of laboratory measurements on plugs from several cores, and the Page data are closely spaced minipermeameter measurements on one intact core. The frequency distributions of all incremental data exhibited heavy tails at small lags, some of which decayed toward the Gaussian with increasing lag. Treating the data as if they were subordinated to fractional Brownian motion through a lognormal subordinator, the author was able to reproduce frequency distributions of increments associated with any lag without, however, transitioning automatically from one such distribution to another with changing lag. A model that does transition automatically from heavy tailed to Gaussian with increasing lag is that based on fractional Laplace motions due to Meerschaert et al. (2004) and Kozubowski et al. (2006). Their model generates double or stretched exponential tails which are lighter than Lévy but heavier than Gaussian. Meerschaert et al. (2004) cite examples of log hydraulic conductivity data from four sites (including those from the Columbus Air Force Base) and from the fields of finance and turbulence to which the fractional Laplace model provides acceptable fits at intermediate ranges of lags; an application to sediment transport data was described in Ganti et al. (2009).

Riva et al. (2013) pointed out a well-documented but heretofore little-noticed and unexplained phenomenon that whereas the frequency distribution of log permeability data often seems to be Gaussian or nearly so (e.g., Ricciardi et al. 2005; Paleologos and Sarris (2011), that of corresponding increments tends to exhibit heavy tails which decay with separation distance or lag. Riva et al. illustrated the phenomenon on 1 m scale log air permeabilities from pneumatic tests in 6 vertical and inclined boreholes completed in unsaturated fractured tuff near Superior, Arizona (Guzman et al. 1996). Whereas fractional Laplace motions reproduce such behavior for data increments, the corresponding model (Meerschaert et al. 2004; Kozubowski et al. 2006) says nothing about the distribution of the data themselves.

It is thus clear that no previously known model reproduces in a consistent manner all of the following statistical and scaling behaviors exhibited by many earth and environmental data: nonlinear power-law scaling in a midrange of lags, breakdown in power-law scaling at small and large lags, extension of power-law scaling to all lags via ESS, apparent lack of compatibility between sample frequencies of data and their increments, and decay of increment sample frequency tails with increased separation scale or lag.

In this chapter, we summarize and expand upon recent work by the authors that reconciles all of these behaviors within a single theoretical framework. The framework builds on the concept of truncated fractional Brownian motion (tfBm) introduced by Di Federico and Neuman (1997) and Di Federico et al. (1999) on the basis of earlier work by Neuman (1990). It rests on the notion of sub-Gaussian fields (or processes) subordinated to tfBm, with heavy-tailed subordinators such as lognormal or Lévy, described and explored by Neuman (2010a, 2010b, 2011), Guadagnini et al. (2012), and Riva et al. (2013). These authors have demonstrated theoretically and numerically that square or absolute increments of samples from such fields exhibit all symptoms of multifractal scaling (most notably nonlinear scaling and intermittency) at intermediate ranges of separation scales, with breakdown in power-law scaling at small and large lags as is commonly exhibited by data. In the case of Lévy subordinators the behavior is spurious. As tfBm is a truncated version of additive, self-affine, monofractal fBm, multifractal scaling of samples derived on its basis must be apparent rather than real; in fact, it is an artifact of sampling. Our earlier work (Siena et al. 2012) and this chapter demonstrate that ESS is consistent, at all separation scales, with sub-Gaussian processes subordinated to tfBm. This makes it possible to identify the functional form and estimate all parameters of such models based solely on sample structure functions of the first and second orders (Siena et al. 2012; Riva et al. 2013). The work of Riva et al. resolves the apparent lack of compatibility between sample frequencies of data and their increments, showing how samples from certain sub-Gaussian processes subordinated to tfBm cause increment sample frequency tails to decay with increased lag. We illustrate some of these findings below.

1.2 Sub-Gaussian Random Fields Subordinated to Truncated Fractional Brownian Motion

The following developments build on a multidimensional scaling theory of anisotropic and/or lacunary truncated fBm due to Di Federico and Neuman (1997) and Di Federico et al. (1999). In this section, we present a brief summary of its extension to sub-Gaussian random fields (or processes) subordinated to tfBm introduced by Neuman (2010a, 2010b, 2011) and Guadagnini et al. (2012). Though the extension is valid for anisotropic and/or lacunary sub-Gaussian fields, for simplicity, we limit its discussion below to one spatial (or temporal) dimension as did the latter authors.

Let $Y(x;\lambda_l,\lambda_u) = \langle Y(\lambda_l,\lambda_u)\rangle + Y'(x;\lambda_l,\lambda_u)$ be a random field defined on a continuum of points x in space (or time) with constant ensemble mean (statistical expectation) $\langle Y(\lambda_l,\lambda_u)\rangle$ and zero-mean random fluctuation $Y'(x;\lambda_l,\lambda_u)$ about the mean. The parameters λ_l and λ_u are lower and upper cutoff integral (autocorrelation) scales, respectively, the first proportional to a lower measurement support or resolution limit on data and the second to an upper domain or window size beyond which data are not sampled. We represent the random fluctuations in sub-Gaussian form

$$Y'(x;\lambda_l,\lambda_u) = W^{1/2}G'(x;\lambda_l,\lambda_u), \tag{1.4}$$

where W is an $\alpha/2-$stable random variable, totally skewed to the right of zero with width parameter $\sigma_W = \left(\cos\frac{\pi\alpha}{4}\right)^{2/\alpha}$, unit skewness, and zero shift (Samorodnitsky and Taqqu 1994; Adler et al. 2010) independent of the zero-mean Gaussian random field $G'(x;\lambda_l,\lambda_u)$. The latter has variance

$$\sigma^2(\lambda_l,\lambda_u) = \sigma^2(\lambda_u) - \sigma^2(\lambda_l), \tag{1.5}$$

autocovariance

$$\sigma^2(\lambda_l,\lambda_u) - \gamma_i^2(s;\lambda_l,\lambda_u), \tag{1.6}$$

truncated power variogram (TPV)

$$\gamma_i^2(s;\lambda_l,\lambda_u) = \gamma_i^2(s;\lambda_u) - \gamma_i^2(s;\lambda_l), \tag{1.7}$$

and integral autocorrelation scale

$$I(\lambda_l,\lambda_u) = \frac{2H}{1+2H}\frac{\lambda_u^{1+2H} - \lambda_l^{1+2H}}{\lambda_u^{2H} - \lambda_l^{2H}} \tag{1.8}$$

where, for $m = l,u$,

$$\sigma^2(\lambda_m) = A\lambda_m^{2H}/2H, \tag{1.9}$$

$$\gamma_i^2(s;\lambda_m) = \sigma^2(\lambda_m)\rho_i(s/\lambda_m) \qquad i = 1 \text{ or } 2, \tag{1.10}$$

$$\rho_1(s/\lambda_m) = \left[1 - \exp\left(-\frac{s}{\lambda_m}\right) + \left(\frac{s}{\lambda_m}\right)^{2H}\Gamma\left(1-2H,\frac{s}{\lambda_m}\right)\right] \quad 0 < H < 0.5, \tag{1.11}$$

$$\rho_2(s/\lambda_m) = \left[1 - \exp\left(-\frac{\pi}{4}\frac{s^2}{\lambda_m^2}\right) + \left(\frac{\pi}{4}\frac{s^2}{\lambda_m^2}\right)^{H}\Gamma\left(1-H,\frac{\pi}{4}\frac{s^2}{\lambda_m^2}\right)\right] \quad 0 < H < 1, \tag{1.12}$$

and $\Gamma(\cdot,\cdot)$ is the incomplete gamma function. For $\lambda_u < \infty$, spatial (or temporal) increments $\Delta Y(x,s;\lambda_l,\lambda_u) = Y(x;\lambda_l,\lambda_u) - Y(x+s;\lambda_l,\lambda_u) = W^{1/2}\Delta G(x,s;\lambda_l,\lambda_u)$ are stationary zero-mean symmetric Lévy stable characterized by $1 < \alpha \leq 2$ and scale or width function (Samorodnitsky and Taqqu 1994, p. 89)

$$\sigma^\alpha(s;\lambda_l,\lambda_u) = \left[\gamma_i^2(s;\lambda_l,\lambda_u)\right]^{\alpha/2}, \tag{1.13}$$

$\Delta G(x,s;\lambda_l,\lambda_u) = G(x;\lambda_l,\lambda_u) - G(x+s;\lambda_l,\lambda_u)$ being stationary Gaussian increments.

In the limits $\lambda_l \to 0$ and $\lambda_u \to \infty$, the TPV $\gamma_i^2(s;\lambda_l,\lambda_u)$ in (1.10) converges to a power variogram (PV) $\gamma_i^2(s) = A_i s^{2H}$, where $A_1 = A\Gamma(1-2H)/2H$ and $A_2 = A(\pi/4)^{2H/2}\Gamma(1-2H/2)/2H$. Correspondingly, $\sigma^\alpha(s;\lambda_l,\lambda_u)$ in (1.13) converges to an $\alpha-$order PV $\gamma_i^\alpha(s) = A_i s^{\alpha H}$, where $A_1 = A\Gamma(1-\alpha H)/\alpha H$ and $A_2 = A(\pi/4)^{\alpha H/2}\Gamma(1-\alpha H/2)/\alpha H$. The resultant nonstationary fluctuation $G'(x;0,\infty)$ thus constitutes fBm, its stationary increments $\Delta G(x,s;0,\infty)$ forming fGn; the nonstationary fluctuation $Y'(x;0,\infty)$ constructed from increments $\Delta Y(s;0,\infty) = W^{1/2}\Delta G(x,s;0,\infty)$ constitutes fractional Lévy motion (fLm; fBm when $\alpha = 2$), the increments forming sub-Gaussian fractional Lévy noise (fLn or fsn for fractional stable noise; Samorodnitsky and Taqqu 1994, p. 367; Samorodnitsky 2006).

It is possible to select a subordinator $W^{1/2} \geq 0$ having a heavy-tailed distribution other than Lévy; we consider below the lognormal case obtained upon setting $W^{1/2} = e^V$ with $\langle V \rangle = 0$ and $\langle V^2 \rangle = (2-\alpha)^2$.

1.3 Extended Power-Law Scaling of Sub-Gaussian Random Fields Subordinated to tfBm

The extended power-law scaling (ESS) expression (1.3) is obtained from (1.2) simply upon rewriting the latter as $S^q(s) = C(q)\,s^{\xi(q)}$ and $S^p(s) = C(p)\,s^{\xi(p)}$, solving the first of these expressions for s and substituting into the second. Whereas (1.2) implies (1.3), the reverse is generally not true, (1.3) being equivalent instead to

$$S^q(s) \propto f(s)^{\xi(q)}, \tag{1.14}$$

where $f(s)$ is some, possibly nonlinear, function of s (Kozubowski and Molz 2011; Siena et al. 2012). Consider subordinators $W^{1/2} \geq 0$ that have finite moments $\langle W^{q/2} \rangle$ of all orders q, such as the lognormal subordinator mentioned earlier. Then, in analogy to Siena et al. (2012), one can show that central qth-order moments of absolute increments $\Delta Y(x,s;\lambda_l,\lambda_u)$ are given by

$$S^q = \langle |\Delta Y(s;\lambda_l,\lambda_u)|^q \rangle = \left\langle W^{q/2} \right\rangle \left[\sqrt{2\gamma_i^2(s;\lambda_l,\lambda_u)} \right]^q$$
$$(q-1)!! \begin{cases} \sqrt{\frac{2}{\pi}} & if\ \ q\ \ is\ \ odd \\ 1 & if\ \ q\ \ is\ \ even \end{cases} \qquad q = 1,2,3\ldots \tag{1.15}$$

where !! indicates double factorial defined as $q!! = q(q-2)(q-4)\ldots 2$ if q is even and $q!! = q(q-2)(q-4)\ldots 3$ if q is odd. It follows that the ratio between structure functions of order $q+1$ and q is

$$\frac{S^{q+1}}{S^q} = g(q) \begin{cases} \sqrt{\pi}\frac{q!!}{(q-1)!!}\sqrt{\gamma_i^2(s;\lambda_l,\lambda_u)} & if\ \ q\ \ is\ \ odd \\ \frac{2}{\sqrt{\pi}}\frac{q!!}{(q-1)!!}\sqrt{\gamma_i^2(s;\lambda_l,\lambda_u)} & if\ \ q\ \ is\ \ even \end{cases} \qquad q = 1,2,3\ldots \tag{1.16}$$

where $g(q)$ depends on the choice of subordinator but not on s. In the lognormal case $\langle W^{q/2} \rangle = \exp[q^2(2-\alpha)^2/2]$ and $g(q) = \langle W^{(q+1)/2} \rangle / \langle W^{q/2} \rangle = \exp[(1+2q)(2-\alpha)^2/2]$. Using (1.15) to express $\gamma_i^2(s;\lambda_l,\lambda_u)$ as a function of S^q and substituting into (1.16) yields, after some manipulation,

$$S^{q+1} = g(q) \begin{cases} \sqrt{\frac{\pi}{2}} \left[\sqrt{\frac{\pi}{2}} \frac{1}{(q-1)!!} \right]^{\frac{1}{q}} \frac{q!!}{(q-1)!!} \left[S^q\right]^{1+\frac{1}{q}} & if\ \ q\ \ is\ \ odd \\ \sqrt{\frac{2}{\pi}} \left[\frac{1}{(q-1)!!} \right]^{\frac{1}{q}} \frac{q!!}{(q-1)!!} \left[S^q\right]^{1+\frac{1}{q}} & if\ \ q\ \ is\ \ even \end{cases} \qquad q = 1,2,3\ldots \tag{1.17}$$

This makes clear that S^{q+1} is linear in S^q on log–log scale, in accord with the ESS expression (1.3), regardless of the choice of subordinator or the functional form of the TPV $\gamma_i^2(s;\lambda_l,\lambda_u)$. The slope of this line decreases asymptotically from 2 at $q = 1$ to 1 as $q \to \infty$. Equation (1.17) and its asymptotic behavior follow from the fact that (1.15) is equivalent to the ESS expression (1.14) in which $f(s) = \left[\sqrt{2\gamma^2(s;\lambda_l,\lambda_u)} \right]$. It shows that extended power-law scaling, or ESS, at all lags is an intrinsic property of sub-Gaussian processes subordinated to tfBm with subordinators, such as the lognormal, which have finite moments of all orders.

We noted earlier that, in the limits $\lambda_l \to 0$ and $\lambda_u \to \infty$, the TPV $\gamma_i^2(s;\lambda_l,\lambda_u)$ converges to a PV $\gamma_i^2(s) = A_i s^{2H}$ and so (1.15) reduces to a power law

$$S^q = \left\langle W^{q/2} \right\rangle (q-1)!! \left[\sqrt{2A_i} \right]^q s^{qH} \begin{cases} \sqrt{\frac{2}{\pi}} & if\ \ q\ \ is\ \ odd \\ 1 & if\ \ q\ \ is\ \ even \end{cases} \qquad q = 1,2,3\ldots \tag{1.18}$$

In this case, a log–log plot of S^q versus s is linear, with constant slope qH, at all lags.

Consider now subordinators $W^{1/2} \geq 0$ that have divergent moments $\left\langle W^{q/2} \right\rangle$ of all orders $q \geq 2\alpha$, as does the previously discussed Lévy subordinator with stability index α. Let $\Delta y(x_{mn}, s; \lambda_l, \lambda_u) = y(x_{mn} + s; \lambda_l, \lambda_u) - y(x_{mn}; \lambda_l, \lambda_u)$, $n = 1, 2 \ldots N_m(s) < \infty$, be one among $m = 1, 2 \ldots M < \infty$ independent sets of increments of sampled $Y(x_{mn}; \lambda_l, \lambda_u)$ values, $y(x_{mn}; \lambda_l, \lambda_u)$. Examples may include a temporal sequence of M independent storm events or a spatial sequence of M permeability profiles measured in different boreholes or along different transects, as in the Topopah Spring tuff sample discussed in this chapter. Each sample y is subordinated to a tfBm sample g. Whereas samples g corresponding to different m values may be mutually correlated, subordination destroys such correlation among associated non-Gaussian y samples, rendering them virtually independent of each other. Here, instead of (1.1), one can compute a sample structure function according to

$$S^q_{|\Delta Y|,N,M}(s; \lambda_l, \lambda_u) = \frac{1}{M} \sum_{m=1}^{M} \frac{1}{N_m(s)} \sum_{n=1}^{N_m(s)} |\Delta y(x_{mn}, s; \lambda_l, \lambda_u)|^q \quad q = 1, 2, 3 \ldots \tag{1.19}$$

Writing $\Delta y(x_{mn}, s; \lambda_l, \lambda_u) = w_m^{1/2} \Delta g(x_{mn}, s; \lambda_l, \lambda_u)$ where w_m and $\Delta g(x_{mn}, s; \lambda_l, \lambda_u)$ represent samples of W and $\Delta G(s;\ \lambda_l, \lambda_u)$, respectively, allows rewriting (1.19) as

$$S^q_{|\Delta Y|,N,M}(s; \lambda_l, \lambda_u) = \frac{1}{M} \sum_{m=1}^{M} \frac{w_m^{q/2}}{N_m(s)} \sum_{n=1}^{N_m(s)} |\Delta g(x_{mn}, s; \lambda_l, \lambda_u)|^q \quad q = 1, 2, 3 \ldots \tag{1.20}$$

Since order $q \geq 2\alpha$ moments of $w_m^{1/2}$ diverge while all moments of $\Delta g(x_{mn}, s; \lambda_l, \lambda_u)$ converge, one can approximate (1.20) for sufficiently large sample sizes $N_m(s)$ by

$$\begin{aligned} S^q_{|\Delta Y|,N,M}(s; \lambda_l, \lambda_u) &\approx \left(\frac{1}{M} \sum_{m=1}^{M} w_m^{q/2} \right) \langle |\Delta G(s;\ \lambda_l, \lambda_u)|^q \rangle \\ &= \left(\frac{1}{M} \sum_{m=1}^{M} w_m^{q/2} \right) \left[\sqrt{2\gamma_i^2(s;\ \lambda_l, \lambda_u)} \right]^q (q-1)!! \begin{cases} \sqrt{\frac{2}{\pi}} & \mathit{if\ \ q\ \ is\ \ odd} \\ 1 & \mathit{if\ \ q\ \ is\ \ even} \end{cases} \\ q = 1, 2, 3 \ldots \end{aligned} \tag{1.21}$$

which, for finite M, is always finite. From (1.21), it follows that the ratio between sample structure functions of order $q + 1$ and q is

$$\frac{S^{q+1}_{|\Delta Y|,N,M}(s; \lambda_l, \lambda_u)}{S^q_{|\Delta Y|,N,M}(s; \lambda_l, \lambda_u)} \approx \frac{\sum\limits_{m=1}^{M} w_m^{(q+1)/2}}{\sum\limits_{m=1}^{M} w_m^{q/2}} \begin{cases} \sqrt{\pi} \frac{q!!}{(q-1)!!} \sqrt{\gamma_i^2(s;\ \lambda_l, \lambda_u)} & \mathit{if\ \ q\ \ is\ \ odd} \\ \frac{2}{\sqrt{\pi}} \frac{q!!}{(q-1)!!} \sqrt{\gamma_i^2(s;\ \lambda_l, \lambda_u)} & \mathit{if\ q\ is\ even} \end{cases} \quad q = 1, 2, 3 \ldots \tag{1.22}$$

or, in analogy to (1.17),

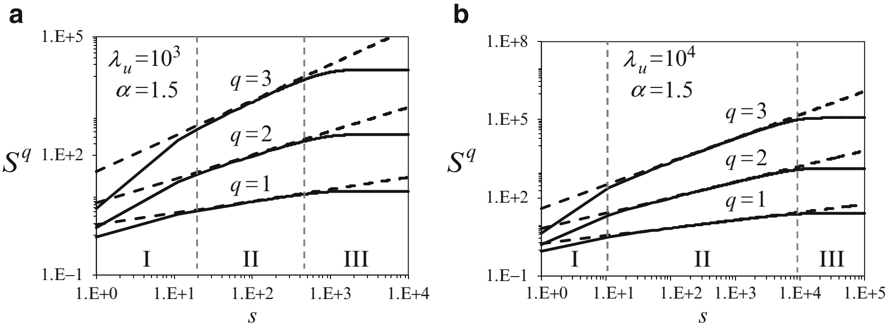

Fig. 1.1 Comparison of S^q computed at q =1, 2, 3 by means of (1.15) (solid) using TPV $\gamma_2^2(s;\lambda_l,\lambda_u)$ having parameters $A=1$, $H=0.3$, $\lambda_l=1$, and (**a**) $\lambda_u=10^3$, (**b**) $\lambda_u=10^4$ with (1.18) (dashed) using a corresponding PV for lognormal subordinator $W^{1/2}$ with $\alpha=1.5$. All quantities are in consistent units

$$
\begin{aligned}
&S^{q+1}_{|\Delta Y|,N,M}(s;\lambda_l,\lambda_u)\\
&\quad\approx\frac{\sum\limits_{m=1}^{M} w_m^{(q+1)/2}}{\sum\limits_{m=1}^{M} w_m^{q/2}}\begin{cases}\sqrt{\frac{\pi}{2}}\left[\sqrt{\frac{\pi}{2}}\frac{1}{(q-1)!!}\right]^{\frac{1}{q}}\frac{q!!}{(q-1)!!}\left[S^q_{|\Delta Y|,N,M}(s;\lambda_l,\lambda_u)\right]^{1+\frac{1}{q}} & \mathit{if\ q\ is\ odd}\\ \sqrt{\frac{2}{\pi}}\left[\frac{1}{(q-1)!!}\right]^{\frac{1}{q}}\frac{q!!}{(q-1)!!}\left[S^q_{|\Delta Y|,N,M}(s;\lambda_l,\lambda_u)\right]^{1+\frac{1}{q}} & \mathit{if\ q\ is\ even}\end{cases}\\
&\quad q=1,2,3\ldots
\end{aligned}
\tag{1.23}
$$

The analogy makes clear that extended power-law scaling, or ESS, at all lags is an approximate property of samples from sub-Gaussian processes subordinated to tfBm with subordinators, such as Lévy, which have divergent moments of orders $q\geq 2\alpha$. In the limits $\lambda_l\to 0$ and $\lambda_u\to\infty$, (1.23) becomes a power law

$$
S^q\approx\left(\frac{1}{M}\sum_{m=1}^{M} w_m^{q/2}\right)(q-1)!!\left[\sqrt{2A_i}\right]^q s^{qH}\begin{cases}\sqrt{\frac{2}{\pi}} & \mathit{if\ q\ is\ odd}\\ 1 & \mathit{if\ q\ is\ even}\end{cases}\qquad q=1,2,3\ldots
\tag{1.24}
$$

Like (1.18), this renders a log–log plot of S^q versus s linear, with constant slope qH, at all lags.

Figure 1.1 compares S^q of three different orders computed by means of (1.15) using TPV $\gamma_2^2(s;\lambda_l,\lambda_u)$ having parameters $A=1$, $H=0.3$, $\lambda_l=1$, and $\lambda_u=10^3,10^4$ (all quantities are in consistent units) with (1.18) using a corresponding PV (the limit of the former as $\lambda_l\to 0$ and $\lambda_u\to\infty$). The comparison is based on a lognormal subordinator $W^{1/2}$ with $\alpha=1.5$. In each case, the slopes of TPV- and PV-based curves coincide in a midrange of lags (labeled Zone II in Fig. 1.1) but not in the outer ranges of small and large lags (labeled Zones I and III, respectively). This breakdown in power-law scaling at small and large lags is due entirely to lower and

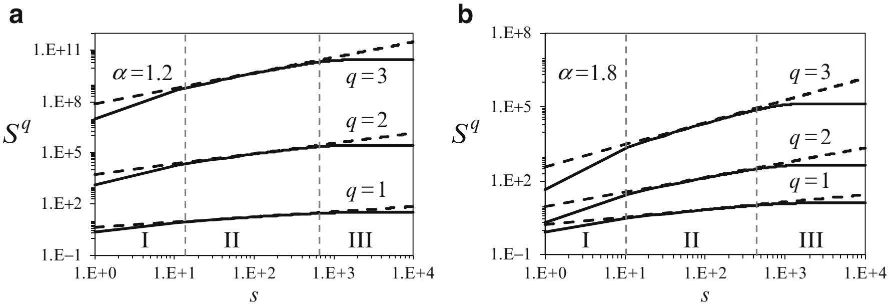

Fig. 1.2 Comparison of S^q computed at $q = 1, 2, 3$ by means of (1.21) (solid) using TPV $\gamma_2^2(s; \lambda_l, \lambda_u)$ having parameters $A = 1$, $H = 0.3$, $\lambda_l = 1$, and $\lambda_u = 10^3$ with (1.24) (dashed) using a corresponding PV based on $M = 50,000$ samples, w_m, from $\alpha/2$-stable subordinators W with (**a**) $\alpha = 1.2$ and (**b**) 1.8. All quantities are in consistent units

upper cutoffs λ_l and λ_u, respectively, unrelated to noise or oversampling which play no role in our computation of the curves in Fig. 1.1. Yet according to (1.17), log S^{q+1} is linear in log S^q for all q, in accord with ESS expression (1.3).

Figure 1.2 compares S^q of three different orders computed by means of (1.21) using TPV $\gamma_2^2(s; \lambda_l, \lambda_u)$ having parameters $A = 1$, $H = 0.3$, $\lambda_l = 1$, and $\lambda_u = 10^3$ with (1.24) using a corresponding PV. The comparison is based on $M = 50,000$ samples, w_m, from α/2-stable subordinators W with $\alpha = 1.2$ and 1.8. Here again, the slopes of TPV- and PV-based curves coincide in the central Zone II but not in the outer Zones I and III. Like before, the phenomenon is due entirely to cutoffs, noise and oversampling playing no role in our computation of the curves in Fig. 1.2. Yet according to (1.23), log S^{q+1} is linear in log S^q for all q, in accord with ESS expression (1.3).

Curves based on TPV and PV at intermediate scales (Zones II) in Figs. 1.1 and 1.2 are consistent with both power-law scaling (1.2) and ESS expression (1.14). Hence, the definition of $\beta(q, p)$ in ESS expression (1.3), derived from (1.2), applies and allows one to compute the power-law scaling exponents $\xi(q)$ for all q uniquely and unambiguously if $\xi(p)$ is known for any p. Siena et al. (2012) applied this approach to measured log air permeability data from a block of Topopah Spring tuff. Tidwell and Wilson (1999) measured air permeabilities, k, on six faces of the block by means of a multisupport permeameter (MSP) at intervals of $\Delta = 0.85$ cm on a grid of 36×36 points along each face using four tip-seal sizes. Siena et al. (2012) computed directional increments, ΔY, of $Y = \ln k$ at various lags (taken to be integer multiples of grid spacing, Δ, for each tip size) parallel to the x, y, and z coordinates on five faces of the cube. Figure 1.3 depicts log $S_N^q(s_x)$ computed according to (1.1) as function of log s_x (lag in the x direction) for $0.1 \leq q \leq 2.5$ and tip size 1.27 cm. The range of lags within which these relationships are linear, identified in Fig. 1.3 by dashed vertical lines, is seen to be quite narrow. Setting ξ(1.1) equal to the

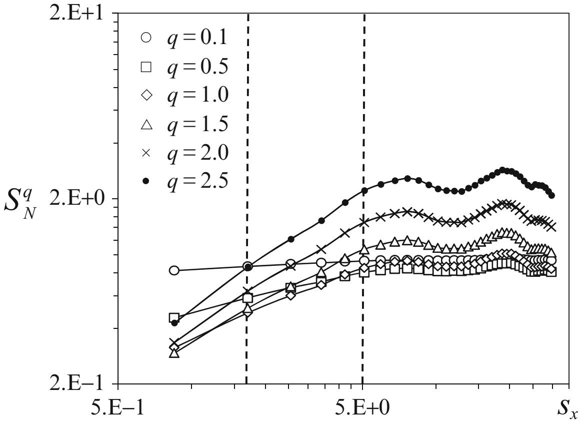

Fig. 1.3 Log–log plots of sample structure functions S_N^q of absolute ln*k* increments for tip size 1.27 cm and $0.1 \leq q \leq 2.5$ versus lag, s_x, along *x* axis on 5 block faces. Dashed lines delineate ranges of lags where power-law scaling is noted

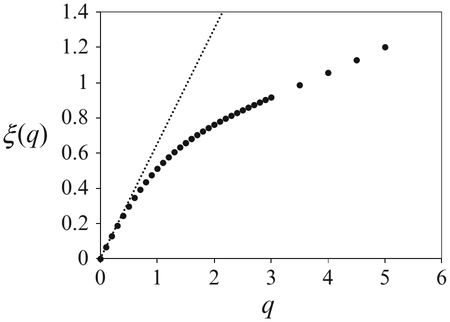

Fig. 1.4 Scaling exponent $\xi(q)$ versus q evaluated by ESS based on $\xi(1)$ obtained from Fig. 1.3. Dotted line has slope identical to that of $\xi(q)$ near $q = 0$

slope of this relationship at $q = 1$ and using it to compute $\xi(q)$ for other orders in the above manner shows $\xi(q)$ to be a nonlinear concave function of q (Fig. 1.4). Though such behavior would typically be interpreted to imply that increments of ln k are multifractal, Siena et al. note that the data are in several other respects consistent with tfBm, suggesting that multifractality in this case is apparent rather than real. Replotting the data in Fig. 1.3 as log S_N^q versus log S_N^{q-1} for $2.0 \leq q \leq 5.0$ (at intervals of 0.5) reveals much less ambiguous power-law scaling over a much wider range of lags in Fig. 1.5. The slopes of the lines, representing $\beta(q, q-1)$ in ESS expression (1.3), decrease asymptotically with q toward unity in accord with the above theory.

Siena et al. (2012) concluded from their analysis of the Topopah Spring tuff data that ESS is generally a more reliable method of inference than the method of moments. For this reason, we shall use ESS in all examples given in the rest of this chapter.

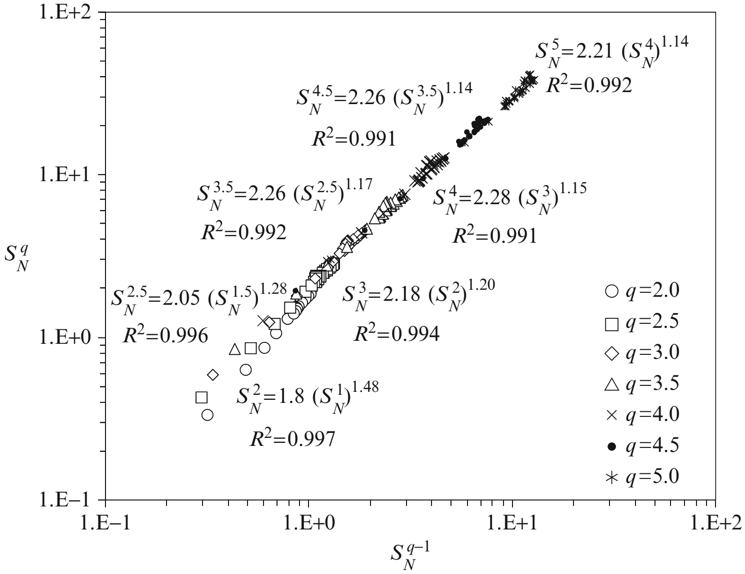

Fig. 1.5 S_N^q versus S_N^{q-1} for $2.0 \le q \le 5.0$ and tip size 1.27 cm along x axis on five block faces. Linear regression equations and relative regression coefficients (R^2) are included

1.4 Generation of Sub-Gaussian Random Fields Subordinated to tfBm

To generate a sample $y'(x_{mn};\lambda_l,\lambda_u)$ of $Y'(x_{mn};\lambda_l,\lambda_u)$ for any m, one may:

(a) Generate a random sample $g'(x_{mn};\lambda_l,\lambda_u)$, $n = 0,1,2,\ldots N_m(s_{\min})$, where $s_{\min}$ is the smallest lag of interest, representing a discrete realization of $G'(x;\lambda_l,\lambda_u)$; we do so using SGSIM, a sequential Gaussian simulation code due to Deutsch and Journel (1998), modified to accommodate TPVs (1.7); all our subsequent examples utilize a TPV with exponential modes and parameters $A = 1.0$, $H = 0.25$, $\lambda_l = 10^{-4}$, and $\lambda_u = 1$. Samples associated with diverse m values may, but need not, be mutually correlated.

(b) Draw a random number w_m from the distribution of W and multiply its square root by $g'(x_{mn};\lambda_l,\lambda_u)$, $n = 0,1,2,\ldots N_m(s_{\min})$, to generate a random sample $y'(x_{mn};\lambda_l,\lambda_u) = w_m^{1/2} g'(x_{mn};\lambda_l,\lambda_u)$. This destroys correlations between such non-Gaussian samples, rendering them virtually independent of each other.

(c) Compute a sequence of increments $\Delta y(x_{mn},s;\lambda_l,\lambda_u) = y'(x_{mn};\lambda_l,\lambda_u) - y'(x_{mn}+s;\lambda_l,\lambda_u)$ for any lag $s = ks_{\min}$, $k = 1,2,\ldots N(s_{\min})$.

We generate a collection of M such samples mutually independent. In the case of tfBm, a single sample, $M = 1$, may suffice; otherwise, M must be large enough to provide a statistically meaningful sample, w_m, $m = 1,2,\ldots M$, of random

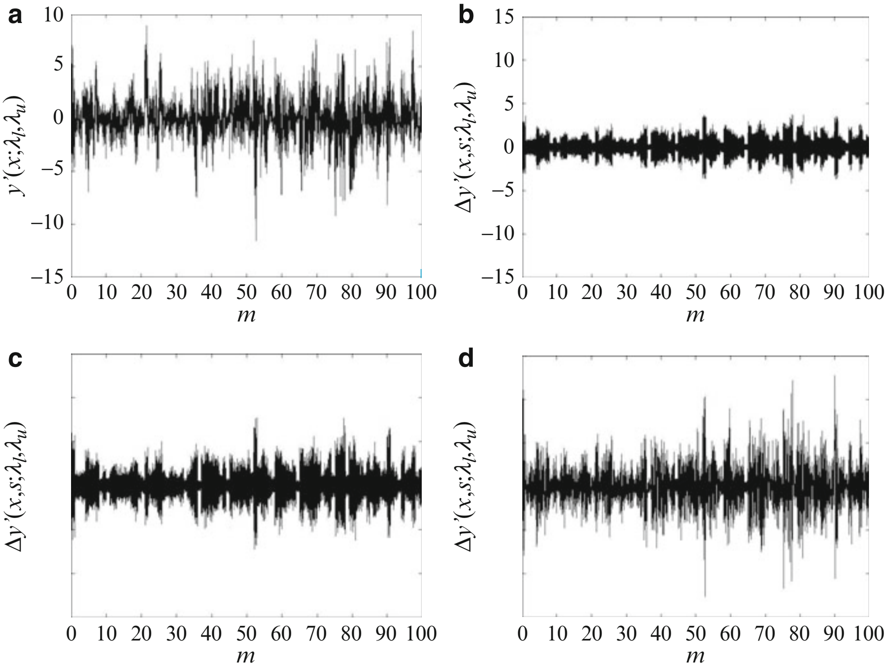

Fig. 1.6 Sequences of (**a**) $y'(x_{mn};\lambda_l,\lambda_u)$ generated with lognormal subordinator, $\alpha = 1.5$, $N = 10,000$, $M = 100$, and corresponding $\Delta y(x_{mn},s;\lambda_l,\lambda_u)$ for lags (**b**) $s = 10\ s_{\min}$, (**c**) $s = 100\ s_{\min}$, and (**d**) $s = 1,000\ s_{\min}$ where $s_{\min} = 10^{-4}$

subordinator W values. Figures 1.6 and 1.7 depict sequences of lognormal and Lévy $y'(x_{mn};\lambda_l,\lambda_u)$, respectively, generated with $\alpha = 1.5$, $N =$ 10,000, $M = 100$, and corresponding $\Delta y(x_{mn},s;\lambda_l,\lambda_u)$ for lags $s = 10\ s_{\min}, 100\ s_{\min}$, and 1,000 $s_{\min}$ where $s_{\min} = 10^{-4}$.

Figure 1.8 depicts frequency distributions of the increments in Fig. 1.6 generated with a lognormal subordinator. The distributions are seen to broaden and flatten with increasing lag. This is similar to behavior exhibited by a model subordinated to fBm (as compared to our tfBm), with a lognormal subordinator, considered by Painter (2001, Fig. 1.5). The latter author shows that the behavior is caused by an increase in the semivariance of the increments with lag.

Figure 1.9 compares frequency distributions of $y'(x_{mn};\lambda_l,\lambda_u)$ generated with Lévy subordinator, $\alpha = 1.5$, $N = 10,000$, $M = 100$, and 1,000. Also shown are maximum likelihood (ML) fits of Lévy distributions to these increments, estimates of corresponding parameters, and the generating probability density function (pdf). Increasing the number, M, of samples in the realization from 100 to 1,000 is seen to reduce skewness (reflected in a decrease in the estimated skewness parameter, β, from 0.197 to 0.047, the generating value of which was 0), lighten the tails of the distribution (reflected in an increase in the estimated Lévy index, α, from 1.363 to

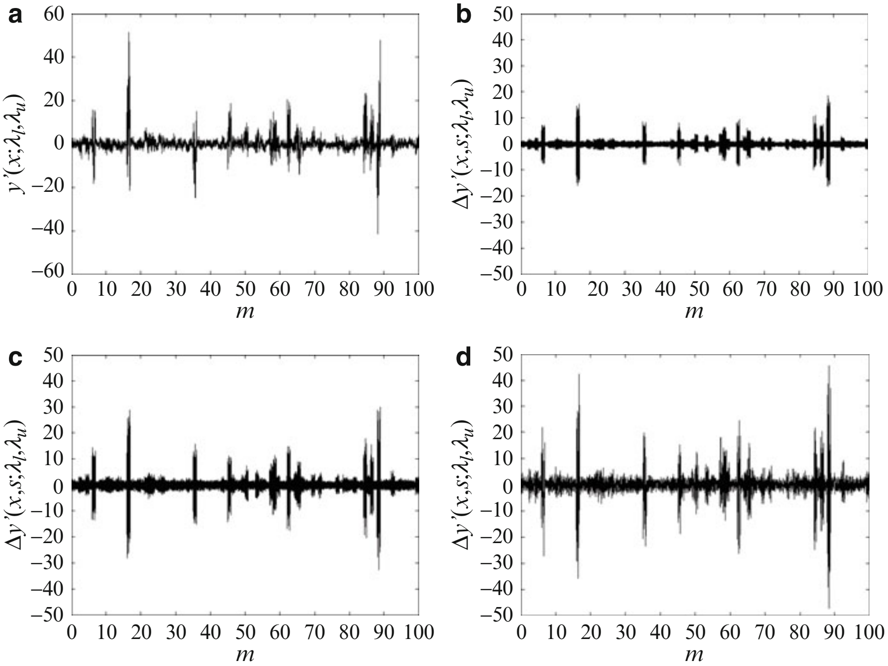

Fig. 1.7 Sequences of (**a**) Lévy $y'(x_{mn};\lambda_l,\lambda_u)$ generated with $\alpha = 1.5$, $N = 10{,}000$, $M = 100$, and corresponding $\Delta y(x_{mn}, s;\lambda_l,\lambda_u)$ for lags (**b**) $s = 10\ s_{\min}$, (**c**) $s = 100\ s_{\min}$, and (**d**) $s = 1{,}000\ s_{\min}$ where $s_{\min} = 10^{-4}$

1.412, the generating value of which was 1.5), and cause it to broaden and flatten (reflected in an increase in the estimate C of the scale parameter from 0.93 to 0.99, the generating value of which was 1.0). It is evident that parameter estimates are sensitive to the number of samples contributing to a realization. The estimated pdf exaggerates the tails (underestimates α) which is clearly seen to be undersampled.

Figure 1.10 depicts frequency distributions, ML estimates, and the generating pdf of sequences of $\Delta y(x_{mn}, s;\lambda_l,\lambda_u)$ corresponding to a Lévy subordinator, $\alpha = 1.5$, $N = 10{,}000$, and $M = 100$ for lags $s = 10\ s_{\min}$, $s = 100\ s_{\min}$, and $s = 1{,}000\ s_{\min}$ where $s_{\min} = 10^{-4}$. ML estimates of the Lévy index α vary from 1.37 for lag $s = 10\ s_{\min}$ through 1.36 for $s = 100\ s_{\min}$ to 1.39 for $s = 1{,}000\ s_{\min}$, the generating value being 1.5. The estimated pdf again exaggerates the tails (underestimates α) due to conspicuous undersampling. The same happens when M is increased from 100 to 1,000, yielding corresponding α estimates 1.403, 1.388, and 1.389. The estimates are clearly sensitive to sample size.

Figure 1.11 provides a close-up look on log–log scale at the tails of frequency distributions, their ML estimates based on the entire distribution, and generating models of sequences of $\Delta y(x_{mn}, s;\lambda_l,\lambda_u)$ corresponding to a Lévy subordinator, $\alpha = 1.5$, $N = 10{,}000$, and $M = 1{,}000$ for lags $s = 10\ s_{\min}, s = 100\ s_{\min}$, and

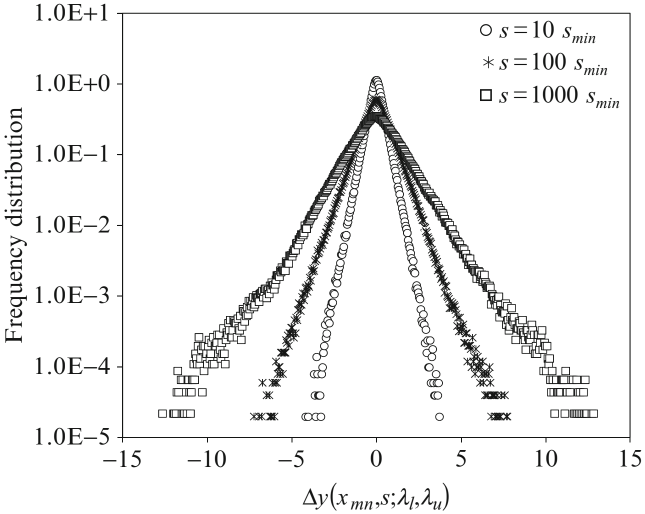

Fig. 1.8 Frequency distributions of sequences of $\Delta y(x_{mn}, s; \lambda_l, \lambda_u)$ corresponding to lognormal subordinator, $\alpha = 1.5$, $N = 10{,}000$, and $M = 100$ for lags $s = 10\ s_{\min}$, $100\ s_{\min}$, and $1{,}000\ s_{\min}$ where $s_{\min} = 10^{-4}$

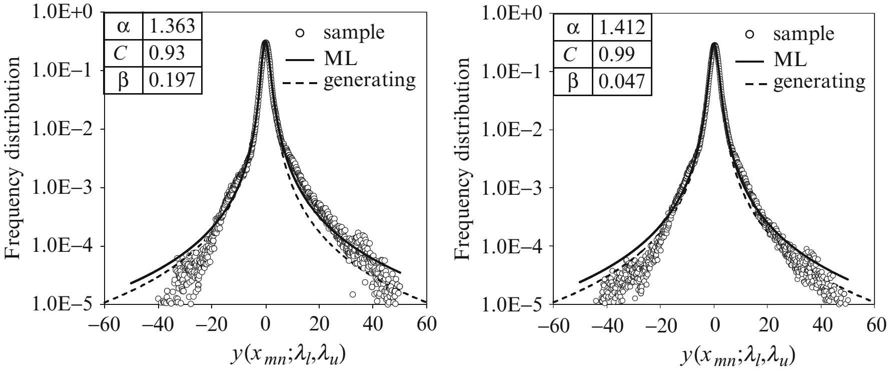

Fig. 1.9 Frequency distributions (dots), ML estimates (solid), and generating model (dashed) of sequences of $y'(x_{mn}; \lambda_l, \lambda_u)$ generated with Lévy subordinator, $\alpha = 1.5$, $N = 10{,}000$, $M = 100$ (left), and 1,000 (right). α = ML estimate of Lévy index, β = ML estimate of skewness parameter, and C = ML estimate of scale parameter

$s = 1{,}000\ s_{\min}$. The fitted portions of the tails are power laws characterized by Lévy index estimates α that are lower than the generating value, 1.5. Indeed, power laws corresponding to the generating distributions are steeper than their ML counterparts. The extreme tails of the sample distributions die off at relatively rapid rates that are a clear indication of undersampling.

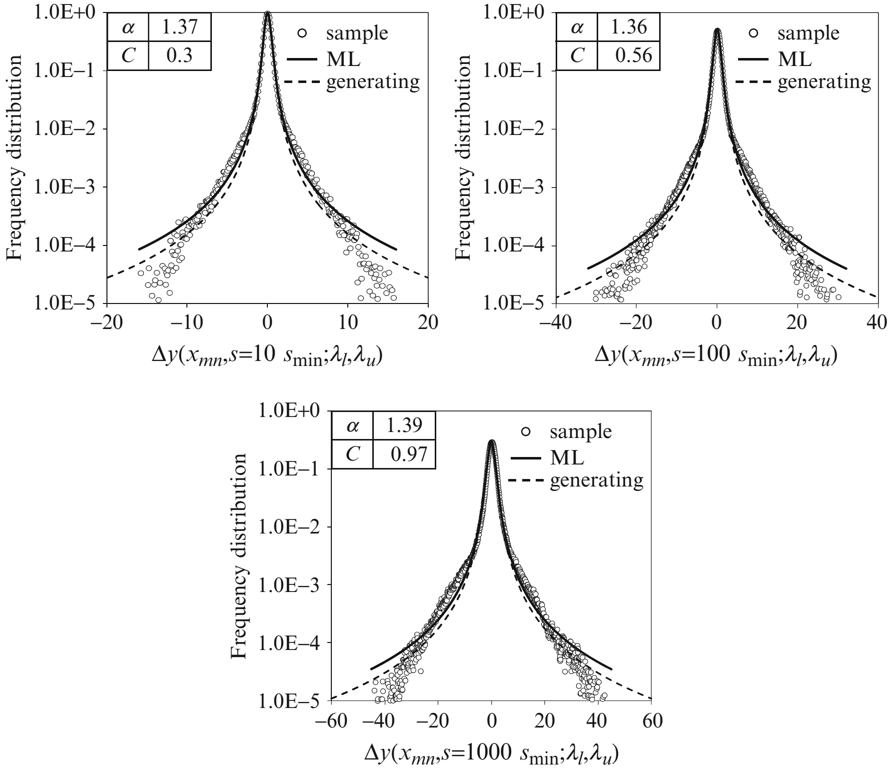

Fig. 1.10 Frequency distributions (dots), ML estimates (solid), and generating model (dashed) of sequences of $\Delta y(x_{mn}, s; \lambda_l, \lambda_u)$ corresponding to Lévy subordinator, $\alpha = 1.5$, $N = 10{,}000$, and $M = 100$ for lags $s = 10 s_{\min}$, $100\ s_{\min}$, and $1{,}000\ s_{\min}$ where $s_{\min} = 10^{-4}$. α = ML estimate of Lévy index and C = ML estimate of scale parameter

Figure 1.12 compares ML estimate C of the scale parameter as function of lag (at $s = 1\ s_{\min}$, $10\ s_{\min}$, $100\ s_{\min}$, $1{,}000\ s_{\min}$, $5{,}000\ s_{\min}$, and $9{,}000\ s_{\min}$) with theory (1.13) for sequences of $\Delta y(x_{mn}, s; \lambda_l, \lambda_u)$ corresponding to Lévy subordinator, $\alpha = 1.5$, $N = 10{,}000$, and $M = 100$. The estimates correspond closely to theory. Their increase with lag causes the distributions of increments to broaden and flatten with increasing lag in a way reminiscent of that seen earlier in Fig. 1.8. In the case of relatively small data sets, this would cause the tails of the distribution to be increasingly undersampled in comparison to the center of the distribution as lag increases, giving the appearance of approach to Gaussianity with increasing lag as is often observed in practice.

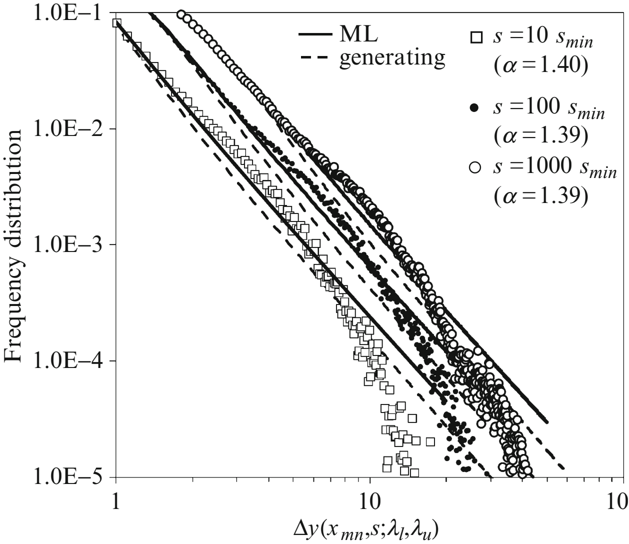

Fig. 1.11 Tails of the frequency distributions (symbols), ML estimates based on the entire distribution (solid), and generating model (dashed) of sequences of $\Delta y(x_{mn}, s; \lambda_l, \lambda_u)$ corresponding to a Lévy subordinator, $\alpha = 1.5$, $N = 10{,}000$, and $M = 1{,}000$ for lags $s = 10\, s_{\min}$, $s = 100\, s_{\min}$, and $s = 1{,}000\, s_{\min}$. ML estimates of α are given in parentheses

Fig. 1.12 ML estimate C of scale parameter (diamonds) versus lag compared with theory (Equation (1.13), solid curve) for sequences of $\Delta y(x_{mn}, s; \lambda_l, \lambda_u)$ corresponding to Lévy subordinator, $\alpha = 1.5$, $N = 10{,}000$, $M = 100$, and lags $s = 1\, s_{\min}$, $10\, s_{\min}$, $100\, s_{\min}$, $1{,}000\, s_{\min}$, $5{,}000\, s_{\min}$, and $9{,}000\, s_{\min}$ where $s_{\min} = 10^{-4}$

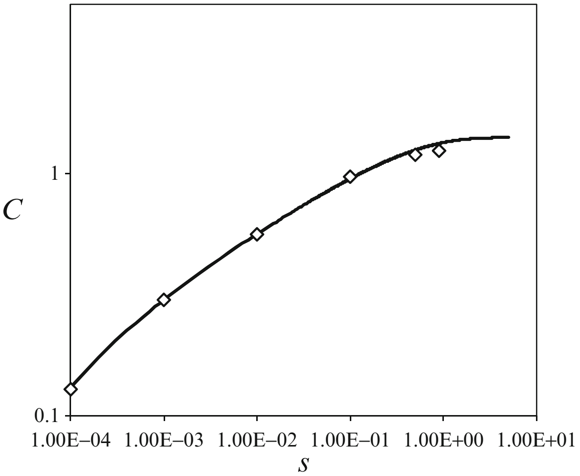

1.5 Apparent Multifractality of Sub-Gaussian Random Fields Subordinated to tfBm

In the Gaussian case $M = 1$ and $W = 1$ so that (1.20) simplifies to

$$S^q_{|\Delta G|,N}(s;\lambda_l,\lambda_u) = \frac{1}{N(s)}\sum_{n=1}^{N(s)} |\Delta g(x_n,s;\lambda_l,\lambda_u)|^q. \tag{1.25}$$

The autocorrelation between $\Delta G(x_n,s;\lambda_l,\lambda_u)$ and $\Delta G(x_0,s;\lambda_l,\lambda_u)$ is (Neuman 2010b; Guadagnini et al. 2012)

$$\rho_{\Delta G}(ns;\lambda_l,\lambda_u) = \frac{\gamma_i^2\left[(n+1)s;\lambda_l,\lambda_u\right] - 2\gamma_i^2(ns;\lambda_l,\lambda_u) + \gamma_i^2\left[(n-1)s;\lambda_l,\lambda_u\right]}{2\gamma_i^2(s;\lambda_l,\lambda_u)} \quad n > 0. \tag{1.26}$$

In the limits $\lambda_l \to 0$ and $\lambda_u \to \infty$, this converges to the classical autocorrelation $\rho_{\Delta G}(ns) = (|n+1|^{2H} - 2|n|^{2H} + |n-1|^{2H})/2$ of fGn. A necessary condition for $\Delta G(x,s;\lambda_l,\lambda_u)$ to be mean ergodic within the finite range $s \le L_u$, i.e., for its sample mean to approximate $\langle \Delta G(s;\lambda_l,\lambda_u)\rangle$, is that its integral scale be much smaller than the size, L_u, of the sampling domain. Ergodicity of order q, i.e., the ability to approximate $\langle \Delta G(s;\lambda_l,\lambda_u)^q\rangle$ by the sample mean of $\Delta G(x,s;\lambda_l,\lambda_u)^q$, requires that the integral scale of the latter satisfy this same condition (e.g., Papoulis 1984, pp. 250–251). The higher is q the more do sample statistics depart from their ensemble counterparts. Correspondingly, $S^q_{|\Delta G|,N}(s;\lambda_l,\lambda_u)$ in (1.25) approximates $\langle |\Delta G(s;\lambda_l,\lambda_u)|^q\rangle$ to a lesser and lesser degree as q increases. By the same token, $S^q_{|\Delta Y|,N}(s;\lambda_l,\lambda_u)$ in (1.1) approximates $\langle |\Delta Y(s;\lambda_l,\lambda_u)|^q\rangle$ to a lesser and lesser degree as q goes up.

$S^q_{|\Delta G|,N}(s;\lambda_l,\lambda_u)$ being finite and proportional to the sum of autocorrelated quantities raised to powers dependent on q, setting $S^q_{|\Delta G|,N}(s;\lambda_l,\lambda_u) \propto (s/\lambda_u)^{\xi(q)}$ generally renders $\xi(q)$ nonlinear in q as is the case with multifractals (Neuman 2010a). By the same token, $S^q_{|\Delta Y|,N}(s;\lambda_l,\lambda_u)$ being finite for any given set of data, setting $S^q_{|\Delta Y|,N}(s;\lambda_l,\lambda_u) \propto (s/\lambda_u)^{\xi(q)}$ renders $\xi(q)$ nonlinear in q. The same is true of $S^q_{|\Delta Y|,N,M}(s;\lambda_l,\lambda_u)$ in (1.20); setting $S^q_{|\Delta Y|,N,M}(s;\lambda_l,\lambda_u) \propto (s/\lambda_u)^{\xi(q)}$ renders $\xi(q)$ nonlinear in q. One should therefore expect the relationship between $\xi(q)$ and q to deviate from linearity more and more as N decreases; since $w_m^{q/2}$ in (1.20) are statistically independent and identically distributed, one should not expect the same to be true of M. Indeed, Figs. 1.13 and 1.14 illustrate how $\xi(q)$ may vary with q when ESS is applied to Lévy sequences $y'(x_{mn};\lambda_l,\lambda_u)$ generated with $\alpha = 1.5$, $N = 100$, 1,000, and 10,000 and $M = 10$ and 100, respectively. One observes in these figures a tendency of $\xi(q)$ to be nonlinear (concave or convex) in q when N is

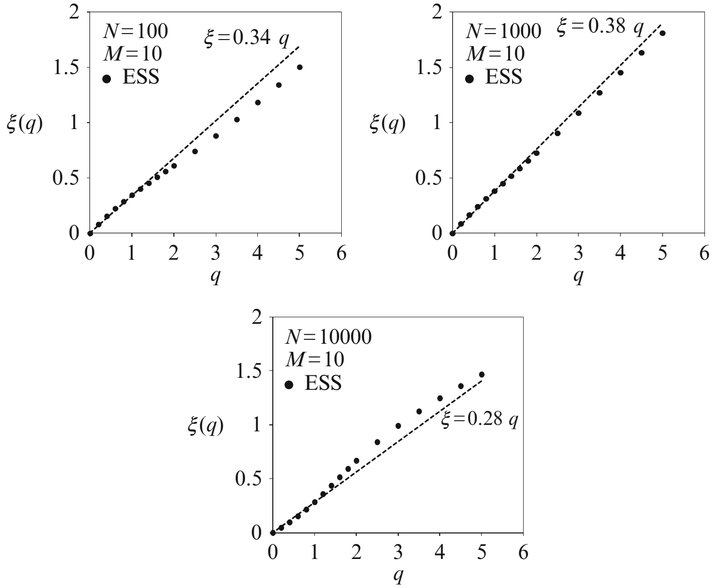

Fig. 1.13 Variation of $\xi(q)$ with q obtained upon applying ESS to a Lévy sequence $y'(x_{mn};\lambda_l,\lambda_u)$ generated with $\alpha = 1.5$, $M = 10$, and $N = 100$, 1,000, and 10,000. Broken line has slope identical to that of $\xi(q)$ near $q = 0$

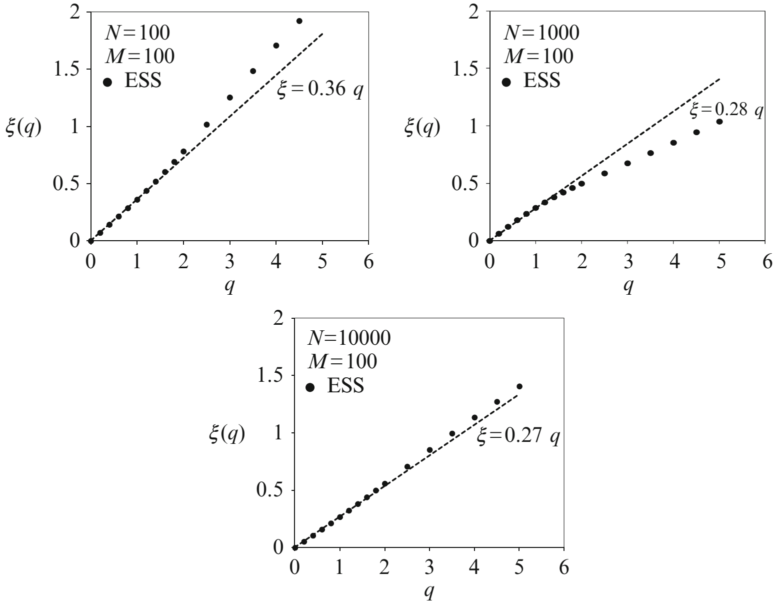

Fig. 1.14 Variation of $\xi(q)$ with q obtained upon applying ESS to a Lévy sequence $y'(x_{mn};\lambda_l,\lambda_u)$ generated with $\alpha = 1.5$, $M = 100$, and $N = 100$, 1,000, and 10,000. Broken line has slope identical to that of $\xi(q)$ near $q = 0$

relatively small, regardless of M, and to approach linearity as N increases. Variations in M do not appear to influence this tendency in any consistent way.

1.6 Conclusions

Recent work by the authors and new analyses in this chapter demonstrate that:

1. Many earth and environmental (including hydrologic) data scale in ways that are consistent with samples from truncated (monofractal, self-affine) fractional Brownian motion (tfBm) or from sub-Gaussian random fields or processes subordinated to tfBm. Whereas tfBm and its increments are Gaussian, the distributions of sub-Gaussian processes subordinated to tfBm, and their increments, may be heavy tailed (e.g., lognormal or Lévy).
2. Square or absolute increments of such samples exhibit apparent multifractality at intermediate ranges of separation lags, with breakdown in power-law scaling at small and large lags. In the case of Lévy processes, the corresponding scaling behavior is spurious.
3. In many cases, the range of lags exhibiting power-law scaling can be enlarged significantly, at both ends of the spectrum, via a procedure known as extended self-similarity (ESS). No theoretical basis for ESS has previously been proposed except in the special case of Burger's equation which has limited earth and environmental applications. Our work is the first to demonstrate that ESS is consistent, at all separation scales, with sub-Gaussian processes subordinated to tfBm.
4. ESS provides a more reliable way to infer linear or nonlinear power-law scaling from data than does the more common method of moments.
5. The consistency between ESS and sub-Gaussian processes subordinated to tfBm allows inferring the functional form, and estimating all corresponding parameters, of such processes solely from sample structure functions of the first and second orders.
6. In this chapter, we have introduced a way to generate realizations of sub-Gaussian processes subordinated to tfBm, and their increments, as collections of mutually independent tfBm samples each of which is ascribed a random variance. A collection may represent a temporal sequence of independent storm events or spatial data collected along various boreholes or transects spanning a multi-dimensional domain, as in our Topopah Spring tuff example. If the data are Gaussian (as in the Topopah case), they may be correlated among storms, boreholes or transects. If they are non-Gaussian, subordination to tfBm destroys such correlations and renders data associated with different storms, boreholes or transects virtually independent of each other. Our generation scheme is rigorously consistent with theory.
7. The smaller is the size of each sample generated in this manner, the more pronounced is the nonlinear scaling behavior of the entire realization (i.e., the more

it resembles a multifractal even though it is not). The number of samples making up the realization does not influence scaling behavior in any consistent way.

8. Heavy tails of increment frequency distributions exhibited by some published data tend to decay as lag increases, giving the appearance of approach to Gaussianity. Our results suggest that this may be due to a theoretical broadening and flattening of these distributions with increasing lag, which may cause the tails of the distribution to be increasingly undersampled in comparison to the center of the distribution with growing lag.
9. Riva et al. (2013) have shown that similar behavior is also consistent with synthetic data generated through selective sampling from a collection of the above type. Either approach may explain the well-documented but heretofore little-noticed and unexplained phenomenon that whereas the frequency distribution of log permeability data often seems to be Gaussian (or nearly so), that of corresponding increments tends to exhibit heavy tails that sometimes decay with increasing lag.
10. The above suggests that probability distributions of earth and environmental variables should be inferred jointly and consistently from measured values of these variables, and their increments, in a manner consistent with theory.
11. Nonlinear power-law scaling inferred from data must not be interpreted to imply multifractality unless one has compelling reasons to do so. We are not aware of any published example, regardless of discipline, in which this has been the case.

Acknowledgements Our work was supported in part through a contract between the University of Arizona and Vanderbilt University under the Consortium for Risk Evaluation with Stakeholder Participation (CRESP) III, funded by the US Department of Energy. Funding from the Politecnico di Milano (GEMINO, Progetti di ricerca 5 per mille junior) is also acknowledged. We are grateful to Vince Tidwell for sharing with us the Topopah Spring tuff block experimental database.

References

Adler RJ, Samorodnitsky G, Taylor J (2010) Excursion sets of stable random fields. Adv Appl Probab 42:293–318

Benzi R, Ciliberto S, Baudet C, Chavarria GR, Tripiccione R (1993a) Extended self-similarity in the dissipation range of fully developed turbulence. Europhys Lett 24:275–279, doi:10.1209/0295–5075/24/4/007

Benzi R, Ciliberto S, Tripiccione R, Baudet C, Massaioli F, Succi S (1993b) Extended self-similarity in turbulent flows. Phys Rev E 48:R29–R32, doi:10.1103/PhysRevE.48.R29

Benzi R, Biferale L, Ciliberto S, Struglia MV, Tripiccione R (1996) Generalized scaling in fully developed turbulence. Phys D 96:162–181, doi:10.1016/0167–2789(96)00018–8

Boffetta G, Mazzino A, Vulpiani A (2008) Twenty-five years of multifractals in fully developed turbulence: a tribute to Giovanni Paladin. J Phys A Math Theory 41:363001

Caniego FJ, Espejo R, Martin MA, San José F (2005) Multifractal scaling of soil spatial variability. Ecol Model 182:291–303, doi:10.1016/j.ecolmodel.2004.04.014

Chakraborty S, Frisch U, Ray SS (2010) Extended self-similarity works for the Burgers equation and why. J Fluid Mech 649:275–285, doi:10.1017/S0022112010000595

Deutsch CV, Journel AG (1998) GSLIB: geostatistical software library and user's guide, 2nd edn. Oxford University Press, New York

Di Federico V, Neuman SP (1997) Scaling of random fields by means of truncated power variograms and associated spectra. Water Resour Res 33:1075–1085, doi:10.1029/97WR00299

Di Federico V, Neuman SP, Tartakovsky DM (1999) Anisotropy, lacunarity, upscaled conductivity and its covariance in multiscale fields with truncated power variograms. Water Resour Res 35(10):2891–2908

Fama EP, Roll R (1971) Parameter estimates for symmetric stable distribution. J Am Stat Assoc 66(334):331–338

Fraysse A (2007) Generic validity of the multifractal formalism. SIAM J Math Anal 39(2):593–607

Frisch U (1995) Turbulence. Cambridge University Press, Cambridge

Ganti V, Singh A, Passalacqua P, Foufoula-Georgiu E (2009) Subordinated Brownian motion model for sediment transport. Phys Rev E 80:011111, doi: 1539–5663755/2009/80(1)/011111(9)

Gaynor GC, Chang EY, Painter S, Paterson L (2000) Application of Levy random fractal simulation techniques in modeling reservoir mechanisms in the Kuparuk River field, North Slope, Alaska. SPE Reservoir Eval Eng 3(3):263–271

Goggin DJ, Chandler MA, Kocurek G, Lake LW (1989) Permeability transects in eolian sands and their use in generating random permeability fields. Soc Petrol Eng 19586:149–164

Goggin DJ, Chandler MA, Kocurek G, Lake LW (1992) Permeability transects of eolian sands and their use in generating random permeability fields. SPE Form Eval 92(3):7–16

Guadagnini A, Neuman SP (2011) Extended power-law scaling of self-affine signals exhibiting apparent multifractality. Geophys Res Lett 38:L13403, doi:10.1029/2011GL047727

Guadagnini A, Neuman SP, Riva M (2012) Numerical investigation of apparent multifractality of samples from processes subordinated to truncated fBm. Hydrol Process 26(19):2894–2908, doi:10.1002/hyp.8358

Guzman AG, Geddis AM, Henrich MJ, Lohrstorfer CF, Neuman SP (1996) Summary of air permeability data from single-hole injection tests in unsaturated fractured tuffs at the apache leap research site: results of steady-state test interpretation. NUREG/CR-6360. U.S. Nuclear Regulatory Commission, Washington, D.C

Koscielny-Bunde E, Kantelhardt JW, Braun P, Bunde A, Havlin S (2006) Long-term persistence and multifractality of river runoff records: detrended fluctuation studies. J Hydrol 322:120–137

Kozubowski TJ, Meerschaert MM, Podgorski K (2006) Fractional Laplace motion. Adv Appl Probab 38:451–464, doi:10.1239/aap/1151337079

Kozubowski TJ, Molz FJ (2011) Interactive discussion of the discussion paper "Extended power-law scaling of air permeabilities measured on a block of tuff" by Siena M, Guadagnini A, Riva M, Neuman SP. Hydrol. Earth Syst. Sci. Discuss. 8:7805–7843, doi:10.5194/hessd-8–7805–2011

Kumar P, Foufoula-Georgiou E (1993) Multicomponent decomposition of spatial rainfall fields: 2. Self-similarity in fluctuations. Water Resour Res 29(8):2533–2544

Lilley M, Lovejoy S, Desaulniers-Soury N, Schertzer D (2006) Multifractal large number of drops limit in rain. J Hydrol 328:20–37

Liu HH, Molz FJ (1997a) Multifractal analyses of hydraulic conductivity distributions. Water Resour Res 33:2483–2488, doi: 10.1029/ 97WR02188

Liu HH, Molz FJ (1997b) Comment on "Evidence for non-Gaussian scaling behavior in heterogeneous sedimentary formations" by S. Painter. Water Resour Res 33:907–908, doi:10.1029/96WR03788

Liu K, Boult P, Painter S, Paterson L (1996) Outcrop analog for sandy braided stream reservoirs: permeability patterns in the Triassic Hawkesbury Sandstone, Sydney Basin, Australia. AAPG Bull 80(12):1850–1865

Lovejoy S, Schertzer D (1995) Multifractals and rain. In: Kundzewicz AW (ed) New uncertainty concepts in hydrology and hydrological modelling. Cambridge University Press, New York, pp 61–103

Lu S, Molz FJ (2001) How well are hydraulic conductivity variations approximated by additive stable processes? Adv Environ Res 5:39–45

Mandelbrot B, Hudson RL (2004) The (mis)behavior of markets. Basic Books, New York, NY

Meerschaert MM, Kozubowski TJ, Molz FJ, Lu S (2004) Fractional Laplace model for hydraulic conductivity. Geophys. Res. Lett. 31:L08501, doi:10.1029/2003GL019320

Meng H, Salas JD, Green TR, Ahuja LR (2006) Scaling analysis of space-time infiltration based on the universal multifractal model. J Hydrol 322:220–235, doi: 10.1016/j.jhydrol.2005.03.016

Molz FJ, Dinwiddie CL, Wilson JL (2003) A physical basis for calculating instrument spatial weighting functions in homogeneous systems. Water Resour Res 39:1096, doi: 10.1029/2001WR001220

Monin AS, Yaglom AM (1975) Statistical fluid mechanics: mechanics of turbulence. MIT Press, Cambridge, MA, 874 p

Movahed MS, Hermanis E (2007) Fractal analysis of river fluctuations. Phys A 387:915–932

Neuman SP (1990) Universal scaling of hydraulic conductivities and dispersivities in geologic media. Water Resour Res 26(8):1749–1758

Neuman SP (1994) Generalized scaling of permeabilities: validation and effect of support scale. Geophys Res Lett 21(5):349–352

Neuman SP (2010a) Apparent/spurious multifractality of data sampled from fractional Brownian/Lévy motions. Hydrol Process 24:2056–2067, doi:10.1002/hyp.7611

Neuman SP (2010b) Apparent/spurious multifractality of absolute increments sampled from truncated fractional Gaussian/Lévy noise. Geophys Res Lett 37:L09403, doi:10.1029/2010GL043314

Neuman SP (2011) Apparent multifractality and scale-dependent distribution of data sampled from self-affine processes. Hydrol Process 25:1837–1840, doi:10.1002/hyp.7967

Neuman SP, Di Federico V (2003) Multifaceted nature of hydrogeologic scaling and its interpretation. Rev Geophys 41:1014, doi:10.1029/2003RG000130

Nikora V (2005) High-order structure functions for planet surfaces: A turbulence metaphor. IEEE Geosci Remote Sens Lett 2(3):362–365

Nikora VI, Goring DG (2001) Extended self-similarity in geophysical and geological applications. Math Geol 33:251–271, doi:10.1023/A:1007630021716

Painter S (1996) Evidence for non-Gaussian scaling behavior in heterogeneous sedimentary formations. Water Resour Res 32:1183–1195, doi:10.1029/96WR00286

Painter S (2001) Flexible scaling model for use in random field simulation of hydraulic conductivity. Water Resour Res 37:1155–1163

Paleologos EK, Sarris TS (2011) Stochastic analysis of flux and head moments in a heterogeneous aquifer system. Stoch Env Res Risk Assess 25(6):747–759. doi: 10.1007/s00477–011–0459–7

Papoulis A (1984) Probability, random variables, and stochastic processes.McGraw-Hill Book Company, New York

Paschalis A, Molnar P, Burlando P (2012) Temporal dependence structure in weights in a multiplicative cascade model for precipitation. Water Resour Res 48:W01501, doi: 10.1029/2011WR010679

Press SJ (1972) Estimation of univariate and multivariate stable distributions. J Am Stat Assoc 67(340):842–846

Qian J (2000) Closure approach to high-order structure functions of turbulence. Phys Rev Lett 84(4):646–649

Ricciardi KL, Pinder GF, Belitz K (2005) Comparison of the lognormal and beta distribution functions to describe the uncertainty in permeability. J Hydrol 313:248–256

Richardson LF (1922) Weather prediction by numerical process. Cambridge University Press, Cambridge

Riva M, Neuman SP, Guadagnini A (2013) Sub-Gaussian model of processes with heavy-tailed distributions applied to air permeabilities of fractured tuff. Stoch Env Res Risk Assess 27(1): 195–207, doi:10.1007/s00477-012-0576-y

Rodriguez-Iturbe I, Rinaldo A (1997) Fractal river basins. Cambridge University Press, Cambridge

Samorodnitsky G (2006) Long memory and self-similar processes. Annales de la Faculte' des Sciences de Toulouse 15:107–123

Samorodnitsky G, Taqqu MS (1994) Stable non-gaussian random processes. Chapman & Hall, New York

Schertzer D, Lovejoy S (1987) Physical modeling and analysis of rain and clouds by anisotropic scaling multiplicative processes. J Geophys Res 92:9693–9714, doi:10.1029/JD092iD08p09693

Siena M, Guadagnini A, Riva M, Neuman SP (2012) Extended power-law scaling of air permeabilities measured on a block of tuff. Hydrol Earth Syst Sci 16:29–42, doi:10.5194/hess-16–29–2012

Singh A, Stefano L, Wilcock PR, Foufoula-Georgiou E (2011) Multiscale statistical characterization of migrating bed forms in gravel and sand bed rivers. Water Resour Res 47:W12526, doi: 10.1029/2010WR010122

Stumpf MPH, Porter MA (2012) Critical truths about power laws. Science 335:665–666

Tennekoon L, Boufadel MC, Lavallée D, Weaver J (2003) Multifractal anisotropic scaling of the hydraulic conductivity. Water Resour Res 39:1193, doi:10.1029/2002WR001645

Tessier Y, Lovejoy S, Schertzer D (1993) Universal multifractals: Theory and observations for rain and clouds. J Appl Meteorol 32:223–250, doi:10.1175/1520–0450(1993)032<0223:UMTAOF>2.0.CO;2

Tidwell VC, Wilson JL (1999) Upscaling experiments conducted on a block of volcanic tuff: results for a bimodal permeability distribution. Water Resour Res 35:3375–3387, doi: 10.1029/1999WR900161

Turcotte DL (1997) Fractals and chaos in geology and geophysics. Cambridge University Press, Cambridge

Veneziano D, Langousis A, Furcolo P (2006) Multifractality and rainfall extremes: A review. Water Resour Res 42:W06D15, doi:10.1029/2005WR004716

Yang C-Y, Hsu K-C, Chen K-C (2009) The use of the Levy-stable distribution for geophysical data analysis. Hydrogeol J 17:1265–1273, doi:10.1007/s10040–008–0411–1

Zeleke TB, Si BC (2006) Characterizing scale-dependent spatial relationships between soil properties using multifractal techniques. Geoderma 134:440–452, doi:10.1016/j.geoderma.2006.03.013

Zeleke TB, Si BC (2007) Wavelet-based multifractal analysis of field scale variability in soil water retention. Water Resour Res 43:W07446, doi: 10.1029/2006WR004957

Zhang Q, Xu C-Y, Yu Z, Chen YD, Liu C-L (2008) Multifractal detrended fluctuation analysis of streamflow series of the Yangtze River basin, China. Hydrol Process 22:4997–5003, doi:10.1002/hyp.7119

Zhang Q, Xu C-Y, Yu Z, Liu C-L, Chen YD (2009) Multifractal analysis of streamflow records of the east River basin (Pearl River), China. Phys A 388:927–934

Chapter 2
An Advanced Constitutive Law in Multiphase Flow Model for Simulations in Compressible Media

C.H. Tsai and G.T. Yeh

Abstract The purpose of this investigation is to implement a new constitutive law of saturation–capillary pressure into a fractional flow-based multiphase flow model to simulate compressible subsurface flow problems. Using the new constitutive law to describe the saturation–capillary pressure relations alleviates an undue constraint on pressure distributions inherent in a widely used law. This makes the present model able to include all possible solutions of pressure distributions in subsurface flow modeling. Finite element methods (FEM) are used to discretize the three governing equations for three primary variables—saturation of water, saturation of total liquid, and total pressure. Four examples with different pressure distributions are presented to show the feasibility and advantage of using the new constitutive law. The results verify the feasibility and capability of the present model for subsurface flow systems to cover all possible pressure distributions.

2.1 Introduction

In general, it is challenging to simultaneously measure degrees of saturation and capillary pressures in subsurface flow systems. Therefore, a complete and possible analytic model of constitutive law is essential for the multiple-phase flow simulation. A widely used saturation–capillary pressure relationship for three-phase flow was proposed by Parker et al. (1987a). Since the closed-form expression of the saturation–capillary pressure relationship is quite simple, the model has been widely

---

C.H Tsai (✉) • G.T. Yeh
Graduate Institute of Applied Geology, National Central University, Jhongli City,
Taoyuan 32001, Taiwan
e-mail: f92521314@ntu.edu.tw; gyeh@ncu.edu.tw

P.K. Mishra and K.L. Kuhlman (eds.), *Advances in Hydrogeology*,
DOI 10.1007/978-1-4614-6479-2_2,

© Springer Science+Business Media New York 2013

used in systems of two- and three-phase flows (e.g., Parker and Lenhard 1987b; Kaluarachchi and Parker 1989; Celia and Binning 1992; White and Oostrom 1996; Guarnaccia and Pinder 1997; Binning and Celia 1999; Suk and Yeh 2007; Suk and Yeh 2008; Khoei and Mohammadnejad 2011).

An undue constraint in Parker et al.'s model, the product of the scaling factor and capillary pressure between nonaqueous phase liquid (NAPL) and air must be less than or equal to that between water and NAPL (Tsai and Yeh 2012). This constraint has not been supported theoretically or experimentally. To our knowledge, this constraint has not been discussed in the literature. Moreover, due to the widespread use of Parker et al.'s model, many available multiphase flow simulations may be incomplete. For problems with pressure distributions that do not satisfy the constraint, negative saturations might be obtained and thus leads the simulations stymied using fractional flow-based approaches (e.g., Binning and Celia 1999; Guarnaccia and Pinder 1997; Suk and Yeh 2007; Suk and Yeh 2008). Possible solutions will be excluded without physical justifications using the variable-switch technique (White and Oostrom 1996) in pressure-based approaches (e.g., Kaluarachchi and Parker 1989; Celia and Binning 1992), i.e., the variable-switch algorithm implemented in those models would exclude some prescribed conditions due to the use of Parker's constitutive law. For example, simulations with those models will exclude initial and boundary conditions that might otherwise be possible.

A new constitutive relation between the degree of saturation and capillary pressure was proposed to overcome the undue constraint (Tsai and Yeh 2012). The main objective of this chapter is to implement the new constitutive law in a compressible multiple-phase flow model using fractional flow-based approaches. The implementation yields solutions even when the initial and boundary pressure distribution does not satisfy the constraint. Had it been implemented in a pressure-based approach numerical model, it will not have to exclude some possible solutions.

In multiphase flow simulations, the fractional flow-based approach is widely used due to two advantages. First, the primary variables in the fractional flow-based approach are degrees of saturation and total pressure. Therefore, the change of phase configuration, phase appearance, and phase disappearance are automated. For example, the number of simulated phases in a three-phase flow problem can degenerate from three to two or one and conversely extend from one to two or three (Suk and Yeh 2008). Second, for incompressible three-phase flow problems, one solves an elliptic-type equation for total pressure and two hyperbolically dominant types of transport equations for degrees of saturation with the fractional flow-based approach, instead of solving three strongly coupled nonlinear mixed hyperbolic and parabolic-type equations with the pressure-based approach. Although this requires an extra task of iterating boundary conditions, only two or three iterations will suffice (Suk and Yeh 2008). From the viewpoint of numerical computation, the fractional flow-based approach is quite efficient (Suk and Yeh 2008).

In this investigation, the fractional flow-based approach is employed to simulate compressible multiphase flow problems. The primary variables of the three governing equations are the saturation of water, the saturation of total liquid, and the total pressure. Because the compressibility of each flow phase is considered, we simulate one parabolic-dominant equation for total pressure and two hyperbolic-dominant equations for degrees of saturation. Three governing equations and compressibility are presented in Sect. 2.2. In Sect. 2.3, both Parker et al.'s and Tsai and Yeh's constitutive models are presented and discussions are made on why the former results in the undue constraint while the latter does not. The numerical discretizations with FEM for three governing equations are given in Appendix A. The standard Galerkin FEM is used to discretize the governing equation for total pressure, and either the standard Galerkin FEM or the upstream FEM are used to discretize two equations for saturations of water and total liquid. The resulting matrix is solved with the Bi-CGSTAB (vant der Vorst 1992). In Sect. 2.4, four numerical examples are used to verify the feasibility and capability of the present numerical model to include all possible conditions that are prescribed. The conclusions are made in Sect. 2.5.

2.2 Problem Formulations

The present multiphase flow model is assumed to consist of a compressible media and three compressible fluid phases consisting of water, NAPL, and air The porosity is assumed constant in the simulation. Each phase is assumed to have an average property, since each phase contains one component in this investigation. These assumptions do not alter the key points to be addressed in this chapter. However, a model without these assumptions is under development to make it more applicable to real-world problems.

2.2.1 Governing Equations

The mass conservation equation for each phase in porous media is given as follows (Yeh et al. 2010):

$$\begin{aligned}
&\frac{\partial\left(\phi\rho_i S_i\right)}{\partial t}+\nabla\cdot\left(\mathbf{M}_i\right)+\nabla\cdot\left(\rho_i\phi S_i\mathbf{V}_s\right)=Q_i,\quad i=1,2,3.\\
&\frac{\partial\rho_s\left(1-\phi\right)}{\partial t}+\nabla\cdot\left[\rho_s\left(1-\phi\right)\mathbf{V}_s\right]=0,
\end{aligned}\tag{2.1}$$

in which

$$\mathbf{M}_i=\rho_i\mathbf{V}_i=-\frac{\rho_i k_{ri}\mathbf{k}}{\mu_i}\cdot\left(\nabla P_i+\rho_i g\nabla z\right),\quad i=1,2,3,\tag{2.2}$$

where i is the subscript index relating to Phase 1 for water, Phase 2 for NAPL and Phase 3 for air; ϕ is the effective porosity; t is the time, [T]; ρ_i is the density for phase i, $\left[\mathrm{M/L^3}\right]$; ρ_s is the density for solid phase, $\left[\mathrm{M/L^3}\right]$; Q_i is the source or sink for phase i, $\left[\mathrm{M/\left(L^3T\right)}\right]$; S_i is the degree of saturation for phase i;M_i is the Darcy's mass flux, $\left[\mathrm{M/\left(L^2T\right)}\right]$; $\mathbf{v}_i$ is the Darcy's velocity for phase i, [L/T]; $\mathbf{v}_s$ is the velocity for solid phase, [L/T]; $\mathbf{k}$ is the intrinsic permeability tensor, $\left[\mathrm{L^2}\right]$; k_{ri} is the relative permeability for phase i; μ_i is the dynamic viscosity for phase i, [M/L/T]; P_i is the pressure for phase i $\left[\mathrm{M/L/T^2}\right]$; g is the gravitational constant $\left[\mathrm{L/T^2}\right]$; and z is the elevation, [L].

With some manipulations, Eq (2.1) becomes

$$\phi\frac{\partial(\rho_i S_i)}{\partial t}+\rho_i S_i(\nabla\cdot\mathbf{V}_s)+\nabla\cdot(\mathbf{M}_i)=Q_i,\quad i=1,2,3. \tag{2.3}$$

With small and vertical displacement (Yeh et al. 2010), Eq (2.3) becomes

$$\phi\frac{\partial(\rho_i S_i)}{\partial t}+\rho_i S_i\left(\alpha_p\sum_{j=1}^{3}\frac{\partial(S_j P_j)}{\partial t}\right)+\nabla\cdot(\mathbf{M}_i)=Q_i,\quad i=1,2,3, \tag{2.4}$$

where α_p is the compressibility parameter of the medium, $\left[\left(\mathrm{T^2L}\right)/\mathrm{M}\right]$

Substituting Eq (2.2) into Eq (2.4) and summing the resulting equations over three phases one obtains the following equation for the total pressure:

$$\begin{aligned}&C_{pt}\frac{\partial P_t}{\partial t}+C_{s1}\frac{\partial S_1}{\partial t}+C_{st}\frac{\partial S_t}{\partial t}-\nabla\cdot\boldsymbol{\kappa}\cdot(\nabla P_t+\bar{\rho}g\nabla z)=Q_t\\&-\left[(\rho_1-\rho_2)S_1+(\rho_2-\rho_3)S_t+\rho_3\right]\left[\alpha_p\left((P_1-P_2)S_1+(P_2-P_3)S_t+P_3\right)\right],\end{aligned} \tag{2.5}$$

in which

$$\boldsymbol{\kappa}=\mathbf{k}\left(\rho_1k_{r1}/\mu_1+\rho_2k_{r2}/\mu_2+\rho_3k_{r3}/\mu_3\right), \tag{2.6}$$

$$\bar{\rho}=\kappa_1\rho_1+\kappa_2\rho_2+\kappa_3\rho_3, \tag{2.7}$$

$$\kappa_i=\rho_ik_{ri}/\mu_i\Big/\sum_{j=1}^{3}\rho_jk_{rj}/\mu_j,\quad\text{for}\quad i=1,2\ and\ 3, \tag{2.8}$$

$$\begin{aligned}P_t=&\frac{P_1+P_2+P_3}{3}\\&+\frac{1}{3}\left(\int_0^{P_{C12}}(\kappa_1-\kappa_2)\,\mathrm{d}\eta+\int_0^{P_{C13}}(\kappa_1-\kappa_3)\,\mathrm{d}\eta+\int_0^{P_{C23}}(\kappa_2-\kappa_3)\,\mathrm{d}\eta\right),\end{aligned} \tag{2.9}$$

$$C_{pt} = \phi S_1 \frac{\partial \rho_1}{\partial P_1} + \phi S_2 \frac{\partial \rho_2}{\partial P_2} + \phi S_3 \frac{\partial \rho_3}{\partial P_3} + (\rho_1 S_1 + \rho_2 S_2 + \rho_3 S_3)\,\alpha_p, \tag{2.10}$$

$$\begin{aligned} C_{s1} = {} & \phi S_1 \frac{\partial \rho_1}{\partial P_1}(1-\kappa_1)\frac{\mathrm{d}P_{C12}}{\mathrm{d}S_1} - \phi S_2 \frac{\partial \rho_2}{\partial P_2}\kappa_1 \frac{\mathrm{d}P_{C12}}{\mathrm{d}S_1} \\ & - \phi S_3 \frac{\partial \rho_3}{\partial P_3}\kappa_1 \frac{\mathrm{d}P_{C12}}{\mathrm{d}S_1} + \phi\,(\rho_1 - \rho_2) \\ & + (\rho_1 S_1 + \rho_2 S_2 + \rho_3 S_3)\,\alpha_p \left[P_{C12} + (S_1 - \kappa_1)\frac{\mathrm{d}P_{C12}}{\mathrm{d}S_1}\right], \end{aligned} \tag{2.11}$$

$$\begin{aligned} C_{st} = {} & \varphi S_1 \frac{\partial \rho_1}{\partial P_1}\kappa_3 \frac{\mathrm{d}P_{C23}}{\mathrm{d}S_t} + \phi S_2 \frac{\partial \rho_2}{\partial P_2}\kappa_3 \frac{\mathrm{d}P_{C23}}{\mathrm{d}S_t} \\ & - \phi S_3 \frac{\partial \rho_3}{\partial P_3}(1-\kappa_3)\frac{\mathrm{d}P_{C23}}{\mathrm{d}S_t} + \phi\,(\rho_2 - \rho_3) \\ & + (\rho_1 S_1 + \rho_2 S_2 + \rho_3 S_3)\,\alpha_p \left[P_{C23} + (S_t - 1 + \kappa_3)\frac{\mathrm{d}P_{C23}}{\mathrm{d}S_t}\right] \end{aligned} \tag{2.12}$$

$$Q_t = Q_1 + Q_2 + Q_3 \tag{2.13}$$

$$S_t = S_1 + S_2 = 1 - S_3 \tag{2.14}$$

where $\boldsymbol{\kappa}$ is the total mobility, [T]; $\overline{\rho}$ is the mobility weighted average fluid density, $\left[\mathrm{M}/\mathrm{L}^3\right]$; κ_1, κ_2, and κ_3 are, respectively, the fractional mobility for water, NAPL and air; P_t is the total pressure, $\left[\mathrm{M}/\mathrm{T}^2/\mathrm{L}\right]$; S_1, S_2, S_3, and S_t are, respectively the saturation of water, NAPL, air, and total liquid; $P_{C12} \equiv P_1 - P_2$ is the capillary pressure of waterNAPL; $P_{C13} \equiv P_1 - P_3 = -P_{C31}$ is the capillary pressure of waterair; and $P_{C23} \equiv P_2 - P_3$ is the capillary pressure of NAPLair Substituting Eq (2.2) with Phases 1 and 3 into Eq (2.4) and with some manipulations, the transport equations for the saturation of water S_1 and the saturation of total liquid S_t, respectively, are given as

$$\begin{aligned} & \left(\phi S_1 \frac{\partial \rho_1}{\partial P_1} - \kappa_1 C_{pt} + \rho_1 S_1 \alpha_p\right)\frac{\partial P_t}{\partial t} + \left(\begin{array}{c} \phi S_1 \frac{\partial \rho_1}{\partial P_1}(1-\kappa_1)\frac{\mathrm{d}P_{C12}}{\mathrm{d}S_1} + \rho_1 \phi - \kappa_1 C_{s1} \\ + \rho_1 S_1 \alpha_p \left[P_{C12} + (S_1 - \kappa_1)\frac{\mathrm{d}P_{C12}}{\mathrm{d}S_1}\right]\frac{\partial S_1}{\partial t} \end{array}\right) \\ & + \left(\phi S_1 \frac{\partial \rho_1}{\partial P_1}\kappa_3 \frac{\mathrm{d}P_{C23}}{\mathrm{d}S_t} - \kappa_1 C_{st} + \rho_1 S_1 \alpha_p \left[P_{C23} + (S_t - 1 + \kappa_3)\frac{\mathrm{d}P_{C23}}{\mathrm{d}S_t}\right]\right)\frac{\partial S_t}{\partial t} \\ & + \mathbf{M}_t \cdot \frac{\mathrm{d}\kappa_1}{\mathrm{d}S_1}\nabla S_1 + \mathbf{M}_t \cdot \frac{\mathrm{d}\kappa_1}{\mathrm{d}S_t}\nabla S_t \\ & = -\kappa_1 Q_t + \nabla \cdot \kappa_1 \boldsymbol{\kappa} \cdot \left((1-\kappa_1)\frac{\mathrm{d}P_{C12}}{\mathrm{d}S_1}\nabla S_1 + \kappa_3 \frac{\mathrm{d}P_{C23}}{\mathrm{d}S_t}\nabla S_t + (\rho_1 - \overline{\rho})\, g \nabla z\right) + Q_1 \end{aligned} \tag{2.15}$$

and

$$\begin{aligned}
&-\left(\phi S_3 \frac{\partial \rho_3}{\partial P_3} - \kappa_3 C_{pt} + \rho_3 S_3 \alpha_p\right)\frac{\partial P_t}{\partial t} + \left(\begin{array}{l} \phi S_3 \frac{\partial \rho_3}{\partial P_3}\kappa_1 \frac{\mathrm{d}P_{C12}}{\mathrm{d}S_1} + \kappa_3 C_{s1} \\ -\rho_3 S_3 \alpha_p \left[P_{C12} + (S_1 - \kappa_1)\frac{\mathrm{d}P_{C12}}{\mathrm{d}S_1}\right]\end{array}\right)\frac{\partial S_1}{\partial t} \\
&+\left(\phi S_3 \frac{\partial \rho_3}{\partial P_3}(1-\kappa_3)\frac{\mathrm{d}P_{C23}}{\mathrm{d}S_t} + \kappa_3 C_{st} + \rho_3 \phi - \rho_3 S_3 \alpha_p \right. \\
&\left. \times \left[P_{C23} + (S_t - 1 + \kappa_3)\frac{\mathrm{d}P_{C23}}{\mathrm{d}S_t}\right]\right)\frac{\partial S_t}{\partial t} \\
&-\mathbf{M}_t \cdot \frac{\mathrm{d}\kappa_3}{\mathrm{d}S_1}\nabla S_1 - \mathbf{M}_t \cdot \frac{\mathrm{d}\kappa_3}{\mathrm{d}S_t}\nabla S_t \\
&= +\kappa_3 Q_t + \nabla \cdot \kappa_3 \boldsymbol{\kappa} \cdot \left(\kappa_1 \frac{\mathrm{d}P_{C12}}{\mathrm{d}S_1}\nabla S_1 + (1-\kappa_3)\frac{\mathrm{d}P_{C23}}{\mathrm{d}S_t}\nabla S_t - (\rho_3 - \overline{\rho})\, g \nabla z\right) - Q_3,
\end{aligned} \tag{2.16}$$

in which

$$\mathbf{M}_t = \mathbf{M}_1 + \mathbf{M}_2 + \mathbf{M}_3, \tag{2.17}$$

where M_i is the total mass flux, $\left[\mathrm{M}/\left(\mathrm{L}^2\mathrm{T}\right)\right]$

These three equations must be supplemented with the constitutive laws for the relative permeability versus degree of saturation and the degree of saturation versus capillary pressure.

2.2.2 *Compressibility of Three Fluid Phases*

The equations of state for water and NAPL are individually given as

$$\frac{\partial \rho_1}{\partial P_1} = \beta_1 \rho_1^0, \tag{2.18}$$

$$\frac{\partial \rho_2}{\partial P_2} = \beta_2 \rho_2^0, \tag{2.19}$$

where β_1 and β_2 are compressibility of water and NAPL, respectively, $\left[\mathrm{T}^2\mathrm{L}/\mathrm{M}\right]$ and ρ_1^0 and ρ_2^0 are the reference densities of water and NAPL, respectively, $\left[\mathrm{M}/\mathrm{L}^3\right]$. In addition, the compressibility of air is given as

$$\frac{\partial \rho_3}{\partial P_3} = \frac{\mathrm{M}}{\mathrm{RT}} \tag{2.20}$$

where M is the mole weight of air, $\left[\mathrm{Mmole}^{-1}\right]$; R is the gas constant, $\left[\mathrm{ML}^2\mathrm{T}^{-2}\mathrm{mole}^{-1}\mathrm{K}^{-1}\right]$; and T is the absolute temperature, [K].

2.3 The Constitutive Laws

The constitutive law relating the capillary pressure to the degree of saturation can be derived based on the fundamental Young–Laplace equation (Laplace 1806). The equation relating the relative hydraulic conductivity to the degree of saturation can be derived based on the theory proposed by Mualem (1976).

2.3.1 Parker et al.'s Model for Three-Phase Fluids

Parker et al.'s three-phase model is an extension of the renown two-phase model proposed by van Genuchten (1980).

2.3.1.1 The Relations of Saturation and Capillary Pressure

Based on the assumption that fluid wettability follows the sequence water → NAPL → air, Parker et al. (1987a) extended the saturation–capillary pressure relationship (van Genuchten, 1980) from two-phase fluids to three-phase fluids. With the definition of the accumulated liquid saturation, a straightforward extension of van Genuchten's model results in the following relationship (Parker et al. 1987a):

$$\begin{aligned} &S_1 = 1 \text{ for } h_{C21} \le 0 \quad \text{and} \quad S_1 = \left[1 + (\alpha_{21} h_{C21})^n\right]^{-m} \text{ for } h_{C21} > 0; \\ &S_t = 1 \text{ for } h_{C32} \le 0 \quad \text{and} \quad S_t = \left[1 + (\alpha_{32} h_{C32})^n\right]^{-m} \text{ for } h_{C32} > 0; \\ &S_2 = S_t - S_1; \quad \text{and} \quad S_3 = 1 - S_t \end{aligned} \tag{2.21}$$

in which

$$m = 1 - 1/n, \tag{2.22}$$

where m and n are the curve shape parameters; α_{32} is the scaling factor of capillary pressure head between air and NAPL, $[1/\mathrm{L}]$; α_{21} is the scaling factor of capillary pressure head between NAPL and water $[1/\mathrm{L}]$; h_{C32} is the capillary pressure head between air and NAPL, $[\mathrm{L}]$; and h_{C21} is the capillary pressure head between NAPL and water $[\mathrm{L}]$.

From Eq. (2.21), it is seen that as the degree of saturation increases, the scaled capillary pressure decreases. According to the definition of the total liquid saturation, S_t is greater than or equal to S_1. Thus, one can conclude that capillary pressure between NAPL and air must be less than or equal to that between water and NAPL as

$$(\alpha_{32} h_{C32}) \le (\alpha_{21} h_{C21}) \,. \tag{2.23}$$

Obviously, Parker et al.'s model implies that the closed-form expression in Eq. (2.21) is workable only if the products of the scaling factor and capillary pressure head, $(\alpha_{32}h_{C32})$ and $(\alpha_{21}h_{C21})$, satisfy the constraint in Eq. (2.23). This constraint seems to have little physical relevance. In other words, some possible distributions of pressure head among phase fluids are excluded due to the constitutive law by Parker et al., not due to physical justifications. To our knowledge, no literature exists confirming the validity of Inequality (2.23).

2.3.1.2 The Relations of Relative Permeability and Saturation

In Parker et al.'s model, the relative permeability as a function of the degree of saturation is proposed by Parker et al. (1987a), which is the modified van Genuchten's model of two-phase flow (van Genuchten 1980):

$$k_{r1} = \overline{S}_1^{1/2}\left[1-\left(1-\overline{S}_1^{1/m}\right)^m\right]^2, \tag{2.24}$$

$$k_{r2} = \left(\bar{S}_t-\bar{S}_1\right)^{1/2}\left[\left(1-\bar{S}_1^{1/m}\right)^m-\left(1-\bar{S}_t^{1/m}\right)^m\right]^2, \tag{2.25}$$

$$k_{r3} = \left(1-\bar{S}_t\right)^{1/2}\left(1-\bar{S}_t^{1/m}\right)^{2m}, \tag{2.26}$$

in which

$$\bar{S}_1 = (S_1-S_{1r})/(1-S_{1r}), \tag{2.27}$$

$$\bar{S}_t = (S_1+S_2-S_{1r})/(1-S_{1r}), \tag{2.28}$$

where $\overline{S}_1$ is the effective degree of saturation for water, S_{1r} is the irreducible saturation of water and $\overline{S}_t$ is the effective degree of saturation for total liquid.

2.3.2 Tsai and Yeh's Model for L-Phase Fluids

Because of the undue constraint in Parker et al.'s model, a new model was proposed to alleviate this constraint. The model was derived based on two hypotheses (Yeh and Tsai 2011): (1) the capillary pressure function is homogeneous, i.e., it is independent of phases and (2) the capillary pressure function is a function of the accumulated degrees of saturation of two neighboring phases only, i.e. the capillary pressure function is of degree 1. Then, it was postulated that the capillary pressure is a unique function of a single variable defined as the ratio of the two total accumulated degree of saturation (Tsai and Yeh 2012).

2.3.2.1 The Relations of Saturation and Capillary Pressure

Specifically, analogous to the van Genuchen's model (van Genuchten 1980),the model proposed by Tsai and Yeh (2012) is given as follows:

$$\frac{S_{t,i}}{S_{t,i+1}} \equiv \Theta_i = \begin{cases} 1 \text{ for } h_{Ci+1,i} \le 0 \\ \left[1 + (\alpha_{i+1,i} h_{Ci+1,i})^n\right]^{-m} \text{ for } h_{Ci+1,i} > 0, \end{cases}$$
$$i = 1, 2, \ldots, L-1; \Theta_0 = 0; \Theta_{\mathrm{L}} = 1, \tag{2.29}$$

where $S_{t,i}$ is the total degree of saturation accumulated up to the $i-$th phase, $S_{t,i+1}$ is the total degree of saturation accumulated up to the $(i+1)-$th phase, Θ_i is the ratio of the total accumulated degree of saturation of the relatively wetting phase ($i-$th phase) to that of the relatively non-wetting phase ($(i+1)-$th phase), $\alpha_{i+1,i}$ is the scaling factor between the $(i+1)-$phase and $i-$phase and $h_{Ci+1,i} \equiv h_{i+1} - h_i$ is the capillary pressure head between the $(i+1)-$phase and $i-$phase, [L].

For three-phase flow (water-NAPL-air) problems, the expression of saturation–capillary pressure head relationship (2.29) is given as follows:

$$\Theta_1 \equiv \frac{S_1}{S_t} = 1 \text{ for } h_{C21} \le 0 \quad \text{and} \quad \Theta_1 \equiv \frac{S_1}{S_t} = \left[1 + (\alpha_{21} h_{C21})^n\right]^{-m} \text{ for } h_{C21} > 0;$$
$$\Theta_2 \equiv \frac{S_t}{1} = 1 \text{ for } h_{C32} \le 0 \quad \text{and} \quad \Theta_2 \equiv \frac{S_t}{1} = \left[1 + (\alpha_{32} h_{C32})^n\right]^{-m} \text{ for } h_{C32} > 0;$$
$$S_2 = S_t - S_1; \text{ and } S_3 = 1 - S_t, \tag{2.30}$$

Examining Eq. (2.30), we see that both the numerator and denominator in the second line are greater than or equal to those in the first line. Hence, it is not necessary that $(\alpha_{32} h_{c32})$ must be less than or equal to $(\alpha_{21} h_{c21})$, i.e., Inequality (2.23) does not have to hold The unjustified constraint on capillary pressures is therefore alleviated.

2.3.2.2 The Relations of Relative Permeability and Saturation

Based on Mualem's model 1976), the relative permeability as a function of the degree of saturation in this model is derived by modifying van Genuchten's model of two-phase flow (van Genuchten 1980):

$$k_{r1} = \bar{S}_1^{1/2} \left\{ \bar{S}_t \left[1 - \left(1 - \bar{S}_1^{1/m} \right)^m \right] \right\}^2, \tag{2.31}$$

$$k_{r2} = \left(\bar{S}_t - \bar{S}_1 \right)^{1/2} \left[\left(1 - \bar{S}_1^{1/m} \right)^m - \left(1 - \bar{S}_t^{1/m} \right)^m \right]^2, \tag{2.32}$$

$$k_{r3} = \left(1 - \bar{S}_t \right)^{1/2} \left(1 - \bar{S}_t^{1/m} \right)^{2m}. \tag{2.33}$$

Equations (2.32) and (2.33) are identical to Eqs (2.25) and (2.26) in formality, though they are derived from different relations of saturations and capillary pressures.

2.4 Numerical Results and Discussion

Four numerical examples are presented to show the feasibility and advantage of the present model. In Example 1, the initial and boundary pressure distributions satisfy the constraint ($\alpha_{21}h_{C21} \geq \alpha_{32}h_{C32}$), and thus these two constitutive models (Parker et al. 1987a; Tsai and Yeh 2012) are both executable. In the remaining examples (Examples 2, 3, and 4), however, the initial and prescribed boundary pressure distributions do not satisfy the constraint. Therefore, many available multiphase flow models which used Parker et al.'s model (e.g., Suk and Yeh 2007; Suk and Yeh 2008) either cannot yield solutions using fractional flow-approach or exclude possible solutions without physical justifications using variable-switch technique in pressure-based approach. In contrast, the present model yields simulations without excluding possible solutions, showing the advantage and capability of using the present model.

2.4.1 Example 1: Water Infiltration Problem

In this three-phase flow problem, water is infiltrated into a 40 cm long soil column shown in Fig. 2.1. The initial pressure distributions among three phases in the column satisfy the constraint, $\alpha_{21}h_{C21} > \alpha_{32}h_{C32}$. The initial conditions are the water pressure $P_1 = 7.156 \times 10^{15}\mathrm{g/cm/day}^2$, the NAPL pressure $P_2 = 7.415 \times 10^{15}\mathrm{g/cm/day}^2$, and the air pressure $P_3 = 7.465 \times 10^{15}\mathrm{g/cm/day}^2$. Water infiltrates into the top of column with a constant mass flux of 10 $\mathrm{g/cm}^2\mathrm{/day}$ and zero NAPL and air mass fluxes. At the bottom of the column, the pressure distributions of three phases are in equilibrium with the initial state. The boundary conditions are thus specified as follows. At the top, the mass fluxes of water, NAPL, and air are $\mathbf{n}\cdot\mathbf{M}_1 = -10\mathrm{g/cm}^2\mathrm{/day}$, $\mathbf{n}\cdot\mathbf{M}_2 = 0$, and $\mathbf{n}\cdot\mathbf{M}_3 = 0$, respectively. At the bottom, the pressure of water is $P_1 = 7.156 \times 10^{15}\mathrm{g/cm/day}^2$, the pressure of NAPL is $P_2 = 7.415 \times 10^{15}\mathrm{g/cm/day}^2$, and the pressure of air is $P_3 = 7.465 \times 10^{15}\mathrm{g/cm/day}^2$. The fluid and material properties are given in Fig. 2.1 as well. The initial time-step size is 5.0×10^{-5}day, and each subsequent time-step size is increased by 10% until a maximum time-step size of 1.0×10^{-3}day is reached.

The product of the capillary pressure and the scaling factor between NAPL and water and that between air and NAPL satisfy the constraint ($\alpha_{21}h_{C21} \geq \alpha_{32}h_{C32}$). Therefore, both the employments of Tsai and Yeh's model and Parker et al.'s model

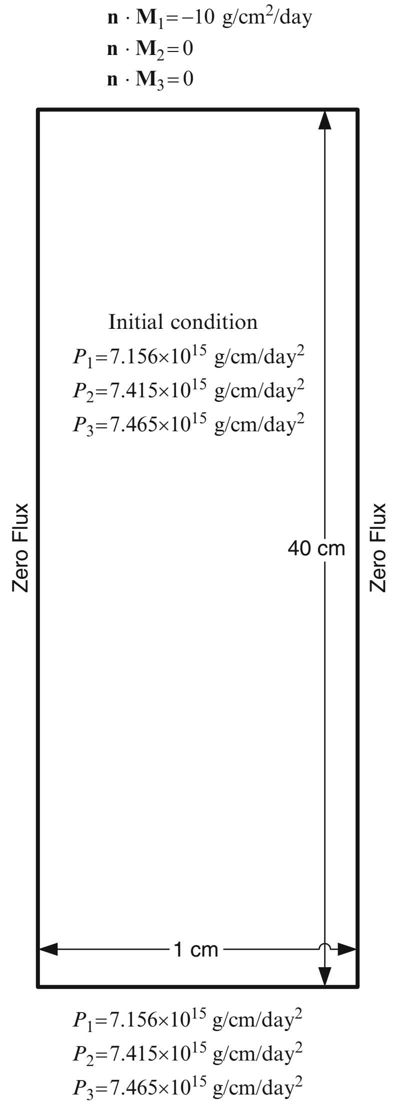

Finite element discretization

Total number of nodes = 82
Total number of elements = 40

Fluid properties

$\rho_1^0 = 1.0$ g/cm^3
$\rho_2^0 = 1.4$ g/cm^3
$\rho_3^0 = 1.0 \times 10^{-3}$ g/cm^3
$\mu_1 = 841.0828$ g/cm/day
$\mu_2 = 690.0828$ g/cm/day
$\mu_3 = 15.81$ g/cm/day
$\beta_1 = 6.162 \times 10^{-21}$ cm day^2/g
$\beta_2 = 4.086 \times 10^{-21}$ cm day^2/g
$\alpha_p = 2.057 \times 10^{-21}$ cm day^2/g
$\frac{M}{RT} = 1.557 \times 10^{-19}$ day^2/cm^2

Material properties

$\mathbf{k} = 4.27 \times 10^{-8}$ cm^2
$\phi = 0.25$
$\alpha_{31} = 0.044$ cm^{-1}
$\alpha_{32} = 0.099$ cm^{-1}
$\alpha_{21} = 0.11$ cm^{-1}
$n = 2.2$
$S_{ir} = 0$

Remark

$\alpha_{21} h_{21} > \alpha_{32} h_{32}$
Satisfying the constraint in Parker et al.'s constitutive laws.

Fig. 2.1 The problem description and relevant parameters of Example 1

yield solutions. Figure 2.2 shows the solutions for saturations of water, NAPL, and air, as simulated with the present model and Parker et al.'s model. Since the expressions of saturation–capillary pressure relations in the present model and those in Parker et al.'s model are different, it is seen that the degrees of saturation for all three phases are similar in trend but quite different in magnitudes. The present

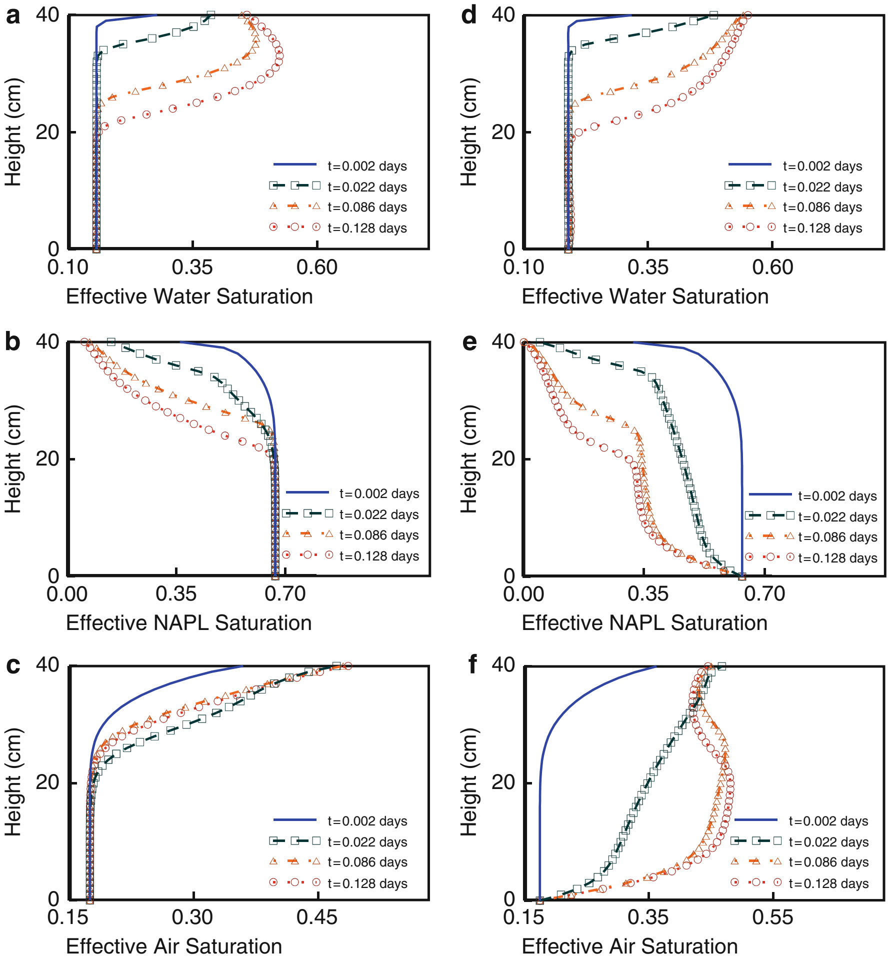

Fig. 2.2 Distributions of the degrees of saturation for Example 1: (**a**) water saturation (Tsai and Yeh's model), (**b**) NAPL saturation (Tsai and Yeh's model), (**c**) air saturation (Tsai and Yeh's model), (**d**) water saturation (Parker et al.'s model), (**e**) NAPL saturation (Parker et al.'s model), and (**f**) air saturation (Parker et al.'s model)

model yields more smoothly evolutional simulations than Parker et al.'s model. As to which model yields more reasonable results, only extensive calibrations and validations can resolve the question, which is beyond the scope of, and certainly is not the objective of, this investigation. In addition, Fig. 2.3 shows the distributions of density of air. The variation of air density providing a demonstration that compressibility is considered in the present simulator.

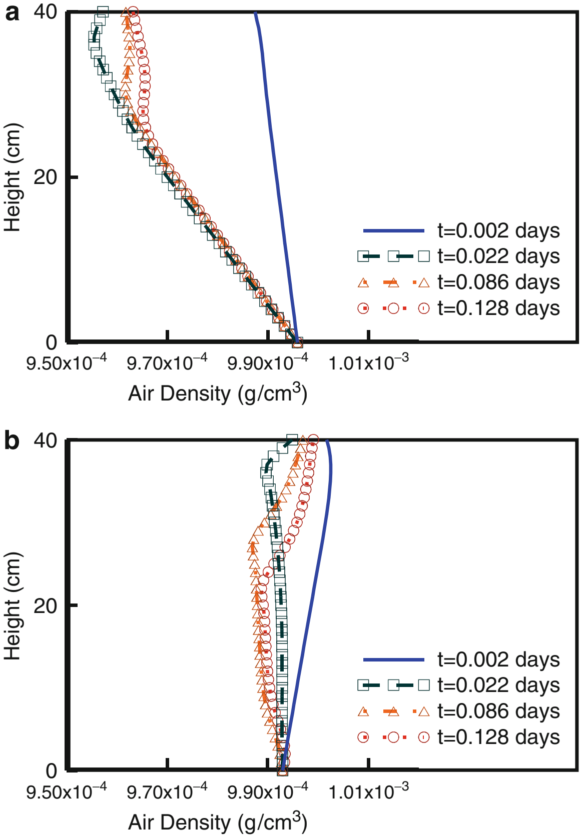

Fig. 2.3 Distributions of the density of air for Example 1: (**a**) Tsai and Yeh's model; (**b**) Parker et al.'s model

2.4.2 Example 2: Water Infiltration Problem

This example is similar to Example 1 except for the initial and bottom boundary conditions. The main differences are the initial and boundary pressure distributions do not satisfy the constraint $(\alpha_{21}h_{C21} \geq \alpha_{32}h_{C32})$ in this example while they do in Example 1. This example is presented to demonstrate the feasibility and advantage of using the Tsai and Yeh's model over that of Parker et al.'s model for the multiple flow problems of more than two fluid phases.

In many currently available pressure-based three-phase flow models that used Parker et al.'s law, negative degrees of saturation are obtained with these prescribed initial and boundary conditions. The variable-switch algorithm implemented in those models would reject these prescribed conditions. It is obvious that the rejection is due to Parker's constitutive law used, not based on any physical grounds. Therefore, simulations with those models will exclude initial and boundary conditions that might otherwise be possible. On the other hand, in many currently available fractional flow-based three-phase flow models, the occurrence of negative degrees of saturation would have stymied the simulation. In other words, an otherwise feasibly prescribed initial and boundary pressure distribution would not produce simulations.

In this example, were Parker's model used, negative degree of saturation for NAPL would have resulted. On the other hand, the use of present model will not result in negative degrees of saturation, and thus, the prescribed initial and boundary pressure distribution would not stymie the simulation as demonstrated in this example.

Figure 2.4 shows the domain of interest. Similar to Example 1, water infiltrates into the top of the soil column with a constant mass flux of $10\,\mathrm{g/cm^2/day}$ and zero NAPL and air mass fluxes. At the bottom of the column, the pressure distributions of three phases are maintained at their initial values. The pressure distributions are specified such that they do not satisfy the constraint $(\alpha_{21}h_{C21} > \alpha_{32}h_{C32})$. The initial and bottom boundary values are given as follows. The pressure of water is $7.156 \times 10^{15}\mathrm{g/cm/day^2}$, the pressure of NAPL is $7.235 \times 10^{15}\,\mathrm{g/cm/day^2}$, and the pressure of air is $7.465 \times 10^{15}\mathrm{g/cm/day^2}$. The boundary conditions at the top are the same as that in Example 1: the mass fluxes of water, NAPL, and air are $\mathbf{n} \cdot \mathbf{M}_1 = -10\mathrm{g/cm^2/day}$, $\mathbf{n} \cdot \mathbf{M}_2 = 0$, and $\mathbf{n} \cdot \mathbf{M}_3 = 0$, respectively. The fluid and material properties are given in Fig. 2.4. The initial time-step size is 5.0×10^{-5}day, and each subsequent time-step size is increased by 10% until a maximum time-step size of 1.0×10^{-3}day is reached.

Plausible solutions are obtained with the present model. The solution for degrees of saturation in each phase is depicted in Fig. 2.5. It is seen that NAPL and air are displaced downward from the top of the soil column, while water infiltrates into the column, as expected. Additionally, because NAPL is squeezed by the constant infiltration of water, it is observed that the peak of NAPL saturation moves downward with increasing simulation times, as expected. The variations in air density are shown in Fig. 2.6. It is seen that the air density increases while water constantly infiltrates into the system, as expected.

The initial and prescribed boundary pressure distributions in Example 2 do not satisfy the constraint inherent in Parker et al.'s model. Therefore, for such pressure distributions, using Parker et al.'s model either will not yield solutions using fractional flow-based models or may generate wrong solutions using pressure-based models due to the switch of primary variables. In contrast, with the use of Tsai and Yeh's model, the present multiphase flow model is more physically realistic and is capable of simulating the problems which cover all possible pressure distributions.

2.4.3 Example 3: NAPL Infiltration Problem

In Example 3, NAPL constantly infiltrates into a 165 cm long by 65 cm high soil block shown in Fig. 2.7. The initial conditions of three phases are the following: the water saturation is $S_1 = 0.1$, the NAPL saturation is $S_2 = 0.1$, and the air saturation is $S_3 = 0.8$. Since a $10\,\mathrm{g/cm^2/day}$ NAPL mass flux, zero water, and air

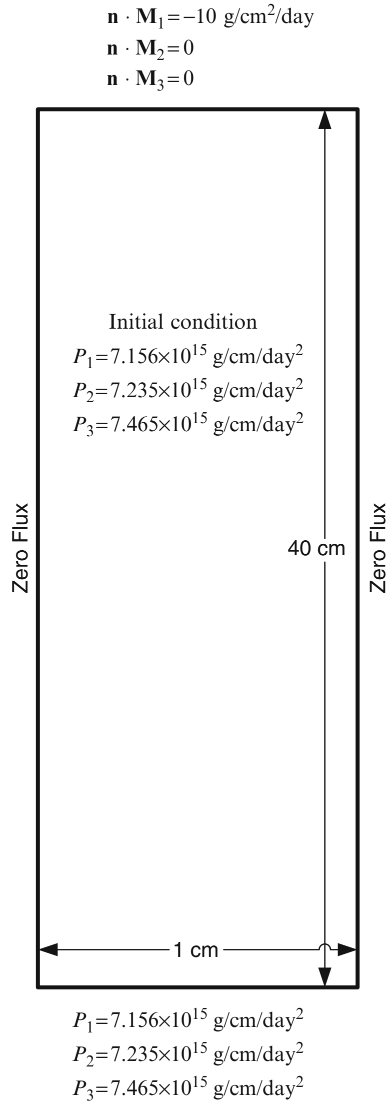

Finite element discretization

Total number of nodes = 82
Total number of elements = 40

Fluid properties

$\rho_1^0=1.0$ g/cm^3
$\rho_2^0=1.4$ g/cm^3
$\rho_3^0=1.0\times10^{-3}$ g/cm^3
$\mu_1=841.0828$ g/cm/day
$\mu_2=690.0828$ g/cm/day
$\mu_3=15.81$ g/cm/day
$\beta_1=6.162\times10^{-21}$ cm day^2/g
$\beta_2=4.086\times10^{-21}$ cm day^2/g
$\alpha_p=2.057\times10^{-21}$ cm day^2/g
$\frac{M}{RT}=1.557\times10^{-19}$ day^2/cm^2

Material properties

$\mathbf{k}=4.27\times10^{-8}$ cm^2
$\phi=0.25$
$\alpha_{31}=0.044$ cm^{-1}
$\alpha_{32}=0.099$ cm^{-1}
$\alpha_{21}=0.11$ cm^{-1}
$n=2.2$
$S_{ir}=0$

Remark

$\alpha_{21}h_{21}<\alpha_{32}h_{32}$
Not satisfying the constraint in Parker et al.'s constitutive laws.

Fig. 2.4 The problem description and relevant parameters of Example 2

mass fluxes infiltrate into an opening on the top, the boundary conditions therein are specified as the mass flux of water is $\mathbf{n}\cdot\mathbf{M}_1=0$, the mass flux of NAPL is $\mathbf{n}\cdot\mathbf{M}_2=-10\text{g}/\text{cm}^2/\text{day}$, and the mass flux of air is $\mathbf{n}\cdot\mathbf{M}_3=0$. On the left side of the block, the pressure distributions are specified as follows: the pressure of water is $P_1=7.234\times10^{15}\,\text{g}/\text{cm}/\text{day}^2$, the pressure of NAPL is $P_2=7.336\times10^{15}\,\text{g}/\text{cm}/\text{day}^2$, and the pressure of air is $P_3=7.611\times10^{15}\,\text{g}/\text{cm}/\text{day}^2$. On the right side, the

Fig. 2.5 Distributions of the degrees of saturation for Example 2: (**a**) water saturation, (**b**) NAPL saturation, and (**c**) air saturation

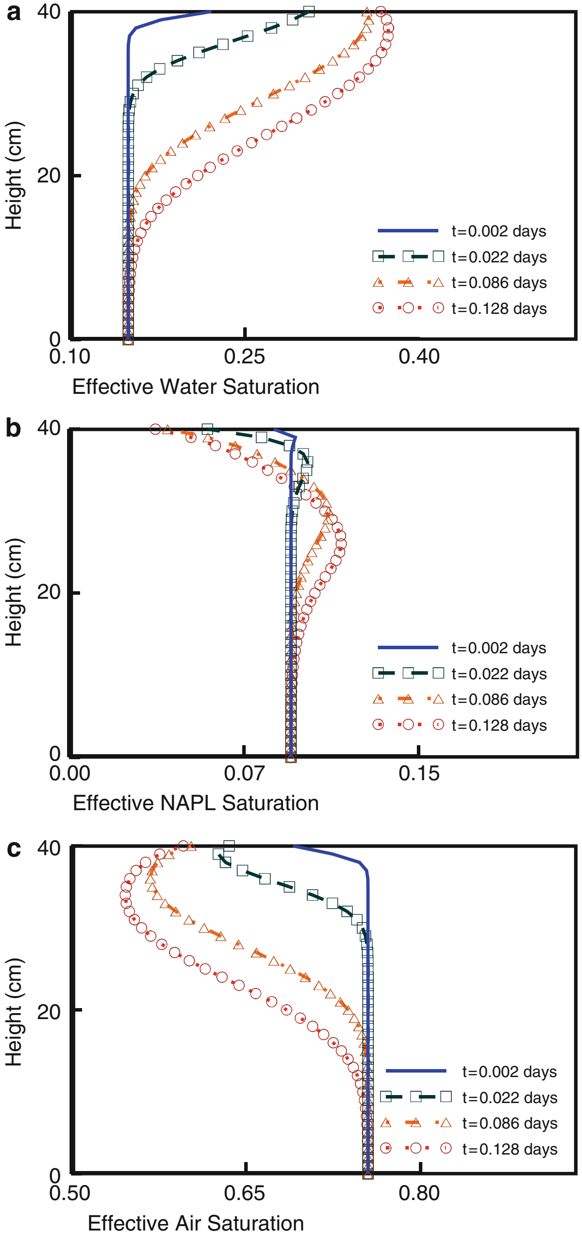

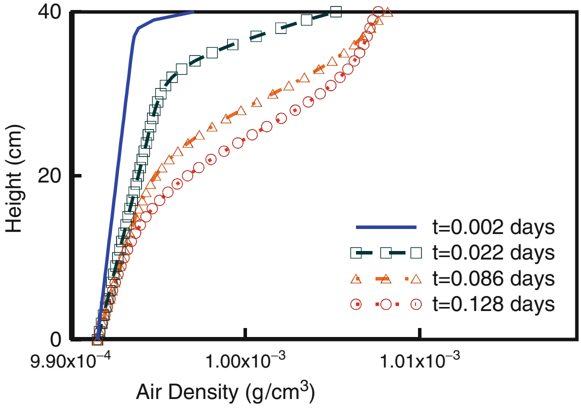

Fig. 2.6 Distributions of the density of air for Example 2

pressure distribution is the pressure of water is $P_1 = 7.087 \times 10^{15}\,\mathrm{g/cm/day^2}$, the pressure of NAPL is $P_2 = 7.189 \times 10^{15}\,\mathrm{g/cm/day^2}$, and the pressure of air is $P_3 = 7.465 \times 10^{15}\,\mathrm{g/cm/day^2}$. On the bottom, the boundary condition is specified as the water saturation is $S_1 = 0.1$, the NAPL saturation is $S_2 = 0.1$, and the air saturation is $S_3 = 0.8$. The block is pumped with a flux rate $-50\,\mathrm{cm^3/day}$ at five well points 0.2 days after the infiltration began. The fluid and material properties are given in Fig. 2.7 as well. The initial time-step size is 1.0×10^{-4}day, and each subsequent time-step size is increased by 10% until a maximum time-step size of 1.0×10^{-3}day is reached.

The distributions of NAPL, water, and air saturation through time are given in Figs. 2.8, 2.9, and 2.10, respectively. It is seen that the water and NAPL saturations approximate to zero around the well due to the effect of pumping. In Fig. 2.8, the pumping affects the distributions of NAPL contour obviously at 0.284 and 0.984 days but has little effects at 2.984 days. The continuous pumping leads the NAPL saturation near well points to approximate zero and hence reduces its conductivity. Therefore the infiltrated NAPL will not flow to the well. As a result, the pore space near the well is occupied mostly by the air phase (Fig. 2.10) via its high conductivity. Figure 2.9 indicates that the water saturation changes little through the entire domain of interest except for a small region near the well. This example implies that a pump and treat strategy of NAPL removal would not work for this particular case.

2.4.4 *Example 4: NAPL Infiltration Problem*

In this example, NAPL infiltrates into a 165 cm long by 65 cm highly unsaturated block with zero mass fluxes of water and air shown in Fig. 2.11. The majority of the block is filled with sands. Three additional materials are included in small portions of the domain, which are clay, silt, and gravel. The initial conditions of three phases

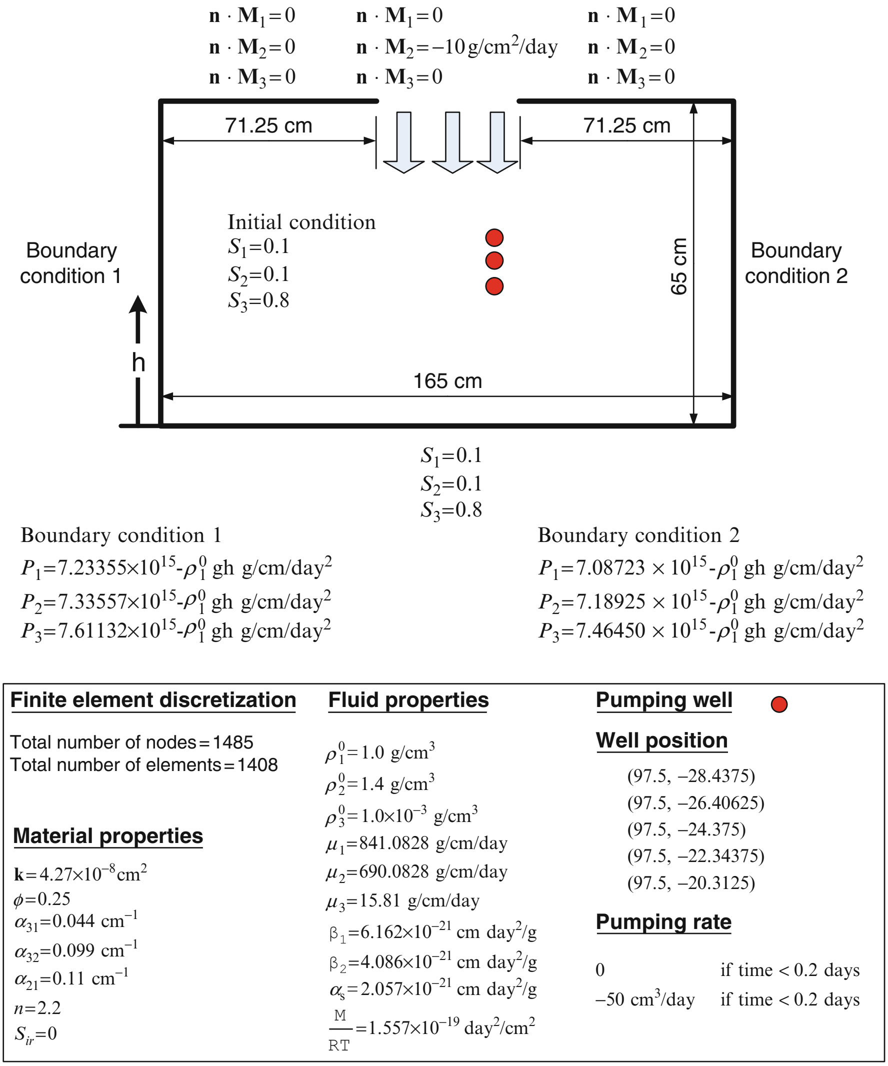

Fig. 2.7 The problem description and relevant parameters of Example 3

are: the water saturation is $S_1 = 0.2$, the NAPL saturation is $S_2 = 0.1$, and the air saturation is $S_3 = 0.7$. Since a $10\,\mathrm{g/cm^2/day}$ NAPL mass flux, zero water, and air mass fluxes infiltrate into an opening on the top, the boundary conditions therein are specified as: the mass flux of water is $\mathbf{n}\cdot\mathbf{M}_1 = 0$, the mass flux of NAPL is $\mathbf{n}\cdot\mathbf{M}_2 = -10\mathrm{g/cm^2/day}$, and the mass flux of air is $\mathbf{n}\cdot\mathbf{M}_3 = 0$. On the left and right sides, the pressure distributions of three phases are specified as follows: the

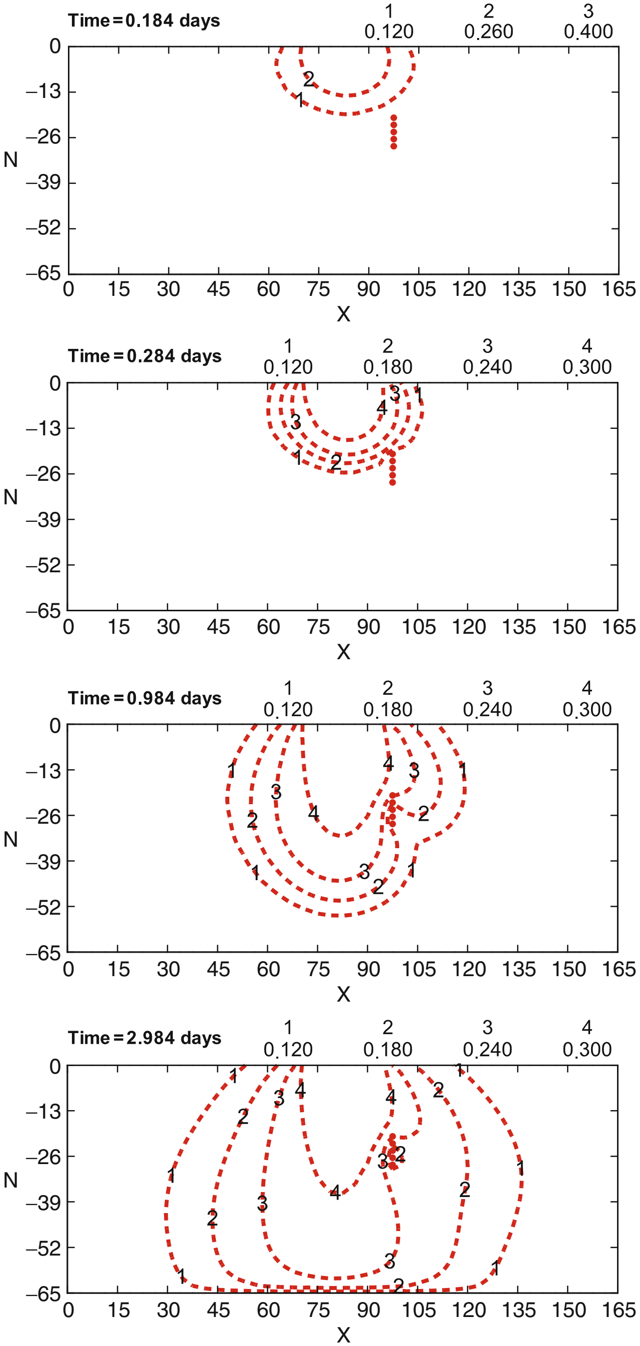

Fig. 2.8 Distributions of the degrees of saturation of NAPL for Example 3

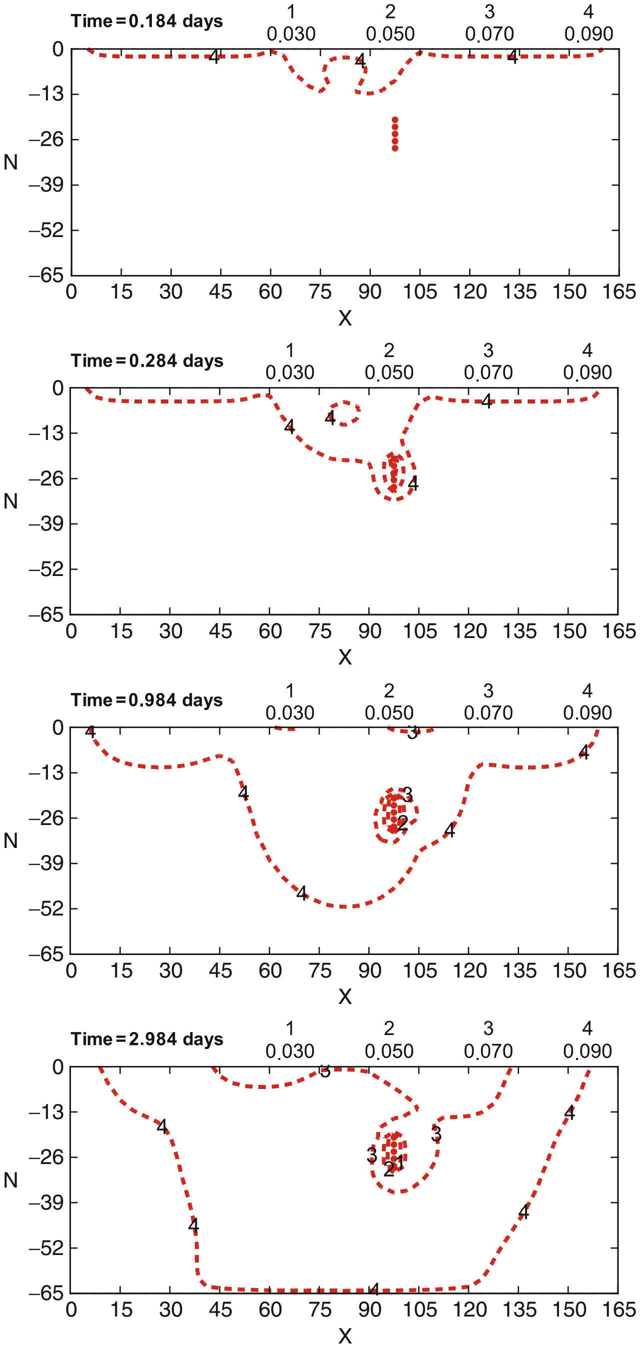

Fig. 2.9 Distributions of the degrees of saturation of water for Example 3

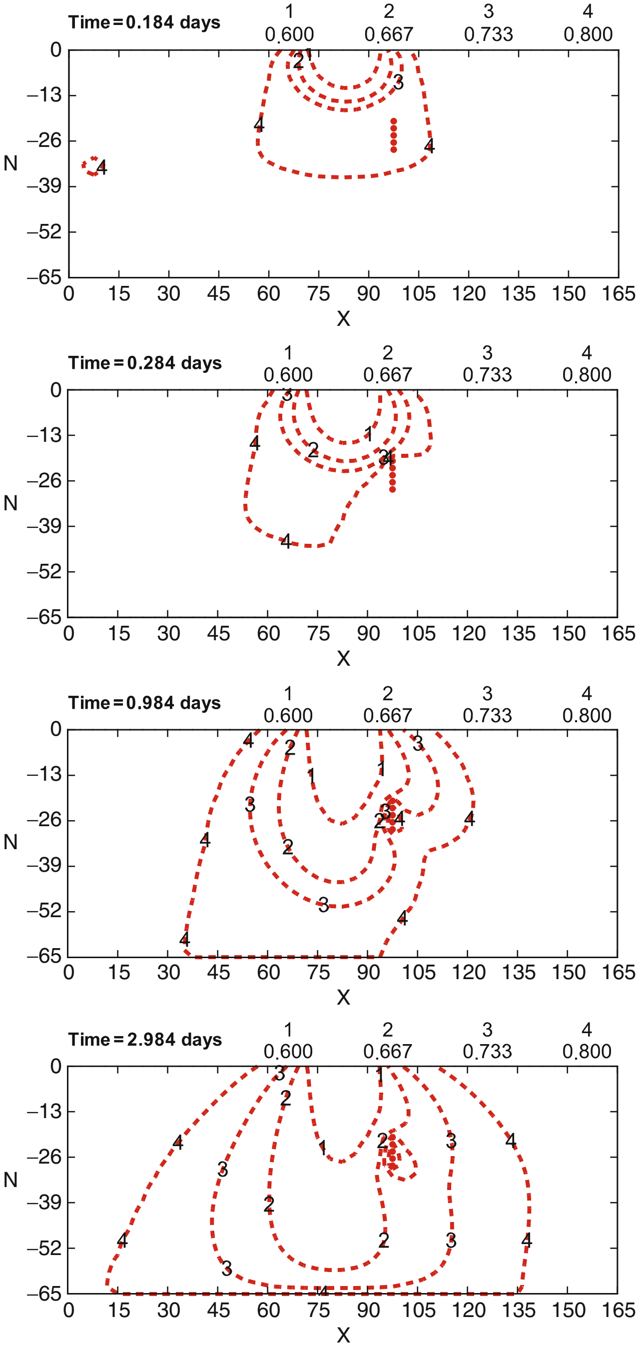

Fig. 2.10 Distributions of the degrees of saturation of air for Example 3

pressure of water is $P_1 = 7.351 \times 10^{15}\,\mathrm{g/cm/day^2}$, the pressure of NAPL is $P_2 = 7.420 \times 10^{15}\,\mathrm{g/cm/day^2}$, and the pressure of air is $P_3 = 7.611 \times 10^{15}\,\mathrm{g/cm/day^2}$. On the bottom, the boundary condition is specified as: the water saturation is $S_1 = 0.2$, the NAPL saturation is $S_2 = 0.1$, and the air saturation is $S_3 = 0.7$. The fluid properties are also given in Fig. 2.11. The initial time-step size is 1.0×10^{-4}day, and each subsequent time-step size is increased by 10% until a maximum time-step size of 1.0×10^{-3}day is reached.

The distributions of degrees of saturation for NAPL, water, and air are depicted in Figs.2.12, 2.13, and 2.14, respectively. Two liquid phases (water and NAPL) behave similarly in this highly heterogeneous system of media. When they reach the gravel, they flow through it quickly because the permeability of gravel is much higher than that of the sand. When they reach the silt, they flow on its surface and move sideway and flow down with a small portion going through the silt. When they reach the very impermeable clay, they almost completely float on its surface and flow sideway then downward, with very little going through the clay. It is seen from Fig. 2.14 that as NAPL infiltrates, air is to first move to both sides and then upward because of its low density. As the air moves up, it bypasses the relatively impermeable silt and clay but goes through the very permeable gravel quickly. The results show the capability of the present model to generate reasonable simulations for the NAPL infiltration problem.

2.5 Conclusions

In this investigation, the constitutive law proposed by Tsai and Yeh is successfully implemented in a fractional flow-based multiphase flow model to simulate compressible subsurface flow problems with different possible pressure distributions. To demonstrate the feasibility and advantage of the developed model, four examples are presented. The results clearly show the feasibility and advantage of implementing the new constitutive law to simulate compressible flow problems, especially with the cases that prescribed pressure distributions do not satisfy the constraint required by Parker et al.'s model. With the implementation of the new saturationcapillary pressure relationship, plausible solutions are obtained with all possible initial and boundary pressure distributions. In summary, the implementation of the advanced constitutive law makes the present multiphase flow model complete and physically realistic to simulate the compressible flow problems with all possible pressure distributions.

Acknowledgements Research is supported by National Science Council under Contract No. NSC 99–2116-M-008–020 with National Central University.

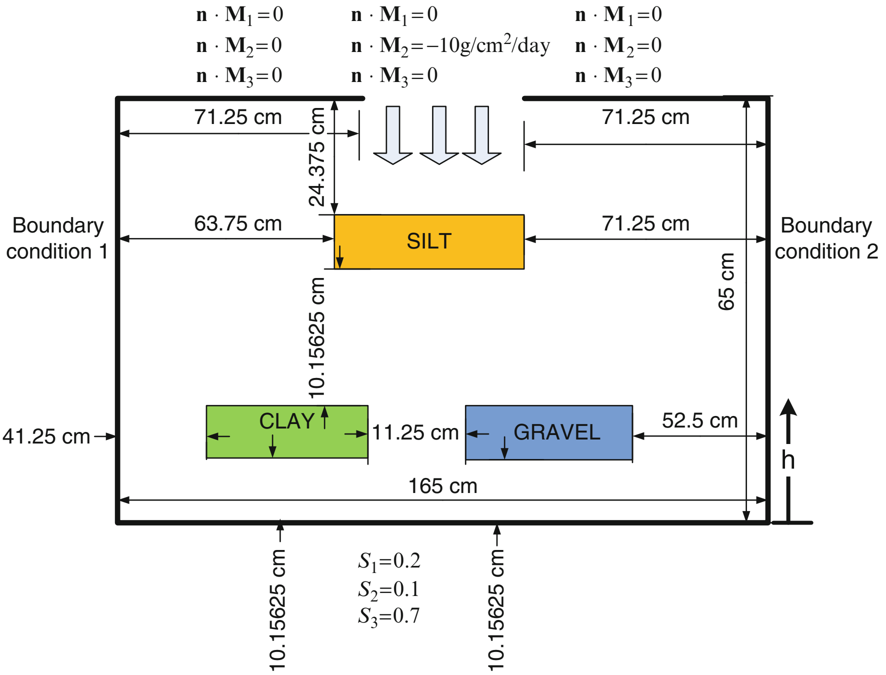

Initial condition
$S_1=0.2$
$S_2=0.1$
$S_3=0.7$

Boundary condition 1
$P_1=7.35063\times10^{15}\text{-}\rho_1^0\,\text{gh g/cm/day}^2$
$P_2=7.42017\times10^{15}\text{-}\rho_1^0\,\text{gh g/cm/day}^2$
$P_3=7.61132\times10^{15}\text{-}\rho_1^0\,\text{gh g/cm/day}^2$

Boundary condition 2
$P_1=7.35063\times10^{15}\text{-}\rho_1^0\,\text{gh g/cm/day}^2$
$P_2=7.42017\times10^{15}\text{-}\rho_1^0\,\text{gh g/cm/day}^2$
$P_3=7.61132\times10^{15}\text{-}\rho_1^0\,\text{gh g/cm/day}^2$

Finite element discretization

Total number of nodes = 1485
Total number of elements = 1408

Material properties

$\mathbf{k}=4.27\times10^{-8}\,\text{cm}^2$
$\phi=0.25$
$\alpha_{31}=0.044\ \text{cm}^{-1}$
$\alpha_{32}=0.099\ \text{cm}^{-1}$
$\alpha_{21}=0.11\ \text{cm}^{-1}$
$n=2.2$
$S_{ir}=0$

GRAVEL
$\mathbf{k}=4.27\times10^{-6}\ \text{cm}^2$
$\phi=0.25$

CLAY
$\mathbf{k}=4.27\times10^{-12}\ \text{cm}^2$
$\phi=0.40$

SILT
$\mathbf{k}=4.27\times10^{-10}\ \text{cm}^2$
$\phi=0.35$

Fluid properties

$\rho_1^0=1.0\ \text{g/cm}^3$
$\rho_2^0=1.4\ \text{g/cm}^3$
$\rho_3^0=1.0\times10^{-3}\ \text{g/cm}^3$
$\mu_1=841.0828\ \text{g/cm/day}$
$\mu_2=690.0828\ \text{g/cm/day}$
$\mu_3=15.81\ \text{g/cm/day}$
$\beta_1=6.162\times10^{-21}\ \text{cm day}^2\text{/g}$
$\beta_2=4.086\times10^{-21}\ \text{cm day}^2\text{/g}$
$\alpha_s=2.057\times10^{-21}\ \text{cm day}^2\text{/g}$
$\frac{\text{M}}{\text{RT}}=1.557\times10^{-19}\ \text{day}^2\text{/cm}^2$

Fig. 2.11 The problem description and relevant parameters of Example 4

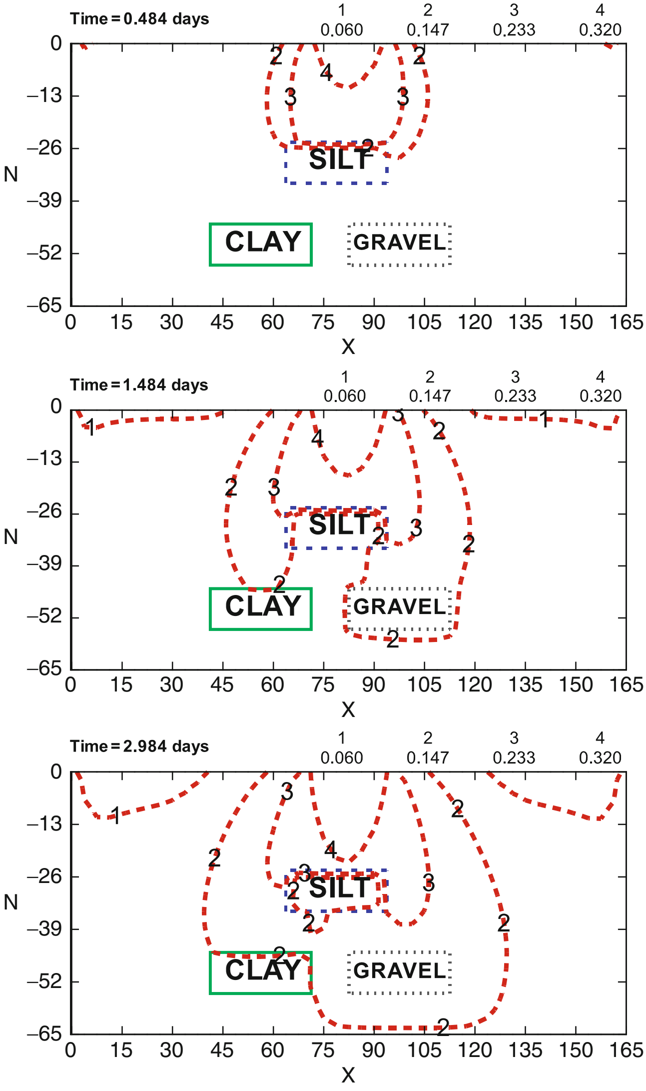

Fig. 2.12 Distributions of the degrees of saturation of NAPL for Example 4

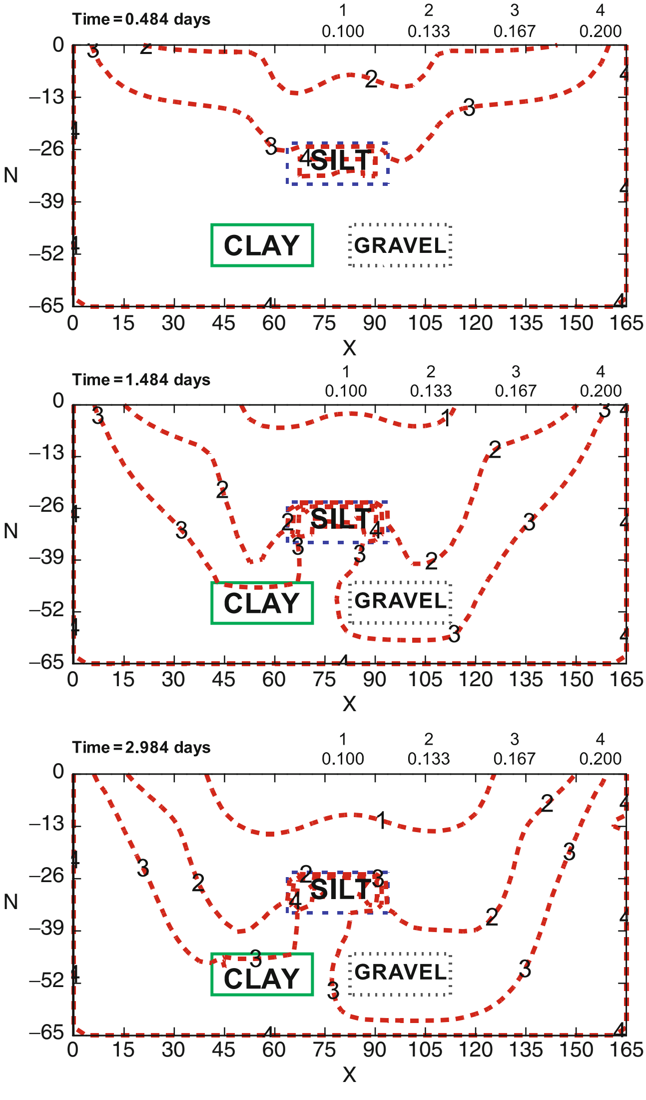

Fig. 2.13 Distributions of the degrees of saturation of water for Example 4

Appendix A: Numerical Discretizations with FEM

The governing equation for the total pressure, Eq. (2.5), is discretized with the standard Galerkin FEM as follows:

$$[C^p]\left\{\frac{\partial P_t}{\partial t}\right\} + [C^p_{s1}]\left\{\frac{\partial S_1}{\partial t}\right\} + [C^p_{st}]\left\{\frac{\partial S_t}{\partial t}\right\} + [DD_p]\{P_t\} = \{f_p\}, \qquad (A.1)$$

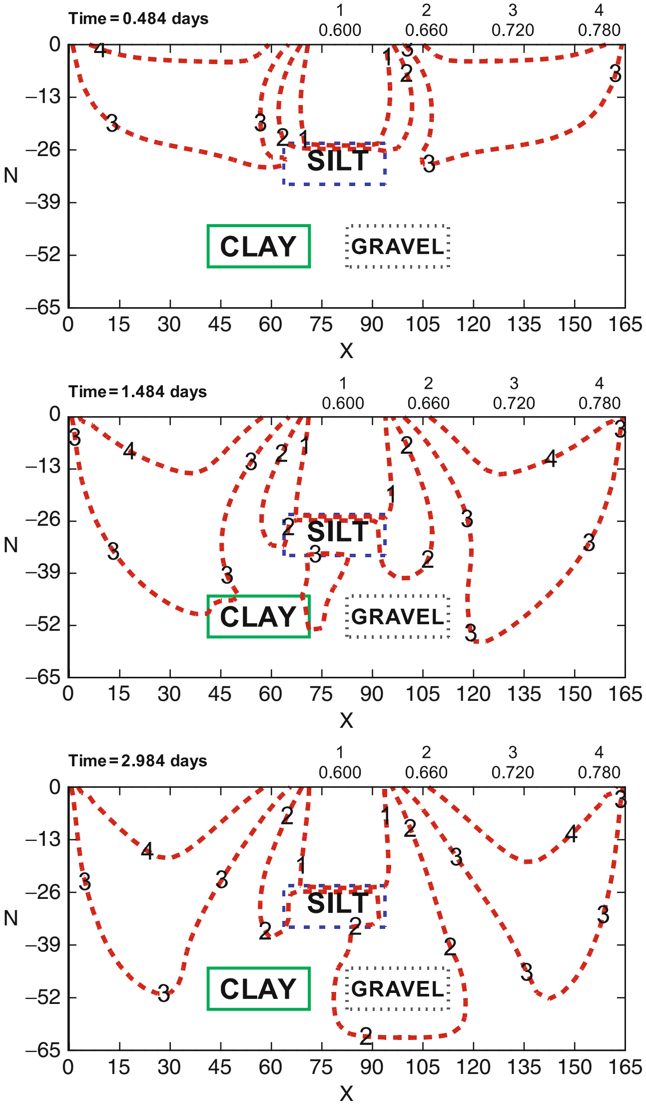

Fig. 2.14 Distributions of the degrees of saturation of air for Example 4

in which

$$[C^p]_{i,j} = \int_{\Omega} (C_{pt}) \nabla N_i \cdot \nabla N_j \mathrm{d}R, \tag{A.2}$$

$$\left[C_{s1}^{p}\right]_{i,j}=\int\limits_{\Omega}(C_{s1})\nabla N_i\cdot\nabla N_j\mathrm{d}R, \tag{A.3}$$

$$\left[C_{st}^{p}\right]_{i,j}=\int\limits_{\Omega}(C_{st})\nabla N_i\cdot\nabla N_j\mathrm{d}R, \tag{A.4}$$

$$[DD_p]_{i,j}=\int\limits_{\Omega}\nabla N_i\cdot\nabla N_j\mathrm{d}R, \tag{A.5}$$

$$\{f_p\}_i=-\int\limits_{\Omega}\nabla N_i\bullet[\overline{\rho}g\nabla z]\,\mathrm{d}R-\int\limits_{B}\mathbf{n}\bullet[N_i(\mathbf{M}_t)]\,\mathrm{d}B+\int\limits_{\Omega}N_i[Q_t]\mathrm{d}R, \tag{A.6}$$

where $[C^p]$ is the mass matrix associated with total pressure, $[C_{s1}^p]$ is the mass matrix associated with water saturation for total pressure, $[C_{st}^p]$ is the mass matrix associated with total liquid saturation for total pressure, $[DD_p]$ is the dispersion-diffusion matrix associated with P_t in the governing equation for total pressure, and $\{f_p\}$ is the flux due to advection, dispersion-diffusion, and gravity in the governing equation for total pressure.

The governing equations for the saturations of water and total liquid, Eqs. (2.15) and (2.16), are discretized by the standard Galerkin and the upstream FEMs. The optimized weighting parameters for the upstream FEM are found in the literature (e.g., Carrano and yeh 1995; Christie et al. 1976). Other more robust numerical discretization methods may be employed, but that will not alter the key points addressed in this chapter. The formulations are given as follows:

$$\begin{aligned}&[C_1^p]\left\{\frac{\partial P_t}{\partial t}\right\}+[C_1^w]\left\{\frac{\partial S_1}{\partial t}\right\}+[C_1^t]\left\{\frac{\partial S_t}{\partial t}\right\}+[ADW_1]\{S_1\}+[ADT_1]\{S_t\}+[DDW_1]\{S_1\}\\&\quad+[DDT_1]\{S_t\}+[DST_1]\{S_1\}=\{f_1\},\end{aligned} \tag{A.7}$$

and

$$\begin{aligned}&[C_2^p]\left\{\frac{\partial P_t}{\partial t}\right\}+[C_2^w]\left\{\frac{\partial S_1}{\partial t}\right\}+[C_2^t]\left\{\frac{\partial S_t}{\partial t}\right\}+[ADW_2]\{S_1\}+[ADT_2]\{S_t\}+[DDW_2]\{S_1\}\\&\quad+[DDT_2]\{S_t\}+[DST_2]\{S_t\}=\{f_2\},\end{aligned} \tag{A.8}$$

in which

$$[C_1^p]_{i,j}=\int\limits_{\Omega}\left(\phi S_1\frac{\partial\rho_1}{\partial P_1}-\kappa_1C_{pt}+\rho_1S_1\alpha_p\right)N_iN_jdR, \tag{A.9}$$

$$[C_1^w]_{i,j}=\int\limits_{\Omega}\left(\phi S_1\frac{\partial\rho_1}{\partial P_1}(1-\kappa_1)\frac{\mathrm{d}P_{C12}}{\mathrm{d}S_1}+\rho_1\phi-\kappa_1C_{s1}+\rho_1S_1\alpha_p\left[P_{C12}+(S_1-\kappa_1)\frac{\mathrm{d}P_{C12}}{\mathrm{d}S_1}\right]\right)N_iN_j\mathrm{d}R, \tag{A.10}$$

$$[C_1^t]_{i,j}=\int\limits_{\Omega}\left(\phi S_1\frac{\partial\rho_1}{\partial P_1}\kappa_3\frac{\mathrm{d}P_{C23}}{\mathrm{d}S_t}-\kappa_1C_{st}+\rho_1S_1\alpha_p\left[P_{C23}+(S_t-1+\kappa_3)\frac{\mathrm{d}P_{C23}}{\mathrm{d}S_t}\right]\right)N_iN_j\mathrm{d}R, \tag{A.11}$$

$$[ADW_1]_{i,j} = \int_{\Omega} W_i \frac{\mathrm{d}\kappa_1}{\mathrm{d}S_1} \mathbf{M}_t \bullet \nabla N_j \mathrm{d}R - \int_{\Omega} W_i \left[\frac{\mathrm{d}\left(\kappa_1 \boldsymbol{\kappa} \bullet (\rho_1 - \overline{\rho})\, g \nabla z\right)}{\mathrm{d}S_1} \right] \bullet \nabla N_j \mathrm{d}R, \tag{A.12}$$

$$[ADT_1]_{i,j} = \int_{\Omega} W_i \frac{\mathrm{d}\kappa_1}{\mathrm{d}S_t} \mathbf{M}_t \bullet \nabla N_j \mathrm{d}R - \int_{\Omega} W_i \left[\frac{\mathrm{d}\left(\kappa_1 \boldsymbol{\kappa} \bullet (\rho_1 - \overline{\rho})\, \rho_1 g \nabla z\right)}{\mathrm{d}S_t} \right] \bullet \nabla N_j \mathrm{d}R, \tag{A.13}$$

$$[DDW_1]_{i,j} = \int_{\Omega} \nabla N_i \bullet \left[\kappa_1 \boldsymbol{\kappa} \bullet (1 - \kappa_1) \frac{\mathrm{d}P_{C12}}{\mathrm{d}S_1} \nabla N_j \right] \mathrm{d}R + \int_{\Omega} \nabla N_i \bullet \left[\kappa_1 \boldsymbol{\kappa} \bullet \kappa_3 \frac{\mathrm{d}P_{C23}}{\mathrm{d}S_1} \nabla N_j \right] \mathrm{d}R, \tag{A.14}$$

$$[DDT_1]_{i,j} = \int_{\Omega} \nabla N_i \bullet \left[\kappa_1 \boldsymbol{\kappa} \bullet (1 - \kappa_1) \frac{\mathrm{d}P_{C12}}{\mathrm{d}S_t} \nabla N_j \right] \mathrm{d}R + \int_{\Omega} \nabla N_i \bullet \left[\kappa_1 \kappa \bullet \kappa_3 \frac{\mathrm{d}P_{C23}}{\mathrm{d}S_t} \nabla N_j \right] \mathrm{d}R, \tag{A.15}$$

$$[DST_1]_{i,j} = \int_{\Omega} N_i \left(\frac{\kappa_1 Q_t - Q_1}{S_1} \right) N_i \mathrm{d}R, \tag{A.16}$$

$$\{f_1\}_i = \int_{B} N_i \mathbf{n} \bullet [\kappa_1 \mathbf{M}_t] \mathrm{d}B - \int_{B} N_i \mathbf{n} \bullet [\mathbf{M}_1] \mathrm{d}B - \int_{B} N_i \mathbf{n} \bullet [\kappa_1 \kappa \bullet (\rho_1 - \overline{\rho})\, g \nabla z] \mathrm{d}B, \tag{A.17}$$

$$[C_2^p]_{i,j} = -\int_{\Omega} \left(\phi S_3 \frac{\partial \rho_3}{\partial P_3} - \kappa_3 C_{pt} + \rho_3 S_3 \alpha_p \right) N_i N_j \mathrm{d}R, \tag{A.18}$$

$$[C_2^w]_{i,j} = \int_{\Omega} \left(\phi S_3 \frac{\partial \rho_3}{\partial P_3} \kappa_1 \frac{\mathrm{d}P_{C12}}{\mathrm{d}S_1} + \kappa_3 C_{s1} - \rho_3 S_3 \alpha_p \left[P_{C12} + (S_1 - \kappa_1) \frac{\mathrm{d}P_{C12}}{\mathrm{d}S_1} \right] \right) N_i N_j \mathrm{d}R, \tag{A.19}$$

$$[C_2^t]_{i,j} = \int_{\Omega} \left(\phi S_3 \frac{\partial \rho_3}{\partial P_3} (1 - \kappa_3) \frac{\mathrm{d}P_{C23}}{\mathrm{d}S_t} + \kappa_3 C_{st} + \rho_3 \phi - \rho_3 S_3 \alpha_p \left[P_{C23} + (S_t - 1 + \kappa_3) \frac{\mathrm{d}P_{C23}}{\mathrm{d}S_t} \right] \right) N_i N_j \mathrm{d}R, \tag{A.20}$$

$$[ADW_2]_{i,j} = -\int_{\Omega} W_i \mathbf{M}_t \bullet \left[\frac{\mathrm{d}\kappa_3}{\mathrm{d}S_1} \nabla N_j \right] \mathrm{d}R + \int_{\Omega} W_i \left[\frac{\mathrm{d}\left(\kappa_3 \kappa \bullet (\rho_3 - \overline{\rho})\, g \nabla z\right)}{\mathrm{d}S_1} \right] \cdot \nabla N_j \mathrm{d}R, \tag{A.21}$$

$$[ADT_2]_{i,j} = -\int_{\Omega} W_i \mathbf{M}_t \bullet \left[\frac{\mathrm{d}\kappa_3}{\mathrm{d}S_t} \nabla N_j \right] \mathrm{d}R + \int_{\Omega} W_i \left[\frac{\mathrm{d}\left(\kappa_3 \boldsymbol{\kappa} \bullet (\rho_3 - \overline{\rho})\, g \nabla z\right)}{\mathrm{d}S_t} \right] \bullet \nabla N_j \mathrm{d}R, \tag{A.22}$$

$$[DDW_2]_{i,j} = \int_{\Omega} \nabla N_i \bullet \left[\kappa_3 \boldsymbol{\kappa} \bullet \kappa_1 \frac{\mathrm{d}P_{C12}}{\mathrm{d}S_1} \nabla N_j \right] \mathrm{d}R + \int_{\Omega} \nabla N_i \bullet \left[\kappa_3 \boldsymbol{\kappa} \bullet (1 - \kappa_3) \frac{\mathrm{d}P_{C23}}{\mathrm{d}S_1} \nabla N_j \right] \mathrm{d}R, \tag{A.23}$$

$$[DDT_2]_{i,j} = \int_{\Omega} \nabla N_i \bullet \left[\kappa_3 \boldsymbol{\kappa} \bullet \kappa_1 \frac{\mathrm{d}P_{C12}}{\mathrm{d}S_t} \nabla N_j \right] \mathrm{d}R + \int_{\Omega} \nabla N_i \bullet \left[\kappa_3 \boldsymbol{\kappa} \bullet (1 - \kappa_3) \frac{\mathrm{d}P_{C23}}{\mathrm{d}S_t} \nabla N_j \right] \mathrm{d}R, \tag{A.24}$$

$$[DST_2]_{i,j} = \int_{\Omega} N_i \left(\frac{-\kappa_3 Q_t + Q_3}{S_t} \right) N_i \mathrm{d}R, \tag{A.25}$$

$$\{f_2\}_i = -\int_{B} N_i \mathbf{n} \bullet [\kappa_3 \mathbf{M}_t] \mathbf{d}B + \int_{B} N_i \mathbf{n} \bullet [\mathbf{M}_3] \mathbf{d}B + \int_{B} N_i \mathbf{n} \bullet [\kappa_3 \boldsymbol{\kappa} \bullet (\rho_3 - \overline{\rho})\, g \nabla z] \mathbf{d}B, \tag{A.26}$$

where $[C_1^p]$ is the mass matrix associated with total pressure for water saturation; $[C_1^w]$ is the mass matrix associated with water saturation; $[C_1^t]$ is the mass matrix associated with total liquid saturation for water saturation; $[ADW_1]$ is the advection and gravity matrix associated with water saturation; $[ADT_1]$ is the advection and gravity matrix associated with total liquid saturation; $[DDW_1]$ is the dispersion-diffusion matrix associated with water saturation; $[DDT_1]$ is the dispersion-diffusion matrix associated with total liquid saturation; $[DST_1]$ is the matrix from the sink or source; $\{f_1\}$ is the flux due to advection, dispersion-diffusion, and gravity; $[C_2^p]$ is the mass matrix associated with total pressure for total liquid saturation; $[C_2^s]$ is the mass matrix associated with water saturation for total liquid saturation; $[C_2^t]$ is the mass matrix associated with total liquid saturation; $[ADW_2]$ is the advection and gravity matrix associated with water saturation; $[ADT_2]$ is the advection and gravity matrix associated with total liquid saturation; $[DDW_2]$ is the dispersion-diffusion matrix associated with water saturation; $[DDT_2]$ is the dispersion-diffusion matrix associated with total liquid saturation; $[DST_2]$ is the matrix from the sink or source; $\{f_2\}$ is the flux due to advection, dispersion-diffusion, and gravity; W_i is the upstream weighting function; N_i is the Galerkin interpolation function; $\mathbf{n}$ is the outward normal vector; Ω is the region of interest; and B is the boundary. Note that the subscripts 1 and 2 in the definitions of all matrices denote the first and second equation of two saturation equations, respectively. By assembling Eqs. (A.7) and (A.8), the resulting coupled matrix for saturations of water and total liquid is given as follows:

$$\begin{bmatrix} C_1^w & C_1^t \\ C_2^w & C_2^t \end{bmatrix} \begin{Bmatrix} \frac{\partial S_1}{\partial t} \\ \frac{\partial S_t}{\partial t} \end{Bmatrix} + \begin{bmatrix} DDW_1 + ADW_1 + DST_1 & DDT_1 + ADT_1 \\ DDW_2 + ADW_2 & DDT_2 + ADT_2 + DST_2 \end{bmatrix} \begin{Bmatrix} S_1 \\ S_t \end{Bmatrix} = \begin{Bmatrix} f_1 \\ f_2 \end{Bmatrix} - \begin{Bmatrix} C_1^p \frac{\partial P_t}{\partial t} \\ C_2^p \frac{\partial P_t}{\partial t} \end{Bmatrix}. \tag{A.27}$$

To obtain the solutions for the total pressure, saturations of water, and total liquid, we use the Bi-CGSTAB method proposed by vant der Vorst (1992).

References

Binning P, Celia MA (1999) Practical implementation of the fractional flow approach to multiphase flow simulation. Adv Water Resour 22:461–478

Carrano CS Jr, Yeh GT (1995) A Fourier analysis of dynamic optimization of the Petrov-Galerkin finite element method. Int J Numer Methods Eng 38:4123–4155

Christie I, Griffiths DF, Mitchell AR, Zienkiewicz OC (1976) Finite element methods for second order differential equations with significant first derivatives. Int J Numer Methods Eng 10:1389–1443

Celia MA, Binning P (1992) Two-phase unsaturated flow: one-dimensional simulation and air-phase velocities. Water Resour Res 28:2819–2828

Guarnaccia JF, Pinder GF (1997) NAPL: A mathematical model for the study of NAPL contamination in granular soils, equation development and simulator documentation. The University of Vermont, RCGRD #95–22

Kaluarachchi JJ, JC Parker (1989) An efficient finite elements method for modeling multiphase flow. Water Resour Res 25:43–54

Khoei AR, Mohammadnejad T (2011) Numerical modeling of multiphase fluid flow in deforming porous media: a comparison between two- and three-phase models for seismic analysis of earth and rockfill damps. Comput Geotech 38:142–166

Laplace PS (1806) Méchanique céleste, suppl. 10th vol

Mualem Y (1976) A new model for predicting the hydraulic conductivity of unsaturated porous media. Water Resour Res 12:513–522

Parker JC, Lenhard RJ, Kuppusamy T (1987a) A parametric model for constitutive properties governing multiphase flow in porous media. Water Resour Res 23(4):618–624

Parker JC, Lenhard RJ (1987b) A model for hysteretic constitutive relations governing multiphase flow 1. saturation-pressure relations. Water Resour Res 23(12):2187–2196

Suk H, Yeh GT (2007) 3D, three-phase flow simulations using the Lagrangian-Eulerian approach with adaptively zooming and peak/valley capturing scheme. J Hydrol Eng 12:14–32

Suk H, Yeh GT (2008) Multiphase flow modeling with general boundary conditions and automatic phase-configuration changes using a fractional-flow approach. Comput Geosci 12:541–571

Tsai CH, Yeh GT (2012) Retention characteristics for multiple-phasefluid systems, Terr Atmos Ocean Sci 23:451–458

van der Vorst HA (1992) Bi-CGSTAB: a fast and smoothly converging variant of Bi-CG for the solution of nonsymmetric linear systems. SIAM Sci Stat Comput 13:631–644

van Genuchten MTh (1980) A closed-form equation for predicting the hydraulic conductivity of unsaturated soils. Soil Sci Soc Am J 44:892–898

White MD, Oostrom M (1996) STOMP subsurface transport over multiple phases, Theory guide, PNL-11217. Pacific Northwest Laboratory, Richland, WA

Yeh GT, Fang YL, Zhang F, Sun JT, Li Y, Li MH, Siegel MD (2010) Numerical modeling of coupled fluid flow and thermal and reactive biogeochemical transport in porous and fractured media. Comput Geosci 14(1):149–170

Yeh GT, Tsai CH (2011) Proposing a new retention function for multiple phase-fluids. Abstract and Program, 2011 AGU Fall Meeting, CD, December 5–9, 2011

Chapter 3
Fluid Pressure Redistribution Events Within a Fault: Impact of Material Property Correlation

Sean A. McKenna and Darin Q. Pike

Abstract Cellular automata (CA) models employ local rules to simulate large-scale behavior. A previously developed CA model of fluid pressure redistribution events within a 2D planar fault system undergoing compression is used to model the size distribution of these events over time. Local fluid pressures exceeding a threshold value cause a rupture (failure) of the surrounding rock, and the fluid pressure is redistributed to surrounding cells. Spatial correlation of the fault compressibility (β) is varied over a range of nearly three orders of magnitude in a model domain of 10^6 cells. The size distribution of all pressure redistribution events changes from a power-law exponential form with a single slope when β is uncorrelated to a power-law exponential form with two slopes at increasing correlation lengths and then back to a single power-law exponential distribution that approximates a uniform distribution as correlation lengths exceed the ergodic limit. The spatially and temporally uniform pattern of events seen in the uncorrelated model rapidly evolve to exhibit emergent behavior as the correlation length increases beyond the grid cell size. Increasing spatial correlation leads to delays in the time to first failure and decreases the time necessary for the ruptures to coalesce and span the fault domain. The resulting spatial pattern of events demonstrates deviations from the random point process associated with uncorrelated β towards increased spatial clustering of events with increasing correlation of the β field. Vertical effective permeability of the fault system at the point where connected failures span the

---

S.A. McKenna (✉)
Geoscience Research and Applications, Sandia National Laboratories
Currently: IBM Research, Smarter Cities Technology Centre, Bldg-3, Damastown Industrial Estate. Mulhuddart, Dublin 15, Ireland
e-mail: seanmcke@ie.ibm.com

D.Q. Pike
Chemical and Biological Systems, Sandia National Laboratories,
P.O. Box 5800, Albuquerque, NM 87185-073, USA
e-mail: dqpike@sandia.gov

P.K. Mishra and K.L. Kuhlman (eds.), *Advances in Hydrogeology*,
DOI 10.1007/978-1-4614-6479-2_3,

© Springer Science+Business Media New York 2013

domain shows that effective permeability is a nonlinear function of the correlation length and is strongly controlled by the size (area) of the domain-spanning failed cluster.

3.1 Introduction

The coupled processes of fluid flow and mechanical behavior of rocks in the Earth's crust are important in a number of geologic processes including earthquakes (Claesson et al. 2007; Sarr and Manga 2003; Rojstaczer et al. 1995), geysers (Ingebritsen and Rojstaczer 1993), and crustal-scale fluid flow (Rojstaczer et al. 2008; Miller et al. 2004). Coupled hydromechanical processes are also the focus of a number of research areas driven by engineering applications including CO_2 sequestration (e.g., Rutqvist et al. 2007; Lucier et al. 2006), enhanced geothermal energy production (Majer et al. 2007), and deep borehole injection of fluids (Hsieh and Bredehoeft 1981; Healy et al. 1968; Zoback and Harjes 1997; Rutledge et al. 2004). Here, we examine coupled hydromechanical processes in a fault using a cellular automata model with a focus on the impact of spatially correlated material properties on the evolution of fault system behavior.

The "toggle-switch" permeability model developed by Miller and Nur (2000) considers permeability to be either zero or infinite, and changes between these two extreme states, due to hydraulic fracturing and then resealing, are essentially instantaneous. The fault is conceptualized as a fluid-saturated, two-dimensional planar feature with spatially heterogeneous rock compressibility β. As compressive normal stress is applied to the fault, the spatially heterogeneous β transforms the stress into locally varying amounts of strain as exhibited by changes in the fluid pressure within the fault. If the local fluid pressure exceeds a threshold rupture pressure at any cell, the pressure is redistributed to the surrounding cells; the new pressure is recalculated and again compared to the threshold rupture pressure. The pressure redistribution continues until pressure in all cells is below the threshold pressure. The normal stress continues and the strain is updated at the next time step and the process continues. Miller and Nur (2000) used this model to study how simple small-scale processes can describe the evolution of pore pressures in a fault and lead to the development of large-scale fluid flow networks. Wang and Manga (2010) postulated a process analogous to the toggle-switch idea for rapid changes in the permeability and pore pressure redistribution of a magmatic melt due to earthquake-induced fracturing. Claesson et al. (2007) observed rapid, earthquake-induced changes in ground water flow systems followed by a less rapid fault-sealing process.

To paraphrase the definition of a CA proposed by Mitchell (2009) in the context of the pressure redistribution problem, a CA is a grid of cells, where each cell is in one of two states (e.g., closed/open) depending on the current states of cells within its local neighborhood. The two key components of a CA model are the definition of the local neighborhood and the cell update rule. The cell update rule defines the state of the cell in the next time step as a function of the states within the neighborhood at the current time step. The cell update rule is identical for all cells at all times (i.e., spatially and temporally stationary). Taken as a whole, CA models have large numbers of simple components that respond to conditions in the local environment without any centralized or hierarchical controller. From these simple cells, having limited intercell communication and all following the same simple, local rule, complex behavior can arise at the macroscale (hundreds of thousands of cells) that is not predictable from consideration of the cell update rule on its own. The resulting macroscale behavior, which is unpredictable given the simple rule set and the initial conditions, is termed "emergent behavior" (Mitchell 2009). We use the toggle-switch model of permeability to demonstrate the evolution of emergent behavior as a function of the spatial correlation length of β.

The CA model of Miller and Nur (2000) is analogous to many statistical physics models that are characterized by initial localized failures that lead to a cascading failure that spans the system (e.g., spring and block models of fracturing; sandpile models of cascading failures; percolation processes for domain-spanning features). We examine behavior of the cellular automata model under the condition of spatially correlated material properties within the fault. This approach expands on previous application of this model where only uncorrelated material properties were studied (Miller and Nur 2000). This approach is contrary to the majority of applications of cellular automata models and studies of self-organized criticality across a wide variety of applications that rely on random uncorrelated properties, perturbations, or failure thresholds (e.g., Ferer and Smith 2011; De Menech et al. 1998; Cowie et al. 1993, 1995; Miller et al. 1996). There are notable exceptions to this assumption of uncorrelated property fields including work on percolation networks with correlation (e.g., Sahimi and Mukhopadhyay 1996). Our approach can be summarized as local (quasi-independent) rules acting on connected (correlated) properties.

In this chapter, we define the CA model and the model of spatial correlation of β within the fault. These two models are used to examine the impact of β spatial correlation on the resulting timing, location, and size distribution of the pressure redistribution events. The size distributions are fit with power-law models having exponential decay at the largest sizes. Changes in the β spatial correlation lead to complex spatial-temporal patterns of events that exemplify emergent behavior. Insights on the impact of β spatial correlation on event initiation and fluid flow patterns within the fault are summarized.

3.2 Cellular Automata Model

A previously developed CA model is used here (Miller and Nur 2000). Conceptually, a two-dimensional fault plane within the Earth's crust is modeled as a lattice of cells. Each cell has a different value of rock compressibility, and normal stresses orthogonal to the fault plane place the fault in compression. The evolution of the fluid pressure within each cell is the quantity of interest. The toggle-switch permeability model is used, meaning that if the pressure in a cell is below a critical value, it is impermeable with respect to fluid flow ($k \sim 0$, where k is permeability). Above the critical value, the cell is at failure and fluid can immediately migrate into neighboring cells ($k \sim \infty$). This process results in the fluid pressure of all connected cells being equilibrated to the same value. When the pressure of a cell falls below the critical value, it has healed and is again impermeable until a future rupture (see details in Miller and Nur 2000).

The relationship between the change in fluid pressure, P_f, and the plastic deformation or fluid source causing the change is

$$\frac{\partial P_f}{\partial t} = \frac{1}{\phi(\beta_\phi + \beta_f)} \left[\frac{k}{v} \nabla^2 P_f - (\dot{\phi}_{\mathrm{plastic}} - \dot{\Gamma}) \right], \tag{3.1}$$

where $\dot{\Gamma}$ is the time-varying fluid source, $\dot{\phi}_{\mathrm{plastic}}$ is the time-dependent porosity reduction, k is the permeability, v is the fluid viscosity, and ϕ is the porosity. The compressibility of the rock matrix and the fluid are β_ϕ and β_f, respectively. Further details on this pressure diffusion model are given in Segal and Rice (1995) and Walder and Nur (1984).

The "toggle-switch" model of Miller and Nur (2000) limits the permeability values to $k = 0$ and $k \cong \infty$ depending on the local fluid pressure. Under the zero permeability mode ($k = 0$), pressure redistribution by diffusion does not occur and the following simplified pressure differential is used:

$$\left.\frac{\partial P_f}{\partial t}\right|_{\mathrm{noflow}} = \frac{(\dot{\Gamma} - \dot{\phi}_{\mathrm{plastic}})_i}{\phi_i \beta_i}, \tag{3.2}$$

where P_f is the pressure in the ith cell at time t and β_i is the sum of matrix and fluid compressibility for cell i. In the calculations to follow, $(\dot{\Gamma} - \dot{\phi}_{\mathrm{plastic}})_i$ is constant throughout time and space. A constant ϕ is employed and β is varied across the domain making the spatial correlation of β the focus in the remainder of the chapter.

Prior application of the toggle-switch model to pressure redistribution considered either $(\dot{\Gamma} - \dot{\phi}_{\mathrm{plastic}})_i$ or $\phi_i \beta_i$ within each cell to be independently drawn from a uniform or Gaussian distribution (Miller and Nur 2000). Here, we follow this approach by drawing β_i from a Gaussian distribution while adding spatial correlation between the cells defined through a Gaussian kernel (see below).

At each time step, a constant compressional strain increases P_f by decreasing ϕ_{plastic} within each cell through Eq. (3.2). When P_f in a cell reaches a threshold pressure, P_{thresh}, the cell "fails," permeability suddenly increases from 0 to infinity, and the pressure is redistributed to the four adjacent cells. Each cell within this neighborhood ($m = 4$) is then assigned the same weighted average pressure, computed as

$$\bar{P} = \frac{\sum_{i=1}^{m} (\phi\beta)_i P_i}{\sum_{i=1}^{m} (\phi\beta)_i}. \tag{3.3}$$

Equation (3.3), coupled with the threshold pressure, is the cell update rule for the CA model. Here, the local neighborhood for the CA model is defined as the 4 adjacent (non-diagonal) cells in the grid. After the pressure redistribution, if all cells are below the critical pressure, the system proceeds to the next time step via Eq. (3.2). If, on the other hand, there are still cells with $P_f > P_{\text{thresh}}$, the pressure redistribution process is repeated until $P_f \leq P_{\text{thresh}}$ in all cells. The size of a pressure redistribution event is measured as the number of cells involved in the pressure redistribution starting from a single cell with $P_f > P_{\text{thresh}}$ until all cells are below P_{thresh}. Many of the cells involved in the redistribution event never reach failure; they are only involved in the redistribution of the fluid pressure. These "event clusters" differ from the definition of failure clusters of Miller and Nur (2000), where all cells in the cluster must have reached failure at some point. The event cluster plots have the same behavior as the failure cluster plots, but with larger sizes. Event clusters are used here to be consistent with fluid pressure as the primary object of study.

3.3 Spatial Correlation

Statistical physics models typically apply local rules to fields of uncorrelated properties. From application of these rules, a spatial correlation in the resulting state arises. A classic example of this behavior is the standard percolation model (Stauffer and Aharony 1994). The probability of any cell in the domain being conductive is a random variable with correlation length equal to that of the grid spacing leading to an uncorrelated random field. As the probability threshold for turning any cell in the domain to being conductive increases, a point is reached where a connected path of conducting cells spans the domain. At this point, the domain is said to "percolate" and the correlation length of the percolating cells relative to the domain size is now infinite.

Here, we examine the impact of another correlation length, that of the material properties on which the CA rules operate, on the overall results of the CA model. Spatial correlation is imposed on β by averaging a white-noise (uncorrelated) multivariate Gaussian field with a kernel. Here the kernel, $G(x,y)$, also has a Gaussian shape and the resulting correlated fields are also multivariate Gaussian:

$$G(x,y) = \frac{1}{2\pi|\Sigma|^{\frac{1}{2}}} \exp\left(-\frac{1}{2}\mathrm{d}\Sigma^{-1}\mathrm{d}^T\right), \tag{3.4}$$

where d is the Euclidean distance vector (d_x, d_y) from any point to the origin of the Gaussian function. For the isotropic fields considered here, the covariance matrix $\Sigma = \sigma^2 I$, where I is the identity matrix and σ is the standard deviation of the Gaussian kernel, is diagonal because the kernel is aligned with the grid axes. The measure of the correlation length of the resulting field is the full width at half maximum, δ, defined as $\delta = \sigma\sqrt{8\ln(2)}$. This is the width of the Gaussian kernel used to create the correlated field at one-half the maximum kernel height. For each δ, 15 individual realizations of the β field are created and used as input to the CA model.

3.4 Results

Calculations were conducted on a grid of 1.0×10^6 $(1,000 \times 1,000)$ cells. Although no explicit scale is assigned here, this model domain could be considered representative of a fault domain of tens to hundreds of meters on a side. The initial pressure of each cell was independently set to a random number between 15 and 16 MPa—an elevation-dependent starting pressure is not considered. The failure condition was set to 28 MPa, an overburden pressure representative of an approximate 1.5 km depth. The time step used was $dt = 0.1$ year, and the numerator of Eq. (3.2) $(\dot{\Gamma} - \dot{\phi}_{\text{plastic}})$ was set to 1×10^{-5} year $^{-1}$ for all cells. The values of β_i had a mean of 0.01 MPa^{-1} and standard deviation of 0.0025 MPa^{-1} where $\phi = 0.02$ and all spatial variation is due to β.

Calculations were run with the following full width at half maximum values: $\delta =$ 0.39, 2.35. 4.71, 9.42, 18.8, 23.5, 47.1, 94.2 188, 235, and 471 grid cells. The lowest δ value, 0.39, represents the uncorrelated case where the value of β_i at each cell is independent of its neighbors. The uncorrelated case is consistent with each cell encompassing 99.7% of the full width ($\pm 3\sigma$) of the Gaussian kernel. Four example β fields are shown in Fig. 3.1.

For each of the 165 input β fields (15 realizations for each of 11 values of δ), the CA model simulations were run from the initial pressure conditions until a domain-spanning cluster of failed cells was reached. At every time step, the coordinates of the centroid of the pressure redistribution event and the event (cluster) size in terms of grid cells are recorded. Additionally, the final spatial distribution of the failed and intact rock as well as the failed rock that is connected to the domain-spanning cluster is recorded. Figure 3.2 shows example results from compressibility fields with three correlation lengths: 0.39, 9.4, and 94 units. The spatial-temporal distribution of the events is summarized in a two-dimensional plot by only showing the vertical (y-dimension) location of each event as a function of time (Fig. 3.2). The time in these plots has been normalized between the start of the simulation and the onset of the domain-spanning cluster.

The domain-spanning clusters in the left column of Fig. 3.2 show that as δ increases, the nature of the clusters changes substantially. At the lowest δ value (Fig. 3.2, upper left), the cluster is rough-edged and surrounds isolated regions of intact rock with a range of sizes. The black region is not at all continuous, containing within it many intact (white) regions of various size as well as other smaller, disconnected regions of failed rock (grey). In general, the domain-spanning cluster and the regions of contained intact and failed rock occurring at multiple

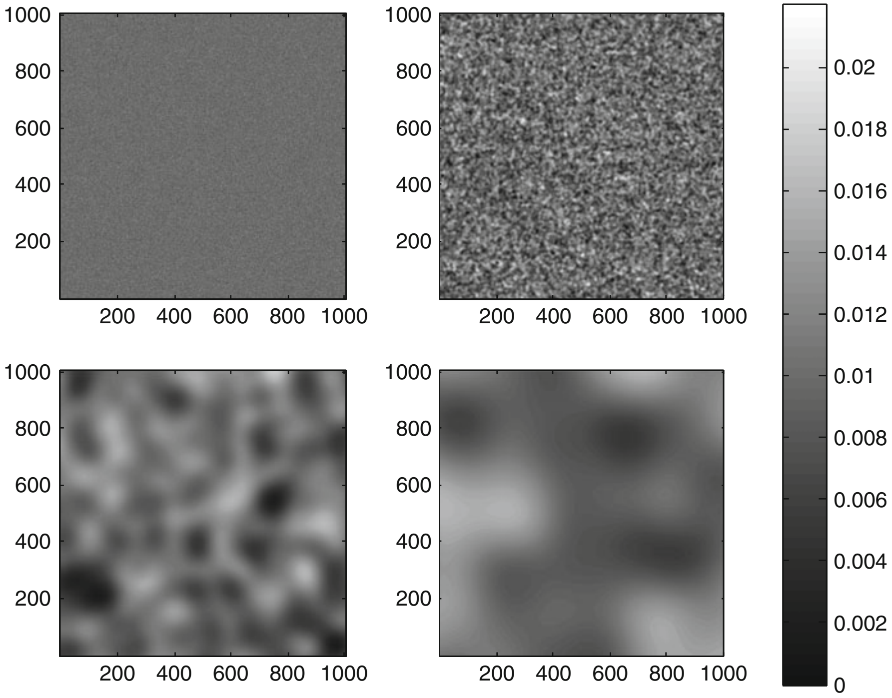

Fig. 3.1 Example of four realizations of the β field showing four different correlation lengths. The values of δ are 0.39 (*upper left*), 9.4 (*upper right*), 94 lower left, and 235 (*lower right*). The color scale is in units of 1/MPa

scales resemble a fractal object. Results from the next largest δ shown in Fig. 3.2 (9.4 cells) similarly show the domain-spanning cluster surrounding regions of white and grey, with less variability in the size distribution of these surrounded regions. Notably, there are no small white regions mixed evenly within the black as seen in the upper image. Finally, at the largest δ value (94 cells), the domain-spanning cluster is almost completely uninterrupted, with the exception of a single enclosed area of intact (white) rock. There are only a few grey regions in the entire image. The perimeter to area ratio of the domain-spanning cluster decreases as δ increases.

The spatial-temporal evolution of the events is summarized in the right column of Fig. 3.2. For the uncorrelated case (upper image), there are 10–12 locations that fail repeatedly over time plus additional events that occur at apparently random locations. The intensity of these randomly located events increases with increasing time until the domain-spanning cluster is formed. In general, the events appear to remain local and have little impact on the formation of events in surrounding locations. As δ increases to 9.4 cells (middle image), the pattern is similar to the uncorrelated case with more locations (25–30) having early failures that repeat continuously through time along with a more abrupt increase in the density of the randomly located events at late times relative to the uncorrelated case. Additionally,

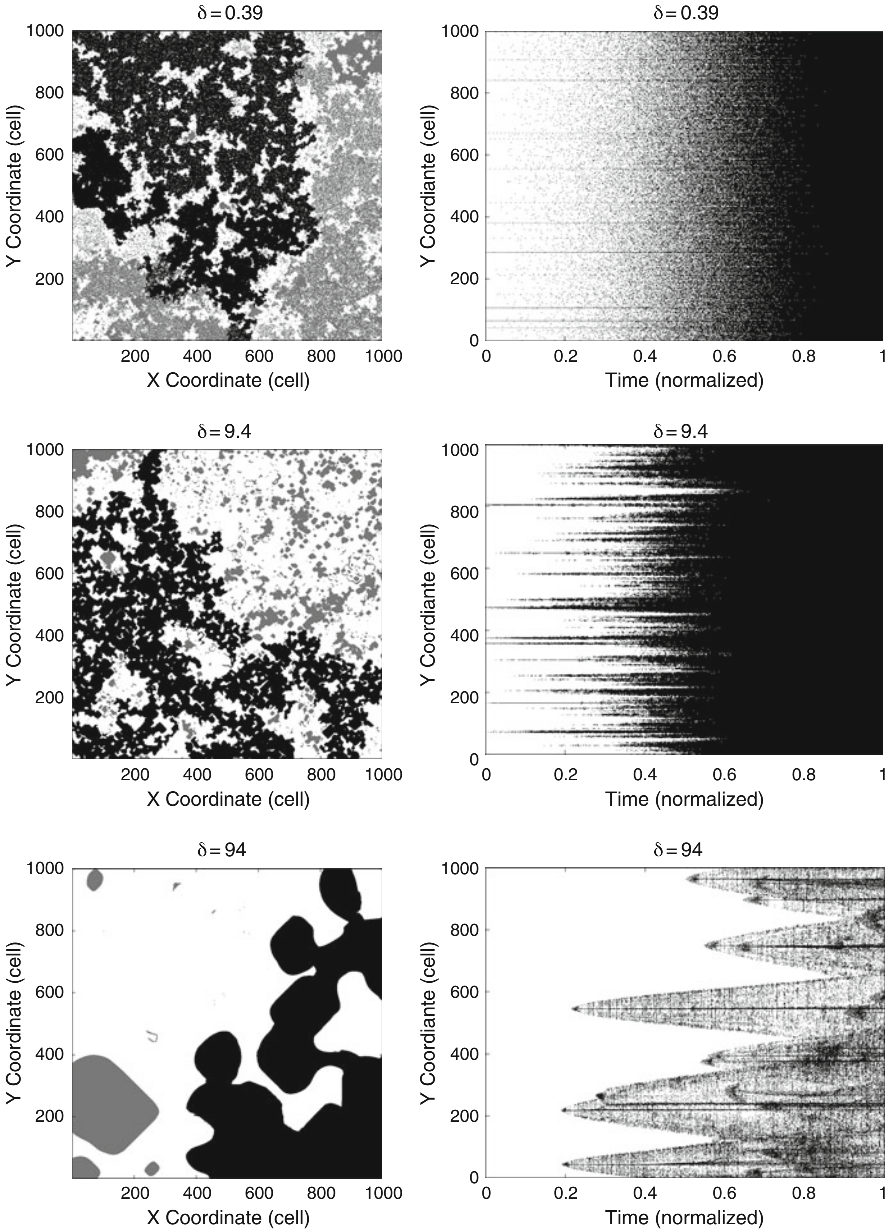

Fig. 3.2 For three different values of $\delta(0.39, 9.4$, and 94, *top to bottom*) the images on the left show the areas of rupture in *black and grey* at the time when the domain-spanning ruptured region is reached. Cells within the domain-spanning cluster are *black*, other ruptured cells are *grey*, and intact rock is *white*. *On the right*, the y-coordinate of the centroid of each rupture event is plotted vs. normalized time, where time ranges from the start of the simulation to the point where the ruptured material spans the domain, as illustrated in the images *on the left*

Fig. 3.3 The time to first failure and the time at which the ruptured region achieves percolation across the domain. For each value of δ, averages over the 15 realizations are plotted (*circles and squares*) along with the minimum and maximum values

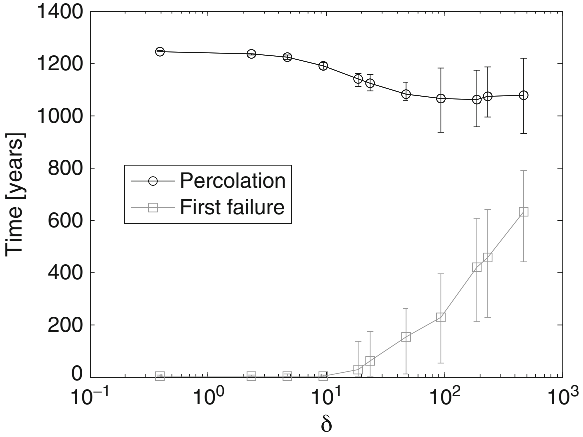

the size of the neighborhood of locations where the failures are nearly continuous from early time grows as time increases indicating an outward growth of the failure locations from an original single nucleation point. At the largest δ (94 cells) in the lower image, the pattern changes markedly such that there are a relatively small number (10–12) of locations with repeating failures. A halo of failure locations moves outward from these repeating locations as time increases and all failures occur within one of these halos—there is no random component of failure locations outside of these halos. There is a significant delay in the time to first failure relative to the results from the smaller δ values; in this example, the first failure does not occur until 20% of the simulation time has passed. These unexpected complex patterns arising from operation of simple local rules on increasingly correlated material property fields signify emergent behavior in fluid pressure redistribution events.

Figure 3.3 plots the time to first failure, the first point when any cell has a pressure above the failure threshold (28 MPa), and the time to reach the domain-spanning (bottom to top) cluster. Since all cells start with similar pressures, the cells with the smaller values of β_i fail first. Increasing spatial correlation acts to increase the time to the first rupture and decrease the time to reach the domain-spanning cluster. These results show that correlated fields of rock compressibility can accommodate more strain before failing than can uncorrelated fields, but once failure is initiated, there is a more rapid progression to domain-spanning failure relative to the uncorrelated case.

For δ values up to 10.0 units, the initial failure occurs nearly instantaneously as the strain begins and there is no variation in this value between realizations. Above a δ of 10.0, the initial failure is delayed to times beyond the initiation of strain. Additionally, the variability in this time to initial rupture is nearly ±200 years across the realizations for each δ. The variability in the results between realizations becomes considerable as δ reaches one-tenth of the domain length ($\delta = 100$). As a rule of thumb, a correlation length of one-tenth the domain size is the ergodic limit.

As correlation lengths go beyond this limit, the statistics (e.g., the mean β) are no longer constant from one realization to the next creating increased inter-realization variability as seen here (see additional details on ergodic limits in Zhang 1999).

At each time step, each percolation cluster is recorded with its size. For each value of δ, the number of clusters of each size is counted, summing over all time steps up to the point of domain-spanning cluster formation. All 15 realizations are aggregated, and these results are used to produce curves of the complementary cumulative distribution function (1—CDF) in log–log space. Similar curves were produced by Miller and Nur (2000), but their failure clusters were used instead of event clusters, as noted previously. The event cluster curves are nearly identical to failure cluster curves in terms of slope; they are merely shifted to the right. In the case of uncorrelated values of β, the cluster size distribution value as a function of cluster size, $D(S)$, can be fit to (Miller and Nur 2000):

$$D(S) = S^{-\alpha} \exp\left(-\frac{S}{L}\right), \tag{3.5}$$

where S is the cluster size, α is the power-law exponent, and L is a correlation length distinct from δ. Both α and L are fit to the data. The best fit is obtained with $f(\alpha, L) = \log(D)$ using the Matlab function nlinfit (MATLAB 2011). To accurately fit results with Eq.(3.5), the data must first exhibit linear behavior on the log-log plot with slope of -α followed by an exponential decay at the largest sizes. This equation does not provide the best fit to the data from correlated fields, especially at larger values of δ. A noticeable deviation between these data and Fig. 3.8 of Miller and Nur (2000) is that approximately 30%–50% of their clusters have size $S = 2$. Here, there are no clusters of size $S = 2$ due to the redefinition of clusters and only a negligible amount of them have size $S = 3$ or $S = 4$ (due to edge artifacts), and the most frequently observed size is $S = 5$ consistent with the 5-point star pattern used in the pressure redistribution process.

The results in Fig. 3.4 show the size distribution of the rupture events. As δ increases, this distribution changes from a power-law model with exponential roundoff at the largest sizes to a double power law with exponential roundoff and finally back to the original single power law with exponential roundoff, but a much shallower slope than the models for smaller δ values. Especially at higher values of δ, it can be seen that the slope of the linear section changes prior to the onset of exponential decay.

In order to better fit the results across the range of δ values, a piecewise function with two power-law slopes prior to the exponential decay was constructed:

$$D(S) = \begin{cases} cS^{-\alpha_1} \exp\left(-\frac{S}{L}\right) \exp\left(\frac{1}{L}\right) & \text{if } S \leq \gamma, \\ cS^{-\alpha_2} \gamma^{\alpha_2 - \alpha_1} \exp\left(\frac{S}{L}\right) \exp\left(\frac{1}{L}\right) & \text{if } S \geq \gamma. \end{cases} \tag{3.6}$$

Compared to Eq. (3.5), α has been split into α_1 and α_2, and additional dependent variables, c and γ, have been introduced. γ is the value of S where the change in

Fig. 3.4 Distributions of cluster sizes for each δ value. The size distribution curves shift to the top right corner as δ increases. For each δ, the data points are *grey*, the equation fit is *black*, the point of change in slope (γ) is a *square*, the δ related area is a *circle*, and the maximum cluster size for each individual realization is a *triangle*. For each δ, each distribution is calculated over all 15 realizations

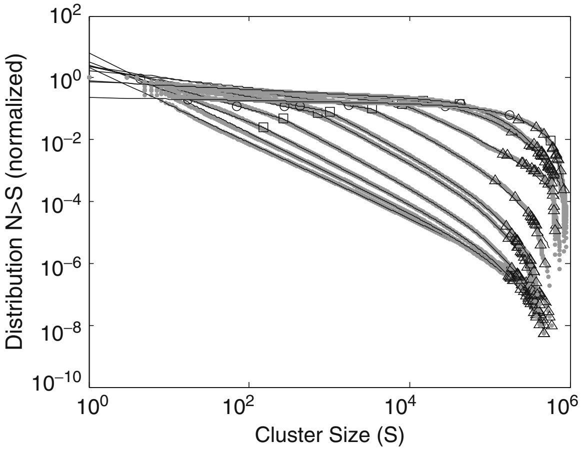

Table 3.1 Variables c, α_1, α_2, L, and γ from Eq. (3.6) are fit to match the cluster size data produced. The coefficient of determination, R^2, is included for each δ. Also included is the characteristic size of the compressibility field calculated as the area of a circle with diameter $\delta : \pi(\delta/2)^2$

δ	c	α_1	α_2	L	γ	$\pi(\delta/2)^2$	R^2
0.392	2.25	–	1.22	370,000	0	0.121	0.9996
2.35	6.38	–	1.29	144,000	0	4.36	0.9990
4.71	3.26	0.972	1.35	111,000	150	17.4	0.9997
9.42	2.63	0.717	1.41	103,000	266	69.7	0.9998
18.8	2.30	0.525	1.39	99,100	710	279	0.9995
23.5	2.29	0.482	1.40	110,000	1,010	436	0.9996
47.1	2.32	0.386	1.30	150,000	3,350	1,740	0.9983
94.2	1.71	0.273	1.14	384,000	8,120	6,970	0.9926
188	0.778	0.145	0.427	147,000	14,600	27,900	0.9917
235	0.756	0.128	0.481	151,000	42,400	43,600	0.9974
471	0.230	0.0481	5.81	227,000	582,000	174,000	0.9941

slope from α_1 to α_2 occurs. The factor $\exp(1/L)$ has been added to ensure $D(1) = c$. While the actual data will always be $D(1) = 1$, there are very few data points at $S = 1$ and not restricting the model to go through this point by introducing the variable c improves the overall fit. However, the model should be used for $S \geq 5$, the size of the pressure redistribution stencil, to avoid spurious results. When $S \leq \gamma$ the log-log plot yields a slope of -α_1. When $S \geq \gamma$ the slope changes to -α_2 and then decays exponentially for the largest S. The function is continuous, but there is a discontinuity in the slope at $S = \gamma$. This function is recast using an approximation of the Heaviside function for parameter estimation using the Matlab *nlinfit* function (MATLAB 2011). The resulting fits of Eq. (3.6) to the size distributions are shown in Fig. 3.4. The parameters used to fit the size distributions are shown in Table 3.1.

Equation (3.6) provides excellent fits ($R^2 > 0.99$) to the observed size distribution for all values of δ. Up to the point of reaching the ergodic limit ($\delta \sim 100$), the quantity $\pi(\delta/2)^2$ provides a reasonable lower bound on the estimated value of γ; however, decreasing the number of estimated parameters by replacing γ with $\pi(\delta/2)^2$ decreased the goodness of fit. The values of α_1 define a decreasing negative slope with increasing δ. The values of α_2 remain above 1.0 and are relatively constant up to the ergodic limit where they begin to decrease (a less negative slope). The value of α_2 at $\delta = 471$ is somewhat of an outlier as it does not take effect until the curve is already into the exponential decay region. In all cases, the piecewise curve fits the data better than the single power-law function (3.5). The curves produced from the data in Table 3.1 are plotted in Fig. 3.4 along with the original data. The maximum cluster size for each realization is highlighted.

Figure 3.4 shows that for the uncorrelated case ($\delta = 0.39$), 99% of all events have a size of 100 cells or less, whereas for a correlation length of $\delta = 94$, 99% of the events have a size of 10,000 cells or less. This result shows the size distribution moving from a power-law distribution ranging over multiple orders of magnitude to a distribution closer to uniform with an exponential decay at the highest end. This behavior is indicative of a wide range of cluster sizes merging to create a domain-spanning cluster in an uncorrelated field and a much more uniformly sized set of clusters joining to create the domain-spanning cluster at larger values of δ.

The spatial patterns of the event centroids are compared to a completely random spatial point process using the distribution of nearest neighbor distances between events at each time step. Specifically, the event locations are compared to the case of complete spatial randomness (CSR). To satisfy CSR, data points must be an uncorrelated random sample from a uniform distribution. When this is the case, the nearest neighbor distance from a data point, r, on average is (Diggle 2003)

$$\mu = 0.5(n^{-1}A)^{\frac{1}{2}} + (0.051 + 0.042n^{-\frac{1}{2}})n^{-1}P, \tag{3.7}$$

where μ is the expected value of r, n is the number of data points, A is the area of the region considered, and P is its perimeter. As soon as observed patterns emerge, CSR is no longer present.

Figure 3.5 shows the results of this analysis for three example simulations, with the right image of Fig. 3.5 showing a closer look at the last half of the simulation time. The y-axis shows the difference between the mean observed r and μ. In the uncorrelated case, the difference is near zero for the majority of the simulation. At 95% of the simulation time, there is a slight deviation towards negative values indicating a slight clustering of the events. Results with a δ of 9.4 show moderate spatial clustering of the events throughout the simulation until very near the end when they become more spatially random. With a δ of 94, the spatial clustering is extreme for the first 50% of the simulation and then moves towards a more random pattern at the end. The results with $\delta = 94$ show considerable variability with large increases and decreases in the difference throughout time. Only events created under

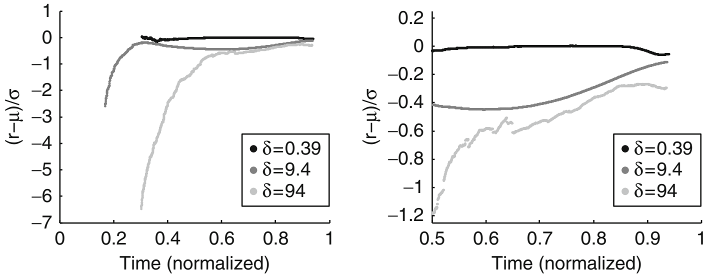

Fig. 3.5 Results of the spatial clustering analysis for three example realizations at three different δ values. The *right image* is a zoomed in portion of the *left image*. Values near zero indicate spatial randomness, while positive and negative values indicate regularity and clustering, respectively

Fig. 3.6 Normalized effective fault permeability (*vertical*) as a function of δ. The mean, minimum, and maximum values across 15 realizations are shown for each δ. The effective values are normalized by the permeability value assigned to the failed rock

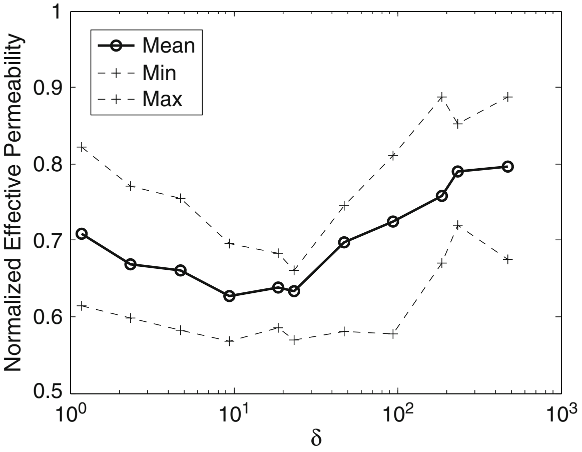

the uncorrelated case fit the pattern of complete spatial randomness throughout the simulation.

The failure patterns within the fault at the point of domain-spanning percolation are used to examine the effective permeability (vertical) of the fault. Steady-state, single-phase, isothermal flow is simulated across the fault in the vertical direction and the applied gradient and resulting flux are used to calculate the effective permeability. The permeability of the failed regions is set to be four orders of magnitude higher than that of the intact regions and the effective permeability of the fault domain is normalized by the permeability value assigned to the failed regions (Fig. 3.6). The connected high-permeability path across the fault ensures that all mean effective permeability values are at least 60% of the maximum permeability assigned to the failed regions.

For the uncorrelated case, the mean effective permeability is just over 70% of the failed region permeability. The minimum mean effective permeability value occurs at $\delta = 9.42$ before rising again to a maximum of near 80% of the failed region permeability for $\delta = 492$. This behavior is controlled by the proportion of the fault domain that is contained within the spanning cluster, which also reaches a minimum at $\delta = 9.42$. At lower δ values, the spanning cluster is larger and complex with multiple continuous pathways connecting the top and bottom boundaries as well as many intact rock fragments contained within, or surrounded by, the spanning cluster (e.g., Fig. 3.2, top left image). At δ values of 9.42, the number of pathways connecting the top and bottom boundaries of the fault decreases to near 1 (e.g., Fig. 3.2, center left image) causing decreased mean effective permeability. For larger values of δ, a single connected pathway remains, but it is larger and less complex, containing less intact material, than at lower values of δ (e.g., Fig. 3.2, bottom left images). Emergence of a single dominant flow path at larger correlation lengths is consistent with results of Pyrak-Nolte and Morris (2000) in a study of fracture stiffness and fluid flow.

3.5 Conclusions

Geologic media are commonly observed to have spatially correlated material properties. In particular, within a fault, prior movement along the fault and a changing stress history will lead to zones of preferential strength and weakness. Simulation of pressure redistribution events within a fault using a CA model clearly shows the impact of rock compressibility (β) spatial correlation on both the size distributions and the spatial and temporal patterns of the pressure redistribution events.

Increasing the spatial correlation (δ) of β leads to a field that can sustain larger amounts of strain prior to the first failure. Higher δ values also decrease the time until a fault-spanning cluster of failed material is achieved. As δ increases, the more uniform distribution of event sizes leads to higher numbers of larger events and faster connection of failed regions across the fault relative to the uncorrelated case. Once a location ruptures, the surrounding area, having a similar compressibility, is already at a similar fluid pressure and therefore the excess pressure is quickly redistributed to the edge of this region and new ruptures occur in material with a higher compressibility (more compliant material). This process results in the “halo” effect of a central rupture location surrounded by a ring of associated failures (see Fig. 3.2 center and bottom right images). The final pattern of intact and failed regions within the fault results in an effective permeability for the fault that is a nonlinear function of δ. At small to moderate δ, the failed region is complex and more poorly connected than for the uncorrelated case leading to a minimum value of the effective permeability. At the largest δ, a dominant, uninterrupted failed region emerges that maximizes the fault effective permeability.

In almost all applications of CA models and other studies of self-organized criticality, the material properties are represented as uncorrelated random fields. This study demonstrates that local rules in a CA model operating on correlated properties lead to emergent behavior. This behavior is significantly different from that seen on the standard uncorrelated fields. The emergent behavior identified here is the evolution of increasingly complex spatial-temporal patterns of failure within the fault as exemplified in the right-hand side of Fig. 3.2. As the amount of spatial correlation increases, the event size distribution changes from a single power law to a double power law and then back to a single power-law distribution. The slope for the initial power law in the cases with double power-law behavior is always shallower than for the case of uncorrelated material properties. In all cases, the largest events fit a distribution model with exponential tailing.

The simulations done here are for rock compressibility fields with isotropic spatial correlation. Future simulations will look at the impact of anisotropic correlation patterns as may result from normal or strike-slip displacement along the fault. The multivariate Gaussian model adopted here for the random fields is parametrically and computationally efficient, but other, non-Gaussian, field models may better represent aspects of observed faults. This study uses a CA model with several simplifying assumptions to evaluate the impact of material property correlation on fluid pressure redistribution. Some of those assumptions including conceptualization of permeability as only being zero or infinite and the closed boundary conditions should be reevaluated in future studies. Field observations of earthquake activity in faults with high fluid pressures and microseismic activity at subsurface injection sites should be able to provide information that can distinguish between the independent and correlated property field models examined here.

Acknowledgements This material is based upon work supported as part of the Center for Frontiers of Subsurface Energy Security, an Energy Frontier Research Center funded by the US Department of Energy, Office of Science, Office of Basic Energy Sciences under Award Number DE-SC0001114. Sandia National Laboratories is a multiprogram laboratory managed and operated by Sandia Corporation, a wholly owned subsidiary of Lockheed Martin Corporation, for the US Department of Energy's National Nuclear Security Administration under contract DE-AC04–94AL85000.

References

Claesson L, Skelton A, Graham C, Morth C-M (2007) The timescale and mechanisms of fault sealing and water-rock interaction after an earthquake. Geofluids 7(4):427–440

Cowie PA, Sornette D, Vanneste C (1995) Multifractal scaling properties of a growing fault population. Geophys J Int 122:457–469

Cowie PA, Vanneste C, Sornette D (1993) Statistical physics model for the spatiotemporal evolution of faults. J Geophys Res 98(B12):21,809–21,821

De Menech M, Stella AL, Tebaldi C (1998) Rare events and breakdown of simple scaling in the abelian sandpile model. Phys Rev E 58(3):R2677–R2680

Diggle PJ (2003) Statistical analysis of spatial point patterns, 2nd edn. Oxford University Press, Oxford

Ferer M, Smith DH (2011) Characterising the correlations of failure events: A 2-D Block-and-Springs model. Strain 47(2):187–195, doi:10.1111/j.1475–1305.2010.00758.x

Healy JH, Rubey WW, Griggs DT, Raliegh CB (1968) The Denver earthquakes. Science 161(3848):1301–1310

Hsieh PA, Bredehoeft JD (1981) A reservoir analysis of the Denver earthquakes: a case study of induced seismicity. J. Geophys Res 86: 903–920

Ingebritsen SE, Rojstaczer SA (1993) Controls on geyser periodicity. Science 262(5135):889–892

Lucier A, Zoback M, Gupta N, Ramakrishnan TS (2006) Geomechanical aspects of CO2 sequestration in a deep saline reservoir in the Ohio River Valley region. Environ Geosci 13(2): 85–103

Majer EL, Baria R, Stark M, Oates S, Bommer J, Smith B, Asanuma H (2007) Induced seismicity associated with Enhanced Geothermal Systems. Geothermics 36:185–222

MATLAB (2011) The MathWorks Inc., version 7.13.0, Natick, Massachusetts

Miller SA, Collettini C, Chiaraluce L, Cocco M, Barchi M, Kaus BJP (2004) Aftershocks driven by a high pressure CO2 source at depth. Nature 427:724–727

Miller SA, Nur A (2000) Permeability as a toggle switch in fluid-controlled crustal processes. Earth Planet Sci Lett 183(133):146

Miller SA, Nur A, Olgaard DL (1996) Earthquakes as a coupled shear stress – high pore pressure dynamical system. Geophys Res Lett 23(2):197–200

Mitchell M (2009) Complexity: a guided tour. Oxford University Press, Oxford, 349 p

Pyrak-Nolte LJ, Morris JP (2000) Single fractures under normal stress: The relation between fracture specific stiffness and fluid flow. Int J Rock Mech Min Sci 37:245–262

Rojstaczer S, Ingebritsen SE, Hayba DO (2008) Permeability of the continental crust influenced by internal and external forcing. Geofluids 8:128–139

Rojstaczer S, Wolf S, Michel R (1995) Permeability enhancement in the shallow crust as a cause of earthquake-induced hydrological changes. Nature 373:237–238

Rutledge JT, Phillips WS, Mayerhofer MJ (2004) Faulting induced by forced fluid injection and fluid flow forced by faulting: an interpretation of hydraulic-fracture microseismicity, carthage cotton valley gas field. Texas. Bull Seismol Soc Am 94(5):1817–1830

Rutqvist J, Birkholzer J, Cappa F, Tsang C-F (2007) Estimating maximum sustainable injection pressure during geological sequestration of CO_2 using coupled fluid flow and geomechanical fault-slip analysis. Energ Conserv Manag 48:1798–1807

Sahimi M, Mukhopadhyay S (1996) Scaling properties of a percolation model with long-range correlations. Phys Rev E 54:3870–3880

Sarr MO, Manga M (2003) Seismicity induced by seasonal groundwater recharge at Mt. Hood, Oregon. Earth Planet Sci Lett 214:605–618

Segal P, Rice JR (1995) Dilatancy, compaction, and slip instability of a fluid infiltrated fault. J Geophys Res 100:22155–22171

Stauffer D, Aharony A (1994) Introduction to percolation theory, revised 2nd edition. Taylor and Francis Inc., Philadelphia, 181p

Walder J, Nur A (1984) Porosity reduction and pore pressure development. J Geophys Res 89:11539–11548

Wang C-Y, Manga M (2010) Hydrologic responses to earthquakes and a general metric. Geofluids 10:206–216

Zhang H (1999) On the ergodicity hypothesis in heterogeneous formations. Math Geol 31(1): 113–134

Zoback MD, Harjes HP (1997) Injection-induced earthquakes and crustal stress at 9 km depth at the KTB deep drilling site, Germany. J Geophys Res Solid Earth 102:18,477–18,491

Chapter 4
Sparsity-Promoting Solution of Subsurface Flow Model Calibration Inverse Problems

Behnam Jafarpour

Abstract Identification of heterogeneous hydraulic aquifer properties from limited dynamic flow measurements typically leads to underdetermined nonlinear inverse problems that can have many solutions, including solutions that are geologically implausible and fail to predict future performance of the system. The problem is usually regularized by incorporating implicit or explicit prior information to stabilize the solution techniques and to obtain plausible solutions. A meaningful regularization must be informed by the physics of the problem, distinct properties of the formation under investigation, and other available sources of information (e.g., outcrop, well logs, and seismic). This chapter proposes sparsity as an intrinsic property of spatially distributed aquifer hydraulic properties that can be used to regularize the solution of the related ill-posed inverse problem. Inspired by recent advances in *sparse* signal processing, formalized under the *compressed sensing* paradigm, proper sparsifying bases are introduced to describe aquifer hydraulic conductivity distribution. Such descriptions give rise to a sparse reconstruction formulation of the subsurface flow model calibration inverse problem, which can be efficiently solved following recent algorithmic developments in sparse signal processing. The compressed sensing paradigm specifies the conditions under which unique solutions to underdetermined linear system of equations exist and can be computed efficiently. Sparsity is a fundamental notion in compressed sensing, and is often present in many natural images. In particular, sparsity is prevalent in describing many spatially correlated aquifer properties. The practical implications of compressed sensing are as far reaching as the solution of underdetermined system of equations is in science and engineering. This chapter introduces the guidelines set

---

B. Jafarpour (✉)
Department of Chemical Engineering and Materials Science, University of Southern California,
925 Bloom Walk, HED 313 Los Angeles, CA 90089-1211, USA
e-mail: behnam.jafarpour@usc.edu

P.K. Mishra and K.L. Kuhlman (eds.), *Advances in Hydrogeology*,
DOI 10.1007/978-1-4614-6479-2_4,
© Springer Science+Business Media New York 2013

forth by sparse reconstruction techniques and the compressed sensing paradigm and incorporates them to formulate and solve ill-posed groundwater model calibration inverse problems.

4.1 Groundwater Model Calibration

Development of underground hydrological, environmental, and energy resources relies on accurate modeling and prediction of fluid flow and transport in these heterogeneous and anisotropic porous environments. However, understanding subsurface physical, chemical, and biological rock properties and the related transport processes is severely complicated by our inability to "see into the earth". Determination of rock hydraulic properties and the underlying flow and transport processes inherently involves significant uncertainty because we can neither observe nor easily access these properties from the surface (National Research Council 2000; Yeh et al. 2008). Data limitation results in extensive interpolation and interpretation efforts that lead to the introduction of a significant level of uncertainty and bias in characterizing subsurface flow property distributions.

To reduce the uncertainty in describing the subsurface flow and transport properties, it is common to calibrate subsurface models against dynamic performance data such as pressure and flow rates. Model calibration is accomplished by formulating and solving an inverse problem where limited dynamic data is used to infer a large number of unknown parameters. Since the number of unknowns to identify is often overwhelmingly greater than the available data, the resulting inverse problems tend to be severely ill-posed and have non-unique solutions. In general, however, the true dimensionality of subsurface flow and transport models is far less than the size of the discretized numerical models used to describe them. This is attributed to the intrinsic geologic continuity that leads to extensive spatial correlations in the rock physical property distributions. An obvious way to improve the solution of ill-posed inverse problems is to collect more independent data. However, data acquisition is an expensive endeavor that is limited by economic constraints. In addition to increasing the data, advanced computational tools may be used to reduce the number of unknown parameters in the model calibration inverse problem. Several explicit and implicit parameter reduction (parameterization) techniques are available to perform this. In this chapter, a novel model calibration approach is proposed based on recent developments in sparse signal processing and approximation theory, formalized as the *compressed sensing* paradigm (Donoho 2006).

4.1.1 Flow Equations and Inverse Modeling Formulation

Mathematical modeling of multiphase fluid flow in porous media is widely used to quantify and predict fluid displacement patterns in the subsurface environment.

The general form of the governing equations for two-phase immiscible flow in porous media can be derived from the mass conservation principle and Darcy's law as (Aziz and Settari 1979; Bear and Verruijt 1987)

$$\begin{aligned}\nabla\cdot\left(\frac{\lambda_w}{B_w}u\left(\nabla P_w-\gamma_w\nabla Z\right)\right)&=\frac{\partial}{\partial t}\left(\phi\frac{S_w}{B_w}\right)+q_w\\ \nabla\cdot\left(\frac{\lambda_n}{B_n}u\left(\nabla P_n-\gamma_n\nabla Z\right)\right)&=\frac{\partial}{\partial t}\left(\phi\frac{S_n}{B_n}\right)+q_n,\end{aligned}\tag{4.1}$$

where subscripts w and n indicate wetting and non-wetting phases, λ represents the phase mobility, B the volume of a phase as a function of pressure relative to its volume at standard pressure, u the intrinsic permeability, ϕ the porosity of the medium as a function in space, P the phase pressure, γ the phase density, Z the gravity potential, S the phase saturation, and q sink and source fluxes.

The partial differential equations (PDEs) in (4.1) contain four unknown state variables, i.e., P_w, P_n, S_w, S_n. For a given set of model inputs, the system is closed by the following two constitutive equations that account for capillary pressure and the physical saturation constraint in a fully saturated medium:

$$\begin{aligned}P_n-P_w&=P_c\left(S_w\right)\\ S_n+S_w&=1.\end{aligned}\tag{4.2}$$

Forward integration of Eqs. (4.1) and (4.2) is used to compute pressure and saturation solutions in time, as a function of model inputs.

Solutions to (4.1) and (4.2) are only reliable and meaningful when accurate model inputs are used. Since direct measurement of rock hydraulic properties is difficult, we frequently need to estimate these parameters by inverting scattered point measurements and indirect data. An estimate for the unknown parameter vector $\mathbf{u}$ can be obtained by minimizing a suitable objective function, such as

$$\begin{aligned}&\min_{\mathbf{u}\in\mathcal{R}^N} J\left(\mathbf{u}\right)=\left(\mathbf{d}_{\text{obs}}-\mathbf{g}\left(\mathbf{u}\right)\right)^{\mathrm{T}}\mathbf{C}_{\mathbf{d}}^{-1}\left(\mathbf{d}_{\text{obs}}-\mathbf{g}\left(\mathbf{u}\right)\right)+Reg\left(\mathbf{u}\right)\\ &s.t.\quad \mathbf{f}\left(\mathbf{u},\mathbf{x}(\mathbf{u}),\mathbf{z}\right)=0.\end{aligned}\tag{4.3}$$

Here, J is the objective function, $\mathbf{u}$ denotes the unknown parameters such as permeability, $\mathbf{d}_{\text{obs}}$ represents a vector of observed quantities, $\mathbf{g}\left(\mathbf{u}\right)$ is the predicted observations, $\mathbf{C}_{\mathbf{d}}$ refers to the covariance of measurement errors, $\mathbf{f}$ is a constraint vector containing the conservation Eqs. (4.1) and (4.2), $\mathbf{x}(\mathbf{u})$ refers to the dependent state variables, and $\mathbf{z}$ represents a vector containing other known model input parameters. Note that in the above notation, $\|\mathbf{d}_{\text{obs}}-\mathbf{g}\left(\mathbf{u}\right)\|_{\mathbf{C}_{\mathbf{d}}^{-1}}^{2}=\left(\mathbf{d}_{\text{obs}}-\mathbf{g}\left(\mathbf{u}\right)\right)^{\mathrm{T}}\mathbf{C}_{\mathbf{d}}^{-1}\left(\mathbf{d}_{\text{obs}}-\mathbf{g}\left(\mathbf{u}\right)\right)$, and the term $Reg\left(\mathbf{u}\right)$ is used to represent a general regularization term that will be discussed later. A major issue encountered when solving the resulting inverse problem is the choice of parameterization. The standard grid-based descriptions for the unknown field $\mathbf{u}$ often result in ill-posed inverse problems that have more unknowns than can be uniquely estimated from available data. As a result, multiple solutions can be found that reproduce the observed flow and pressure data but provide different predictions of the flow and transport behavior in the future. In the last decade, however, significant progress has been made in conditioning numerical groundwater and hydrocarbon reservoir models to flow and transport data (see Kitanidis and Vomvoris 1983; McLaughlin and Townley 1996; Carrera et al. 2005; Hill and Tiedeman 2007; Oliver et al. 2008). Deterministic and stochastic inversion algorithms with varying levels of complexity have been developed and applied to solve subsurface flow inverse problems. Two common approaches for mitigating instability and non-uniqueness issues in solving ill-posed inverse problems are (a) reducing the number of unknown parameters, i.e., parameterization (e.g., Jacquard and Jain 1965; Doherty 2003; Gavalas et al. 1976), and (b) incorporating prior information in the form of constraints, i.e., regularization (e.g., Tikhonov and Arsenin 1977; Tonkin and Doherty 2005; Hill and Tiedeman 2007; Oliver et al. 2008).

4.1.2 Parameterization and Regularization

Parameterization methods can be broadly classified into spatial and transform-domain methods. Spatial parameterization methods were introduced to subsurface inverse modeling as early as 1965 in the form of zonation (Jacquard and Jain 1965) and have evolved into adaptive multiscale estimation methods (e.g., Chavent and Bissell 1998; Grimstad et al. 2003; Aanonsen 2008). The general objective of this approach is to identify spatial regions (zones) in the aquifer model that can be aggregated and assigned a single constant property value for the inversion purpose. The main difficulties in implementing zonation are related to the identification of zones with similar properties and the non-geologic sudden discontinuities at the boundaries of the identified regions. Transform-domain parameterization methods reduce the redundancy in grid-based property descriptions by recognizing that geologic features exhibit strong spatial correlations. Hence, adopting high-resolution grid-based spatial descriptions for inverse modeling is inefficient since the goal is to estimate spatially correlated geologic features from low-resolution flow data. Several transform-domain parameterization techniques have been applied to subsurface flow and transport inverse problems including principle component analysis (PCA) (Gavalas et al. 1976), discrete cosine transform (DCT) (Ahmed et al. 1974; Jafarpour and McLaughlin 2009a,b), and discrete wavelet transform (DWT) (Mallat 2008; Jafarpour et al. 2010; Sahni and Horne 2005). These methods attempt to provide a compact representation of the parameters to substantially reduce the number of unknowns in the inverse problem. A key issue in implementing these techniques is identifying the significant basis components that explain the main variability in the parameter fields. This issue has been elegantly addressed by the recent developments in sparse signal processing, which is the central topic of this chapter.

Regularization of ill-posed subsurface inverse problems can also be carried out by constraining the solution to honor explicit prior models, available static data, and/or some global attributes of the parameter field such as smoothness (e.g., Tikhonov and Arsenin 1977; Constable et al. 1987; Tonkin and Doherty 2005). In general, regularization serves two primary purposes: it (a) stabilizes the solution of an ill-posed inverse problem and (b) constrains the solution to adequately reproduce the observed data without generating unjustifiably complex artifacts (Constable et al. 1987). By using prior information about the parameters, directly or indirectly, regularization is applied to mathematically improve the behavior of the inverse modeling objective function and/or implicitly reduce the dimensionality of the parameter search space. Several regularization methods with varying levels of sophistication have been applied to subsurface characterization inverse problems (e.g., Tikhonov and Arsenin 1977; Portniaguine and Zhdanov 1999; Tonkin and Doherty 2005; Hill and Tiedeman 2007; Oliver et al. 2008). In some cases (Jafarpour et al. 2010), a combination of parameterization and regularization may prove more effective as certain solution attributes (e.g., sparsity) may only be realized and effectively exploited in a properly selected transform domain. An instance of this combined case is discussed in more detail next. To motivate the use of sparse reconstruction for model calibration, the fundamental concept and practical implications of compressed sensing paradigm are briefly introduced first, followed by a simple illustrative example.

4.2 Sparse Reconstruction and Compressed Sensing

Consider the problem of solving the system of equations $\mathbf{\Phi v} = \mathbf{u}$, where $\mathbf{\Phi} \in \mathbb{R}^{M \times N}$. In many realistic applications $M \ll N$, rendering the problem severely underdetermined. From classical linear algebra for $M < N$, this system of equations does not yield a unique solution. When the solution vector $\mathbf{v}$ is known to be sparse (i.e., many of its components are zero), however, one may hope to find a unique solution by taking advantage of the knowledge about the solution sparsity. This situation is illustrated with a simple example in Fig. 4.1. In this figure, an underdetermined linear system of equations with $M = 4$ equations and $N = 20$ unknowns is sketched. In this case, the true solution vector $\mathbf{v}$ has only $S = 4$ nonzero components. Without exact knowledge of its sparsity (i.e., the number and location of its nonzero elements), $\mathbf{v}$ cannot be identified from the available measurements. As shown on the bottom part of Fig. 4.1, if the sparsity structure of the solution $\mathbf{v}$ is perfectly known in advance, the system can be reduced to an even-determined $M = N = 4$ linear system of equations. For many sparse vectors, an apparently underdetermined problem often may be reduced to an (even-) overdetermined problem if the sparsity structure is known. However, in reality, exact a priori knowledge about the sparsity structure in the solution is not available. That is, while it may be known that a given problem is likely to have sparse solutions, the exact sparsity structure is usually unknown. When the solution is sufficiently

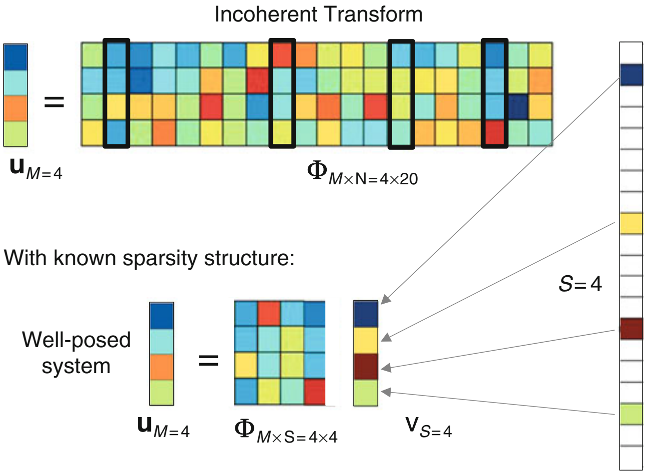

Fig. 4.1 Schematic illustration of how knowledge of solution sparsity can lead to finding a unique solution of underdetermined linear system of equations: a key unknown is the sparsity structure, which must be estimated along with the value of the nonzero (active) elements

sparse, with increasing number of independent measurements, it is less likely to find solutions that are sparser than the true solution and that satisfy the measurement constraints. In the limit, as the number of independent measurements exceeds a certain threshold, the true solution becomes the sparsest solution that satisfies the linear measurement equations. *Compressed sensing* (Donoho 2006) formalizes the conditions under which unique solutions to sparse underdetermined linear systems of equations exist and can be computed efficiently. A general approach to finding a sparse solution to $\mathbf{\Phi v} = \mathbf{u}$ is to formulate and solve a minimization problem of the form

$$(P_J): \quad \min_{\mathbf{v}} J(\mathbf{v}) \quad s.t. \quad \mathbf{u} = \mathbf{\Phi v} \tag{4.4}$$

in which $J(\mathbf{v})$ promotes solution sparsity. A good choice for $J(\mathbf{v})$ is the number of nonzero elements of the solution vector $\mathbf{v}$. This leads to the sparse reconstruction problem

$$(P_0): \quad \min_{\mathbf{v}} \|\mathbf{v}\|_0 \quad s.t. \quad \mathbf{u} = \mathbf{\Phi v}, \tag{4.5}$$

where $\|\mathbf{v}\|_0$ counts the number of nonzero components of $\mathbf{v}$. Solving (P_0) leads to a combinatorial problem that requires an exhaustive search over all possible sparse subsets of $\mathbf{v}$, which is NP-hard (Natarajan 1995). There is a vast literature concerned with finding a reliable, efficient, and robust solution approach to (P_0). It can be shown (Donoho and Elad 2003) that a solution $\mathbf{v}$ with the number of nonzero entries

$$\|\mathbf{v}\|_0 < \frac{1}{2}\left(1 + \frac{1}{\mu(\mathbf{\Phi})}\right), \tag{4.6}$$

where

$$\mu(\boldsymbol{\Phi}) = \min_{1\leq k,j,\leq m,k\neq j} \frac{\left|\phi_k^{\mathrm{T}}\phi_j\right|}{\left\|\phi_k\right\|_2 \left\|\phi_j\right\|_2} \tag{4.7}$$

is the mutual coherence of $\boldsymbol{\Phi}$ and ϕ_j is the jth column of $\boldsymbol{\Phi}$, is necessarily the sparsest solution.

From Eqs. (4.6) and (4.7), the (nearly) orthogonal sensing matrix $\boldsymbol{\Phi}$ has low mutual coherence; thus, the solution of ℓ_p-norm optimization ($p \leq 1$) is equivalent to that of ℓ_0-norm optimization. Examples of sparse sampling matrices with low mutual coherence that are frequently used in sparse reconstruction literature are the Gaussian and Bernoulli random matrices. Compressive bases such as DCT and DWT also have incoherent columns and are examples of possible candidates for sparse reconstruction.

Efficient approximate solutions known as *pursuit algorithms* have been developed to solve (P_0). The main practical algorithms are classified as the *greedy algorithms* (GA), also known as *matching pursuit* (MP) (Tropp and Gilbert 2007; Mallat and Zhang 1993; Couvreur and Bresler 2000), and the *convex relaxation* techniques (Santosa and Symes 1986; Chen et al. 1998; Rao and Kreutz-Delgado 2003; Karlovitz 1970; Gorodnitsky and Rao 1997). A *greedy* strategy for finding a solution is to avoid the exhaustive combinatorial search by taking locally optimal steps (Tropp and Gilbert 2007). In this approach, starting with an initially empty matrix and $\mathbf{v}^0 = 0$, iterative construction of a k-term approximation $\mathbf{v}^k$ is obtained by maintaining a set of active columns and adding an additional column at each step. The added column is chosen to maximally reduce the residual ℓ_2 error in approximating $\mathbf{u}$ with currently active columns (Tropp and Gilbert 2007). This procedure is continued until a stopping criterion, usually an error threshold, is reached. The computational complexity of the above greedy algorithm is significantly better than an exhaustive search; however, the variants of this method mainly suffer from a lack of robustness and guaranteed convergence to a sparse solution.

Convex relaxation methods (Chen et al. 1998; Donoho 2006) try to make the problem more tractable by replacing the highly discontinuous ℓ_0-norm with a more continuous sparsity-promoting penalty function. The ℓ_p-norm, i.e., $J(\mathbf{v}) = \|\mathbf{v}\|_p = \left(\sum_{i=1}^{N} |v_i|^p\right)^{\frac{1}{p}}$, with $p \in (0,1]$, and $J(\mathbf{v}) = \sum_j v_j^2 / \left(\beta^2 + v_j^2\right)$, with $\beta \to 0$ (referred to as compactness constraint), are possible choices that behave similarly to the ℓ_p-norm, for small p values (see Fig. 4.2). When the ℓ_p-norm with $p \in (0,1]$ is used to promote sparsity, a popular class of approximate algorithms to find a solution is the iteratively reweighted least-squares (IRLS) technique (Chartrand and Yin 2008). Note that although for $p < 1$ the norm definition is violated, the term ℓ_p-norm is commonly used in the literature.

For $p = 1$, the problem reduces to a convex optimization problem of the form

$$(P_1): \quad \min_{\mathbf{v}} \|\mathbf{v}\|_1 \quad s.t. \quad \mathbf{u} = \boldsymbol{\Phi}\mathbf{v}, \tag{4.8}$$

which is widely studied in the literature and recently formalized under compressed sensing paradigm.

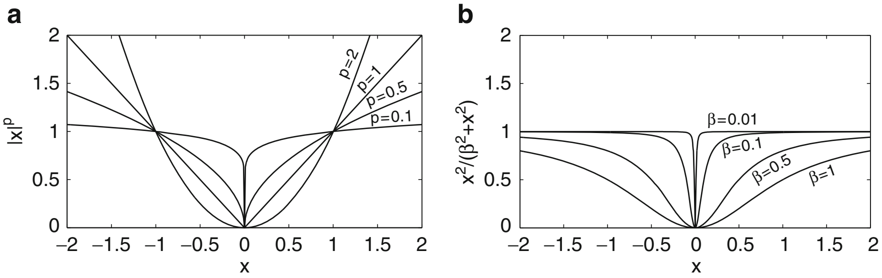

Fig. 4.2 Behavior of $|\mathsf{x}|^p$ for different values of p: (**a**) as $p \to 0$, larger penalties are given to small values of x (the function is convex for $p \geq 1$). (**b**) Behavior of compactness constraint for different values of β and as $\beta \to 0$

For sufficiently sparse solutions when enough measurements are available and the columns of $\mathbf{\Phi}$ are incoherent, the solution to the convex ℓ_1-norm minimization problem is equivalent to the original problem in (P_0). The main advantage of the above convexification over other approximate solution techniques is mainly related to the well-established efficient linear programming techniques (such as interior point method) that can be used to solve the resulting optimization problem (Chen et al. 1998). Several efficient methods have also been recently introduced for solving the (P_1) problem, including *iteratively reweighted least-squares* (Daubechies et al. 2004), *iterated shrinkage algorithms* (Daubechies et al. 2004; Figueiredo and Nowak 2003; Elad et al. 2007), and step-wise algorithms such as *least angle regression* (LARS) (Efron et al. 2004). Some of these greedy-type methods have been applied to the general linear inverse problems in imaging applications (Daubechies et al. 2004, 2008).

4.2.1 Illustrative Example

Let us now consider M direct observations of a parameter field $\mathbf{u}$ with dimension $N = 100$. Under matrix transformation $\mathbf{\Phi}$, the vector $\mathbf{v}$ is a $S = 10$-sparse representation of $\mathbf{u}$. Figure 4.3 displays the compressed sensing solutions for different values of M. As can be verified from this figure, with inadequate observations, the solutions are sparse, match the observed values perfectly, and have smaller ℓ_1-norm than the reference vector. As M increases, it becomes more difficult to match the increased number of measurements without increasing the ℓ_1-norm. At some value of M, perfect reconstruction of the reference model is obtained because no solutions with lower ℓ_1-norm can be found to reproduce the observations. Three observations regarding this example are given as follows. First, replacing ℓ_0-norm with ℓ_1-norm introduces a shrinkage property that, under equal observation match quality, gives preference to solutions with underestimated coefficients. This implies that the shrinkage property can lead to underestimated solutions in realistic problems

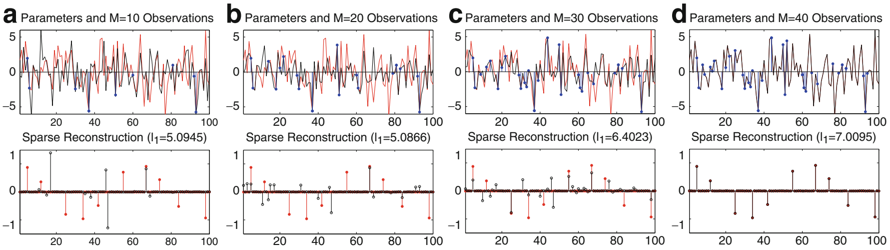

Fig. 4.3 Compressed sensing solution of a simple underdetermined linear system of equations for a $S = 10$-sparse parameter for different values of M; perfect reconstruction is achieved for $M = 40$; *top row* shows the spatial representation of the reference (*red*) and estimated parameters (*black*); the M observed elements are shown with *blue dots*; *bottom row* shows the reference (*red*) and reconstructed (*black*) sparse solutions in the transform domain

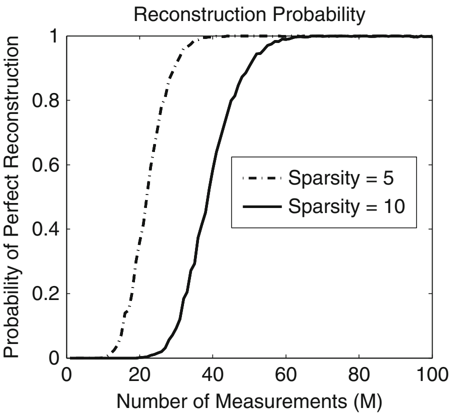

Fig. 4.4 The commutative distribution function (CDF) of perfect reconstruction for a similar example as that shown in Fig. 4.4, but for two cases $S = 5$ and $S = 10$, as a function number of measurements M. The CDF is obtained by repeating the reconstruction for 1,000 times with random measurements and counting the number of times perfect reconstruction was achieved

where perfect reconstruction is impossible due to observations noise. Second, the convex nature of the problem implies that the identified solutions in each case are the global minima. Third, the number of measurements required for perfect reconstruction depends on the specifics of the problem, including the measurement matrix and the measured components of the parameters. For Bernoulli and Gaussian random measurements and sufficiently spare solutions, perfect reconstruction can be achieved with a very high probability for $M > O(S\log(N/S))$. For the example shown in Fig. 4.3, the cumulative probabilities of perfect reconstruction over 1,000 trials with different number of random measurements are shown in Fig. 4.4 for both $S = 5$ and $S = 10$. Perfect reconstruction with smaller number of measurements is possible with lower probability, depending on the measured components.

While compressed sensing provides theoretical guarantees for solving underdetermined linear problems when the solution is sufficiently sparse, such general conditions cannot be specified for nonlinear subsurface flow model calibration problems. Nonetheless, the important guidelines derived from the linear case can be used to facilitate the solution of nonlinear inverse problems. The most remarkable feature of the above sparsity-promoting algorithms is the selection property of the ℓ_p-norm (for $p \in (0, 1]$) that can identify the significant components of the solution. This norm can be exploited to regularize nonlinear inverse problems where limited observations are used to identify, from a large set of components with potentially many irrelevant elements, a small subset with significant contribution in reproducing the observations. In the next section, typical subsurface flow model calibration is reformulated as a selection problem in which the sparsity-promoting nature of the ℓ_p-norm is invoked to find the solution.

4.3 Sparsity-Promoting Groundwater Model Calibration

To formulate groundwater model calibration as a sparse reconstruction problem, a sparse representation (approximation) of the unknown model parameters must be available. An important step in this direction is to recognize that spatially correlated features often have sparse representations in a properly designed transform domain. In particular, geologic formations are piecewise continuous and exhibit strong spatial correlations. Hence, a proper choice of decorrelating basis functions can be applied to remove the spatial correlation, thereby substantially decreasing the dimension of the parameter field. Such low-dimensional representations give rise to reduced-order approximations that tend to preserve the most salient features of a given geologic model while compromising insignificant details.

4.3.1 Sparse Representations of Aquifer Properties

Physical properties of geologic formations exhibit strong spatial correlations. This strong correlation implies that the underlying physical property maps are amenable to highly sparse or compact representations in a properly designed decorrelating transform domain. *Preconstructed* compression bases and *empirically learned* sparsifying transforms can be used to sparsely represent spatially variable aquifer properties. While generic compressive bases can compactly approximate any given image (property map), they are not as effective as sparse dictionaries that are learned from reliable prior information for a particular application, e.g., subsurface modeling. Sparse geologic dictionaries can be learned from reliable prior training data and are more effective in capturing the expected variability in the formation of interest.

4.3.1.1 Preconstructed (Generic) Sparsifying Transforms

Among notable preconstructed compression transforms are the discrete cosine transform (DCT) that is used in the JPEG image compression (Ahmed et al. 1974;

Britanak et al. 2006) and the discrete wavelet transforms (DWT) that is the basis for the JPEG2000 compression standard (Daubechies 1988; Mallat 2008; Jafarpour 2011). In both methods, the property image is decomposed into its frequency content. For most natural images, after transformation, only a fraction of the basis components have significant contributions to reconstructing the original image, implying that most natural images have sparse approximations in the DCT or DWT domains.

The Discrete Cosine Transform

The DCT is a unitary linear transform that is widely used for image compression because of its well-known near-optimal energy compaction and signal decorrelation power. The one-dimensional forward DCT $v(k), 0 \leq k \leq N-1$, of a signal $\mathbf{u}_N$ of length N and its inverse transform can be expressed as (Britanak et al. 2006)

$$v(k) = \alpha(k) \sum_{n=0}^{N-1} u(n) \cos\left[\frac{\pi(2n+1)k}{2N}\right] \tag{4.9}$$

$$u(n) = \sum_{k=0}^{N-1} \alpha(k) v(k) \cos\left[\frac{\pi(2n+1)k}{2N}\right], \tag{4.10}$$

where $\alpha(k_{1:N-1}) = \sqrt{2}\alpha(0) = \sqrt{\frac{2}{N}}$. The DCT can be interpreted as a real-valued case of the discrete Fourier transform (DFT) and inherits many of the properties of the DFT. For an image with strong spatial correlation, the first few low-frequency modes often adequately explain the main variability in the image. For example, Fig. 4.5a shows the application of the DCT basis in compressing a channelized permeability field. The DCT parameterization has recently been applied to inversion of rock flow properties from flow data (Jafarpour and McLaughlin 2009a,b, 2008). Extension of the DCT to more realistic three-dimensional problems with irregular boundaries and unstructured grid systems is discussed in Bhark et al. (2011).

The Wavelet Transform

A wavelet is a function $\psi(x)$ such that an orthonormal basis of wavelets $\psi_{jk}(x) = 2^{-j/2}\psi(2^{-j}x - k)$ can be generated by dilating and translating this function (Daubechies 1988; Mallat 1989). The idea of the wavelet transform is to represent any measurable, square-integrable 1-D function $f(x) \in L^2(R)$ as a limit of successive approximations, i.e.,

$$f = \sum_{j,k} \langle f, \psi_{jk} \rangle \psi_{jk}. \tag{4.11}$$

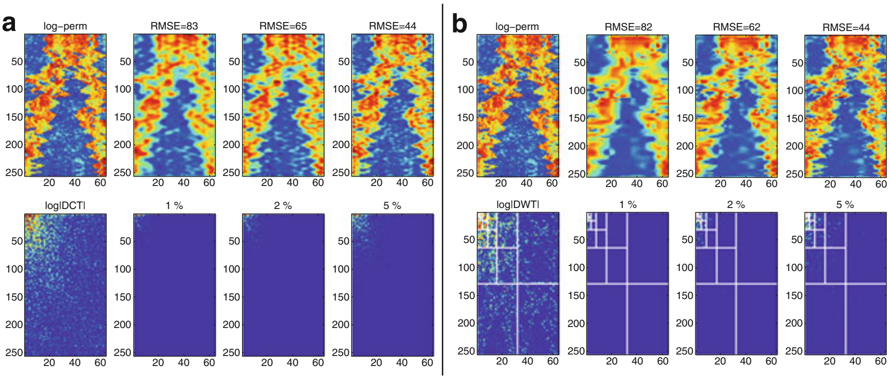

Fig. 4.5 Compression power of the discrete cosine transform (**a**) and the discrete wavelet transform (**b**). In each case, the *first row* shows the spatial representations, while the *second row* displays the transformed coefficients; the *first columns* are related to the original images, while the *remaining columns* show approximations with increasing number of retained coefficients (*left to right*). The number on top of the plots in the second row shows the percentage of coefficients retained in the approximated expansion. The DCT coefficients are usually clustered around the low-frequency basis components (*top-left corner*), and the DWT coefficients have space localization property. Both of these properties will be exploited to incorporate prior information in our sparse reconstruction framework

Moreover, for $j \in [1,2,\ldots]$, $\sum_{k\in\mathbb{Z}}\langle f,\psi_{jk}\rangle\psi_{jk}$ expresses the difference between the approximations of f with resolutions 2^j and 2^{j-1}. This leads to a multiresolution analysis of $L^2(R)$ consisting of a ladder of spaces $\cdots \subset V_2 \subset V_1 \subset V_0 \subset V_{-1} \subset V_{-2} \subset \cdots$ and the existence of a function $\phi \in V_0$ such that $\phi_{0n}(x) = \phi(x-n)$ constitute an orthonormal basis of V_0.

Since ϕ generates a multiresolution analysis, it is called a *scaling function*. The wavelet and scaling functions ψ and ϕ are related by

$$\psi(x) = \sum_{n\in Z}(-1)^n c(-n+1)\phi(2x-n). \tag{4.12}$$

For computation of the *wavelet coefficients*, a convolution followed by a "down-sampling" is performed (Daubechies 1988) $\langle f,\psi_{jk}\rangle$:

$$\langle f,\psi_{jk}\rangle = \sum_n g(n-2k)\langle f,\phi_{j-1n}\rangle,\ \ \langle f,\phi_{jk}\rangle = \sum_n h(n-2k)\langle f,\phi_{j-1n}\rangle, \tag{4.13}$$

where $h(n) = c(n)/\sqrt{2}, g(n) = (-1)^n c(-n+1)/\sqrt{2}$. Similarly, the scaling coefficients are

$$\langle f,\phi_{j-1m}\rangle = \sum_k [h(m-2k)\langle f,\phi_{jk}\rangle + g(m-2k)\langle f,\psi_{jk}\rangle]. \tag{4.14}$$

Compared to Fourier-type methods, the DWT has the benefit of space-frequency localization. This property is seen by comparing the first columns in Fig. 4.5a, b, where, unlike the DCT coefficients, the wavelet coefficients reveal local spatial information about the underlying features in the original spatial map. In inverse problems, this localization benefit may be realized when sufficiently high-resolution data is available to identify and resolve the local features in the solution (Jafarpour 2011). Nonetheless, this spatial localization may be exploited in the inversion to incorporate prior sparse structures and/or to implement adaptive multiresolution inversion.

4.3.1.2 Learned Sparse Geologic Dictionaries

As an alternative to generic compression bases, one can construct application-specific sparse dictionaries from a training database. That is, using a training database as prior knowledge, one can construct a matrix $\boldsymbol{\Phi}$ such that the projection of the features in the training database onto $\boldsymbol{\Phi}$ becomes sparse. This approach is widely used in computer vision and object recognition where a training database of a specific object is available (e.g., face or fingerprint features). A learned dictionary is more efficient for reconstructing an object that is similar to those in the training database. In many subsurface characterization applications, such databases can be readily constructed from prior knowledge using geostatistical simulation (Deutsch and Journel 1998).

A relatively simple technique for learning sparse dictionaries from a prior database is the K-SVD algorithm (Kreutz-Delgado et al. 2003; Aharon et al. 2006). Suppose that a database of images containing L samples $\tilde{\mathbf{u}}_{l=1:L}$ is available. Either of the following optimization problems can be solved to find a dictionary that yields a sparse approximation to the samples in the database (Kreutz-Delgado et al. 2003; Aharon et al. 2006):

$$\min_{\boldsymbol{\Phi},\mathbf{v}_l|_{l=1}^{L}} \|\mathbf{v}_l\|_0 \qquad s.t. \quad \|\tilde{\mathbf{u}}_l - \boldsymbol{\Phi}\mathbf{v}_l\|_2 \leq \varepsilon, \qquad \text{or} \tag{4.15}$$

$$\min_{\boldsymbol{\Phi},\mathbf{v}_l|_{l=1}^{L}} \|\tilde{\mathbf{u}}_l - \boldsymbol{\Phi}\mathbf{v}_l\|_2 \qquad s.t. \quad \|\mathbf{v}_l\|_0 = l_0. \tag{4.16}$$

Although there is no known practical algorithm for efficient solution of these equations, heuristic methods such as the method of directions (MOD) and K-SVD, have been shown to perform reasonably well in finding an empirically learned dictionary (Tropp and Gilbert 2007; Aharon et al. 2006). Unfortunately, the computational complexity of these methods for large-scale problems is considerable. In image processing application this issue is addressed through image segmentation to reduce the dimension of the sparse dictionary.

A main difficulty in using learned dictionaries is that their efficiency depends on the quality and representativeness of the prior database. Generic compression bases such as DWT and DCT may be combined with learned sparse dictionaries to gener-

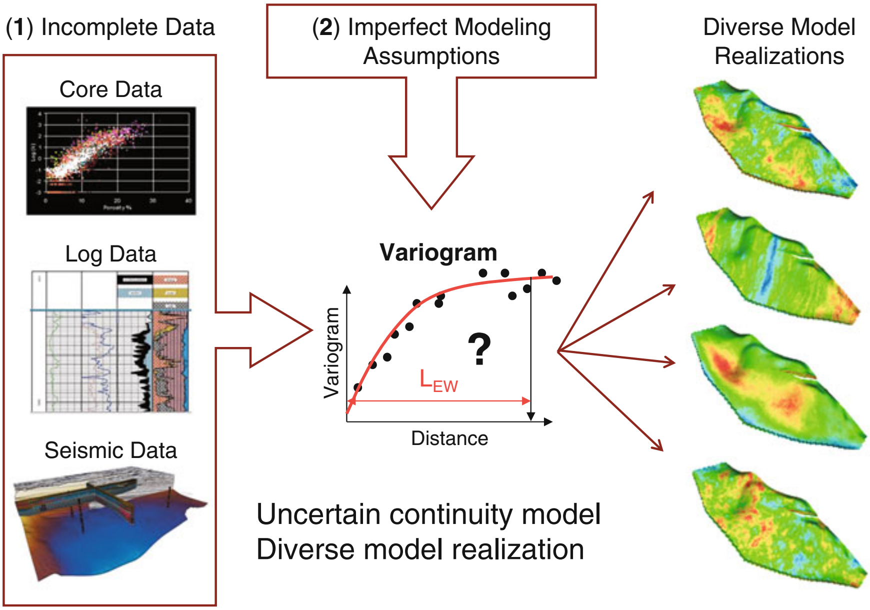

Fig. 4.6 Uncertainty in collected data (**1**) together with imperfect modeling, interpolation, and interpretation assumptions (**2**) can lead to uncertainty in structural continuity model, e.g., variogram. Accounting for uncertainty in structural parameters can result in prior model realizations that have very diverse continuity structure (*right*)

ate hybrid dictionaries that are robust against errors in the prior model (khaninezhad and Jafarpour 2012). When the presumed prior information is incorrect, generic bases with strong compression power are available to approximate the solution of the inverse problem, an important advantage of the hybrid parameterization approach.

4.3.1.3 Sparsity for Identification of Geologic Continuity

The selection property of the sparsity-promoting regularization is the fundamental concept behind sparse inversion algorithms. A sparse reconstruction formulation of an inverse problem is warranted if one expects the solution to be sparse. Sparsifying transforms that were discussed above can be used to justify solution sparsity. Another application in which solution sparsity is expected is when the prior model of geologic continuity (e.g., variogram model) is unknown or uncertain, resulting in very diverse datasets, with many irrelevant content. Figure 4.6 illustrates a scenario where variogram model uncertainty can result in distinctly different model realizations, to the extent that the continuity in most of the realizations becomes irrelevant for reconstruction of the true property distribution. The diversity (uncertainty) in the prior training dataset leads to a geologic dictionary with many

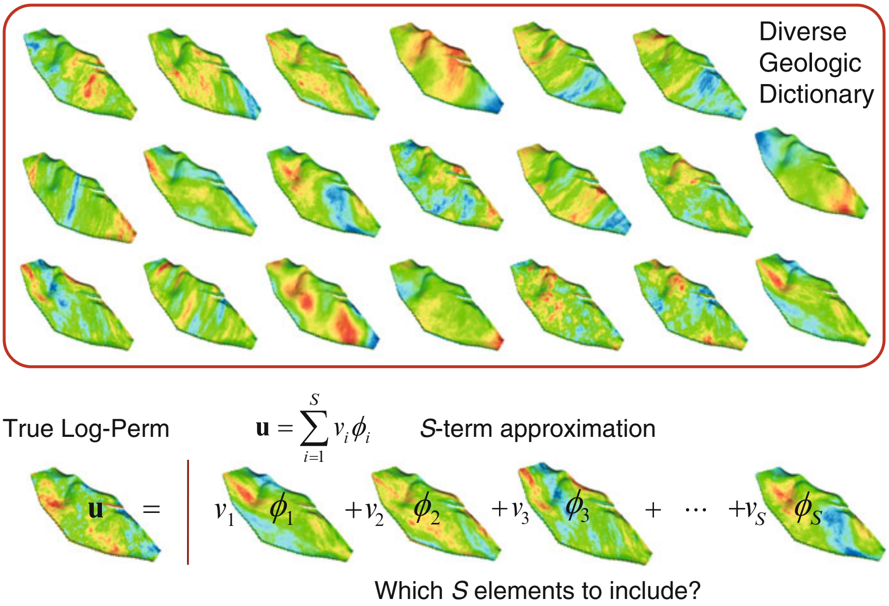

Fig. 4.7 *Top*: diverse geologic dictionaries used to sparsely represent a diverse set of structural continuity in a property field; sparsity is applicable since many of the elements used to represent prior uncertainty are not expected to contribute to the solution. *Bottom*: approximate representation of a reference model as a linear combination of a small subset from the diverse geologic dictionary

elements that have little or no contributions in reconstructing the true solution. As a result, the problem is reduced to selection of very few relevant elements from a diverse geologic dictionary, which can be achieved by sparsity-promoting solution methods. Figure 4.7 shows an example diverse geologic dictionary obtained by treating the variogram model parameters as uncertain random variables. This geologic dictionary can be used to sparsely represent a property field with a given continuity structure.

4.3.2 Sparse Model Calibration Formulation

In groundwater model calibration inverse problems, the relation between measurable quantities (e.g. flow rate and hydraulic head) and unknown parameters (e.g., permeability and porosity) is often nonlinear. While rigorous treatment of the convergence behavior in nonlinear systems is nontrivial, new problem formulation can still be developed to exploit sparsity and regularize the solution. Gradient-based techniques may be used with nonlinear models to search for a sparse solution by minimizing a sparsity-promoting regularized least-squares objective function as discussed next.

4.3.3 Nonlinear Model Calibration Using Sparse Reconstruction

A sparsity-promoting version of the nonlinear inverse problem in (4.3) can be expressed as

$$\min_{\mathbf{v}} J(\mathbf{v}) = \|\mathbf{d}_{\text{obs}} - \mathbf{g}(\boldsymbol{\Phi}\mathbf{v})\|^2_{\mathbf{C}_\mathbf{d}^{-1}} + \gamma^2 \|\mathbf{v}\|_p^p, \tag{4.17}$$

where γ is a regularization parameter, $\mathbf{u} = \boldsymbol{\Phi}\mathbf{v}$, and an ℓ_p-norm approximation to the ℓ_0-norm is used. Since $\boldsymbol{\Phi}$ is a known dictionary, one can compactly express the problem as

$$\min_{\mathbf{v}} J(\mathbf{v}) = \|\mathbf{d}_{\text{obs}} - \mathbf{g}(\mathbf{v})\|^2_{\mathbf{C}_\mathbf{d}^{-1}} + \gamma^2 \|\mathbf{v}\|_p^p. \tag{4.18}$$

When needed, the relation $\mathbf{u} = \boldsymbol{\Phi}\mathbf{v}$ can be used to readily compute the spatial parameter field (e.g., permeability distribution) $\mathbf{u}$ for any instance (iterate) of $\mathbf{v}$. This formulation of the model calibration inverse problem amounts to finding sufficiently sparse solutions in the linear expansion functions $\boldsymbol{\Phi}$. Gradient-based optimization methods can be used to solve the above minimization, for example, by using iteratively reweighted least-squares algorithm (Li and Jafarpour 2010). However, care must be exercised when solving this minimization problem since for $p \leq 1$, the derivative of the ℓ_p-norm sparsity-promoting term is not defined for zero components of $\mathbf{v}$, a condition that is given the sparse nature of the solution. A simple practical way to avoid this issue is to place a lower bound on the magnitude of the components of $\mathbf{v}$, i.e., $|v_i| \geq \varepsilon$.

4.3.4 Example Applications of Sparse Reconstruction

4.3.4.1 Example 1: Travel-Time Tomography

Consider a simple straight-ray cross-well tomography example to demonstrate the effectiveness of sparse reconstruction for solving ill-posed subsurface characterization inverse problems. A simple straight-ray cross-well travel-time tomography setup is shown in Fig. 4.8a. A uniformly spaced system of 10 sources is located on the left end of the domain, and a symmetric array of 10 receivers is placed on the right end of the interval. The resulting 100 arrival-time measurements are used to infer the slowness structure of the medium (see Jafarpour and McLaughlin 2009c for additional details). The true slowness used to generate the synthetic inversion data is shown in Fig. 4.8b. Denoting the spatial description of the medium slowness as $\mathbf{u}$ and the travel-time tomography observations as $\mathbf{d}_{\text{obs}}$, the measurement equations for this example can be written as $\mathbf{d}_{\text{obs}100\times1} = \boldsymbol{\Psi}_{100\times2025}\mathbf{u}_{2025\times1}$. Given the compression property of the DCT basis for correlated spatial images (Jafarpour and McLaughlin 2009a,b), the sparse reconstruction problem can be solved in a

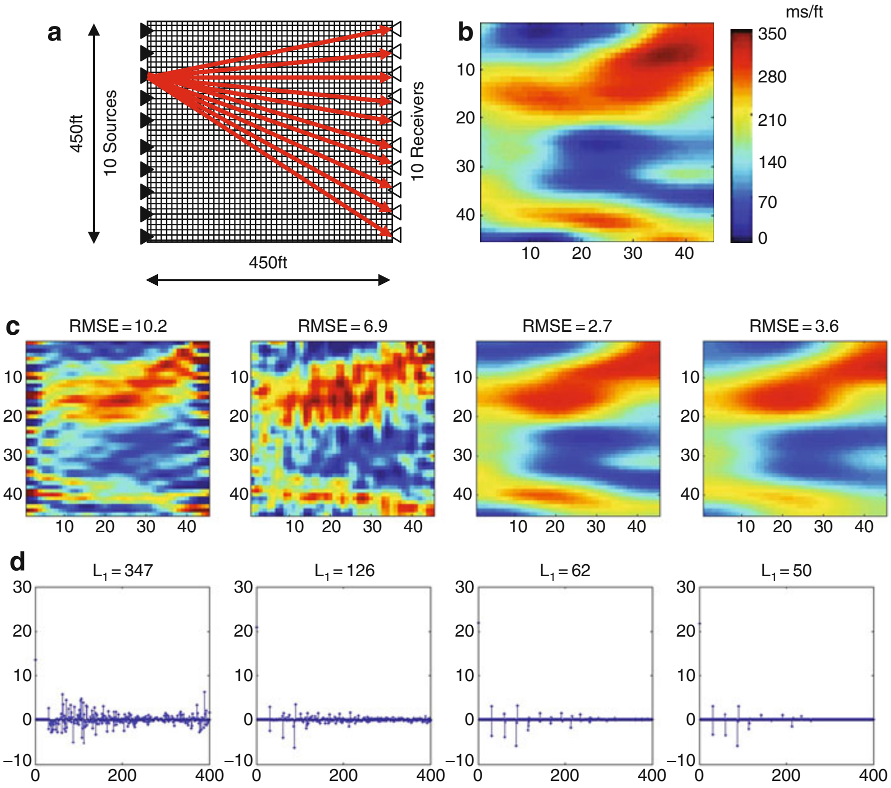

Fig. 4.8 Travel-time tomography example using compressed sensing reconstruction algorithm in a 465-dimensional low-frequency DCT basis: (**a**) experimental setup with 10 transmitters and 10 receivers resulting in a total of 100 measurements, (**b**) reference model with large-scale continuity structure, (**c**) spatial representation of reconstruction results with increasing role of sparsity regularization, and (**d**) reconstructed sparse solution corresponding to the results shown in (**c**)

subspace defined by 465 low-frequency DCT basis components. That is, we write the spatial description of the slowness as $\mathbf{u}_{2025\times 1} = \mathbf{\Omega}_{2025\times 465}\mathbf{v}_{465\times 1}$, where $\mathbf{v}$ stands for the DCT coefficients representing the slowness map and $\mathbf{\Omega}_{2025\times 465}$ denotes the DCT forward transformation matrix (Jafarpour and McLaughlin 2009a,b). For simplicity, the dimension subscripts are dropped hereafter, and the relation between the unknown DCT parameters and arrival-time measurements is expressed as $\mathbf{y} = \mathbf{\Psi u} = \mathbf{\Psi\Omega v}$. Adopting the notation $\mathbf{\Phi} = \mathbf{\Psi\Omega}$, this equation is further simplified to $\mathbf{y} = \mathbf{\Phi v}$. The ℓ_1-norm regularization can now be applied to select and combine the significant DCT components to construct a solution with the best match (in norm-2 sense) to the data. The convex ℓ_1 relaxation sparsity-promoting formulation of the problem can be expressed as

$$\min_{\mathbf{v}} J(\mathbf{v}) = \|\mathbf{u} - \mathbf{\Phi v}\|_2^2 + \gamma^2 \|\mathbf{v}\|_1 . \tag{4.19}$$

In Fig. 4.8c, the spatial representations of the inversion solutions with increasing (from left to right) value of the regularization parameter, γ, are shown. The corresponding DCT coefficients are depicted in Fig. 4.8d. The increasing trend in the regularization parameter (left to right) results in increased sparsity of the solution and in turn relatively larger data mismatches. It can be observed from this example that promoting sparsity in the transform-domain appears to selectively retain the relevant DCT coefficients and estimate their value to match the observed data. It is this selection property of the sparsity penalty that can be exploited to trim irrelevant components that may otherwise remain in the solution and generate artifacts without affecting the data mismatch. When the regularization parameter is too large, the shrinkage property of ℓ_1-norm regularization can lead to solution underestimation (last column of Fig. 4.8c), which is an unintended by-product of approximating ℓ_0-norm with ℓ_1-norm. In our recent publications (Li and Jafarpour 2010; Mohammad-khaninezhad et al. 2012a,b), some of the practical implications of this approximation are discussed, and modified implementations are introduced to mitigate this effect. The above example was used to illustrate how generic transform domain sparse representations of subsurface features can be used to formulate and solve regularized subsurface characterization inverse problems. Next, solution of a nonlinear subsurface flow model calibration inverse problem is presented using geologic dictionaries and a gradient-based minimization method.

4.3.4.2 Example 2: Groundwater Flow Model Calibration

The sparse nonlinear model calibration formulation in Eq. (4.18) is applied to the top layer of the SPE10 model in this section. The model is two-dimensional and has $60 \times 220 = 13{,}200$ grid blocks. The prior model realizations in this case are constructed using the *sgsim* (Deutsch and Journel 1998) algorithm with highly uncertain variogram model parameters to account for the uncertainty in anisotropy direction. In this case, 3600 realizations are used to construct $K = 500$ K-SVD dictionary elements with a sparsity level of $S = 50$ (10%) (Mohammad-khaninezhad et al. 2012a,b). This implies that all model realizations that are similar to those in the prior library are expected to have S-term approximations in this dictionary. Sample realizations from the prior model are shown in Fig. 4.9a. These realizations have very different continuity structures with many patterns that are not relevant to the reference model. The diverse geologic dictionary is used to reflect the significant level of uncertainty that exists in the direction of continuity in this example. As discussed in Mohammad-khaninezhad et al. (2012a,b), the diversity of the dictionary provides additional support for solution sparsity as many of the dictionary elements will have little or no contribution to the solution. For this example, a two-phase (oil/water) simulation with 13 water injectors and 2 oil producers is considered.

A gradient-based iteratively reweighted algorithm is used to solve the optimization problem. The adjoint method is implemented for efficient computation of the required gradients of the objective function with respect to the permeability

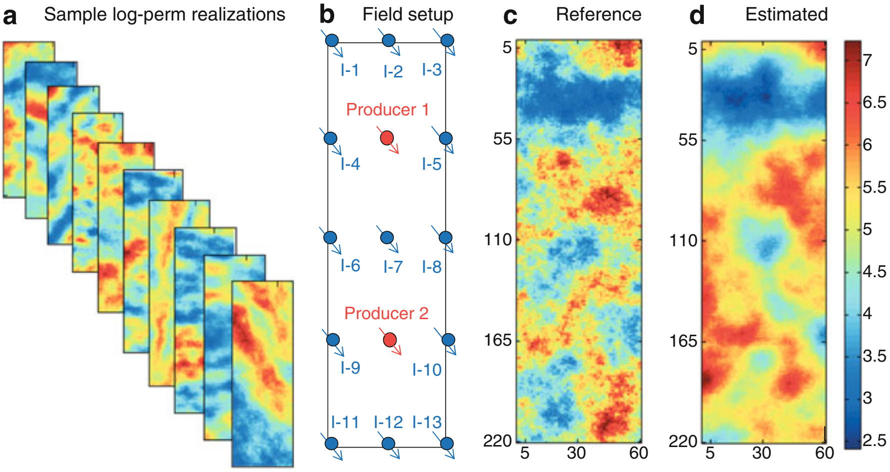

Fig. 4.9 Sparse reconstruction solution of subsurface flow model calibration inverse problem using the top layer of the SPE10 model as an example: (**a**) samples from the initial realizations with diverse continuity structure, (**b**) experimental simulation setup with 15 observation points (wells), (**c**) reference log-permeability field, and (**d**) reconstructed log-permeability model

parameters. Since the permeabilities are linearly related to the K-SVD coefficients ($\mathbf{u} = \mathbf{\Phi v}$), the chain rule of differentiation can be conveniently applied to convert the gradients with respect to the permeability field to the required gradients with respect to the K-SVD coefficients. For brevity, only the final results are presented in here; interested readers are referred to Mohammad-khaninezhad et al. (2012a,b) for additional details about the K-SVD implementation, the problem setup, and the algorithm used to solve the optimization problem. Figure 4.9b shows the well configuration for this example, while Fig. 4.9c depicts the reference log-permeability model. Figure 4.9d displays the log-permeability reconstruction results from dynamic flow measurements collected every 15 days for a total of one year, using the ell_1-norm sparsity-promoting approach. The solution in this case uses a small number of relevant elements from the dictionary to identify the large-scale continuity trends in the reference log-permeability model. The estimated map captures the general permeability trends in the field, with higher accuracy at the vicinity of the observation points (well locations). The performance of the proposed sparsity-promoting model calibration approach is also investigated in several other examples (Jafarpour and McLaughlin 2009c; Jafarpour et al. 2010; Li and Jafarpour 2010; Mohammad-khaninezhad et al. 2012a,b). The preliminary results suggest that sparsity-promoting model calibration methods hold significant potential to improve the solution of ill-posed subsurface model calibration inverse problems. Additional research is underway to explore some of the important properties of this approach and its applicability to realistic field-scale problems.

4.4 Conclusion

A novel subsurface flow model calibration workflow using recent advances in sparse signal processing, known as compressed sensing, was presented. Since its introduction, compressed sensing has received increasing attention in several fields of science and engineering. Here, an overview of the approach and example applications of it were presented. Sparsity is a rich concept and is ubiquitous in subsurface applications. Sparsity-promoting solution of model calibration inverse problems can be achieved by taking advantage of the sparsity in properly designed/selected transform-domain description of aquifer properties (e.g., in DCT and DWT bases and in geologically learned sparse dictionaries). The selection property of the sparsity-promoting inversion implies that the reconstruction results are less sensitive to presence of inconsistent elements in a prior geologic dictionary since these elements are typically given a zero coefficient (contribution) and are removed from the reconstruction. In fact, the diversity of the prior geologic dictionary helps to realize the sparsity of the solution since many of the existing dictionary elements are likely to have little or no contributions to the solution. Overall, sparse model calibration is a promising novel approach for improving the solution of ill-posed subsurface inverse problems that is likely to attract further research attention to develop more effective formulations and efficient implementations algorithms.

References

Aanonsen S (2008) Efficient history matching using a multiscale technique. SPE Reservoir Eval Eng 11(1):154–164

Aharon M, Elad M, Bruckstein A (2006) K-SVD (capitalized): An algorithm for designing overcomplete dictionaries for sparse representation. IEEE Trans Signal Process [see also IEEE Trans Acoust Speech Signal Process] 54(11):4311–4322

Ahmed A, Natarajan T, Rao KR (1974) Discrete cosine transform. IEEE Trans Biomed Eng C23:90–93

Aziz K, Settari A (1979) Petroleum reservoir simulation. Springer, New York

Bear J, Verruijt A (1987) Modeling groundwater flow and pollution (theory and applications of transport in porous media). Applied Science Publishers, London

Bhark E, Jafarpour B, Datta-Gupta A (2011) A generalized grid-connectivity-based parameterization for subsurface flow data assimilation. Water Resour Res 47,W06517:32 PP

Britanak PC, Yip P, Rao K (2007) Discrete cosine transform: general properties, fast algorithms, and integer approximation. Academic Press

Carrera J, Alcolea A, Medina A, Hidalgo J, Slooten LJ (2005) Inverse problem in hydrogeology. Hydrol J 13(1):206–222

Chartrand R, Yin W (2008) Iteratively reweighted algorithms for compressive sensing. IEEE International Conference on Acoustics 2008, Speech and Signal Processing. ICASSP 3869–3872

Chavent G, Bissell R (1998) Indicators for the refinement of parameterization. In: Tanaka M, Dulikravich GS (eds) Inverse Problems in Engineering Mechanics (Proceedings of the International Symposium on Inverse Problems in Engineering Mechanics 1998 (ISIP'98), Nagano, Japan) Elsevier, pp 309–314

Chen SS, Donoho DL, Saunders MA (1998) Atomic decomposition by basis pursuit. SIAM J Sci Comput 20:33–61

Constable S, Parker R, Constable C (1987) Occams inversion: a practical algorithm for generating smooth models from electromagnetic sounding data. Geophysics 52:289–300

Couvreur C, Bresler Y (2000) On the optimality of the backward greedy algorithm for the subset selection problem. SIAM J Matrix Anal Appl 21:797–808

Daubechies I (1988) Multiresolution approximation and wavelet orthonormal bases of $l^2(r)$. Trans Am Math Soc LXI:909–996

Daubechies I, Defrise M, De Mol C (2004) An iterative thresholding algorithm for linear inverse problems with a sparsity constraint. Comm Pure Appl Math 57:1413–1457

Daubechies I, Fornasier M, Loris I (2008) Accelerated projected gradient method for linear inverse problems with sparsity constraints. J Fourier Anal Appl 14,5–6:764–792

Deutsch CV, Journel AG (1998) GSLIB - Geostatistical software library and user's guide. Oxford University Press, New York

Doherty J (2003) Groundwater model calibration using pilot points and regularisation. Ground Water 41(2):170–177

Donoho DL (2006) Compressed sensing. IEEE Trans Inform Theory 52(4):1289–1306

Donoho DL, Elad M (2003) Optimally sparse representation in general (nonorthogonal) dictionaries via l^1 minimization. Proc Natl Acad Sci USA 100(5):2197–2202 (electronic)

Efron B, Hastie T, Johnstine I, Tishirani R (2004) Least angle regression. Ann Stat 32:407–499

Elad M, Matalon B, Zibulevsky M (2007) Coordinate and subspace optimization methods for linear least squares with non-quadratic regularization. Appl Comput Harmonic Anal 23(3):346–367

Figueiredo MAT, Nowak RD (2003) An em algorithm for wavelet-based image restoration. IEEE Trans Image Process 12:906–916

Gavalas GR, Shah PC, Seinfeld JH (1976) Reservoir history matching by bayesian estimation. Soc Petrol Eng J 16(6):337–350

Gorodnitsky IF, Rao BD (1997) Sparse signal reconstruction from limited data using focuss: A re-weighted norm minimization algorithm. IEEE Trans Signal Process 45:600–616

Grimstad AA, Mannseth T, Nvdal G, Urkedal H (2003) Adaptive multiscale permeability estimation. Comput Geosci 7:1–25

Hill MC, Tiedeman CR (2007) Effective groundwater model calibration. Wiley

Jacquard P, Jain C (1965) Permeability distribution from field pressure data. Transactions of the American Institute of Mining, Metallurgical and Petroleum Engineers. (Abbreviated Trans. AIME). Soc Pet Eng J 5(4):281–294

Jafarpour B (2011) Wavelet reconstruction of geologic facies from nonlinear dynamic flow measurements. IEEE Trans Geosci Rem Sens 49(5):1520–1535

Jafarpour B, McLaughlin DB (2008) History-matching with an ensemble kalman filter and discrete cosine parameterization. Comput Geosci 12,2:227–244

Jafarpour B, McLaughlin DB (2009a) Reservoir characterization with discrete cosine transform. part-1: parameterization. SPE Journal, Soc Pet Eng J 14(1):182–201, http://www.onepetro.org/mslib/servlet/onepetropreview?id=SPE-106453-PA

Jafarpour B, McLaughlin DB (2009b) Reservoir characterization with discrete cosine transform. part-2: history matching. SPE Journal, Soc Pet Eng J 14(1):182–201, http://www.onepetro.org/mslib/servlet/onepetropreview?id=SPE-106453-PA

Jafarpour B, Goyal VK, McLaughlin DB, Freeman WT (2009) Transform-domain sparsity regularization for inverse problems in geosciences. Geophysics 74(45):R69–R83, DOI:10.1190/1.3157250

Jafarpour B, Goyal VK, McLaughlin DB, Freeman WT (2010) Compressed history matching: exploiting transform-domain sparsity for regularization of nonlinear dynamic data integration problems. Math Geosci 42:1–27, doi: 10.1007/s11004-009-9247-z

Karlovitz LA (1970) Construction of nearest points in the l_p, p even and l_∞ norms. J Approx Theory 3:123–127

Kitanidis K, Vomvoris EG (1983) A geostatistical approach to the inverse problem in groundwater modeling (steady state) and one-dimensional simulations. Water Resour Res 19(1):677–690

Kreutz-Delgado K, Murray JF, Rao BD, Engan K, Lee TW, Sejnowski TJ (2003) Dictionary learning algorithms for sparse representation. Neural Comput 15(2):349–396

Li L, Jafarpour B (2010) Effective solution of nonlinear subsurface flow inverse problems in sparse bases. Inverse Probl 26(10),105016:24 PP

Mallat S (1989) Multiresolution approximation and wavelet orthonormal bases of $l^2(r)$. Trans Am Math Soc 315:69–88

Mallat S (2009) A wavelet tour of signal processing 3rd edn. Academic Press

Mallat S, Zhang Z (1993) Matching pursuits with time-frequency dictionaries. IEEE Trans Signal Process 41:3397–3415

McLaughlin DB, Townley LR (1996) A reassessment of the groundwater inverse problem. Water Resour Res 32(5):1131–1161

Mohammad-Khaninezhad MR, Jafarpour B, Li L (2012a) Sparse geologic dictionaries for subsurface flow model calibration: Part i. inversion formulation. Adv Water Resour 39:106–121

Mohammad-Khaninezhad MR, Jafarpour B, Li L (2012b) Sparse geologic dictionaries for subsurface flow model calibration: Part ii. robustness to uncertainty. Adv Water Resour 39:122–136

Mohammad-Khaninezhad MR, Jafarpour B (2013) Estimating reservoir connectivity from dynamic data under geologic uncertainty. SPE J (in revision)

Natarajan BK (1995) Sparse approximate solutions to linear systems. SIAM J Comput 24(2):227–234

National Research Council (2000) Seeing into the earth: Noninvasive characterization of the shallow subsurface for environmental and engineering application. Technical report, Washington, DC

Oliver DS, Reynolds AC, Liu N (2008) Inverse theory for petroleum reservoir characterization and history matching. Cambridge University Press, Cambridge

Portniaguine O, Zhdanov MS (1999) Focusing geophysical inversion images. Geophysics 64(3):874–887

Rao BD, Kreutz-Delgado K (2003) An affine scaling methodology for best basis selection. IEEE Trans Signal Process 47:187–200

Sahni I, Horne RN (2005) Multiresolution wavelet analysis for improved reservoir description. SPEREE 8(1):53–69

Santosa F, Symes WW (1986) Linear inversion of band-limited reflection seismograms. SIAM J Sci Stat Comput 7:1307–1330

Tikhonov AN, Arsenin VY (1977) Solution of ill-posed problems. Winston, distributed by Halsted Press, New York

Tonkin M, Doherty J (2005) A hybrid regularized inversion methodology for highly parameterized models. Water Resour Res 41,W10412:170–177

Tropp JA, Gilbert AC (2007) Signal recovery from partial information via orthogonal matching pursuit. IEEE Trans Inf Theory 53:4655–4666

Yeh TCJ, Lee CH, Hsu KC, Illman WA, Barrash W, Cai X, Daniels J, Sudicky E, Wan L, Li G, Winter CL (2008) A view toward the future of subsurface characterization: Cat scanning groundwater basins. Water Resour Res W03301, doi:10.1029/2007WR006375

Chapter 5
Analytic Modeling of Transient Multilayer Flow

Mark Bakker

Abstract An approach is presented for the semi-analytic simulation of transient flow in systems consisting of an arbitrary number of layers. Storage in both aquifer layers and leaky layers is taken into account. Flow in the system is generated by wells and line-sinks. Wells and line-sinks may be open to an arbitrary number of layers, which allows for the simulation of multi-aquifer wells, abandoned wells, partially penetrating streams, and linear fractures that provide a hydraulic connection between aquifer layers.

5.1 Introduction

The objective of this chapter is to present an analytic element approach for the simulation of transient groundwater flow in multilayer systems. The approach allow for the simulation of transient flow in systems consisting of an arbitrary number of layers. The storage in both aquifer layers and leaky layers is taken into account. In this chapter, the flow system may contain an arbitrary number of wells and line-sinks. Wells and line-sinks may be open to an arbitrary number of layers, which allows for the simulation of multi-aquifer wells, abandoned wells, partially penetrating streams, and linear fractures that provide a hydraulic connection between aquifer layers.

Application of an analytic approach has three major benefits over the application of commonly used grid-based models. First, the model domain does not have to be discretized areally in, for example, triangles or rectangles. This means that the accuracy of the solution does not depend on the size of the computational grid, hydrogeological features do not have to be fitted to the computational grid

---

M. Bakker (✉)
Water Resources Section, Civil Engineering and Geosciences, Delft University of Technology, Delft, The Netherlands
e-mail: mark.bakker@tudelft.nl

P.K. Mishra and K.L. Kuhlman (eds.), *Advances in Hydrogeology*,
DOI 10.1007/978-1-4614-6479-2_5,
© Springer Science+Business Media New York 2013

or vice versa, and the hydraulic head may be computed at any location in the aquifer. Second, the head may be evaluated at any time while the accuracy does not depend on a selected time step. And third, the model domain is infinite, avoiding the problem of selecting boundary conditions along the boundaries of the model domain, which is often difficult in the phreatic aquifer and almost impossible in deeper aquifers. Meaningful results are obtained only when significant head changes do not extend beyond hydrogeologic features that are not included in the model.

The approach for transient multilayer modeling presented in this chapter is a culmination and extension of a number of techniques. It applies the theory for transient multi-aquifer flow of Hemker and Maas (1987) and uses concepts of the analytic element method for single aquifer flow (Strack 1989, 2003; Haitjema 1995) and multi-aquifer flow (Bakker and Strack 2003) and the Laplace-transform analytic element method (Furman and Neuman 2003; Kuhlman and Neuman 2009; Bakker and Kuhlman 2011). Analytic element solutions are computed in the Laplace domain. A solution in the physical domain is obtained through numerical Laplace inversion using the algorithm of De Hoog et al. (1982). The presented approach has been implemented in the computer program TTim (ttim.googlecode.com). Several benchmark problems are discussed, and a detailed example of a pumping well near a meandering river in a multilayer setting is discussed at the end of this chapter.

5.2 Main Approximations

Aquifer systems are conceptualized as consisting of two types of horizontal layers: aquifer layers and leaky layers. The Dupuit approximation is adopted for flow in aquifer layers which means that the resistance to flow in the vertical direction is neglected within an aquifer layer (e.g., Strack 2003), but flow is still three-dimensional (Strack 1984). Flow in leaky layers is approximated as vertical. Each layer is approximated as homogeneous. Changes in the transmissivity due to unconfined conditions are not taken into account, as the transmissivity is constant within an aquifer layer in both space and time. The presented approach is applicable to systems that may be approximated as linear. Nonlinear conditions such as streams that carry water only part of the year are not simulated.

5.3 Previous Work

Several approaches have been developed for the analytic solution of specific problems of transient flow in multilayer systems (i.e., no time stepping or areal discretization). Notwithstanding the elegance of many of these solutions, they are not reviewed here. Only a few general approaches have been published that allow for the analytic simulation of transient flow to wells in multilayer systems. Hemker and Maas (1987) and Hemker (1999a,b) present a series of solutions for flow to wells with different types of boundary conditions using a Laplace-transform approach. Superposition of these solutions is allowed as long as the boundary conditions do not interfere with each other. Application of the approach of Hemker and Maas (1987) for the simulation of abandoned wells (multi-aquifer wells with a net zero discharge) is presented in Cihan et al. (2011). Veling and Maas (2009) presented a solution strategy for three-dimensional flow in multilayer systems, i.e., the Dupuit approximation is not adopted and the head varies horizontally and vertically within a layer. In all these papers, the inverse Laplace transform was carried out numerically using either the Schapery or Stehfest algorithms (Schapery 1962; Stehfest 1970). Nordbotten et al. (2004) presented an analytic approximate approach for the simulation of pumping wells and abandoned wells in aquifers that are separated by aquicludes. Strack (2009) presented the generating analytic element approach, which may also be used for the simulation of transient flow (Strack 2006). Fitts (2010) developed a multilayer analytic element approach for the simulation of transient flow that approximates both the areal leakage between aquifers and the release from storage with radial basis functions but relaxes some of the approximations adopted in this chapter, including a transmissivity that varies with the head in unconfined aquifers and horizontal anisotropy. Furman and Neuman (2003) and Kuhlman and Neuman (2009) developed the Laplace-transform analytic element method for single-aquifer flow, which allows for the general simulation of transient flow, and present examples of pumping wells near circular inhomogeneities. Bakker and Kuhlman (2011) apply the Laplace-transform analytic element method to simulate transient flow around impermeable walls in a single aquifer and transient flow between a well and a stream in a two-aquifer system. The cited papers on the Laplace-transform analytic element method compute the inverse Laplace transform numerically with the algorithm of De Hoog et al. (1982), which is also used in this chapter. Some advantages of this algorithm over, for example, Stehfest and Schapery, are discussed later on in this chapter.

5.4 Mathematical Model

The governing system of differential equations in the Laplace domain is derived here. The derivation is given in term of potentials and essentially follows the derivation in terms of heads given in Hemker and Maas (1987). Consider aquifer layer n sandwiched between leaky layers n on top and $n+1$ at the bottom (Fig. 5.1). Three-dimensional Dupuit flow in aquifer layer n is governed by

$$T_n \nabla^2 h_n = S_n \frac{\partial h_n}{\partial t} + q_{b,n} - q_{t,n+1} \tag{5.1}$$

where $h_n(x,y)$ [L] is the head in aquifer layer n, T_n [L^2/T] and S_n [$-$] are the transmissivity and storage coefficient of aquifer layer n, $q_{b,n}$ [L/T] is the upward leakage through the bottom of leaky layer n, $q_{t,n+1}$ is the upward leakage through

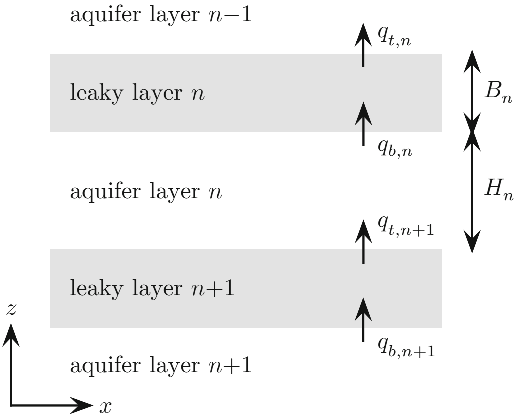

Fig. 5.1 Numbering of aquifer layers and leaky layers in a multilayer system

the top of leaky layer $n+1$, ∇^2 is the two-dimensional horizontal Laplacian, and t is time. The horizontal components of the specific discharge vector, $q_{x,n}$ and $q_{y,n}$, may be obtained with Darcy's law and do not vary vertically within an aquifer layer:

$$q_{x,n} = -k_n \frac{\partial h_n}{\partial x} \qquad q_{y,n} = -k_n \frac{\partial h_n}{\partial y} \tag{5.2}$$

where k_n is the horizontal hydraulic conductivity of layer n. The vertical component of the specific discharge vector varies linearly within an aquifer layer between $q_{t,n+1}$ at the bottom and $q_{b,n}$ at the top (see Fig. 5.1).

The discharge vector in layer n, with components $Q_{x,n}$ and $Q_{y,n}$, is the vertically integrated horizontal specific discharge vector. $Q_{x,n}$ and $Q_{y,n}$ may be written as

$$Q_{x,n} = H_n q_{x,n} = -\frac{\partial \phi_n}{\partial x} \qquad Q_{y,n} = H_n q_{y,n} = -\frac{\partial \phi_n}{\partial y} \tag{5.3}$$

where $\phi_n = T_n h_n$ is the discharge potential, H_n is the thickness of aquifer layer n, and $T_n = k_n H_n$. Equation (5.1) may now be written as

$$\nabla^2 \phi_n = \frac{1}{D_n}\frac{\partial \phi_n}{\partial t} + q_{b,n} - q_{t,n+1} \tag{5.4}$$

where $D_n = T_n/S_n$ is the aquifer diffusivity. Laplace transformation of (5.4) gives

$$\nabla^2 \bar{\phi}_n = \frac{p}{D_n}\bar{\phi}_n + \bar{q}_{b,n} - \bar{q}_{t,n+1} \tag{5.5}$$

where Laplace-transformed variables are indicated with a bar and p is the complex Laplace-transform parameter.

Once a solution is obtained for the Laplace-transformed potential, a solution for the potential in the physical domain is obtained through solution of the Bromwich contour integral (e.g., Sneddon 1972):

$$\phi_n = \mathcal{L}^{-1}\{\bar{\phi}_n\} = \frac{1}{2\pi \mathrm{i}} \int_{\gamma-\mathrm{i}\infty}^{\gamma+\mathrm{i}\infty} \bar{\phi}_n \mathrm{e}^{pt}\, \mathrm{d}p \tag{5.6}$$

where γ is chosen to the right of any singularities in $\bar{\phi}_n$. Integration of the Bromwich integral is carried out numerically in the complex plane using the algorithm of De Hoog et al. (1982).

5.5 Flow Between Aquifer Layers

An equation is derived for the upward flux from aquifer layer n through leaky layer n to aquifer layer $n-1$ by considering one-dimensional vertical flow through leaky layer n (Fig. 5.1); this derivation closely follows (Hemker and Maas 1987). Flow in the leaky layer is governed by

$$\frac{\partial^2 \eta}{\partial z^2} = \frac{\sigma_n}{\kappa_n} \frac{\partial \eta}{\partial t} \tag{5.7}$$

where η is the head in leaky layer n and κ_n [LT^{-1}] and σ_n [L^{-1}] are the vertical hydraulic conductivity and specific storage of leaky layer n, respectively. The head at the top and bottom of the leaky layer are equal to the head in the overlying and underlying aquifers:

$$\eta(z=0) = h_n \qquad \eta(z=B_n) = h_{n-1} \tag{5.8}$$

where B_n is the thickness of leaky layer n (see Fig. 5.1). Laplace transformation of the differential equation and boundary conditions leads to the ordinary differential equation and boundary conditions:

$$\frac{\mathrm{d}^2\bar{\eta}}{\mathrm{d}z^2} = \alpha_n^2 \bar{\eta} \tag{5.9}$$

$$\bar{\eta}(z=0) = \bar{h}_n \qquad \bar{\eta}(z=B_n) = \bar{h}_{n-1} \tag{5.10}$$

where $\alpha_n = \sqrt{p\sigma_n/\kappa_n}$. The solution for $\bar{\eta}$ is straightforward (e.g., Strack 1989)

$$\bar{\eta} = \frac{\bar{h}_{n-1}\sinh(\alpha_n z) + \bar{h}_n \sinh[\alpha_n(B_n - z)]}{\sinh(\alpha_n B_n)} \tag{5.11}$$

so that

$$\frac{\mathrm{d}\bar{\eta}}{\mathrm{d}z} = \frac{\alpha_n \bar{h}_{n-1}\cosh(\alpha_n z) - \alpha_n \bar{h}_n \cosh[\alpha_n(B_n - z)]}{\sinh(\alpha_n B_n)} \tag{5.12}$$

The Laplace-transformed vertical flux $\bar{q}_{t,n}$ at the top of leaky layer n is obtained with Darcy's law as

$$\bar{q}_{t,n} = -\kappa_n \frac{\mathrm{d}\bar{\eta}}{\mathrm{d}z}(z = B_n) = -\frac{\kappa_n \alpha_n \bar{h}_{n-1}}{\tanh(\alpha_n B_n)} + \frac{\kappa_n \alpha_n \bar{h}_n}{\sinh(\alpha_n B_n)} \tag{5.13}$$

The following new variables are introduced:

$$a_n = \frac{\alpha_n B_n}{\tanh(\alpha_n B_n)} \qquad b_n = \frac{\alpha_n B_n}{\sinh(\alpha_n B_n)} \tag{5.14}$$

The flux at the top of leaky layer n (5.13) may now be written as

$$\bar{q}_{t,n} = \frac{-a_n \bar{h}_{n-1} + b_n \bar{h}_n}{c_n} \tag{5.15}$$

where $c_n = B_n/\kappa_n$ is the resistance to vertical flow of leaky layer n. Similarly, the flux at the bottom of leaky layer n is

$$\bar{q}_{b,n} = \frac{-b_n \bar{h}_{n-1} + a_n \bar{h}_n}{c_n} \tag{5.16}$$

For the special case that the top of the leaky layer is impermeable, a similar derivation gives for $\bar{\eta}$ and its derivative:

$$\bar{\eta} = \frac{\cosh[\alpha_n (B_n - z)]}{\cosh(\alpha_n B_n)} \bar{h}_n \tag{5.17}$$

$$\frac{\mathrm{d}\bar{\eta}}{\mathrm{d}z} = -\frac{\alpha_n \sinh[\alpha_n (B_n - z)]}{\cosh(\alpha_n B_n)} \bar{h}_n \tag{5.18}$$

so that the vertical flux at the bottom of the leaky layer is

$$\bar{q}_{b,n} = d_n \frac{\bar{h}_n}{c_n} \tag{5.19}$$

where

$$d_n = \alpha_n B_n \tanh(\alpha_n B_n) \tag{5.20}$$

When aquifer layers n and $n+1$ are not separated by a leaky layer, the vertical flux between aquifer layers is computed with a standard finite difference scheme. The resistance to vertical flow c_n between aquifer layers n and $n-1$ is computed as

$$c_n = \frac{H_n}{2k_{v,n}} + \frac{H_{n+1}}{2k_{v,n+1}} \tag{5.21}$$

where $k_{v,n}$ and H_n are the vertical hydraulic conductivity and thickness of aquifer layer n, respectively. The vertical flux between the aquifer layers is now computed as

$$\bar{q}_{t,n} = \bar{q}_{b,n} = \frac{-\bar{h}_{n-1} + \bar{h}_n}{c_n} \tag{5.22}$$

Comparison with (5.15) and (5.16) shows that for this case, $a_n = b_n = 1$.

5.6 System of Differential Equations

Consider once again the differential equation for aquifer layer n (5.5). Use of (5.15) and (5.16) for the flux through the bottom and top of the aquifer layer, respectively, gives

$$\nabla^2 \bar{\phi}_n = \frac{p}{D_n}\bar{\phi}_n - b_n \frac{\bar{h}_{n-1}}{c_n} + a_n \frac{\bar{h}_n}{c_n} + a_{n+1}\frac{\bar{h}_n}{c_{n+1}} - b_{n+1}\frac{\bar{h}_{n+1}}{c_{n+1}} \tag{5.23}$$

or in terms of the transformed discharge potential

$$\nabla^2 \bar{\phi}_n = -\frac{b_n \bar{\phi}_{n-1}}{c_n T_{n-1}} + \left(\frac{a_n}{c_n T_n} + \frac{a_{n+1}}{c_{n+1} T_n} + \frac{p}{D_n}\right)\bar{\phi}_n - \frac{b_{n+1}\bar{\phi}_{n+1}}{c_{n+1} T_{n+1}} \tag{5.24}$$

This differential equation is valid for any aquifer layer, except for the top layer $(n = 1)$ and the bottom layer $(n = N)$.

The differential equation for aquifer layer 1 is obtained by substituting $n = 1$ into Eq. (5.24). Three options are considered for the top of aquifer layer 1. First, aquifer layer 1 may be bounded on top by an impermeable layer in which case the vertical resistance of leaky layer 1 may be specified as $c_1 = \infty$ and division by ∞ gives zero. Second, aquifer layer 1 may be covered by a leaky layer, which is bounded on top by a fixed water level equal to zero, in which case $\bar{\phi}_0 = 0$. And third, aquifer layer 1 may be covered by a leaky layer, which is bounded on top by an impermeable layer, in which case $\bar{q}_{b,1}$ reduces to (5.19) and the differential equation for aquifer layer 1 becomes

$$\nabla^2 \bar{\phi}_1 = \left(\frac{d}{c_1 T_1} + \frac{a_2}{c_2 T_1} + \frac{p}{D_1}\right)\bar{\phi}_1 - \frac{b_2 \bar{\phi}_2}{c_2 T_2} \tag{5.25}$$

Finally, the bottom aquifer layer is considered to be bounded at the bottom by an impermeable layer (although the other two conditions as applied to the top aquifer layer may be incorporated as well), which means that $c_{N+1} = \infty$ in the differential equation for aquifer layer N.

The system of differential equations (5.24) for $n = 1, \ldots, N$ may be written as a matrix differential equation

$$\nabla^2 \bar{\boldsymbol{\phi}} = \mathbf{A}\bar{\boldsymbol{\phi}} \tag{5.26}$$

where $\bar{\boldsymbol{\phi}}$ is a vector of which component n is $\bar{\phi}_n$. As may be seen from (5.24), matrix $\mathbf{A}$ is a tri-diagonal N by N matrix. For complex Laplace parameters p, $\mathbf{A}$ has N complex eigenvalues w_n $(n = 1,\dots,N)$ and N corresponding complex eigenvectors $\mathbf{v_n}$ $(n = 1,\dots,N)$ and may be factorized as

$$\mathbf{A} = \mathbf{V}\mathbf{W}\mathbf{V}^{-1} \tag{5.27}$$

where column n of $\mathbf{V}$ is formed by eigenvector $\mathbf{v_n}$ and $\mathbf{W}$ is a diagonal matrix with corresponding eigenvalue w_n on the diagonal of row n. Substitution of (5.27) for $\mathbf{A}$ in (5.26) and multiplication of both sides with $\mathbf{V}^{-1}$ gives

$$\nabla^2 \mathbf{f} = \mathbf{W}\mathbf{f} \tag{5.28}$$

where

$$\mathbf{f} = \mathbf{V}^{-1}\bar{\boldsymbol{\phi}}. \tag{5.29}$$

Equation (5.28) represents a system of N uncoupled differential equations, which may be written as

$$\nabla^2 f_n = f_n/\lambda_n^2 \qquad n = 1,\dots,N \tag{5.30}$$

where $\lambda_n^2 = 1/w_n$ is introduced for convenience. This differential equation is referred to as the modified Helmholtz equation. The problem has now been reduced to the solution of N uncoupled modified Helmholtz equations.

Once a solution for all f_n is determined, a solution for $\bar{\boldsymbol{\phi}}$ is obtained as a linear combination

$$\bar{\boldsymbol{\phi}} = \sum_{n=1}^{N} \beta_n f_n \mathbf{v_n} \tag{5.31}$$

where β_n are coefficients that are chosen to meet desired boundary conditions.

5.7 Laplace-Transformed Potential for Multilayer Wells and Line-sinks

Two types of analytic elements are used in this chapter: wells and line-sinks. Equations are discussed here for elements with either a unit impulse discharge or a unit step discharge screened in layer s. The function f_n for a well with discharge $Q(t)$ (positive for taking water out of the aquifer) and radius r_w that fulfills (5.30) is (e.g., Strack 1989)

$$f_n = -\frac{\bar{Q}}{2\pi}\frac{\lambda_n \mathrm{K}_0(r/\lambda_n)}{r_w \mathrm{K}_1(r_w/\lambda_n)} \tag{5.32}$$

The Laplace transform of a unit impulse discharge at $t = 0$ is

$$\bar{Q} = 1 \tag{5.33}$$

while the Laplace transform of a unit step discharge at $t = 0$ is

$$\bar{Q} = \frac{1}{p} \tag{5.34}$$

For a well with an infinitely small radius, (5.32) reduces to

$$f_n = -\frac{\bar{Q}}{2\pi}\mathrm{K}_0(r/\lambda_n) \tag{5.35}$$

The function f_n for a line-sink is obtained through integration of the function for a point sink with infinitely small radius along a line. This integration may be carried out analytically near the line-sink using an infinite series expansion of $\mathrm{K}_0(r/\lambda_n)$ (Gusyev and Haitjema 2011), even when λ_n is complex (Bakker and Kuhlman 2011). Farther away from the line-sink, accurate results are obtained with Gaussian quadrature integration, as the series expansion does not converge on a computer with commonly used finite precision arithmetic (Bakker and Kuhlman 2011).

For both wells and line-sinks, the potential in the Laplace domain may be written as (5.31). The coefficients β_n need to be chosen such that the well or line-sink is screened in the desired layer s by making sure that

$$\mathbf{V}\boldsymbol{\beta} = \mathbf{e_s} \tag{5.36}$$

where $\boldsymbol{\beta}$ is a vector of which component n equals β_n and $\mathbf{e_s}$ is a unit vector with all zeros except for component s, which is equal to 1. To show that this does indeed give the desired result, consider, for example, the behavior of (5.35) for r approaching zero (Digital Library of Mathematical Functions, 2012, Eq. 10.30.3):

$$-\frac{\bar{Q}}{2\pi}\mathrm{K}_0(r/\lambda_n) \sim \frac{\bar{Q}}{2\pi}\ln(r) \qquad \text{for } r \to 0 \tag{5.37}$$

Substitution of (5.37) for f_n in (5.31) and application of (5.36) gives

$$\bar{\boldsymbol{\phi}} \sim \frac{\bar{Q}}{2\pi}\ln(r)\sum_{n=1}^{N}\beta_n\mathbf{v_n} = \frac{\bar{Q}}{2\pi}\ln(r)\mathbf{e_s} \qquad \text{for } r \to 0 \tag{5.38}$$

so that near the well $\bar{\boldsymbol{\phi}}$ indeed behaves as a well in layer s and not in the other layers.

5.8 Analytic Element Solution

In the previous section, equations were presented for the Laplace-transformed potential for a well and line-sink with unit impulse or step discharge screened in one layer. A solution in the Laplace domain is obtained though superposition of these potentials. The discharge of each potential is a free parameter. The free parameter may be specified (e.g., the discharge of a well) or may be computed to meet a certain boundary condition (e.g., the inflow into a stream segment is computed so that the head at the center of a stream segment has a certain value). All free parameters are determined simultaneously as, for example, the inflow of one stream segment influences the head at another stream segment and vice versa. The construction of the system of linear equations that needs to be solved to determine the free parameters of an analytic element model is discussed elsewhere (e.g., Strack 1989). Alternatively, a solution may be obtained iteratively by computing the parameters of one element at a time while keeping the parameters of the other elements fixed and by looping through all elements until the solution converges (Janković and Barnes 1999).

Multilayer wells and line-sinks may be used to model a variety of boundary conditions, including the following five:

1. A well or stream with a head that is fixed through time.
2. A well or stream with a head that varies through time.
3. Wells or stream segments that are screened in a single layer for which the total discharge is known.
4. A well that is screened in an arbitrary number of layers and for which only the net discharge is specified. The discharge of the well in each screened layer needs to be determined such that the head at the well screen is the same in each screened layer. For an abandoned well, the net discharge is zero.
5. A linear fault with a negligible resistance to vertical flow that cuts through multiple aquifer layers. Such a fault may be simulated with a string of line-sinks. Each line-sink is open to multiple layers and has a zero net discharge.

Once an analytic element solution is obtained in the Laplace domain, it is converted back to the physical domain through numerical integration of the Bromwich integral (5.6) using the algorithm of De Hoog et al. (1982). One of the major advantages of using this algorithm is that an accurate solution may be obtained for one base-10 log cycle of time using a single set of M optimal Laplace parameters p, where M is commonly between 30 and 40. This means that M analytic element solutions need to be computed for each log cycle. Once these M solutions are stored, the potential can be evaluated for any time within the log cycle. It is pointed out that this is a major benefit of the De Hoog et al. algorithm. Most other commonly used algorithms, including Stehfest and Schapery, require a solution in the Laplace domain for a different set of p values for each time t, although Schapery only uses 1 real value of p and Stehfest uses on the order of 10–15 real p values.

Stepwise variation of the specified discharge or head of an element through time is simulated using superposition. It is noted that the function f_n for flow to a well (5.35) may be evaluated for any Laplace-transformed discharge $\bar{Q}$. However, back transformation for a step function that starts at an arbitrary time t_0 is difficult for most if not all existing algorithms for inverse Laplace transformations, including the ones mentioned in this chapter.

Superposition through time is fast, however, when the De Hoog et al. algorithm is used. The Laplace-transform solution needs to be computed for a few log cycles after which superposition through time only requires the repeated back transformation of a different linear combination of the Laplace-transform solution.

5.9 Benchmarking

The presented approach has been implemented in the free and open-source computer program TTim, which is written in Python using the packages NumPy and SciPy (Oliphant 2007; Pérez et al. 2011), among others. Some computationally demanding functions are written in FORTRAN and compiled into Python extensions using f2py. The design of TTim is based on the object-oriented design for analytic element models developed by Bakker and Kelson (2009).

Implementation of transient multilayer wells in TTim was benchmarked against results from MLU Lite, the free two-layer version of the commercial MLU code (www.microfem.com/products/mlu.html), which is an implementation of the papers by Hemker referred to earlier. Single layer and multilayer well solutions were also benchmarked against numerical solutions (Louwyck et al. 2011). The line-sink solution has been benchmarked against a row of wells and against a high-resolution numerical solution obtained with MODFLOW (Harbaugh 2005). These benchmarks are presented in the TTim manual (Bakker 2010). Two benchmark problems are presented here. First, TTim is benchmarked against a solution for transient three-dimensional flow in an unconfined aquifer by Neuman (1972), which shows the delayed response of the water table. Second, TTim is benchmarked against an analytic solution for periodic pumping in a multi-aquifer system, which tests the capabilities of TTim for wells with a time-varying discharge in aquifer-aquitard systems.

5.10 Benchmark Against Pumping Well in an Unconfined Aquifer

Consider transient three-dimensional flow to a pumping well in an unconfined aquifer. The well penetrates the aquifer fully, and the inflow is uniform over the thickness of the aquifer. An analytical solution was presented by Neuman (1972), who approximates the aquifer thickness as constant, which is reasonable when the drawdown is small compared to the saturated thickness. Phreatic storage is taken into account through the boundary condition at the top of the aquifer.

Neuman's problem is solved with TTim by also using a constant transmissivity. An unconfined aquifer is divided into ten model layers each with a thickness of 1 m, a hydraulic conductivity of 1 m/d, and elastic storage. A thin eleventh layer of

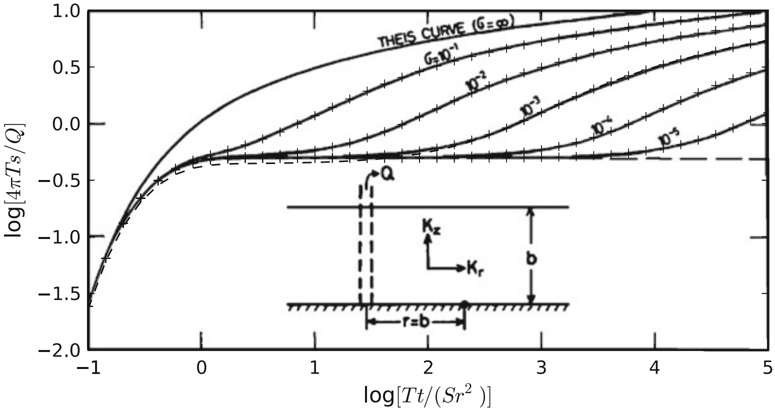

Fig. 5.2 Dimensionless drawdown vs. dimensionless time at one aquifer thickness from a well in an unconfined aquifer. $\sigma = S_{\text{elastic}}/S_{\text{phreatic}}$. *Black lines* are copied from Fig. 2 of Neuman (1972), while the *crosses* are computed with TTim. The *dashed line* is for the case $\sigma = 10^{-3}$ when the well drawdown is uniform rather than the inflow

1 cm thickness is added on top of the aquifer and has phreatic storage $S = 0.1$. Five different values of the elastic storage coefficient are considered (see Fig. 5.2). The ratio of elastic and phreatic storage is called σ.

In the TTim model, one well is screened in layers 2–11. The discharge is specified for each layer to be 1 m^3/d for a total of 10 m^3/d. This facilitates comparison with the solution of Neuman, who specifies a uniform inflow along the well face. A comparison between the TTim solution and the Neuman solution is made for the curves of Fig. 2 in Neuman (1972). This graph (shown in Fig. 5.2) shows dimensionless drawdown vs. dimensionless time, both on a log scale, at the bottom of the aquifer at a distance of one aquifer thickness from the well for an isotropic aquifer. The effect of the delayed response of the water table is clearly visible in Fig. 5.2, but it is noted that this effect is much less pronounced when the curves are plotted on a linear scale rather than a log scale. The curves represent different values of σ. The crosses in Fig. 5.2 represent the drawdown computed with TTim in the bottom layer of the model; they compare well to the Neuman solution. The dashed line is for the case that $\sigma = 10^{-3}$ when the well drawdown is uniform (computed with TTim) and only differs slightly from the uniform inflow case. The difference between uniform head and uniform inflow may be larger for partially penetrating wells, especially near the well.

5.11 Benchmark Against Periodic Pumping in a Multi-aquifer System

Consider periodic pumping in a system of three aquifers separated by two leaky layers (aquitards). All aquifer layers are 10 m thick and all leaky layers are 2 m thick. Aquifer and leaky layer properties are given in Table 5.11; the storage coefficient of the leaky layer is set to zero to facilitate comparison with an exact solution. A well is screened in aquifer 1 and has a discharge that varies periodically on a daily basis as

$$Q = 1{,}000 \cos(2\pi t) \tag{5.39}$$

In TTim, each day is divided into 100 equal intervals with constant discharge. The head variation computed with TTim at a distance of five aquifer thicknesses from the well is shown by the solid line in Fig. 5.3; the largest amplitude represents aquifer 1, while the smallest amplitude represents aquifer 3. The exact solution for this problem is obtained through application of matrix functions, as described by Maas (1986), and is shown with dashed lines in Fig. 5.3. The exact solution is for a well that has been pumping with a periodic discharge forever, while the well in TTim starts pumping at time $t = 0$. Within a day, the effect of the different initial conditions is negated and TTim matches the exact periodic solution closely.

Table 5.1 Aquifer data for periodic pumping benchmark

Layer	T (m^2/d)	S_s (m^{-1})	c (d)
Leaky layer 1	–	0	∞
Aquifer layer 1	200	1e-4	–
Leaky layer 2	–	0	100
Aquifer layer 2	100	1e-4	–
Leaky layer 3	–	0	200
Aquifer layer 3	100	1e-4	–

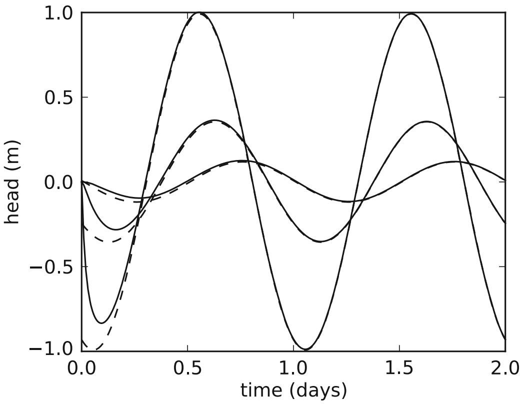

Fig. 5.3 Head vs. time at five aquifer thicknesses from periodic well. TTim solution (*solid*) vs. exact solution (*dash*). TTim well starts at $t = 0$. Largest amplitude is aquifer 1; smallest amplitude is aquifer 3

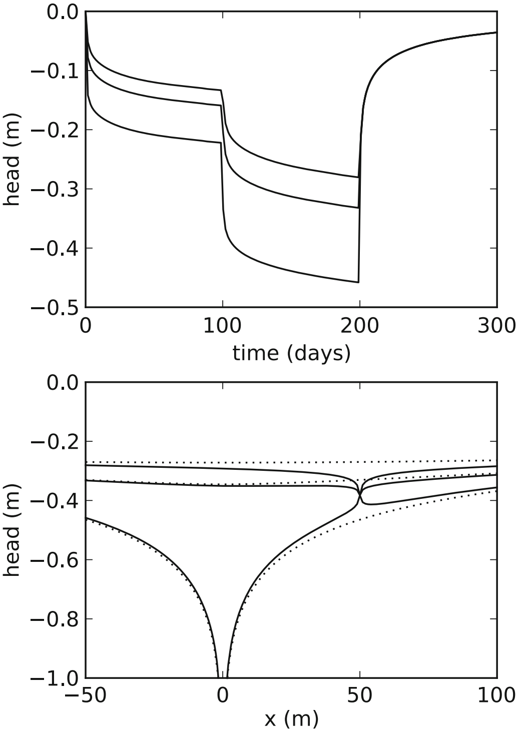

Fig. 5.4 Head vs. time in all three aquifers at $(x,y) = (-50,0)$; drawdown decreases with depth (*upper graph*). Head along $y = 0$ at $t = 200$ days for all three aquifers; drawdown decreases with depth. *Dots* represent same case but with properly sealed abandoned well (*lower graph*)

The same aquifer system is used to demonstrate the effect of an abandoned multi-aquifer well near a pumping well with a variable discharge. The pumping well is located at $(x,y) = (0,0)$ in layer 1. The discharge is 100 m^3/d for 100 days, followed by 100 days with a discharge of 200 m^3/d, after which the pump is turned off. An abandoned multi-aquifer well with a radius of 0.1 m is located at $(x,y) = (50,0)$ and is screened in all three aquifers. The head in the aquifer at $(x,y) = (-50,0)$ is shown as a function of time in the upper graph of Fig. 5.4; the drawdown is smaller in deeper aquifers. In the lower graph of Fig. 5.4, the head is shown along the line $y = 0$ at the end of pumping ($t = 200$ days). The drawdown is again smaller in deeper aquifers. Note that the head is equal in all three aquifers in the abandoned well at $(x,y) = (50,0)$. The dotted line represents the same situation for the case that the abandoned well is properly sealed.

5.12 Drawdown and Stream Depletion for a Well Pumping near a Meandering River

The hypothetical problem of a pumping well near a meandering river is solved to demonstrate some of the capabilities of the method (Fig. 5.5). Consider a stratified

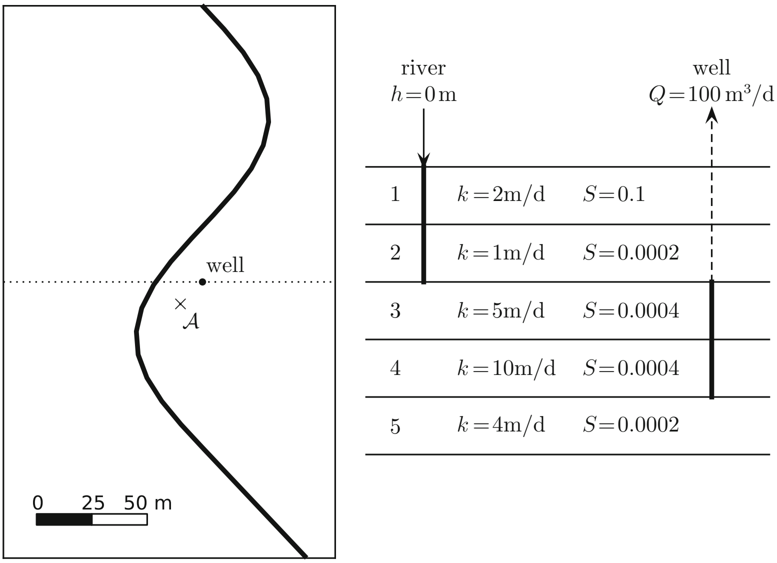

Fig. 5.5 A pumping well and an observation well near a meandering river (*left*). A cross section along the *dotted line* (*right*)

aquifer that consists of 5 layers, each with a thickness of 2 m. The aquifer properties of the five layers are given in Fig. 5.5. The top layer contains the phreatic surface and has phreatic storage. The vertical hydraulic conductivity is 10% of the horizontal one. The river is narrow and penetrates the top 4 m of the aquifer. The water level in the river is constant, and there is no leaky bed, which means that along the river the head in aquifer layers 1 and 2 equals the river level. The well is screened from 4 to 8 m below the top. The well starts pumping with a discharge 100 m^3/d at time $t = 0$. The head is uniform along the well bore and the radius of the well is 0.3 m.

The change of the head in the aquifer caused by the pumping well is simulated. The aquifer is discretized vertically in 5 model layers. The river is modeled with 25 line-sinks that are screened in layers 1 and 2. The modeled part of the river is continued (straight) for another 300 m south and 350 m north of the section shown in Fig. 5.5. The outflow is uniform along each line-sink but varies with time such that the head is zero at the centers of the line-sinks at all times. The well is screened in layers 3 and 4, and the discharge in each layer varies such that the head is the same at the well screen in both layers at all times.

The head change at point $\mathcal{A}$ is shown vs. time for all layers in Fig. 5.6. The horizontal axis represents the time since pumping started and has a log scale. The delayed response of the water table is clearly visible. The head decrease in layers 2–5 seems to plateau after about an hour, but the head decrease continues again after the water table at point $\mathcal{A}$ starts to decrease. It seems that a steady-state situation is approached after 1 year of pumping.

Fig. 5.6 Head vs. time at point $\mathcal{A}$

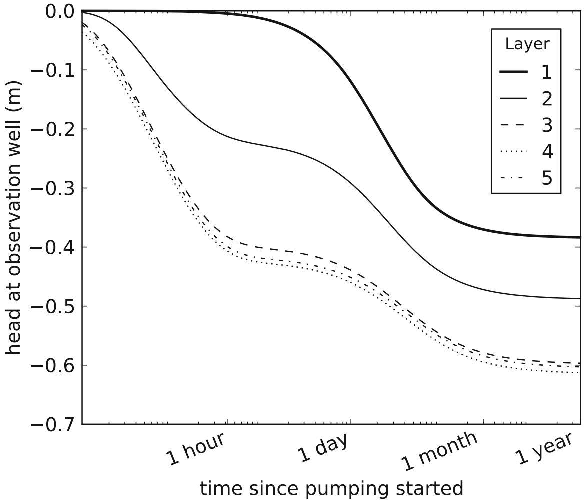

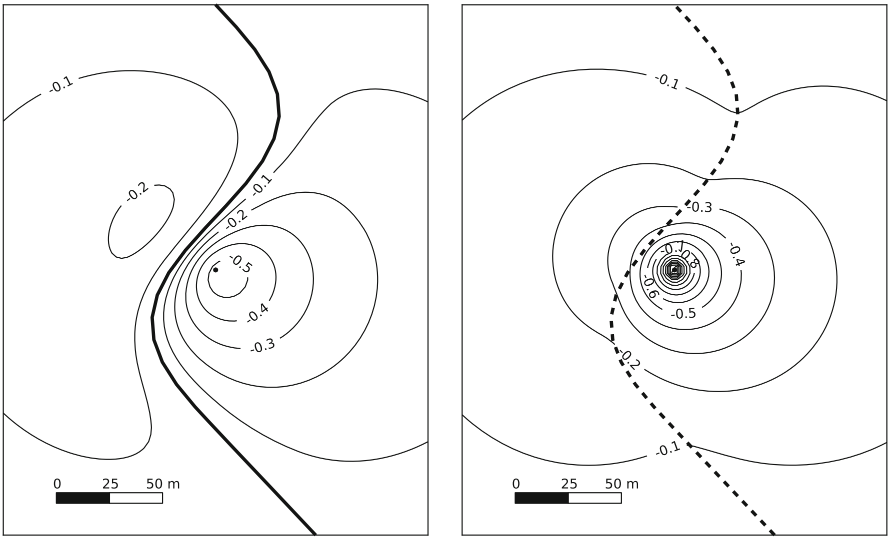

Fig. 5.7 Head contours in layer 1 (*left*) and layer 3 (*right*) after 100 days of pumping

Contour plots of the head in layers 1 and 3 after 100 days of pumping are shown in Fig. 5.7. In the left contour plot of Fig. 5.7, it may be seen that there is drawdown on both sides of the river in layer 1. The maximum drawdown in layer 1 is approximately 55 cm and occurs slightly southeast of the well rather than exactly above the well. The maximum drawdown in layer 1 on the opposite side of the river is slightly more than 20 cm. The drawdown in layer 3 is shown in the right contour plot of Fig. 5.7 and extends well beyond the river, which is screened in layers 1 and 2 only. The drawdown at the well is 2.5 m after 100 days of pumping. Head contours

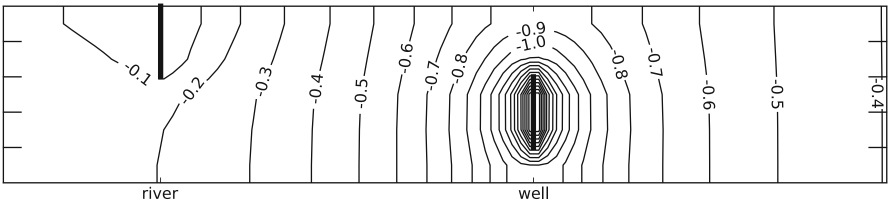

Fig. 5.8 Head contours in cross-section along part of the *dotted line* shown in Fig. 5.5 after 100 days of pumping. *Horizontal and vertical scale* are equal. Layer discretization is shown on *left and right axes*

Fig. 5.9 Stream depletion vs. time

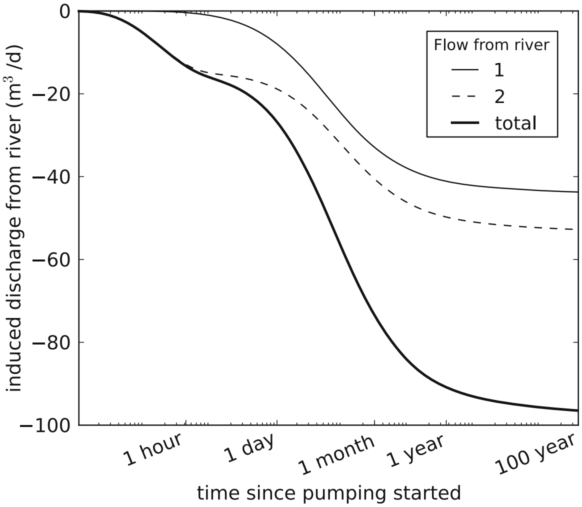

after 100 days of pumping in a cross-sectional view along part of the dotted line in Fig. 5.5 are shown in Fig. 5.8. The lines are created by contouring the heads at the centers of the aquifer layers. The contour lines clearly show the drawdown below the river and around the well screen.

The stream depletion, the induced recharge from the modeled river segment into the aquifer, is shown vs. time in Fig. 5.9. In addition to the total river recharge, the river recharge into layers 1 and 2 is shown separately. It takes approximately 6 days until the recharge from the river segment has reached 50% of the well discharge and 55 days until it has reached 80%. In the absence of any other aquifer features, it is expected that the induced recharge will eventually be equal to the discharge of the well. The induced recharge has only reached 96% of the well discharge after 100 years of pumping. It needs to be realized, however, that only part of the river is simulated in the model (the north–south length is 900 m). At the end of the simulation, the first and last line-sink of the string start to supply water to the aquifer. The remaining 4% of water is supplied by parts of the river or other hydrogeologic features that are not in the model and is supplied in TTim through the release of storage. The omission of these distant features has a minor effect on the solution at later time only.

5.13 Conclusions and Future Direction

An analytic element approach was presented for the modeling of transient flow in multilayer systems. The approach is based on the Laplace-transform analytic element method and may be applied to simulate transient flow in multilayer systems consisting of an arbitrary number of layers while taking storage within both aquifer layers and leaky layers into account. Analytic element solutions are computed in the Laplace domain while the solution in the physical domain is obtained numerically through application of the algorithm by De Hoog et al. (1982). This algorithm may be applied to obtain an accurate solution for one log cycle of time using a single set of ~ 40 complex Laplace parameters, which allows for the efficient computation of analytic element solutions including boundary conditions that vary stepwise through time. Benchmark problems were presented for three-dimensional flow to a fully penetrating well in an unconfined aquifer and for a periodic well in a three-aquifer system. An example was shown for a multilayer well near a partially penetrating meandering stream. The example consists of five aquifer layers with different properties. The delayed response of the water table was simulated and the stream depletion was computed. The presented approach is implemented in the free and open-source computer program TTim (ttim.googlecode.com).

Application of the approach will benefit from development of analytic elements for impermeable or leaky walls, infiltration areas, inhomogeneities, lakes or other surface water features with a leaky bed, and vertical faults with different types of boundary conditions. These elements have all been developed for steady multi-aquifer flow (Bakker 2006, 2007; Anderson and Bakker 2008) and may be modified for transient flow. Application of an integrated flux boundary condition, using the approach of Strack (2009), and applied by Gusyev and Haitjema (2011) may improve performance of some of these new elements.

Extension of the presented approach to nonlinear systems such as ephemeral streams, drains, or aquifer layers that dry up may not be feasible. Some of these problems may be simulated semi-analytically using, for example, the approach of Strack (2006) or Fitts (2010). Strack (2009) presented an approach that allows for analytic element modeling of flow in aquifers with continuously varying properties, which has the potential to rival grid-based methods where a cell-by-cell variation of aquifer properties is trivial.

Analytic element modeling of transient multi-aquifer flow is attractive, as the input files are short and easy, and no grid, time-stepping, or closed model boundaries are needed. Analytic element models are inherently parallel, so that models with large numbers of analytic elements may be run on computer clusters

(Janković et al. 2006). The one-to-one correspondence between analytic elements and hydrogeologic features naturally allow for step-wise modeling to gain insight in the flow system.

Acknowledgements This research was funded by Layne Hydro in Bloomington, IN, and by the US EPA Ecosystems Research Division in Athens, GA, under contract QT-RT-10-000812 to SS Papadopulos and Associates in Bethesda, MD.

References

Anderson EI, Bakker M (2008) Groundwater flow through anisotropic fault zones in multiaquifer systems. Water Resour Res 44(11):1–11

Bakker M (2006) An analytic element approach for modeling polygonal inhomogeneities in multi-aquifer systems. Adv Water Resour 29(10):1546–1555

Bakker M (2007) Simulating groundwater flow to surface water features with leaky beds using analytic elements. Adv Water Resour 30(3):399–407

Bakker M (2010) TTim, a multi-aquifer transient analytic element model version 0.01. Delft University of Technology, 2010. ttim.googlecode.com.

Bakker M, Kelson VA (2009) Writing analytic element programs in python. Ground Water 47(6):828–834

Bakker M, Kuhlman KL (2011) Computational issues and applications of line-elements to model subsurface flow governed by the modified Helmholtz equation. Adv Water Resour 34: 1186–1194

Bakker M, Strack ODL (2003) Analytic elements for multiaquifer flow. J Hydrol 271(1–4): 119–129

Cihan A, Zhou Q, Birkholzer JT (2011) Analytical solutions for pressure perturbation and fluid leakage through aquitards and wells in multilayered-aquifer systems. Water Resour Res 47(10):1–17

De Hoog FR, Knight JH, Stokes AN (1982) An improved method for numerical inversion of Laplace transforms. SIAM J Sci Stat Comput 3(3):357–366

Digital Library of Mathematical Functions (2012) National institute of standards and technology, 2012. http://dlmf.nist.gov/.

Fitts CR (2010) Modeling aquifer systems with analytic elements and subdomains. Water Resour Res 46, W07521, doi:10.1029/2009WR008331

Furman A, Neuman SP (2003) Laplace-transform analytic element solution of transient flow in porous media. Adv Water Resour 26(12):1229–1237

Gusyev MA, Haitjema HM (2011) An exact solution for a constant-strength line-sink satisfying the modified helmholtz equation for groundwater flow. Adv Water Resour 34(4):519–525

Haitjema HM (1995) Analytic element modeling of groundwater flow. Academic Press, San Diego, CA

Harbaugh AW (2005) Modflow-2005, the us geological survey modular ground-water model – the ground-water flow process. Techniques and methods, vol 6-A16, USGS, 1995

Hemker CJ (1999a) Transient well flow in layered aquifer systems: the uniform well-face drawdown solution. J Hydrol 225(1–2):19–44

Hemker CJ (1999b) Transient well flow in vertically heterogeneous aquifers. J Hydrol 225 (1–2):1–18

Hemker CJ, Maas C (1987) Unsteady flow to wells in layered and fissured aquifer systems. J Hydrol 90(3–4):231–249

Janković I, Barnes R (1999) Three-dimensional flow through large numbers of spheroidal inhomogeneities. J Hydrol 226(3–4):224–233

Janković I, Fiori A, Dagan G (2006) Modeling flow and transport in highly heterogeneous three-dimensional aquifers: Ergodicity, gaussianity, and anomalous behavior—1. Conceptual issues and numerical simulations. Water Resour Res 42(6):1–9

Kuhlman KL, Neuman SP (2009) Laplace-transform analytic-element method for transient porous-media flow. J Eng Math 64(2):113–130

Louwyck A, Vandenbohede A, Bakker M, Lebbe L (2011) Simulation of axi-symmetric flow towards wells: A finite-difference approach. Comput Geosci 44:136–145

Maas C (1986) The use of matrix differential calculus in problems of multiple-aquifer flow. J Hydrol 88:43–67

Neuman SP (1972) Theory of flow in unconfined aquifers considering delayed response of the water table. Water Resour Res 8(4):1031–1045

Nordbotten J, Celia MA, Bachu S (2004) Analytical solutions for leakage rates through abandoned wells. Water Resour Res 40(4):1–10

Oliphant TE (2007) Python for scientific computing. Comput Sci Eng 9(3):10–20

Pérez F, Granger BE, Hunter JD (2011) Python: an ecosystem for scientific computing. Comput Sci Eng 13(2):13–21

Schapery RA (1962) Approximate methods of transform inversion for viscoelastic stress analysis. Proc 4th U.S. Natl Congr Appl Mech 2:1075–1085

Sneddon IN (1972) The use of integral transforms. McGraw-Hill, New York

Stehfest H (1970) Algorithm 368, numerical inversion of Laplace transforms. Comm ACM 13(1):47–49

Strack ODL (1984) Three-dimensional streamlines in dupuit-forchheimer models. Water Resour Res 20(7):812–822

Strack ODL (1989) Groundwater mechanics. Prentice Hall, Englewood Cliffs, NJ

Strack ODL (2003) Theory and applications of the analytic element method. Rev Geophys 41(2): 1–16

Strack ODL (2006) The development of new analytic elements for transient flow and multiaquifer flow. Ground Water 44(1):91–98

Strack ODL (2009) The generating analytic element approach with application to the modified Helmholtz equation. J Eng Math 64(2):163–191

Veling EJM, Maas C (2009) Strategy for solving semi-analytically three-dimensional transient flow in a coupled n-layer aquifer system. J Eng Math 64(2):145–161

Chapter 6
Tortuosity and Archie's Law

Yuan Liu and Peter K. Kitanidis

Abstract Despite the popularity of Archie's Law, parameterizing bulk electrical conductivity as a power-law function of porosity seems to lack support from first principles. In this chapter, we renew the discussion on improving the way to upscale electrical current in porous media. We notice that in a solute diffusion problem (without advection), which is mathematically equivalent to the electrical current problem at the pore scale, bulk diffusivity is upscaled to be a linear function of porosity. The paradox of this upscaling problem results from the difficulty in quantifying the effects of the twisted and windings paths of transport in porous media, and from the ambiguous correlation between tortuosity and porosity. We argue that tortuosity is not well defined at the microscale; it is a macroscopic property. We show that the intuitive definition of tortuosity from an effective length is not a fruitful approach in terms of rigorous quantitative analysis, even for simple tubes with non-uniform cross-sectional area. Moreover, even though empirical relationships between tortuosity and porosity widely exist in the literature, our numerical study of electrical current in 3-D porous media demonstrates that tortuosity does not have to exhibit intrinsic correlation with porosity. Furthermore, we show that as a macroscopic parameter to capture the overall impediment that soil grains have on solute diffusion or electric current, the tortuosity is a tensorial property (i.e., directionally dependent), and cannot be predicted from porosity.

6.1 Introduction

The electrical resistivity log is widely used to estimate the characteristics of porous media (Archie 1942; Dalla et al. 2004). The most extensively applied relationship to interpret electrical resistivity in terms of porosity or moisture content is Archie's

---

Y. Liu (✉) • P.K. Kitanidis
Department of Civil and Environmental Engineering, Stanford University,
Stanford, CA 94305, USA
e-mail: liuyuan@stanford.edu; peterk@stanford.edu

P.K. Mishra and K.L. Kuhlman (eds.), *Advances in Hydrogeology*,
DOI 10.1007/978-1-4614-6479-2_6,

© Springer Science+Business Media New York 2013

Law (Archie 1942). For a fully saturated porous block, Archie's Law can be written as

$$R_b = R_w \theta^{-m}, \tag{6.1}$$

where R_b is the electrical resistivity of the block (Ω·m), R_w is the resistivity of the aqueous phase (Ω·m), θ is the porosity (−), and m is known as the cementation exponent (−). Here, Archie introduced the formation resistivity factor (−) as

$$F = \frac{R_b}{R_w} = \theta^{-m}. \tag{6.2}$$

The cementation exponent m is obtained as the slope of the $F - \theta$ plot in a log-log plot. Typical values of m range from 1.3 to 2.0 (Archie 1942; Haro 2006). A significant future of transport in a porous medium, other than in a free open space, is that a particle should follow a longer and twisted path rather than a straight line, because of the obstruction caused by soil grains. To accommodate for this tortuous property of a porous medium, Archie's Law was later generalized to include tortuosity as (e.g., Bussian 1982)

$$F = \frac{R_b}{R_w} = \frac{a}{\theta^m}, \tag{6.3}$$

where a is the tortuosity (−). Although widely applied, Archie's Law is generally treated as an empirical law. Many studies have tried to explore the physical basis of the above relationship and the physical meaning of a and m (Schwartz 1987; Ehrlich et al. 1991; Herrick 1994; Shang et al. 2003; Haro 2006). However, beyond the recognition that a represents the elongation of flow paths and m is affected by porous medium cementation, there is no general agreement on how to quantify these two parameters other than fitting the $F - \theta$ plot of data. On the other hand, solute diffusion studies (solute transport in porous media without advection, which we call pure diffusion in this chapter) are mathematically equivalent to the electrical current problem at the pore scale, generally describe macroscopic diffusion coefficient without applying a cementation exponent. It appears paradoxical that the macroscopic diffusion coefficient or electrical conductivity can be parameterized as either a linear function or a power-law function of the porosity. The key point to this problem is tortuosity. Despite its wide application in flow and transport problems in porous media, tortuosity is not a well-defined concept at the microscale. Even if the geometry of a porous medium is described in full detail, the tortuosity cannot be calculated directly from the geometrical information without fully accounting for the equations of transport. Therefore, understanding the physics and complexity of tortuosity is a significant step to solve the parameterization paradox.

This study renews the discussion on the parameterization of macroscopic electrical conductivity and the definition of tortuosity. From the literature, we recognize that the paradox of parameterizing Archie's Law is due to the difficulty in quantifying the tortuosity and an ambiguous correlation between the tortuosity and porosity. Even though the tortuous effect of porous media is easily observed and tortuosity is widely applied to account for the obstruction caused by soil grains, the essence of what tortuosity is and how it behaves is not well understood. In this chapter, we discuss how to better define tortuosity and the limitation of its intuitive definition from the concept of an effective path length. Based on numerical simulation of electrical current in three-dimensional porous media, we investigate the properties of tortuosity in different pore structures and carefully examine whether tortuosity is correlated to porosity or not. The results improve the understanding of the complexity of tortuosity in both isotropic and anisotropic porous media.

6.2 Governing Equations of Pure Diffusion and Electrical Current Problems

Despite different parameterizations at the macroscale, pure diffusion (i.e., molecular diffusion in the absence of advection) and electrical current in porous media are described by the same mathematical expressions at the microscale. When soil grains are not conductive, steady-state electrical current follows the governing equation, derived from Ohm's Law:

$$\nabla \cdot (\sigma_w \nabla V) = 0, \tag{6.4}$$

where V is the electrical potential (V) and σ_w is the electrical conductivity of the aqueous phase (S/m), $\sigma_w = 1/R_w$.

For a pure diffusion problem under steady conditions, the governing equation for solute concentration derived from Fick's Law is

$$\nabla \cdot (D_w \nabla c) = 0, \tag{6.5}$$

where c is solute concentration of the aqueous phase (mol/m^3) and D_w is the molecular diffusion coefficient (m^2/s). In a solute diffusion problem, there is typically no flux through soil grains; this is not an essential assumption in the electrical current problem. However, to keep them equivalent, we focus on the electrical current through a porous medium with nonconductive soil grains.

The electrical potential V in (6.4) is analogous to the concentration c in the diffusion problem, and the electrical conductivity σ_w is analogous to the molecular diffusion coefficient D_w. Archie's Law incorporates both the tortuosity and cementation exponent, but the macroscopic diffusion coefficient is generally expressed as (Delgado 2005)

$$D_b = \frac{\theta}{\tau} D_w, \tag{6.6}$$

where D_b is the macroscopic diffusion coefficient of the block (m^2/s) and τ is the tortuosity ($-$) when D_b is linearly dependent on θ. Instead of fitting two parameters in Archie's Law, (6.6) considers the reduction of available space through the porosity θ, which can be directly measured for a porous medium, and uses τ as the only additional parameter to account for all the other effects that cannot be directly determined from the geometry. Compared to the difficulty of quantifying a and m, making the tortuosity τ the only fitting parameter is physically straightforward, and also not necessarily less accurate than Archie's Law.

In practical applications, both (6.3) and (6.6) can be used to interpret field and experimental data. However, because the tortuosity and cementation exponent cannot be independently determined without using measured D_b or σ_b, these two parameters cannot avoid being empirical fitting parameters. A possible solution is to define tortuosity at the microscale, so pore-scale models can be used to investigate whether the macroscopic electrical conductivity is a linear function or a power-law function of porosity. In the next section, we will revisit the definition of tortuosity at the microscale and try to make it more than a macroscopic fitting parameter.

6.3 Quantification of Tortuosity

The quantification of tortuous effects in porous media has not yet been satisfactorily resolved. Intuitively, the tortuosity is defined as the ratio of the effective length of the tortuous paths, which particles follow at the pore scale, to the straight-line distance of the ends (e.g., Bear 1972),

$$\tau = L_e/L, \tag{6.7}$$

where L_e is the effective length of the flow path (m) and L is the straight-line distance between the two ends (m). Sometimes, tortuosity is also defined as (Bear 1972)

$$\tau = (L_e/L)^2. \tag{6.8}$$

However, the concept of effective length is not clearly defined. Yu and Li (2004) and Yun et al. (2005) calculated L_e as the average length of different types of streamlines in particular pore-scale geometries. In reality, the geometry of a porous medium is more complicated, and the real tortuosity is not necessarily close to the one calculated from a simple geometry. In addition, although Yu and Li (2004) and Yun et al. (2005) took an arithmetic mean of different streamlines, Koponen et al. (1996) also proposed a weighted average by fluid velocity.

We will focus on a simple case where the pore space can be treated as a set of parallel streamtubes. We explore the meaning of effective length and its connection to tortuosity. We study electrical current in porous media with nonconductive soil grains; the pure diffusion problem is mathematically equivalent. In the ith streamtube, the electrical current is driven by a potential energy loss:

$$f_i = \frac{\sigma_i A_i}{L_{ei}} \Delta V, \tag{6.9}$$

where f_i is the electrical current (A) through the ith streamtube, σ_i is the electrical conductivity (S/m) of the aqueous phase, A_i is the cross-sectional area (m^2), ΔV is the drop in electrical potential (V), and L_{ei} is the curve length of the ith streamtube (m). Since each streamtube contains the same fluid, σ_i's are equal to the electrical conductivity of the aqueous phase, σ_w. At the macroscale, a bulk electrical conductivity is found so that the total electrical current is

$$f = \sum_i f_i = \frac{\sigma_b A}{L} \Delta V, \tag{6.10}$$

where A is the cross-sectional area of the block (m^2) and σ_b is the electrical conductivity of the block (S/m). To simplify (6.9), the pore space is subdivided into streamtubes with equivalent cross-sectional area, i.e., $A_i = \frac{A_e}{n}$, where A_e is the effective cross-sectional area and n is the total number of the streamtubes. Substituting (6.9) into (6.10), we obtain the bulk electrical conductivity

$$\frac{\sigma_b}{\sigma_w} = \frac{A_e}{A}\frac{L}{n}\sum_i \frac{1}{L_{ei}}. \tag{6.11}$$

If the effective cross-sectional area can be simply recognized as the void area (i.e., $A_e = A\theta$), (6.11) becomes

$$\frac{\sigma_b}{\sigma_w} = \frac{\theta}{\tau}, \tag{6.12}$$

which is the same form as (6.6). The tortuosity τ is intuitively defined as (6.7), with the effective path length calculated as a harmonic mean:

$$L_e = \frac{n}{\sum_i \frac{1}{L_{ei}}}. \tag{6.13}$$

Nevertheless, when the effective cross-sectional area A_e is smaller than $A\theta$ due to the existence of pore throats and dead-end pores, (6.13) is no longer applicable. We assume that

$$A_e = \eta A \theta, \tag{6.14}$$

where η is smaller than 1 and represents the ratio of the effective cross-sectional area to the total void area ($-$). Therefore, (6.12) is valid only when the tortuosity is adjusted with η as

$$\tau = \frac{\eta}{\frac{L}{n}\sum_i \frac{1}{L_{ei}}}. \tag{6.15}$$

In this chapter, we study η in tubes with variable width, as shown in Fig. 6.1. The straight-line distance between the ends is 2.1×10^{-3} m. The size of a pore throat can

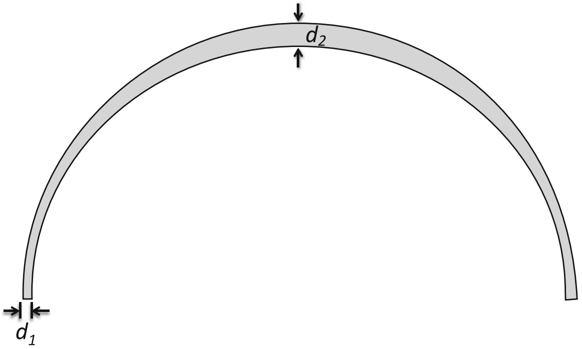

Fig. 6.1 Tube with variable width (d_1 is the smallest width, and d_2 is the largest width of the tube)

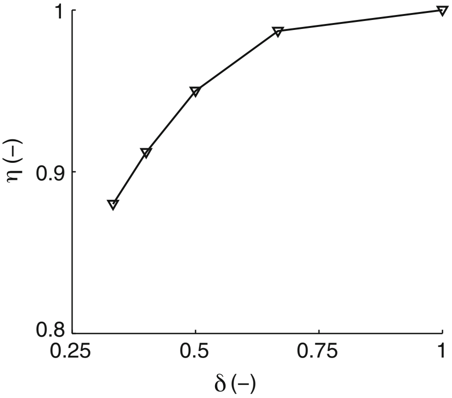

Fig. 6.2 The effect of pore throat characteristic δ on effective cross-sectional area ($\delta = d_1/d_2$, see Fig. 6.1; η is the ratio of the effective cross-sectional area to the total void area, defined in (6.16))

be quantified as the ratio of the smallest width d_1 and the largest width d_2, $\delta = d_1/d_2$ (−), where $d_1 = 1 \times 10^{-4}$ m. With a constant electrical potential difference between the inlet and outlet boundaries, the electrical density field is solved via COMSOL Multiphysics 4.2a (a commercial finite element code). The streamlines of electrical current can be obtained to calculate the effective length L_e via (6.13), which then allows the calculation of η from the electrical current as

$$\eta = \frac{f L_e}{\Delta V \sigma_w} \cdot \frac{1}{\bar{d}}, \tag{6.16}$$

where $\bar{d}$ is the average width of the tube (m) and is calculated as $\bar{d} = \frac{\int_0^{L_e} d \, \mathrm{d}l}{L_e}$. Fig. 6.2 demonstrates the change of η under the pore throat effect. When the width of the tube is uniform ($\delta = 1$), the effective cross-sectional width of the tube is equal to $\bar{d}$ (i.e., $\eta = 1$), and the intuitive definition of the tortuosity is valid with the effective length defined as the harmonic mean. However, when the width of the tube is nonuniform, the tortuosity with the intuitive definition can no longer capture the macroscopic sinuous effect. In this case, the adjusted definition as (6.15) is applied. When the effect of pore throats becomes significant, η declines nonlinearly as δ

decreases. In the previous work of Adisoemarta et al. (2000), where the tortuosity is not adjusted to account for the effect of pore throats, a cementation exponent ($m > 1$) appears to introduce an effective cross-sectional area $A_e = A\theta^m < A\theta$ ($\theta < 1$). However, there is no physical basis to support the power-law dependence on porosity.

Above all, the intuitive definition of tortuosity as the ratio of the effective length to the straight-line distance comes from the analysis in tubes with uniform width. However, additional adjustment is necessary for more complex geometries. Practically, it is impossible to calculate η or the tortuosity directly from the geometry of a porous medium, even for a structure as simple as a width-varying tube. In real porous media, streamlines are twisted with complex paths, and the total cross-sectional area can vary dramatically. Under this complexity, neither the effective length nor the effective cross-sectional area can be determined from the geometry. Moreover, some parameters, although traditionally considered as intrinsic properties, are dependent on particular transport processes. Neuman (2005) concluded that advective porosity, which relates advective velocity to Darcy flux, is directionally dependent and smaller than the interconnected porosity as a result of incomplete mixing. Similarly, tortuosity is not only a function of geometry, because particle paths depend on a particular transport problem (Pisani 2011; Valdes-Parada et al. 2010). Overall, defining tortuosity at the microscale is difficult and vague. It is better to treat the tortuosity as a macroscopic correction coefficient, which not only accounts for the elongation of paths but also the effects of cementation and geometrical complexity in porous media. Macroscopically, it can be calculated from the bulk electrical conductivity as

$$\tau = \frac{\theta}{\sigma_b/\sigma_w}. \tag{6.17}$$

6.4 The Correlation Between Tortuosity and Porosity

In this section, we further explore the properties of the tortuosity as a macroscopic parameter, especially its correlation with porosity. Since porosity is a well-defined concept and can be measured, in practical applications tortuosity is often calculated from empirical relationships with porosity. For example, the appearance of a power-law relationship between the electrical conductivity and porosity in Archie's Law (6.1) can also be explained as

$$\tau = \theta^{1-m}. \tag{6.18}$$

Boudreau (1996) investigated tortuosity and porosity data from several sources, developing the empirical relationship,

$$\tau = 1 - \ln(\theta^2). \tag{6.19}$$

Based on lattice-gas simulations, Koponen et al. (1996) obtained

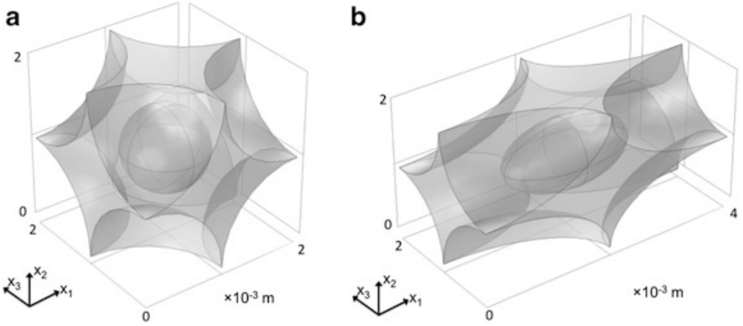

Fig. 6.3 Geometric profile of 3-D unit cells: (**a**) isotropic (spherical grains); (**b**) anisotropic (elliptical grains)

$$\tau = 0.8(1-\theta)+1. \tag{6.20}$$

Similar relationships describing tortuosity as a linear function, power-law function, or logarithmic function of porosity exist in the literature. A summary of these relationships can be found in Boudreau (1996).

In this work, based on pore-scale simulation, we further study the correlation between tortuosity and porosity in three-dimensional cells with spherical (isotropic) and elliptical (anisotropic) grains. The size of the isotropic unit cell with spherical grains (Fig. 6.3a) is $(2\times10^{-3})^3$ m^3, and the radius of corner grains is 10^{-3} m. The porosity is changed by varying the size of the middle grain. When there is no grain in the middle, the unit cell has cubic packing, with a porosity of 47.7%; When the radius of the middle grain is 7.32×10^{-4} m, the unit cell has rhombohedral packing, with a porosity of 27.3%. The anisotropic porous medium (Fig. 6.3b) is composed of elliptical grains, whose major radius is in the x_1 direction. The anisotropy ratio of the porous medium (λ) is defined as the ratio of the major and minor radii of the elliptical grains.

The electrical field is numerically solved using COMSOL. We impose a constant electrical potential ΔV at the boundaries to obtain the macroscopic electrical current f and the bulk electrical conductivity σ_b. As discussed in Sect. 6.3, the tortuosity is treated as the only correction coefficient to account for the obstacles of grains and is calculated from σ_b via (6.17).

As shown on Fig. 6.4, in the isotropic porous medium, the tortuosity monotonically declines as the porosity increases. Herrick (1994) explained that a smaller porosity is generally associated with more tortuous pores. In this porous medium, as the size of the middle grain increases, the overall obstruction on electrical current also increases, which results in a larger tortuosity. The tortuosity data in Fig. 6.4 can be fitted with a power-law function of porosity as described in Archie's Law

$$\tau = \theta^{1-m}+0.15, \tag{6.21}$$

where m in this case is estimated as 1.28.

Fig. 6.4 The dependency of tortuosity on porosity in the isotropic porous medium (spherical grains)

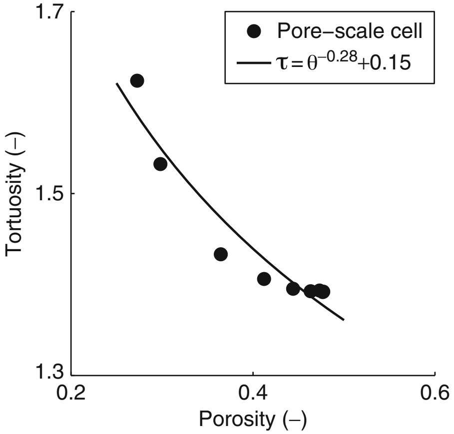

Fig. 6.5 The tortuosity of the anisotropic porous medium ($\lambda = 2$)

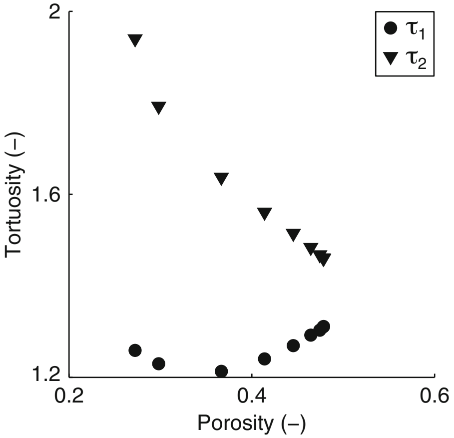

However, the above correlation between the porosity and tortuosity is not valid universally. In the anisotropic porous media with elliptical grains ($\lambda = 2$), Fig. 6.5 demonstrates that the tortuosity not only changes with the porosity but also with the direction. Because the obstruction in the x_2 direction is larger than that in the x_1 direction, the tortuosity in the x_2 direction (τ_2) is larger than that in the x_1 direction (τ_1). Moreover, the tortuosities in the two directions behave differently as the porosity changes. Similar to the tortuosity in the isotropic porous medium, the tortuosity in the x_2 direction decreases monotonically as the porosity increases. On the other hand, the tortuosity in the x_1 direction decreases at low porosity but increases at high porosity. For this particular porous medium, the minimum value of the tortuosity is reached at $\theta = 0.37$, which we call the critical porosity, θ^{cr}. This increasing tortuosity with the porosity is contradictory to the intuitive definition of tortuosity, because the effective path is expected to be shorter when the size of the middle grain decreases and the porosity increases, which would result in a smaller

Fig. 6.6 The change of dimensionless bulk electrical conductivity and porosity

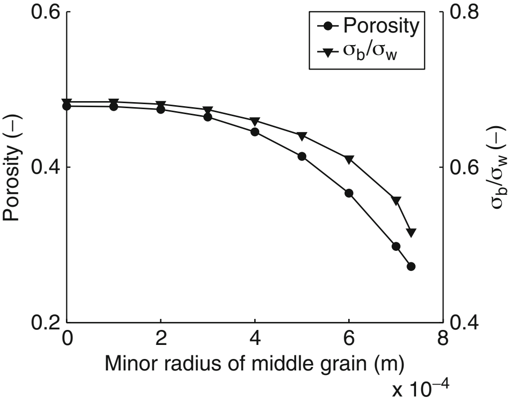

Fig. 6.7 The effect of anisotropy ratio on tortuosity in the x_1 direction

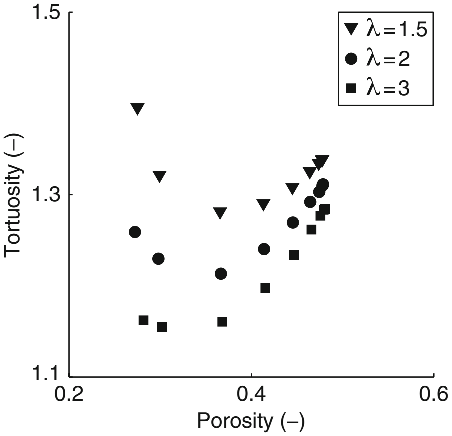

tortuosity according to the intuitive definition. However, as a macroscopic parameter defined in (6.17), the variation of τ is not necessarily related to the effective path length, but instead is determined by the relative change of dimensionless bulk electrical conductivity (σ_b/σ_w) with respect to the porosity. In Fig. 6.6, as the size of the middle grain decreases, the porosity increases faster than the dimensionless bulk electrical conductivity at $\theta > \theta^{\mathrm{cr}}$. Because the obstacle to the electrical current is less significant in the x_1 direction, the middle grain has a larger effect on the void volume than on the macroscopic electrical conductivity at $\theta > \theta^{\mathrm{cr}}$, which results in an increasing tortuosity as the porosity increases. Even though the small grain in the middle of the unit cell reduces the total electrical current, the average electrical current per unit volume increases, increasing the efficiency.

We also investigate τ_1 in porous media with different anisotropy ratios. Fig. 6.7 indicates that a smaller tortuosity is observed for a porous medium with stronger anisotropy, because the obstacle to electrical current in the x_1 direction decreases as λ increases. In addition, an increasing tortuosity with increasing porosity becomes more notable as the anisotropy ratio of a porous medium increases. The critical porosity, θ^{cr}, at which the tortuosity in the x_1 direction reaches its minimum, depends on the anisotropy ratio and the pore-scale geometry.

These results suggest that tortuosity is a complex property that cannot be simply determined from porosity. As the geometric profile changes, the tortuosity has different correlations with respect to the porosity and varies for different directions in anisotropic porous media. In practical applications, it is better to calculate these two parameters separately.

6.5 Conclusions

Although Archie's Law is widely applied to analyze the data of electrical resistivity in porous media, it is an empirical law because there is no solid physical foundation for a power-law relationship between the bulk electrical conductivity and porosity. On the other hand, the macroscopic diffusion coefficient, which is mathematically analogous to the electrical conductivity, is generally upscaled as a linear function of porosity. A paradox of different parameterizations results from the difficulty in quantifying tortuosity. Even though the intuitive definition of the tortuosity (6.7) is widely accepted, we demonstrate that this intuitive definition is based on an oversimplified geometrical structure and is not applicable when the pore structure becomes realistically complex. Overall, tortuosity is a macroscopic property that cannot be well defined at the microscale. It means that we cannot calculate the tortuosity directly from the geometry of a porous medium. In reality, it is better to treat the tortuosity as a correction coefficient that captures all the effects that cause the reduction of diffusivity or electrical conductivity in porous media compared to a free open space.

Based on three-dimensional simulations of an electrical field at the pore scale, this study further explores the properties of tortuosity in both isotropic and anisotropic porous media. Although empirical relationships between the tortuosity and porosity are developed in previous studies, we show that these two properties are intrinsically independent. In an isotropic porous medium, the tortuosity demonstrates an apparent power-law correlation with the porosity, similar to Archie's Law. However, in an anisotropic porous medium, the tortuosity is also directionally dependent. In the direction with less impediments to electrical current, the tortuosity does not decrease monotonically as the porosity increases; here, a power-law relationship clearly does not exist. For a certain porosity, tortuosity can be different values, depending on the geometrical profile of the porous medium.

Above all, because of the complex dependency of tortuosity on geometry, direction, and transport processes, developing an easy and accurate approach for tortuosity estimation is still a challenging problem in practical applications. Topics that need future studies include the following: what are the properties of tortuosity in randomly packed porous media, how is tortuosity affected by heterogeneity at different scales, how tortuosity and porosity may be affected by geological processes, and how tortuosity changes for different transport processes in the same system.

Acknowledgements This material is based upon work supported by the National Science Foundation under Grant No. 0738772. Additional funding was provided by a Stanford Graduate Fellowship. The authors would like to thank the editors for their helpful comments. Suggestions from David Hochstetler and Massimo Rolle on preparing the manuscript are gratefully acknowledged.

References

Adisoemarta PS, Anderson GA, Frailey SM, Asquith GB (2000) Historical use of m and a in well log interpretation: is conventional wisdom backwards? SPE Permian Basin Oil and Gas Recovery Conference, 21–23 March 2000, Midland, Texas, SPE 59699, doi:10.2118/59699-MS

Archie GE (1942) The electrical resistivity as an aid in core analysis interpretation. Trans Am Inst Mining Eng 146:54–62

Bear J (1972) Dynamics of fluids in porous media. Dover Publications, New York

Boudreau BP (1996) The diffusive tortuosity of fine-grained unlithified sediments. Geochimica et Cosmochimica Acta 60(16):3139–3142

Bussian AE (1982) A generalized archie equation. SPWLA Twenty-Third Annu Logging Symp 7:1–8

Dalla E, Cassiani G, Brovelli A, Pitea D (2004) Electrical conductivity of unsaturated porous media: Pore-scale model and comparison with laboratory data. Geophys Res Lett 31:L05609

Delgado JMPQ (2005) A critical review of dispersion in packed beds. Heat Mass Tran 42(4): 279–310

Ehrlich R, Etris EL, Brumfield D, Yuan LP, Crabtree SJ (1991) Petrography and reservoir physics III: physical models for permeability and formation factor. AAPG Bull 75(10):1579–1592

Haro C (2006) Permeability modeling in porous media: setting Archie and Carman–Kozeny right. SPE Europec/EAGE Annual Conference and Exhibition, 12–15 June 2006, Vienna, Austria, SPE 100200, doi:10.2118/100200-MS

Herrick DC (1994) Electrical efficiency — A pore geometric theory for interpreting the electrical properties of reservoir rocks. Geophysics 59:918–927

Koponen A, Kataja M, Timonen J (1996) Tortuous flow in porous media. Phys Rev E 54(1): 406–410

Neuman SP (2005) On the tensorial nature of advective porosity. Adv Water Resour 28(2):149–159

Pisani L (2011) Simple expression for the tortuosity of porous media. Transport Porous Media 88(2):193–203

Schwartz LM (1987) Analysis of electrical conduction in the grain consolidation model. Geophysics 52:1402–1411

Shang B, Hamman J, Caldwell D (2003) A physical model to explain the first Archie relationship and beyond. SPE Annual Technical Conference and Exhibition, 5–8 October 2003, Denver, Colorado: SPE 84300, doi:10.2118/84300-MS

Valdes-Parada FJ, Porter ML, Wood BD (2010) The role of tortuosity in upscaling. Transport Porous Media 88(1):1–30

Yu B-M, Li J-H (2004) A geometry model for tortuosity of flow path in porous media. Chin Phys Lett 21(8):1569–1571

Yun M-J, Yu B-M, Zhang B, Huang M-T (2005) A geometry model for tortuosity of streamtubes in porous media with spherical particles. Chin Phys Lett 22(6):1464–1467

Chapter 7
Measurement of Streaming Potentials Generated During Laboratory Simulations of Unconfined Aquifer Pumping Tests

Bwalya Malama

Abstract The streaming potential method has emerged as a promising hydrogeophysical technique for indirect acquisition of spatially dense measurements of the hydraulic response of aquifers to pumping or other system forcings. The method relies on measurements of electric potentials generated by groundwater flow. They arise due to the existence of the electric double layer at the rock–water interface. Mathematical solutions describing the transient electric potentials associated with pumping tests conducted in confined and unconfined aquifers have been recently developed and demonstrated to yield reasonable estimates of hydraulic parameters when applied to tests conducted at the field-scale. We present results of laboratory experiments conducted to investigate the applicability of the unconfined aquifer model under controlled conditions in a sand tank instrumented with pressure transducers for direct measurement of the hydraulic system state, and nonpolarizable electrodes for measurement of the associated electric field. Measurements show unambiguous transient streaming potential responses to groundwater flow in a bounded cylindrical system. Parameters estimated from streaming potential data are compared to those from drawdown data.

7.1 Introduction

The subsurface through which groundwater flows and contaminants are transported is inherently heterogeneous, making the problem of quantitatively describing this flow and transport challenging. This problem of describing flow and transport, when the physical properties of the heterogeneous subsurface are known exactly, is referred to as the forward problem. However, these physical properties of the

---

B. Malama (✉)
Sandia National Laboratories, 4100 National Parks Highway, Carlsbad, NM 88220, USA
e-mail: bnmalam@sandia.gov

P.K. Mishra and K.L. Kuhlman (eds.), *Advances in Hydrogeology*,
DOI 10.1007/978-1-4614-6479-2_7,
© Springer Science+Business Media New York 2013

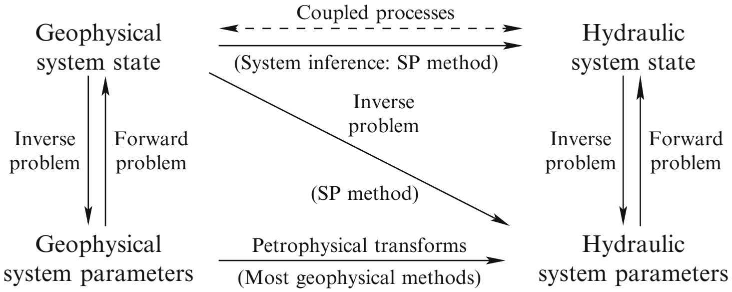

Fig. 7.1 Schematic diagram illustrating the relation between geophysics and hydrology and the distinction between SP and other geophysics techniques. *Dashed arrow* indicates coupled processes, and *solid arrows* indicate possible computations. System inference is in direction of stronger process coupling

subsurface are rarely known exactly at every spatial position in the flow and transport domain. They are typically determined either by (1) taking samples of the subsurface on which standard laboratory tests are conducted to estimate the physical parameters or (2) by performing field-scale tests in which spatiotemporal measurements of system state response to a known perturbation are obtained and used to solve the so-called inverse problem. Sampling the subsurface material and in situ measurement of system state by traditional methods of hydrology require drilling and coring into the formation (Rubin et al. 1992; Butler Jr. 2005), which is laborious and expensive, and can only yield spatially sparse data. Hence, a major limitation of these approaches is that samples of the subsurface and spatiotemporal measurements of subsurface system state cannot be obtained everywhere and at appropriate scales of the subsurface. Thus, there are always information gaps that must be filled in by invoking some upscaling and/or interpolation scheme in order to solve the forward (prediction) problem.

The field of hydrogeophysics has emerged in the attempt to provide complementary datasets and fill these information gaps in space with spatially dense "measurements" of subsurface hydraulic properties or system state using noninvasive geophysics techniques (Hubbard and Rubin 2005). A natural dichotomy has developed in hydrogeophysics between methods that are based on the use of petrophysical transforms and those based on measurement of system state of processes that are directly coupled with groundwater flow (see Fig. 7.1). The former approach, which is the more common in the hydrogeophysics literature/community, involves determination of a physical property, (e.g., electrical resistivity) that controls some geophysical process (electricity flow) in the subsurface and relating it, via petrophysical transforms, to physical properties (e.g., hydraulic conductivity) that are required to solve flow and transport problems (Knight et al. 2010). Typically, the physical properties determined by geophysics techniques are easier to measure at appropriate scales and spatial resolution than the hydraulic and transport properties. Petrophysical transforms are empirical functions that are used to relate parameters of (typically uncoupled) physical processes that occur in the subsurface (Kirsch 2009). For instance, an empirical relation can be developed between a parameter that controls the propagation of electromagnetic waves in the subsurface and hydraulic parameters even though there is no obvious direct relation between flow of groundwater and propagation of EM waves; EM methods, though sensitive to the presence of water in the subsurface under various saturation conditions, cannot distinguish between static and flowing groundwater. Knight et al. (2010) and Kirsch (2009) provide detailed discussion of some of the most commonly used petrophysical transforms in the hydrogeophysics literature.

An alternative to the petrophysical transform approach is the use of techniques that rely on geophysical processes that are directly coupled to groundwater flow, with a view to using measurements of the geophysical system state to infer the hydraulic system state or to directly estimate hydraulic parameters. Such an approach would be most advantageous if the geophysical system state can be measured noninvasively at greater spatial resolution than the hydraulic state. An example of a geophysical process that is directly coupled to groundwater flow is the electrokinetic phenomenon that gives rise to streaming potentials (SP) (Ishido and Mizutani 1981; Sill 1983). Groundwater flow in porous media is known to yield an electric field in the media due to the existence of the electric double layer (EDL) at the water–rock interface. Measurements of the electric potentials associated with this field can be used to infer the hydraulic system state or to directly estimate hydraulic parameters. Jouniaux et al. (2009) provide a review of the SP method. Nuclear magnetic resonance sounding (NMR) has also emerged as an example of method that could be placed in this category (Weichman et al. 2000; Lubczynski and Roy 2004). Though it is primarily an imaging technique used groundwater detection (Goldman et al. 1994; Gev et al. 1996), it can be used to obtain estimates of hydraulic properties (Shushakov 1996; Legchenko and Shushakov 1998).

In this work, the focus is on the SP method, particularly as it pertains to pumping tests used in traditional aquifer characterization. Bogoslovsky and Ogilvy (1973) were among the first to measure SP anomalies associated pumping tests conducted in an aquifer and to relate them to the drawdown cone of depression. They concluded empirically that one can estimate the radial extent of the cone of depression in the vicinity of a pumping well from the SP anomaly measured at the surface without installing piezometers or observation wells. Darnet et al. (2007) developed a solution for the steady-state problem describing the relation between drawdown and the associated SP anomaly for an unconfined aquifer and were able to fit their model to the SP profile data of Bogoslovsky and Ogilvy (1973). Additionally, they were able to obtain estimates of hydraulic conductivity directly from SP data.

Bogoslovsky and Ogilvy (1973) presented their SP and head data in graphical form and did not provide such details as the thickness of the aquifer and the pumping rate needed to obtain meaningful estimates of hydraulic parameters. A more complete data set was needed to provide firm estimates of hydraulic parameters from drawdown data for comparison to estimates from SP data. Such a data was obtained by Rizzo et al. (2004) who reported results of a constant-rate pumping test conducted in a 37 m thick confined aquifer in the Calabria region of Southern Italy. They developed a model to describe the SP response under (pseudo) steady-state flow conditions and invoked linearity to obtain an expression for the transient SP signal observed during the recovery period of the field test. While head data were recorded during both the pumping and recovery phase, the SP response was only monitored during the final 20 min of the pumping phase and continued for most of the recovery phase. This was due to the fact that the model available to Rizzo et al. (2004) was only suited for steady-state and recovery-phase flow analysis.

A more complete model for transient SP response to confined aquifer pumping was developed by Malama et al. (2009a) and was used to invert the data of Rizzo et al. (2004) for hydraulic conductivity and specific storage, the two pertinent hydraulic parameters. Since no transient pumping-phase SP data were collected in the field tests of Rizzo et al. (2004), additional field tests were needed. Such a test was performed at the Boise Hydrogeophysical Research Site (BHRS) in 2007 where a shallow unconfined aquifer is present. Malama et al. (2009b) developed a semi-analytical model for SP associated with pumping tests conducted in an unconfined aquifer and use it to analyze transient SP data collected during the 2007 BHRS field tests. The data were successfully inverted for hydraulic conductivity, anisotropy ratio, specific storage, and specific yield. Estimated values of these parameters were found to compare well to those obtained from drawdown data. This demonstrated that pumping-phase transient SP data can be used to directly estimate hydraulic parameters. Maineult et al. (2008) also demonstrated this with data from periodic pumping tests conducted in a confined aquifer.

SP signals associated with groundwater flow are typically small (a few to tens of millivolts) and vulnerable to corruption by noise from other sources of self-potentials in field applications. In an attempt to better understand the physics of SP generation in noise-free environments, a few workers have performed laboratory experiments under controlled conditions to simulate groundwater flow conditions that are realized during field tests. For instance, Suski et al. (2004) performed laboratory simulations of unconfined aquifer pumping tests in a rectangular $2 \times 6 \times 0.5\ \text{m}^3$ Plexiglas tank, in which hydraulic head and streaming potentials were monitored during the tests. They used tap water with pH=8.3, which can change the surface charges at the rock–water interface. They also used a peristaltic pump, which contaminated the pumping-phase SP responses with harmonic fluctuations and forced the workers to only analyze recovery-phase SP data. Straface et al. (2011) reported results of unconfined aquifer pumping test simulations performed in a large rectangular $10 \times 7 \times 3\ \text{m}^3$ sand tank where they monitored hydraulic head and SP. They obtained very clear transient SP responses during both the pumping and recovery phases, but used a steady-state model to estimate hydraulic conductivity from SP data.

In this work, we report results of unconfined aquifer pumping test simulations performed in a cylindrical sand tank bounded by a water-filled annulus to maintain a constant-head (Dirichlet) boundary condition along its circumference. This configuration conforms more to the radial flow pattern that is realized during aquifer pumping tests than the rectangular domain of Straface et al. (2011).

Drawdown and SP data measured in this laboratory model are analyzed separately to estimate hydraulic conductivity, anisotropy, specific storage, and specific yield. The hydraulic conductivity estimated in this manner is compared to that determined in falling-head permeameter tests, which were also used to estimate the electrokinetic coupling coefficient of the saturated sand in the sand tank. SP data are also used to estimate the formation factor and electrokinetic coupling coefficient of the flow domain. The coupling coefficient estimated in this manner is compared to that obtained from falling-head permeameter tests. The analysis presented herein demonstrates repeatability of results obtained at the field-scale and clearly shows that hydraulic parameters are directly estimable from SP data. The SP signals are strongly impacted by the chemistry of the electrolyte (groundwater), and this can lead to signals that are not analyzable without use of exotic filtering techniques. Research is ongoing to understand how electrolyte chemistry affects the SP signals measured at the surface during pumping tests.

7.2 Electrokinetic Theory and Groundwater Flow

In porous media where the rock matrix is siliceous, the interaction of water and the rock surface gives rise to a negatively charged rock surface at electrolyte pH $<$ 7.0, due to silica protonation. This charge leads to the development of the EDL, which, in its simplest form, consists of an immobile layer of charges that are strongly "adsorbed" to the mineral grain surface and a mobile diffuse layer of charges near the grain surface (see Fig. 7.2). Groundwater flow has the effect of mechanically forcing movement of the ions in the diffuse layer generating a streaming current and a corresponding electric field in the flow domain. The electric field is governed by Revil et al. (2003)

$$\nabla \cdot \mathbf{j} = 0 \tag{7.1}$$

where $\mathbf{j}$ is the electric current density $(\mathrm{A/m^2})$. Revil et al. (2003) and references therein have shown that

$$\mathbf{j} = \sigma \mathbf{E} + \mathbf{j}_f, \tag{7.2}$$

where σ is the electrical conductivity of the porous medium (S/m), $\mathbf{E} = -\nabla\phi$ is the electric field (V/m), $\phi = \varphi - \varphi_0$ is the electric potential change (V) from some initial state φ_0, and $\mathbf{j}_f$ is the electric current density due to fluid flow and is given by (e.g., Sailhac and Marquis 2001, Malama et al. 2009a)

$$\mathbf{j}_f = \sigma C_\ell \mathbf{K}^{-1} \mathbf{q} \tag{7.3}$$

where $C_\ell = -\partial\phi/\partial h$ is the electrokinetic coupling coefficient (V/m), $\mathbf{K}$ is the hydraulic conductivity tensor, $\mathbf{q} = -\mathbf{K}\nabla h$ is the Darcy fluid flux (m/s), and h is hydraulic head (m). C_ℓ is a physical parameter defined as the electric potential drop

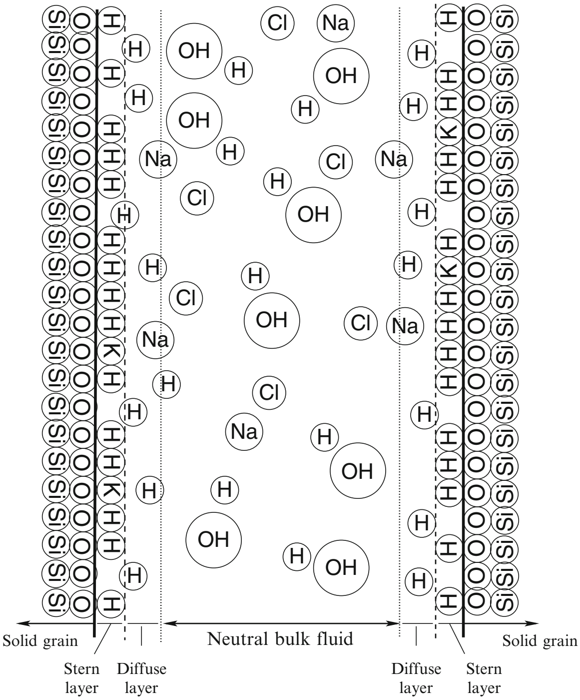

Fig. 7.2 Schematic illustrating the EDL in an idealized water-filled pore at the silica–water interface

across a unit length of a porous medium due to fluid flow generated by a unit hydraulic head differential across that length. No attempt is made in this work to relate it, via petrophysical transforms to hydraulic parameters.

Groundwater flow is governed by the well-known mass continuity equation

$$-\nabla \cdot \mathbf{q} = S_s \frac{\partial h}{\partial t} \tag{7.4}$$

where S_s is specific storage (m^{-1}). Equations (7.1) and (7.4) constitute the system of equations that describes the coupled processes of fluid flow and generation of streaming potentials. In principle, when $\mathbf{q}$ is known from measurements of hydraulic head (h), the total current density $\mathbf{j}$ can be determined. The converse is also true in principle, when $\mathbf{j}$ is known from measurements of electric potentials ϕ. This is the system inference problem and requires knowledge of system parameters $\mathbf{K}$, S_s, σ, and C_ℓ. If these parameters are unknown, they can be estimated directly from spatiotemporal measurements of ϕ and/or h. This is the inverse problem. Inferring the hydraulic system state from measurements of ϕ is easier than the converse, since it is easier to obtain high-resolution measurements of ϕ than h. It should be noted that no attempt is made to develop a set of petrophysical transforms that relate the hydraulic parameters $\mathbf{K}$ and S_s to the electrical parameters C_ℓ and σ.

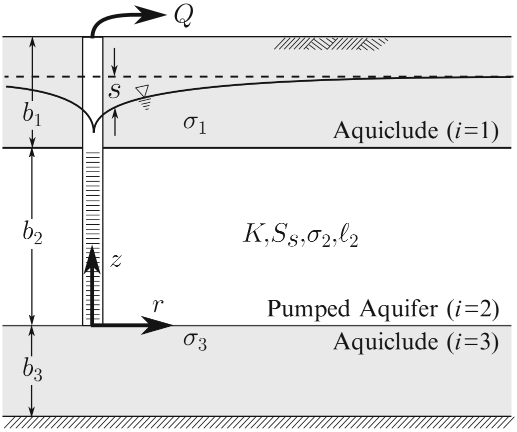

Fig. 7.3 Schematic of the three-layered conceptual model used in Malama et al. (2009a) to derive the SP solution for confined aquifer flow toward a pumping well

7.2.1 Recent Advances: Transient Theory of SP

Malama et al. (2009a,b) recently developed solutions to the coupled problem described by Eqs. (7.1) and (7.4) in cylindrical coordinates (see Appendix A), which solutions are uniquely suited to modeling transient SP responses observed during pumping tests conducted in confined (Malama et al. 2009a) and unconfined aquifers (Malama et al. 2009b).

7.2.1.1 Confined Aquifer Solution

For a confined aquifer Malama et al. (2009a) developed the exact solution for SP response in the aquifer and the confining units using zero-order Hankel and Laplace transforms. All reference hereafter to the Hankel transform implies the zero-order transform. A schematic of the conceptual model used in their work is shown in Fig. 7.3. The solution is based on all the classical assumptions of the Theis solution, namely (Theis 1935),

1. Aquifer is isotropic, homogeneous, and radially infinite.
2. Aquifer is bounded above and below by horizontal boundaries.
3. Pumping well is a line sink (vanishingly small radius) and is fully penetrating.
4. Initial drawdown is zero.

Additional assumptions, which are inherent in the development of the Theis solution, that are explicitly required to solve SP problem are:

1. No flow in the units above and below the aquifer.
2. Quasi-static limit satisfied at all times.
3. Initial potential is zero everywhere in the domain relative to some reference.
4. Homogeneous and isotropic electrical conductivity and coupling coefficient.

They showed that inverse Laplace transform of the resulting solution can be obtained analytically, leading to the following expression for the dimensionless streaming potential, $\phi_{D,i}$, in the ith

$$\phi_{D,i} = \begin{cases} s_{D,c}(u) - \mathcal{H}_0^{-1}\left\{s_{D,c}^* w_D^*\right\} & i=2 \\ \mathcal{H}_0^{-1}\left\{s_{D,c}^* v_{D,i}^*\right\} & i=1,3 \end{cases}, \tag{7.5}$$

where $i = 1,3$ are the upper and lower confining units, respectively, $i = 2$ is the aquifer,

$$\mathcal{H}_0^{-1}\{s_{D,c}^* w_D^*\} = \int_0^\infty s_D^* w_D^* a J_0(a r_D)\mathrm{d}a, \tag{7.6}$$

and

$$\mathcal{H}_0^{-1}\{s_D^* v_{D,i}^*\} = \int_0^\infty s_D^* v_{D,i}^* a J_0(a r_D)\mathrm{d}a, \tag{7.7}$$

where $\mathcal{H}_0^{-1}\{\}$ denotes the inverse Hankel transform, $f^*(a)$ denotes Hankel transform of $f(r_D)$, a is the Hankel transform parameter, $r_D = r/b_2$, and $J_0()$ is the zero-order Bessel function of the first kind. The function $s_{D,c}(x) = E_1(x)$ is the dimensionless drawdown in the aquifer, $s_{D,c}^*$ is its Hankel transform, $E_1(x)$ is the exponential integral (Abramowitz and Stegun 1972), and x is the similarity (Boltzmann) transform defined as $x = r^2/(4\alpha t)$. It can be shown that

$$s_{D,c}^* = \frac{2}{a^2}\left[1 - \exp(-a^2 t_D)\right], \tag{7.8}$$

where $t_D = \alpha t/b_2^2$. The improper integrals in Eqs. (7.6) and (7.7) can be evaluated numerically. The functions w_D^* and $v_{D,i}^*$ were derived by Malama et al. (2009a), and their equivalent forms are summarized in Appendix B. They capture the interaction between the aquifer and the confining units. The solution indicates that the SP signal in the confined aquifer ($i = 2$) is proportional to the drawdown and includes a space convolution of drawdown and the function w_D^*. The SP signal in the confining units ($i = 1,3$) is simply a space convolution of drawdown and the function $v_{D,i}^*$.

The solution for $\phi_{D,1}$ given in Eq. (7.5) provides a means to estimate hydraulic parameters from SP measurements obtained at land surface. Malama et al. (2009a) also showed that the SP signal measured in the upper confining unit could be approximated by

$$\phi_1(t,r,z) \approx A(r,z) - \frac{C_\ell}{\sigma_{D,1} + \sigma_{D,3}} \frac{Q}{4\pi b_2 K} \ln(u) \tag{7.9}$$

for large t, where A is some arbitrary electric potential at the observation point. This is a Jacob–Cooper-type approximation for SP. Thus, if the coupling coefficient and the electrical conductivities of the three layers are known, this equation can be used

Fig. 7.4 A semilog plot of the dimensionless streaming potential response of the upper confining unit, $\phi_{D,2}$, against t_D/r_D^2 for different values of z_D with $\sigma_{D,2} = \sigma_{D,3} = 10^3$

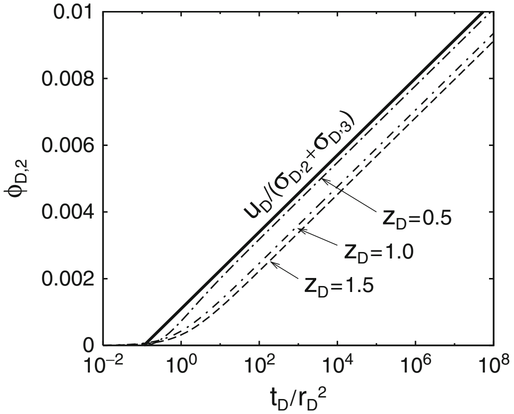

Fig. 7.5 Schematic of the three-layered conceptual model used in Malama et al. (2009b) to derive the SP solution for unconfined aquifer flow toward a pumping well

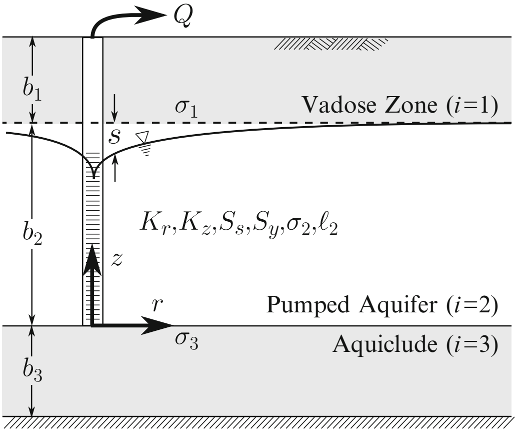

to estimate hydraulic conductivity from the slope of semilog plots of late-time SP data measured at or near land surface. Figure 7.4 illustrates the relation given in Eq. (7.9).

7.2.1.2 Unconfined Aquifer Solution

The solution to the unconfined aquifer SP problem in a cylindrical domain of infinite radial extent was developed by Malama et al. (2009b) and is summarized in Appendix B. A schematic of the conceptual model used in their work is shown in Fig. 7.5. The solution is based on the assumption that the flow problem is described according to Neuman (1972), which is based on the following assumptions:

1. Aquifer is homogeneous but anisotropic ($K_r \neq K_z$).
2. Pumping well is a fully penetrating line sink.
3. Water release is due to medium and water compressibility and gravity drainage associated with water-table displacement.

4. Water-table is a material boundary that physically separates the saturated and unsaturated zones.
5. Water-table kinematic condition linearized in the manner of Dagan (1964).
6. No flow in the unsaturated zone and in the unit underlying the aquifer.

It was further assumed that the electrical conductivities of the unsaturated zone, the aquifer, and the underlying unit are homogeneous, isotropic, and constant in time. As in the confined case, it was also assumed that the initial potential everywhere in the problem domain is zero relative to some reference.

At land surface the solution of Malama et al. (2009b) reduces to

$$\overline{\phi}^*_{D,1}(p,a,1) = \frac{1}{\xi_{1,1}} \cosh(a)\overline{\phi}^*_{D,2}|_{z_D=1} \tag{7.10}$$

where $\overline{\phi}^*_{D,i}(p,a,z_D)$ is the Laplace–Hankel transform of the dimensionless SP response in layer i, $\overline{f}(p)$ is the Laplace transform of $f(t_D)$, and

$$\overline{\phi}^*_{D,2}(p,a,1) = \overline{s}^*_{D,u} + \overline{w}^*_{D,u} \tag{7.11}$$

where a and p are the Hankel and Laplace transform parameters, respectively, $\xi_{1,1} = \cosh(ab_{D,1})$, and $\overline{w}^*_{D,u}$ is defined in Appendix B. The function $\overline{s}^*_{D,u}$ is the Laplace–Hankel transform of unconfined aquifer drawdown and is given by Neuman (1972)

$$\overline{s}^*_{D,u}(a,z_D,p) = \frac{2}{p(p+a^2)}\left[1 - \frac{\cosh(\eta z_D)}{\Delta_1}\right], \tag{7.12}$$

where $\eta^2 = (p+a^2)/\kappa$ and

$$\Delta_1 = \cosh(\eta) + \frac{\eta \alpha_D}{p}\sinh(\eta) \tag{7.13}$$

for the classical linearized kinematic condition at the water-table. The other functions in Eq. (7.10) are defined in Appendix B. Equations (7.10) and (7.11), which are in Laplace–Hankel transform space, can be inverted numerically to space–time. Equation (7.10) is useful for analyzing SP data collected at or near land surface during unconfined aquifer pumping tests. It describes the transient streaming potential field generated by pumping water from an unconfined aquifer and can be used to estimate aquifer hydraulic parameters from measurements of streaming potentials at ground surface.

7.2.1.3 Application to Field Data

The confined and unconfined aquifer solutions have been applied to data collected in aquifer pumping tests yielding good model fits to data and parameter estimates that compare well with those obtained from drawdown data. Malama et al. (2009a) applied the confined aquifer model to SP data collected during the recovery phase

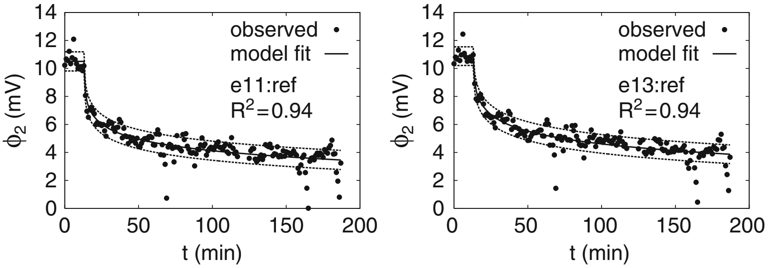

Fig. 7.6 Model fits to recovery-phase data (after Rizzo et al. 2004) obtained during a confined aquifer pumping test near Montalto Uffugo, Italy (after Malama et al. 2009a)

of a pumping test conducted at a site located near Montalto Uffugo, in the region of Calabria in Southern Italy and reported in Rizzo et al. (2004). The aquifer is a silty sand layer with an average thickness of 44 m and is bounded above by a shale formation that is overlain with a layer of gravels and silty sand. A shale substratum lies below the aquifer formation. Additional details of the geology of the site, and on monitoring of the hydraulic and streaming potential responses, may be found in Rizzo et al. (2004). The estimated value of the hydraulic conductivity $K = 2.2 \times 10^{-6}$ m/s was found to be comparable to the value of $K = 2.8 \times 10^{-6}$ m/s estimated from hydraulic head data by Rizzo et al. (2004). However, Rizzo et al. (2004) obtained a value of 1.1×10^{-4} m^{-1} for the specific storage using head data, whereas Malama et al. (2009a) obtained a value of 4.7×10^{-7} m^{-1} from SP data. Examples of model fits to recovery-phase data of Rizzo et al. (2004) are shown in Fig. 7.6.

Malama et al. (2009b) analyzed unconfined aquifer test SP data obtained during tests conducted in the summer of 2007 at the Boise Hydrogeophysical Research Site (BHRS) that were monitored with pressure transducers in observation wells and two electrode arrays for SP and electrical resistivity (ER) tomography (Jardani et al. 2009). The aquifer at the BHRS consists of an unsaturated zone with an average thickness of about 3m and an unconfined aquifer underlain by a clay layer (Barrash and Reboulet 2004). The shallow unsaturated zone and unconfined aquifer at the site, which has a vertical extent not exceeding 20m, consist of unconsolidated cobble and sand fluvial deposits (Barrash and Reboulet 2004). It is bounded to the west by the Boise River. Ten dipole tests, in which water was pumped from one well and injected into another, were conducted in June 2007 at the BHRS. Malama et al. (2009b) analyzed data from one of these dipole tests. The SP data were collected with a Keithley high-impedance voltmeter and 80 nonpolarizing $Pb/PbCl_2$ (Petiau) electrodes (Jardani et al. 2009).

The model was found to fit the field data well, and hydraulic conductivities estimated from transient SP data were of the same order of magnitude as those obtained directly from head data collected during pumping tests conducted at the research site. For instance, Barrash et al. (2006) report aquifer hydraulic conductivities averaging about $K_r = 7 \times 10^{-4}$ m/s and $K_z = 3 \times 10^{-4}$ m/s, and Malama et al. (2009b) and Malama (2011) report average values of $K_r = 4.6 \times 10^{-4}$ m/s

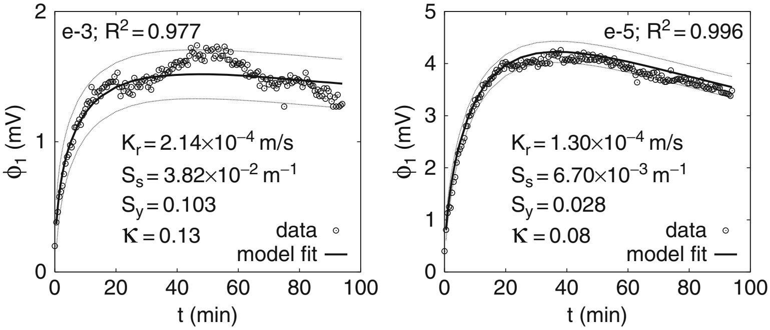

Fig. 7.7 Model fits to transient pumping-phase SP data obtained during an unconfined aquifer pumping test at the BHRS near Boise, Idaho (after Malama et al. 2009b)

and $K_z = 6.5 \times 10^{-4}$ m/s from traditional drawdown analyses. The values estimated here from SP data average $K_r = 2 \times 10^{-4}$ m/s and $K_z = 3 \times 10^{-4}$ m/s (Malama et al. 2009b). The values of the specific storage estimated from SP data ($\sim 10^{-3}$ m^{-1}) were on average found to be larger than those estimated from traditional drawdown analyses ($\sim 10^{-4}$ m^{-1}). *Malama et al. (2009b) attributed these large values of specific storage to the fact that flow in the unsaturated zone above the water-table is neglected in their model. Unsaturated flow above the water-table requires spatially (and temporally) variable unsaturated zone coupling coefficient and electrical conductivity. In the model used by Malama et al. (2009b), these parameters are assumed to be constant, and this appears to affect estimated values of specific storage. Since the SP response is measured in the unsaturated zone, it is more sensitive to unsaturated zone flow than the measured drawdown response.* Figure 7.7 shows examples of model fits obtained by Malama et al. (2009b) during parameter estimation from transient SP data.

7.2.1.4 Finite cylindrical Domain

The solutions given above can be adapted to the case of a cylindrical domain of finite radial extent by use of the finite Hankel transform or by invoking linear superposition. Domains of finite radial or lateral extent are encountered in nature near rivers, lakes, impermeable faults, and as islands. They are also suited for analyzing data collected in laboratory models built to simulate pumping tests. The drawdown $s_f(t,r,z)$ due to flow to a constant rate pumping well at the center ($r = 0$) of a radially finite cylindrical domain where a homogeneous Dirichlet boundary condition of $s_f(t,r=R,z) = 0$ is imposed at $r = R$ can be obtained by linear superposition of the infinite domain solution, $s(t,r,z)$, namely,

$$s_f(t,r,z) = s(t,r,z) - s(t,r=R,z). \tag{7.14}$$

The same is true for the SP response in the ith layer of a finite cylindrical domain with $\phi_{f,i}(t,r=R,z)=0$, i.e.,

$$\phi_{f,i}(t,r,z)=\phi_i(t,r,z)-\phi_i(t,r=R,z), \tag{7.15}$$

where $\phi_i(t,r,z)$ is the solution on a radially infinite domain.

However, since the inversion of two infinite Hankel transforms is required when linear superposition is used, it is more computationally efficient to use the finite Hankel transform approach. Equivalent forms of the solutions for the finite domain are obtainable using the finite Hankel transform. The finite Hankel transform $f^*(a)$ of the function $f(r)$ is given by Miles (1971) as

$$f^*(a)=\int_0^R f(r)J_0(ar)r\mathrm{d}r \tag{7.16}$$

and its inverse by

$$f(r)=\frac{2}{R^2}\sum_a \frac{f^*(a)J_0(ar)}{J_1^2(aR)}. \tag{7.17}$$

The sequence $a_1,a_2,\ldots$ is determined by

$$J_0(aR)=0 \tag{7.18}$$

with $(0<a_1<a_2<\ldots)$.

Hence, for the confined case, Eqs. (7.6) and (7.7), valid for the radially infinite domain, are replaced with

$$\hat{\mathcal{H}}_0^{-1}\{s_D^* w_D^*\}=\frac{2}{R^2}\sum_a \frac{s_D^* w_D^* J_0(ar_D)}{J_1^2(aR)}, \tag{7.19}$$

and

$$\hat{\mathcal{H}}_0^{-1}\{s_D^* v_{D,i}^*\}=\frac{2}{R^2}\sum_a \frac{s_{D,\mathrm{c}}^* v_{D,i}^* J_0(ar_D)}{J_1^2(aR)}, \tag{7.20}$$

where $\hat{\mathcal{H}}_0^{-1}\{\}$ denotes the inverse finite Hankel transform, and the functions s_D^*, $v_{D,i}^*$, and w_D^* are now finite Hankel transforms of s_D, $v_{D,i}$, and w_D, respectively. Equation (7.5) can then be used with Eqs. (7.19) and (7.20) to compute the confined aquifer response in a finite domain. The procedure is the same for the unconfined aquifer problem.

The dimensionless SP response predicted by this solution for different values of the storage ratio $\theta=S_y/S$ is shown in Fig. 7.8. The figure shows the influence of water-table kinematics of the SP signal at land surface. In general, the response shows three distinct phases: an early-time phase where the SP response decreases from its initial value of zero and attains some minimum level, followed by an

Fig. 7.8 Model-predicted dimensionless SP response at land surface ($z_D = 0$) for different values of the storage ratio $\theta = S_y/S$, with $\kappa = 1.0$, $\sigma_{D,1} = 0.5$, and $\sigma_{D,3} = 10$

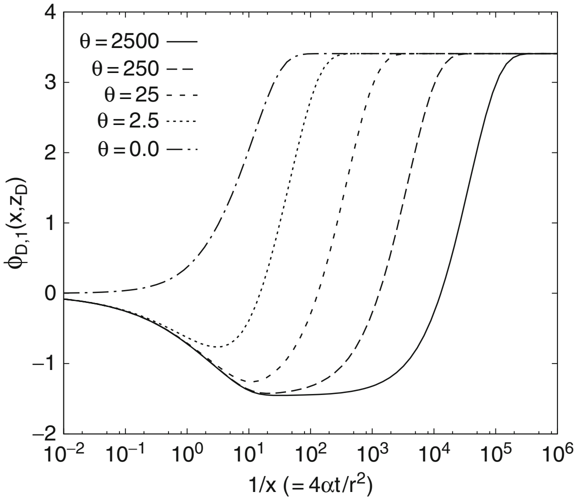

Fig. 7.9 Model-predicted dimensionless SP response at land surface for different values of the anisotropy ratio $\kappa = K_z/K_r$, with $\theta = 2.5 \times 10^3$, $\sigma_{D,1} = 0.5$, and $\sigma_{D,3} = 10$

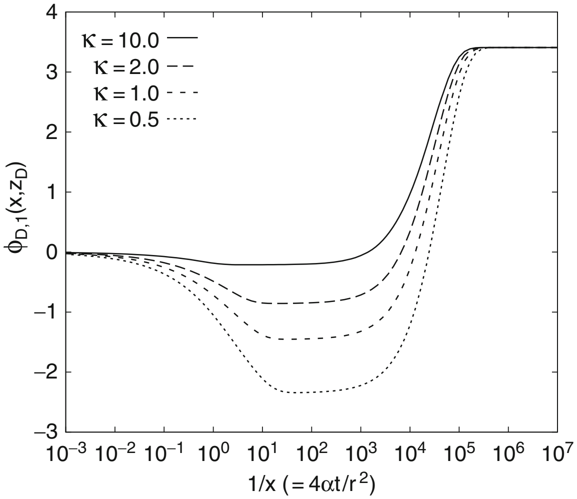

intermediate-time phase during which the SP signal is monotonically increasing and approaching a late-time steady-state phase. Understanding the occurrence of these phases is important since a prolonged stay in the early-time phase could easily be confused with attainment of steady state and could lead to premature termination of a test. The early-time phase diminishes with decreasing values of θ and disappears altogether for $\theta = 0$, which corresponds to a confined aquifer response, or to the case of $S \gg S_y$. The value of the late-time steady-state SP signal is independent of the parameter θ but is attained at increasing later times as θ increases.

Figure 7.9 shows the effect of the anisotropy ratio on the model-predicted dimensionless SP response at $z_D = 0$. Decreasing values of κ accentuate the

Fig. 7.10 Model-predicted dimensionless SP response at land surface for (**a**) different values of $\sigma_{D,1}$ and fixed $\sigma_{D,3} = 10$ and (**b**) different values of $\sigma_{D,3}$ and fixed $\sigma_{D,1} = 0.5$. $\theta = 2.5 \times 10^3$ and $\kappa = 1.0$ in both plots

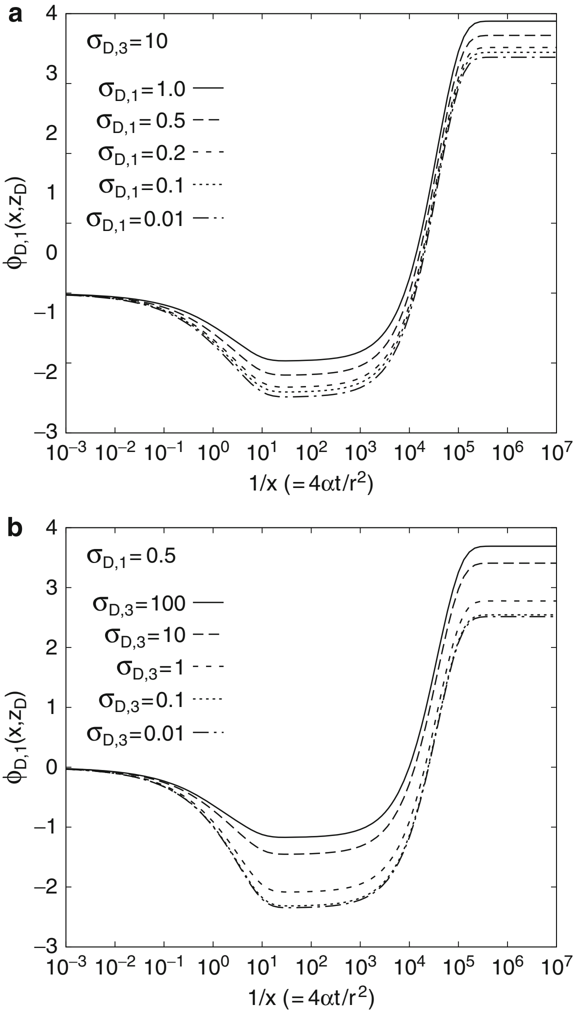

early-time decrease in SP from the initial zero value and lead to an increase in the absolute value of the minimum SP value attained during the early-time phase. For the cases of $\kappa > 1.0$, the effect of the water-table would be to delay the time at which SP values that are significantly larger than the initial zero value are observable. Figure 7.10 shows the effect of (a) the relative electrical conductivity of the unsaturated zone to the saturated zone, $\sigma_{D,1}$ and (b) that of the saturated zone to the underlying confining unit, $\sigma_{D,3}$. Typical physical requirements are such that $\sigma_{D,1} \leq 1.0$, whereas $\sigma_{D,3} \in [0, \infty)$, since the underlying confining unit can be anything from a clay layer to unfractured bedrock. The results indicate decreasing late-time SP signal strength at land surface with increasing electrical conductivity of the saturated zone relative to the unsaturated zone and the underlying confining unit. Beyond some lower limit of these parameters ($\sigma_{D,1}$ and $\sigma_{D,3}$), there is minimal further decrease in signal strength.

7.3 Laboratory Pumping Test Simulations

7.3.1 Experimental Setup and Materials

The experiments reported herein were conducted in a sand tank constructed from two concentric plastic cylinders of diameters 1.70 and 2.44 m, respectively, for the inner and outer tanks. The annulus between the outer and inner tanks was filled with water to simulate a Dirichlet (constant-head) boundary condition at $r = R$ for the flow problem. The inner tank served as the housing for the sand and simulated an aquifer of finite radial extent. It contains a 12 cm layer of gravel overlaid with an 8 cm layer of bentonite that simulates a realistic confining unit. The bentonite layer is overlaid with a 52 cm thick layer of Mescalero sand obtained from desert near Carlsbad, New Mexico. Mescalero sand is fine-grained sand from surficial aeolian deposits in SE New Mexico. The particle size distribution of this sand given in Fig. 7.11 indicates a well-sorted fine-grained sand with an effective particle size of $d_{10} = 120\ \mu\text{m}$. The porosity of the sand determined by the gravimetric method is $n = 0.38$. Hydraulic conductivity estimates obtained from falling-head permeameter tests performed on samples of the Mescalero sand averaged $K = 6.8 \times 10^{-5}$ m/s. The sand is known to contain salt precipitates that dissolve when deionized water is added to the sand, giving the saturated sand an electrical conductivity of ~ 1.0 mS/cm.

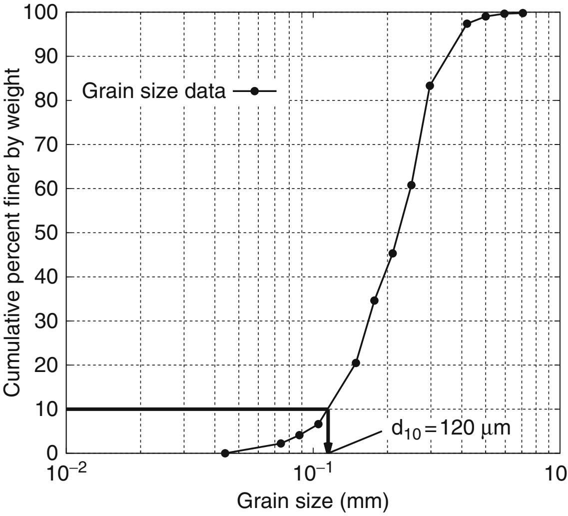

Fig. 7.11 Plot of the cumulative particle size distribution Mescalero sand. *Plot* indicates a well-sorted fine-grained sand with $d_{10} = 120\ \mu\text{m}$

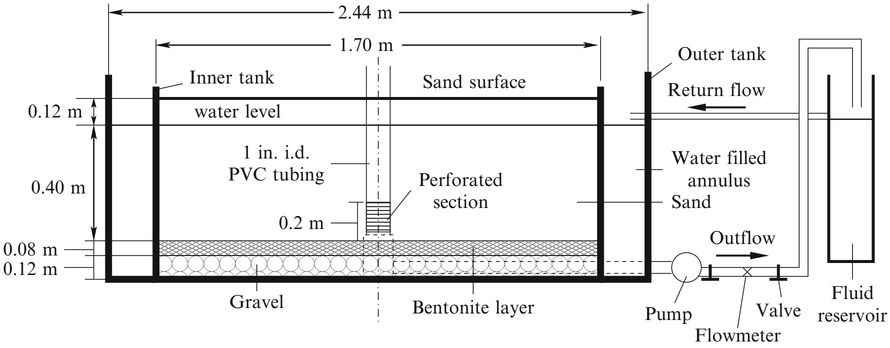

Fig. 7.12 Sand tank used in bench-scale unconfined aquifer pumping test simulations with head and SP measurements of system response

A 1.0 inch PVC tubing with perforations in lower 20 cm serves as a partially penetrating pumping well. At present, the model for the SP response assumes a fully penetrating pumping well. A pump is attached to this PVC tube, and water that is pumped through the center perforated PVC tubing was recirculated into the annulus via a fluid reservoir (see Fig. 7.12). The sand tank is instrumented with nonpolarizable Petiau ($Pb/PbCl_2$) and biomedical electrodes (Ag/AgCl) at various radial distances from the center and depths below the sand surface. Two reference electrodes, one for Petiau and the other for the biomedical electrodes, were installed in screened PVC tubes filled with sand and placed in fluid-filled annulus. The electrodes were installed above the water-table. All SP measurements in the tank are relative to these reference electrodes in the annulus. Atmospheric pressure, annulus water pressure, and saturated zone fluid pressure were measured with Druck transducers. Fluid pressures in saturated sand were monitored in piezometers at radial distances of 20, 41, and 61 cm from the center of the tank and at a depth of 40 cm below the sand surface.

The sand tank was initially saturated with tap water, which has a relatively high dissolved solid content and hardness. The tank was filled to a level such that the water-table was 12 cm below the sand surface. Owing to the fine-grained nature of the sand, the capillary fringe extends from the water-table to the sand surface, leading to a fully saturated zone above the water-table with negative fluid pressure. For an effective pore size of $d_{10} = 120\ \mu\text{m}$, Young's equation predicts a capillary rise of the order of 1 m. Hence, to achieve truly unsaturated conditions above the water-table, one would need a tank larger than that used in this work.

7.3.2 Experimental Procedure

To conduct a pumping test simulation, water is drained from the sand tank through the perforated PVC tubing at the center of the tank at constant rate using a pump

Fig. 7.13 Pumping rate data recorded during a laboratory-scale pumping test simulation

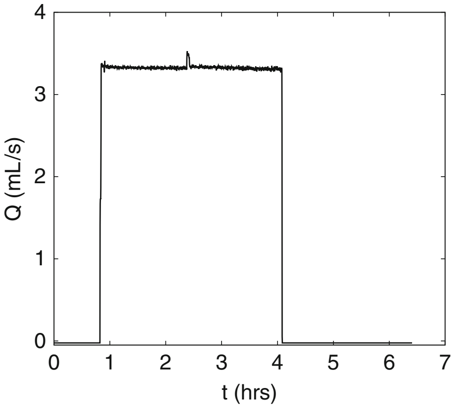

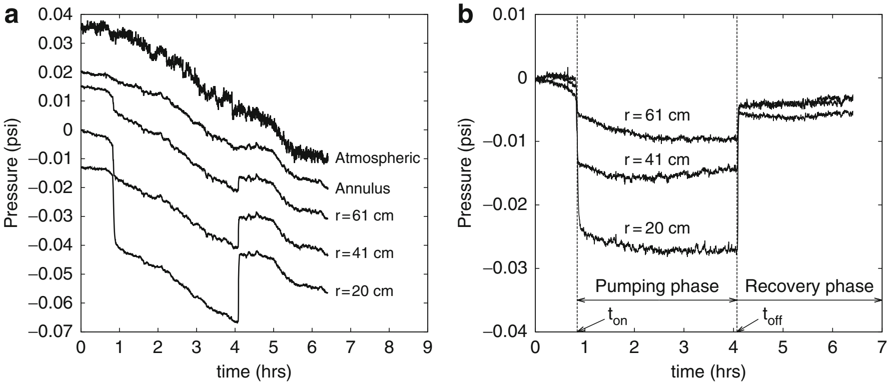

Fig. 7.14 (**a**) Raw and (**b**) corrected pressure response data obtained during a laboratory-scale pumping test simulation. Pressures at $r = \{20, 41, 61\}$ cm are measured at the same depth in the saturated zone. Data in (**b**) were obtained by subtracting the annulus pressure

(see schematic in Fig. 7.12). A flowmeter is attached to the drain pipe and flow rate data are recorded automatically at 10 s intervals with a data logger. Two valves are used to regulate the rate of discharge from the tank. Pumping test simulations reported in this work were conducted at a constant flow rate of 3.33 mL/s. Pumping rate data are shown in Fig. 7.13 and show that a fairly constant rate was achieved during the test. The pumping started about 20 min after onset of data acquisition and continued for about two hours. Pressure data were collected during (pumping phase) and after cessation (recovery phase) of pumping.

7.3.3 Results and Observations

Raw pressure responses recorded from transducers in the saturated zone of the sand tank during the pumping test simulation are shown in Fig. 7.14a, where the

Fig. 7.15 Model fit to drawdown data obtained during pumping test simulations. Estimated parameter values are also shown on the plot

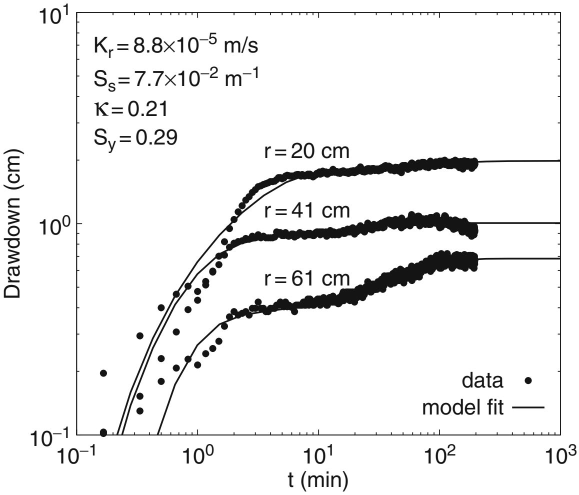

atmospheric and annulus pressures are also shown for reference. The pressure responses are superposed on a quasi-linear barometric trend that is clearly evident in the atmospheric and annulus fluid pressures. Figure 7.14b shows the corrected pressured obtained by subtracting the annulus pressure from the three saturated zone pressures. The onsets of pumping and recovery phases are indicated by t_{on} and t_{off}, respectively. The annulus data clearly indicate no effect of pumping on annulus pressure. Hence, when data are corrected for the quasi-linear trend, the annulus serves as a reasonable constant-head (zero drawdown) boundary condition. Drawdown responses corresponding to these pressure changes are shown in Fig. 7.15. The drawdown responses are as one would expect showing all three (early-, intermediate- and late-time) phases that are characteristic of unconfined aquifer responses. Hence, it can be stated that the laboratory-scale model behaves as an unconfined aquifer.

The raw SP responses measured with nonpolarizable electrodes are presented in Fig. 7.16, where (a) and (b) are plots data collected with Petiau ($Pb/PbCl_2$) electrodes, and (c) and (d) are data collected with biomedical (Ag/AgCl) electrodes. The onset of the pumping and recovery phases are indicated by t_{on} and t_{off}, respectively, and are clearly evident in most of the SP data. Hence, the SP response can be positively attributed to flow during pumping. The responses measured with Petiau electrodes appear to be less consistent than those measured with the biomedical electrodes. They also contain an underlying trend (most evident in recovery data) on which the SP response to pumping is superposed. Petiau electrodes respond by ion exchange by diffusion between the electrolyte within the electrode and groundwater (Petiau 2000). Hence, significant chemical gradients between these electrolytes can lead to the observed SP trend that is not due to pumping. Note that this SP trend cannot be attributed to the quasi-linear barometric trend discussed above since the latter does not induce net groundwater flow.

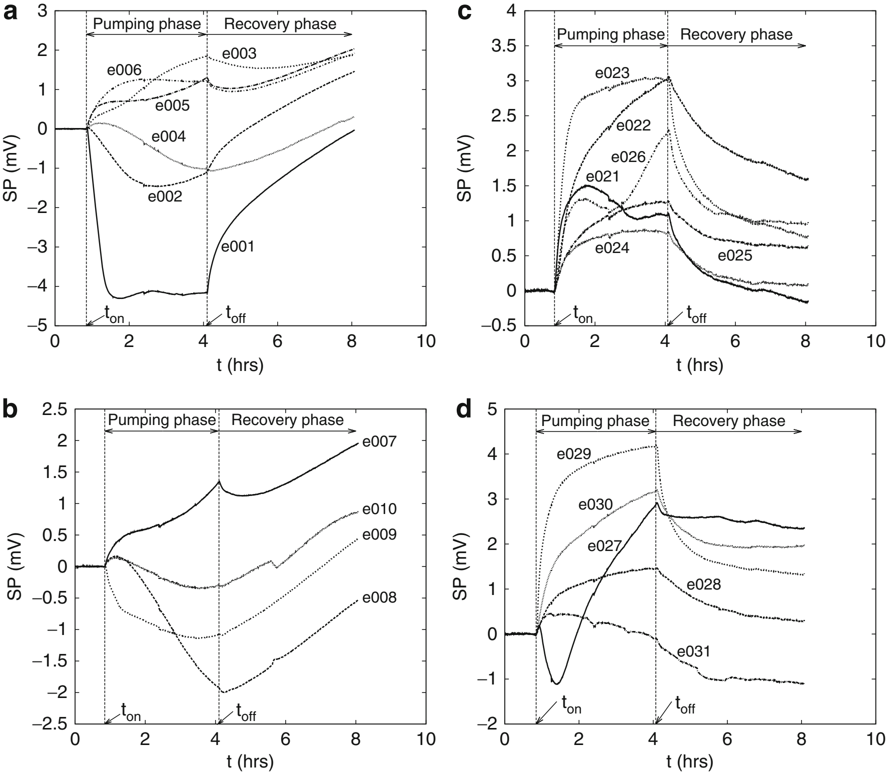

Fig. 7.16 Raw transient streaming potential data measured with (**a**,**b**) Pb/PbCl$_2$ (Petiau) and (**c**,**d**) Ag/AgCl (biomedical) nonpolarizable electrodes during laboratory simulation of a pumping test. Data shows the response during pumping (starting at t_{on}) and recovery (starting at t_{off}) phases

The data in Fig. 7.16c are on a radial profile at a fixed depth from the surface, whereas those in (d) are in a vertical profile at a fixed radial distance from the center. Electrodes e021–e027 are all located in the unsaturated zone (capillary fringe) above the water-table, and e028–e031 are in the saturated sand layer with e028 being almost at the water-table and e030 very close to the sand–bentonite interface.

7.3.4 Model Application to Data

The unconfined flow model of Neuman (1972), adapted to a cylindrical domain of finite radius, was used to invert the drawdown data for hydraulic parameters, yielding values of $K_r = 8.8 \times 10^{-5}$ m/s, $S_s = 7.7 \times 10^{-2}$ m^{-1}, $S_y = 0.29$ and $\kappa = 0.21$. Model fits to the data are shown in Fig. 7.15. The model of Neuman (1972)

Table 7.1 Model parameters estimated from SP data for Mescalero sand. C_ℓ was obtained from SP versus time data and C_ℓ^* from SP versus head data

Electrode	r (cm)	z (cm)	K_r (10^{-5} m/s)	κ	S_s (10^{-2} m^{-1})	S_y (%)	σ_2 (10^{-2} S/m)	C_ℓ (mV/m)
e023	26.7	7.6	3.3	4.2	1.7	10	3.9	16.6
e025	52.1	7.6	2.7	3.9	1.7	15	4.6	11.6
e028	30.5	15.2	2.6	3.9	1.7	21	6.4	6.2
e029	30.5	30.5	3.0	4.1	1.7	10	3.5	20.5

was used since it is the flow model used in the solution of the SP problem. The hydraulic conductivity estimated in this manner compares well to the value of $K_r = 6.8 \times 10^{-5}$ m/s obtained in falling-head permeameter tests conducted on samples of Mescalero sand. The estimated specific storage is much larger than expected and may be due to the low consolidation of the sand in the laboratory model. The sand was allowed to settle under its own weight with no additional mechanical compaction. The sand, however, did settle in layers leading to hydraulic anisotropy reflected in the estimated κ-value of 0.21. The vertical hydraulic conductivity estimated from drawdown data is appreciably smaller than the radial value. The specific yield of $S_y = 0.29$ estimated from the data is slightly smaller than the measured total porosity of the sand of 0.38. This is to be expected since S_y is a measure of drainable porosity under the action of gravity alone.

The SP model for unconfined aquifer flow in a radially bounded cylindrical domain was used to invert measured transient SP data obtained during a laboratory simulation of a pumping test for hydraulic parameters. In addition to hydraulic parameters, the model was used to estimate the coupling term ℓ, which was then used electrokinetic coupling coefficient using $C_\ell = \gamma\ell/\sigma_2$, and the electrical conductivity, σ_2, of the saturated layer. The electrical conductivity ratios $\sigma_{D,1}$ and $\sigma_{D,2}$ were fixed at 0.8 and 10^3, respectively. These ratios could be estimated directly but were fixed to improve identifiability of the hydraulic parameters. Only data from the Ag/AgCl electrodes were analyzed as they did not require significant preprocessing to yield an analyzable signal. The data sets were analyzed separately for each electrode, and only the pumping-phase data were considered. A summary of all the estimated parameter values is given in Table 7.1.

Model fits to the data at parameter estimation optimality are shown in Fig. 7.17 for four select electrodes. Though model fits do not match measured data perfectly, they yield parameter values that are similar to those obtained from drawdown data. The radial hydraulic conductivity and specific storage values estimated from SP data have average values of $K_r = 2.9 \times 10^{-5}$ m/s and $S_s = 1.7 \times 10^{-2}$ m^{-1}. These values are in good (order-of-magnitude) agreement with those estimated by the traditional drawdown data analysis. The anisotropy ratio estimated from SP data is significantly larger than, and appears to be the reciprocal of, that from drawdown data. The specific yield estimate is much smaller than that from drawdown data. Estimates of the C_ℓ and σ_2 are comparable to "measured" values. Measured values

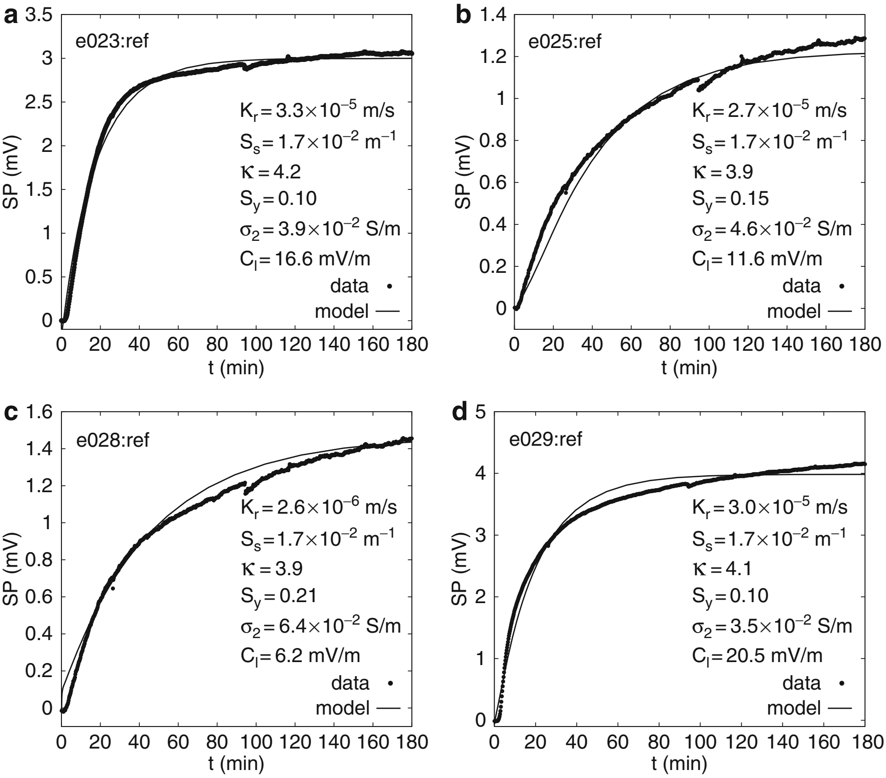

Fig. 7.17 Model fits to transient SP data obtained in laboratory simulations of unconfined aquifer pumping tests

of C_ℓ were obtained through a series of falling-head permeameter test, averaging 20 mV/m. Values of σ_2 were obtained by measurement of electrolyte values, σ_f, using a standard YSI conductivity meter, and are of the order of 0.1 S/m. These are related to σ_2 by $\sigma_2 = F\sigma_f$, where $F < 1.0$ is the so-called formation factor. Values of σ_2 estimated from SP data suggest a formation factor of $F \sim 0.5$. There is minimal variability in the values of the parameters K_r, κ, and S_s among the four electrodes analyzed here. The greatest variability is in the estimated values of the electrokinetic coupling coefficient, with values ranging from 6.2 to 20.5 mV/m.

The temporal variation of the sensitivity coefficients of SP with respect to hydraulic parameters K_r, κ, S_s, and S_y is shown in Fig. 7.18. Sensitivity coefficients provide a measure of the sensitivity of the model-predicted SP response to the respective parameter. The sensitivity coefficients associated with the parameter K_r are largest and increase monotonically with time. Hence, the radial hydraulic conductivity is more easily estimable from transient SP data than the other three parameters. The sensitivity coefficient with respect to the anisotropy ratio, κ, has

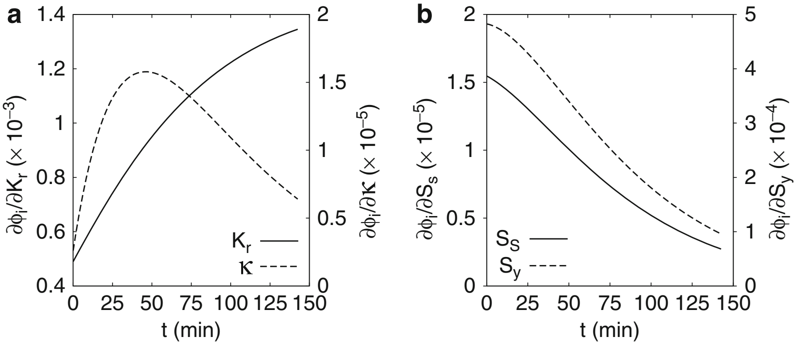

Fig. 7.18 Temporal variation of the sensitivity coefficients of SP with respect to (**a**) K_r and κ and (**b**) S_s and S_y

a peak value in the intermediate-time range of the hydraulic response, after which it decays with time. Hence, the most useful SP data for estimating κ are in the intermediate-time range. The sensitivity coefficients with respect to S_s and S_y are largest at early-time, monotonically decay with time, and show strong linear correlation. This indicates that the sensitivity coefficients with respect to S_s and S_y are not linearly independent for significant portions of the measurement time scale, making their concomitant estimation from SP data difficult and highly uncertain. Similar linear dependence was found to exist between the parameters σ_2 and the coupling term ℓ. The computed sensitivity coefficients with respect to these two parameters were found satisfy

$$\frac{\partial \phi_i}{\partial \sigma_2} \approx -\frac{\partial \phi_i}{\partial \ell}. \tag{7.21}$$

These results suggest that, for the data analyzed here, one can only estimate four of six parameters K_r, κ, S_s and S_y, σ_2, and ℓ. Hence, it may be best to estimate σ_2 and ℓ using alternative techniques and then estimating the hydraulic parameters from pumping test SP data.

7.4 Discussion and Future Directions

Laboratory and field measurement and analyses of transient SP data suggest that hydraulic parameters can be estimated from these data. This has been demonstrated at the field-scale in confined (Malama et al. 2009a) and unconfined (Malama et al. 2009b) flow and herein using laboratory-scale simulations of unconfined aquifer flow. The SP method has potential to be used as nonintrusive interrogation method for the subsurface during pumping tests to yield aquifer hydraulic parameters.

As way of validating the approach, parameter values estimated in this manner have been shown to compare favorably to those estimated by the traditional method of drawdown analysis.

Below is a list, which is not meant to be exhaustive, of some future advances that can, in the opinion of the authors, move the SP method into the purview of the broader hydrogeology field:

- Effects of partial penetration and leakage: As already mentioned elsewhere in this work, laboratory experiments reported herein were performed in a laboratory model with a partially penetrating well, but the analyses of the test results were performed with a mathematical model assuming a fully penetrating line sink. In aquifers of infinite radial extent, effects of partial penetration become negligible at radii satisfying the condition $r > 1.5b\sqrt{\kappa}$, which can be realized in the laboratory-scale model used in this work if $\kappa \sim 0.2$. However, for $\kappa \geq 1.0$, this condition is not achievable in our lab-scale model. Hence, an obvious near-future advance would be to incorporate effects of partial penetration (and pumping wellbore storage) in the SP model.
- Unsaturated zone inclusion: It has long been recognized by several investigators (Neuman 1972, and references therein) that flow in the unsaturated zone above the water-table could affect the drawdown response of unconfined aquifers during pumping tests. Early attempts to explicitly incorporate effects of unsaturated zone flow were through coupled saturated-unsaturated numerical flow models (Rubin 1968; Freeze 1971; Cooley 1971). These works, however, did not demonstrate conclusively that the observed delay mechanism in unconfined aquifer drawdown response could be attributed to water release from the unsaturated zone (Neuman 1972, 1979). However, based on field observations and numerical modeling, Nwankwor et al. (1984, 1992) and Akindunni and Gillham (1992) argued that neglecting unsaturated zone flow would lead to overestimation of specific storage and an underestimation of specific yield, the latter of which is commonly the case with the model of Neuman (1972, 1974). Recently, Tartakovsky and Neuman (2007), and Mishra and Neuman (2010) have developed semi-analytical model that explicitly account for unsaturated flow, the electrokinetic constitutive relations of which have been discussed by Jackson (2010) and others, through a linearized version of the Richards' equation. Hence, a logical future advance would be to incorporate effects of unsaturated zone flow into the SP model using the approach of Mishra and Neuman (2010).
- Other future directions would involve investigating the exact nature of the boundary condition for the SP problem at the interface between a sandy aquifer and a clayey confining unit, conducting additional field tests in varied environments with electrode installation with direct-push techniques to achieve greater depths of interrogation, measurement SP signals with microvolt sensitivity, and extension of current models to heterogeneous subsurface systems.

7.5 Notation

r	Radial distance from pumping well	[L]
z	Vertical distance from aquifer base	[L]
t	Time since start of pumping	[T]
h	Hydraulic head in aquifer	[L]
s	Drawdown in aquifer	[L]
K_r	Radial hydraulic conductivity of aquifer	[L/T]
K_z	Vertical hydraulic conductivity of aquifer	[L/T]
$\kappa = K_z/K_r$	Hydraulic anisotropy	
S_s	Specific storage of aquifer	[1/L]
$S = bS_s$	Storativity	
S_y	Specific yield of aquifer	
$\theta = S_y/S$	Specific yield to storativity ratio	
Q	Pumping rate	[L^3/T]
b_i	Thickness of ith layer	[L]
α	Hydraulic diffusivity of aquifer	[L^2/T]
$\mathbf{q}$	Darcy flux in ith layer	[L/T]
$\mathbf{j}$	Total electric current density	[A/L^2]
$\mathbf{j}_f$	Electric current density due to fluid flow	[A/L^2]
σ_i	Electrical conductivity of ith layer	[S/L]
$\mathbf{E}$	Electric field	[V/L^3]
φ_i	Electric potential in ith layer	[V]
ϕ_i	Electric potential change from initial state in ith layer	[V]
γ	Specific weight of water, ρg	[N/L^2]
ℓ_i	Streaming current coupling coefficient of ith layer	[L^2/VT]
C_ℓ	Electrokinetic coupling coefficient	[V/L]
p	Laplace transform parameter	
a	Hankel transform parameter	

Acknowledgements This research is funded by WIPP programs administered by the Office of Environmental Management (EM) of the US Department of Energy.

Sandia National Laboratories is a multi-program laboratory managed and operated by Sandia Corporation, a wholly owned subsidiary of Lockheed Martin Corporation, for the US Department of Energy's National Nuclear Security Administration under contract DE-AC04-94AL85000.

Appendix A: Governing Equations for Coupled Flow and SP

In cylindrical coordinates with no tangential flow, Eq. (7.4) can be written, for flow in a radially infinite aquifer and in nondimensional, form as (Malama et al. 2009a,b)

$$\frac{\partial s_D}{\partial t_D} = \frac{1}{r_D}\frac{\partial}{\partial r_D}\left(r_D \frac{\partial s_D}{\partial r_D}\right) + \delta\kappa \frac{\partial^2 s_D}{\partial z_D^2}, \tag{A.1}$$

where $s_D = s/H_c$ is dimensionless aquifer drawdown; $s = h(r,z,0) - h(r,z,t)$ is drawdown (m), $r_D = r/b_2$, $z_D = z/b_2$, $t_D = \alpha_r t/b_2^2$; r is radial distance from the pumping well (m); z is vertical position from the base of the aquifer (m); t is elapsed time since onset of pumping (s); $\kappa = K_z/K_r$ is the anisotropy ratio; $\alpha_r = K_r/S_s$ is radial hydraulic diffusivity (m^2/s); K_r and K_z are radial and vertical hydraulic conductivities (m/s), respectively; S_s is specific storage (m^{-1}); b_2 is aquifer or initial saturated thickness (m); $H_c = Q/(4\pi b_2 K_r)$ is system characteristic head (m); and Q is the volumetric pumping rate (m^3/s). The dimensionless parameter δ is zero for confined aquifers, where flow is entirely radial, and unity for unconfined aquifers, where vertical flow is significant.

For confined aquifer flow, Eq. (A.1) is solved subject to the initial condition

$$s_D(r_D, t_D = 0) = 0, \tag{A.2}$$

a Dirichlet far-field boundary condition

$$\lim_{r_D \to \infty} s_D(r_D, t_D) = 0, \tag{A.3}$$

and a Neumann boundary line-sink condition at the well

$$\lim_{r_D \to 0} r_D \frac{\partial s_D}{\partial r_D} = -2. \tag{A.4}$$

For unconfined aquifer flow, two additional boundary conditions are needed because of vertical flow. At the base of the aquifer, a homogeneous (zero-flux) Neumann boundary condition is imposed, namely

$$\left.\frac{\partial s_D}{\partial z_D}\right|_{z_D=0} = 0. \tag{A.5}$$

The linearized kinematic condition of Neuman (1972) is imposed at the water-table, namely,

$$-\left.\frac{\partial s_D}{\partial z_D}\right|_{z_D=1} = \frac{1}{\alpha_D}\left.\frac{\partial s_D}{\partial t_D}\right|_{z_D=1}, \tag{A.6}$$

where $\alpha_D = \kappa/\vartheta$, $\vartheta = S_y/(b_2 S_s)$, and S_y is specific yield or drainable porosity, which is a measure of the fraction of the bulk volume a saturated porous medium would yield when the water is allowed to drain out under the action of gravity.

Solving the flow problem yields $s_{D,c} = E_1(x)$, which is the solution of Theis (1935) for confined aquifer flow. Solving the unconfined flow problem yields the solution of Neuman (1972) given in Eq. (7.12). It should be noted that the flow problem is solved without consideration of the SP problem. This is due to a weaker dependence of fluid flow on electric potential differentials; i.e., the Darcy (pressure gradient) flux term is much greater than the flux term due to the electric field (Ishido and Mizutani 1981; Sill 1983). For the SP problem, however, the current density due pressure differentials (Darcian component) is of comparable magnitude to that due to electric potential differentials (the Ohmic component).

Hence, Eq. (7.1) can be written in nondimensional cylindrical form as (Malama et al. 2009a,b)

$$\frac{1}{r_D}\frac{\partial}{\partial r_D}\left(r_D\frac{\partial \phi_{D,2}}{\partial r_D}\right)+\frac{\partial^2\phi_{D,2}}{\partial z_D^2}-\left[\frac{1}{r_D}\frac{\partial}{\partial r_D}\left(r_D\frac{\partial s_D}{\partial r_D}\right)+\delta\frac{\partial^2 s_D}{\partial z_D^2}\right]=0, \tag{A.7}$$

for the aquifer, with $\delta = 0$ for confined and $\delta = 1$ for unconfined flow. For the upper unit, which is confining in the confined aquifer case, but corresponds to the vadose (unsaturated) zone for the unconfined case, the SP problem is given by

$$\frac{1}{r_D}\frac{\partial}{\partial r_D}\left(r_D\frac{\partial \phi_{D,i}}{\partial r_D}\right)+\frac{\partial^2\phi_{D,i}}{\partial z_D^2}=0, \tag{A.8}$$

where $i = 1$ for the upper unit and $i = 3$ for the lower unit, $\phi_{D,i} = \phi_i/\Phi_c$ for $i = 1,2,3$, and $\Phi_c = (\gamma\ell_2/\sigma_2)H_c$. Note that the Darcian component of the current density (term is square brackets in Eq. (A.7)) does not appear in Eq. (A.8) because it is assumed (Malama et al. 2009a,b) that there is no fluid flow in layers 1 and 3. Additionally, it should be noted that only vertical fluid flow is neglected in the confined case; the electric field, on the other hand, has vertical components, which make it possible for the SP signal to be measured at land surface.

The SP problem is solved subject to the initial condition

$$\phi_{D,i}\big|_{t_D=0} = 0, \tag{A.9}$$

the homogeneous Dirichlet boundary condition at the far-field in all layers,

$$\lim_{r_D\to\infty}\phi_{D,i} = 0, \tag{A.10}$$

the homogeneous Neumann (insulating condition) boundary conditions at ground surface

$$\left.\frac{\partial \phi_{D,1}}{\partial z_D}\right|_{z_D=1+b_{D,1}} = 0 \tag{A.11}$$

and at the base of layer 3

$$\left.\frac{\partial \phi_{D,3}}{\partial z_D}\right|_{z_D=-b_{D,3}} = 0, \tag{A.12}$$

where $b_{D,1} = b_1/b_2$ and $b_{D,3} = b_3/b_2$ are the normalized thicknesses of layers 1 and 3. Note that the insulating condition in Eq. (A.12) is applied at the contact between layer 3 and an underlying highly resistive layer ($z_D = 1 + b_{D,3}$). It has been shown in Malama et al. (2009a) that the line-sink condition at the pumping well can be written as

$$\lim_{r_D \to 0} r_D \frac{\partial \phi_{D,i}}{\partial r_D} = \begin{cases} 0 & i = 1,3 \\ -2 & i = 2 \end{cases}. \tag{A.13}$$

Additionally, continuity conditions are imposed at the upper and lower boundaries of the aquifer, namely,

$$\phi_{D,1}\big|_{z_D=1} = \phi_{D,2}\big|_{z_D=1}, \tag{A.14}$$

$$\phi_{D,3}\big|_{z_D=0} = \phi_{D,2}\big|_{z_D=0}, \tag{A.15}$$

$$\sigma_{D,1} \left.\frac{\partial \phi_{D,1}}{\partial z_D}\right|_{z_D=1} = \left.\frac{\partial \phi_{D,2}}{\partial z_D}\right|_{z_D=1}, \tag{A.16}$$

$$\sigma_{D,3} \left.\frac{\partial \phi_{D,3}}{\partial z_D}\right|_{z_D=0} = \left.\frac{\partial \phi_{D,2}}{\partial z_D}\right|_{z_D=0} \tag{A.17}$$

where $\sigma_{D,i} = \sigma_i/\sigma_2$, the electrical conductivity of the ith layer normalized by that of layer $i = 2$. Malama et al. (2009a,b) developed the analytical solutions to the confined and unconfined SP problems. These are repeated here for completeness (and in a notation that is consistent for the confined and unconfined aquifer problems) in Appendix B.

Appendix B: Analytical SP Solutions

For a confined aquifer, Malama et al. (2009a) derived the exact solution for SP response in the aquifer and the confining units, in double Hankel–Laplace transform space. The details of the derivation, including the appropriate governing equations and initial and boundary conditions, can be found in that work. When derived in the same coordinate system as the unconfined SP solution, the confined SP solution becomes

$$\overline{\phi}^*_{D,i}(p,a,z_D) = \overline{s}^*_{D,\mathrm{c}}(p,a) v^*_{D,i}(a,z_D) \tag{B.1}$$

where $i = 1$ for the upper confining unit, $i = 2$ for the aquifer, $i = 3$ for the lower confining unit, a and p are the Hankel and Laplace transform parameters, respectively and $\overline{s}^*_{D,c}(p,a)$ is the Hankel–Laplace transform of the Theis solution

$$v^*_{D,i}(p,a,z_D) = \begin{cases} \frac{1}{\xi_{1,1}} \cosh[a(b_{D,1} + z'_D)] v^*_{D,2}|_{z_D=1} & i = 1, \\ 1 + w^*_D(a,z_D) & i = 2, \\ \frac{1}{\xi_{3,1}} \cosh[a(b_{D,3} + z_D)] v^*_{D,2}|_{z_D=0} & i = 3, \end{cases} \tag{B.2}$$

$$w^*_D(a,z_D) = \frac{1}{\Delta_2} \left[\xi_{3,2} g_1(z_D) + \xi_{1,2} g_3(z_D)\right] \tag{B.3}$$

where $z'_D = 1 - z_D$,

$$\xi_{1,1} = \cosh(ab_{D,1}) \tag{B.4}$$

$$\xi_{3,1} = \cosh(ab_{D,3}) \tag{B.5}$$

$$\xi_{1,2} = \sigma_{D,1}\sinh(ab_{D,1}) \tag{B.6}$$

$$\xi_{3,2} = \sigma_{D,3}\sinh(ab_{D,3}) \tag{B.7}$$

$$\Delta_2 = |A_1\sinh(a) + A_2\cosh(a)| \tag{B.8}$$

$$A_1 = \xi_{1,2}\xi_{3,2} + \xi_{1,1}\xi_{3,1} \tag{B.9}$$

$$A_2 = \xi_{1,2}\xi_{3,1} + \xi_{1,1}\xi_{3,2} \tag{B.10}$$

$$g_1 = \xi_{1,1}\cosh(az'_D) + \xi_{1,2}\sinh(az'_D) \tag{B.11}$$

$$g_3 = \xi_{3,1}\cosh(az_D) + \xi_{3,2}\sinh(az_D). \tag{B.12}$$

The unconfined aquifer solution obtained by Malama et al. (2009b) is given by

$$\overline{\phi}^*_{D,i}(p,a,z_D) = \begin{cases} \frac{1}{\xi_{1,1}}\cosh[a(b_{D,1}+z'_D)]\overline{\phi}^*_{D,2}|_{z_D=1} & i=1 \\ \overline{s}^*_{D,\mathrm{u}} + \overline{w}^*_{D,\mathrm{u}}(p,a,z_D) & i=2 \\ \frac{1}{\xi_{3,1}}\cosh[a(b_{D,3}+z_D)]\overline{\phi}^*_{D,2}|_{z_D=0} & i=3 \end{cases} \tag{B.13}$$

$$\overline{w}^*_{D,\mathrm{u}}(p,a,z_D) = \frac{1}{\Delta_2}\left[\left(\xi_{1,2} - \frac{p\theta}{a\kappa}\xi_{1,1}\right)g_3(z_D)\overline{s}^*_{D,\mathrm{u}}|_{z_D=1} + \xi_{3,2}g_1(z_D)\overline{s}^*_{D,\mathrm{u}}|_{z_D=0})\right] \tag{B.14}$$

where the various functions and parameters are the same as those given above and $\overline{s}^*_{D,\mathrm{u}}$ is the Laplace–Hankel transform of unconfined aquifer drawdown. The inverse transforms were obtained numerically.

References

Abramowitz M, Stegun IA (1972) Handbook of mathematical functions with formulas, graphs, and mathematical tables. Dover Publications, New York

Akindunni FF, Gillham RW (1992) Unsaturated and saturated flow in response to pumping of an unconfined aquifer: numerical investigation of delayed drainage. Ground Water 30(6):873–884, doi: 10.1111/j.1745–6584

Barrash W, Reboulet E (2004) Significance of porosity for stratigraphy and textural composition in subsurface, coarse fluvial deposits: Boise Hydrogeophysical Research Site. Geol Soc Am Bull 116(9–10):1059–1073, doi:10.1130/B25370.1

Barrash W, Clemo T, Fox JJ, Johnson TC (2006) Field, laboratory, and modeling investigation of the skin effect at wells with slotted casing, Boise Hydrogeophysical Research Site. J Hydrol 326(1–4):181–198, doi:10.1016/j.jhydrol.2005.10.029

Bogoslovsky VA, Ogilvy AA (1973) Deformations of natural electric fields near drainage structures. Geophys Prospect 21(4):716–723, doi:10.1111/j.1365–2478.1973.tb00053.x

Butler Jr JJ (2005) Hydrogeological methods for estimation of spatial variations in hydraulic conductivity. In: Rubin Y, Hubbard SS (eds) Hydrogeophysics, Chap. 2, vol 50. Water science and technology library. Springer, New York, pp 23–58

Cooley RL (1971) A finite difference method for unsteady flow in variably saturated porous media: Application to a single pumping well. Water Resour Res 7(6):1607–1625, doi:10.1029/WR007i006p01607

Dagan G (1964) Second order linearized theory of free surface flow in porous media. La Houille Blanche 8:901–910, doi.org/10.1051/lhb/1964050

Darnet M, Marquis G, Sailhac P (2007) Estimating aquifer hydraulic properties from the inversion of surface Streaming Potential (SP) anomalies. Geophys Res Lett 30(13):1679, doi:10.1029/2003GL017631

Freeze RA (1971) Three-dimensional, transient, saturated-unsaturated flow in a groundwater basin. Water Resour Res 7(2):347–366, doi:10.1029/WR007i002p00347

Gev I, Goldman M, Rabinovich B, Rabinovich M, Issar A (1996) Detection of the water level in fractured phreatic aquifers using nuclear magnetic resonance (NMR) geophysical measurements. J Appl Geophys 34:277–282

Goldman M, Rabinovich B, Rabinovich M, Gilad D, Gev I, Schirov M (1994) Application of the integrated NMR-TDEM method in groundwater exploration in Israel. J Appl Geophys 31:27–52

Hubbard SS, Rubin Y (2005) Introduction to hydrogeophysics. In: Rubin Y, Hubbard SS (eds) Hydrogeophysics, Chap. 1, vol. 50. Water science and technology library. Springer, New York, pp 3–22

Ishido T, Mizutani H (1981) Experimental and theoretical basis of electrokinetic phenomena in rock-water systems and its applications to geophysics. J Geophys Res 86(NB3):1763–1775, doi:10.1029/JB086iB03p01763

Jackson MD (2010) Multiphase electrokinetic coupling: Insights into the impact of fluid and charge distribution at the pore scale from a bundle of capillary tubes model. J Geophys Res Solid Earth 115:B07206, doi:10.1029/2009JB007092

Jardani A, Revil A, Barrash W, Crespy A, Rizzo E, Straface S, Cardiff M, Malama B, Miller C, Johnson T (2009) Reconstruction of the water-table from self-potential data: A Bayesian approach. Ground Water 47(2):213–227, doi:10.1111/j.1745–6584.2008.00513.x

Jouniaux L, Maineult A, Naudet V, Pessel M, Sailhac P (2009) Review of self-potential methods in hydrogeophysics. C R Geosci 341:928–936

Kirsch R (2009) Petrophysical properties of permeable and low-permeable rocks. In: Kirsch R (ed) Groundwater geophysics: a tool for hydrogeology, Chap. 1, 2nd edn. Springer, New York, pp 1–22

Knight R, Pyrak-Nolte LJ, Slater L, Atekwana E, Endres A, Geller J, Lesmes D, Nakagawa S, Revil A, Sharma MM, Straley C (2010) Geophysics at the interface: Response of geophysical properties to solid-fluid, fluid–fluid, and solid–solid interfaces. Rev Geophys 48:RG4002, doi:10.1029/2007RG000242

Legchenko A, Shushakov OA (1998) Inversion of surface NMR data. Geophysics 63(1):75–84

Lubczynski M, Roy J (2004) Magnetic resonance sounding: new method for ground water assessment. Ground Water 42(2):291–303

Maineult A, Strobach E, Renner J (2008) Self-potential signals induced by periodic pumping tests. J Geophys Res Solid Earth 113(B1):B01203, doi:10.1029/2007JB005193

Malama B (2011) Alternative linearization of water-table kinematic condition for unconfined aquifer pumping test modeling and its implications for specific yield estimates. J Hydrol 399(3–4):141–147, doi:10.1016/j.jhydrol.2011.11.007

Malama B, Revil A, Kuhlman KL (2009a) A semi-analytical solution for transient streaming potentials associated with confined aquifer pumping tests. Geophys J Int 176(3):1007–1016, doi:10.1111/j.1365–246X.2008.04014

Malama B, Kuhlman KL, Revil A (2009b) Theory of transient streaming potentials associated with axial-symmetric flow in unconfined aquifers. Geophys J Int 179(2):990–1003, doi:10.1111/j.1365–246X.2009.04336.x

Miles JW (1971) Integral transforms in applied mathematics. Cambridge University Press, New York

Mishra PK, Neuman SP (2010) Improved forward and inverse analyses of saturated–unsaturated flow toward a well in a compressible unconfined aquifer. Water Resour Res 46:W07508, doi:10.1029/2009WR008899

Neuman SP (1972) Theory of flow in unconfined aquifers considering delayed response of the water-table. Water Resour Res 8(4):1031–1045, doi:10.1029/WR008i004p01031

Neuman SP (1974) Effect of partial penetration on flow in unconfined aquifers considering delayed gravity response. Water Resour Res 10(2):303–312, doi:10.1029/WR010i002p00303

Neuman SP (1979) Perspective on ‘delayed yield’. Water Resour Res 15(4):899–908, doi:10.1029/WR015i004p0089

Nwankwor GI, Cherry JA, Gillham RW (1984) A comparative study of specific yield determinations for a shallow sand aquifer. Ground Water 22(6):764–772, doi:10.1111/j.1745–6584.1984.tb01445.x

Nwankwor GI, Gillham RW, van der Kamp G, Akindunni FF (1992) Unsaturated and saturated flow response to pumping of an unconfined aquifer: Field evidence of delayed drainage. Ground Water 30(5):690–700, doi:10.1111/j.1745–6584.1992.tb01555.x

Petiau G (2000) Second generation lead-lead chloride electrodes for geophysical applications. Pure Appl Geophys 157(3):357–382, doi:10.1007/s000240050004

Revil A, Naudet V, Nouzaret J, Pessel M (2003) Principles of electrography applied to self-potential electrokinetic sources and hydrogeological applications. Water Resour Res 39(5):1114, doi:10.1029/2001WR000916

Rizzo E, Suski B, Revil A (2004) Self-potential signals associated with pumping tests experiments. J Geophysical Res Solid Earth 109(B10):B10203, doi:10.1029/2004/JB003049

Rubin J (1968) Theoretical analysis of two-dimensional, transient flow of water in unsaturated and partly unsaturated soils. Soil Sci Soc Am J 32(5):607–615, doi:10.2136sssaj1968.03615995003200050013x

Rubin Y, Mavko G, Harris J (1992) Mapping permeability in heterogeneous aquifers using hydrologic and seismic data. Water Resour Res 28(7):1809–1816

Sailhac P, Marquis G (2001) Analytic potential for the forward and inverse modeling of SP anomalies caused by subsurface fluid flow. Geophys Res Lett 28(9):1851–1854, doi:10.1029/2000GL01245

Shushakov OA (1996) Groundwater NMR in conductive water. Geophysics 61(4):998–1006

Sill WR (1983) Self-potential modeling from primary flows. Geophysics 48(1):76–86, doi:10.1190/1.1441409

Straface S, Rizzo E, Gianpaolo V, Chidichimo F (2011) Estimation of hydraulic conductivity in a large-scale laboratory model by means of the self-potential method. Int Water Tech J 1(1):22–34

Suski B, Rizzo E, Revil A (2004) A sandbox experiment of self-potential signals associated with a pumping test. Vadose Zone J 3(4):1193–1199, doi:10.2114/3.4.1193

Tartakovsky GD, Neuman SP (2007) Three-dimensional saturated–unsaturated flow with axial symmetry to a partially penetrating well in a compressible unconfined aquifer. Water Resour Res 43(1):1–17, doi:10.1029/2006WR005153

Theis CV (1935) The relation between the lowering of the piezometric surface and the rate and duration of discharge of a well using ground-water storage. Trans Am Geophys Union 16(part 2):519–524

Weichman PB, Lavely EM, Ritzwoller MH (2000) Theory of surface nuclear magnetic resonance with applications to geophysical imaging problems. Phys Rev E 62(1):1290–1312

Chapter 8
Description, Analysis, and Interpretation of an Infiltration Experiment in a Semiarid Deep Vadose Zone

Marcel G. Schaap

Abstract Over the past 15 years, the University of Arizona has carried out four controlled infiltration experiments in a $3,600\,\mathrm{m}^2$, 15 m deep vadose zone during which the evolution of moisture content and matric potential was monitored and the subsurface stratigraphy, texture, and bulk density were characterized. This chapter will first provide a brief overview of the site characteristics and the available data. Subsequently a geospatial analysis using old and recently acquired data will be carried out to demonstrate that a vertical domain trend due to alluvial layering must be accounted for. The resulting model for subsurface texture is used to reanalyze a neutron probe calibration set, such that unbiased texture-dependent estimates of soil moisture become possible. The resulting models are applied to the third infiltration experiment conducted at the site (January 2001 to February 2002) and interpreted with moment analysis based on depth-mean moisture contents. The work presented here is a first step towards a full reanalysis of the site's data, which in future publications will also include flow and transport modeling and an assessment how much data and of what kind are needed to build an acceptable vadose zone model.

8.1 Introduction

Our ability to quantify water flow and solute transport through the vadose zone is essential for understanding, mediating, and managing a wide range of agricultural, environmental, and water resource management activities. Movement of soil water and transport of dissolved constituents in the vadose zone is typically complex, nonlinear, and not easily measured. This is especially the case for stratigraphically

---

M.G. Schaap (✉)
Department of Soil, Water and Environmental Science, College of Agriculture and Life Sciences, The University of Arizona, Shantz Building, Room 429, 1177 East Fourth Street, Tucson, AZ 85721–0038, USA
e-mail: mschaap@cals.arizona.edu

P.K. Mishra and K.L. Kuhlman (eds.), *Advances in Hydrogeology*,
DOI 10.1007/978-1-4614-6479-2_8,
© Springer Science+Business Media New York 2013

complex deep vadose zones found in sedimentary basins throughout the (semi-) arid western US, some of which have critical contamination problems. A prime example is the Hanford reserve in the state of Washington where large quantities of mobile uranium and technetium (among a host of other, less mobile, radioactive, or chemical contaminants) pose a significant risk to the local groundwater and ultimately the Columbia River system (DOE 2010). A significant amount of subsurface characterization and geostatistics and vadose zone modeling has been carried out for parts of the "Hanford" site (e.g., Gee et al. 2007), yet, to date the complexities of flow and transport at the site have defied a definitive remediation strategy (DOE 2010). Other well-known deep vadose zone sites with significant vadose zone flow and transport-related risks include the Yucca mountain site for a long-term high-level radioactive waste repository (DOE 2002) and the Idaho National Engineering and Environmental Laboratory which has historic waste repositories with transuranic elements (e.g., Mattson et al. 2004).

Very few well-documented deep vadose zone sites exist that have sufficient data to permit detailed analysis of the effect of subsurface structure on flow and transport processes. One such site is the informally known "Sisson and Lu" infiltration site in the Hanford 200-East area (Sisson and Lu 1984; Gee and Ward 2001) which had led to a range of publications (e.g., Ward et al. 2006, Ye et al. 2007, Deng et al. 2009). Another vadose zone site is the "Las Cruces Trench Site" (Wierenga et al. 1989, 1990) which, although not particularly deep (6 m), has facilitated many vadose zone studies. Here we report on a deep vadose zone experimental site in Maricopa, Arizona. Work at this site was initially funded by the Nuclear Regulatory Commission (NRC), primarily to investigate the suitability of a variety of instrumentation for vadose zone monitoring, including installation techniques, instrument performance, and their appropriateness for field-scale monitoring (Young et al. 1999). In 2004, the National Science Foundation (NSF) funded additional site characterization to support improved vadose zone modeling studies, including characterization of sources of uncertainty.

The major focus points of the "Maricopa" project were four infiltration and drainage experiments conducted from 1997 to 2004, during which moisture was tracked with neutron thermalization and a variety of other instruments. During two of the experiments, a bromide tracer was released to characterize chemical transport. Over the past 15 years, an array of publications (thesis, dissertation, report style, and peer-reviewed literature) has come forth from the project. Young et al. (1999) provided the most comprehensive description to date on the first phase of the project (Experiments 1 and 2; little has been published on Experiments 3 and 4), in particular on the suitability of specific types of instrumentation for deep vadose zone monitoring. Fleming (2001) used a series of laboratory procedures to determine soil hydraulic properties from cores collected along a 1.5 m deep transect at the site, while Graham (2004) conducted an instantaneous profile analysis using moisture and tensiometer data. Wang (2002) carried out a geospatial analysis of the shallow subsurface texture and parameterized flow a transport models for the site. Thomasson and Wierenga (2003) analyzed data from a tracer study from Experiment 1. Yao et al. (2004) conducted an in situ field neutron probe calibration that yielded four textural class-specific calibration relations. Because the textural distribution at depths > 2.5m was still largely unknown at the time of publication, Yao et al. (2004) extended these relations by mapping dry profile neutron count ratios and corresponding textural classes found at the top 2.5 m to those at greater depths. A substantial effort in terms of 1D, 2D, and 3D vadose zone modeling using the data from experiments 1 and 2 was performed by Thomasson and Wierenga (2003) and Wang et al. (2003). They found that simulations based on unsaturated hydraulic properties estimated with a variety of pedotransfer functions that used off-site data did not fit the observed time series of water contents very well. Wang et al. (2003) were able to improve substantially on these results by conducting inverse analyses of temporal water content variations in 1D and 2D sections. Finally, Fang (2009) found that inversion using a site-specific pedotransfer function led to generally better parameter identification that inversions based on layer-specific optimizations.

The above publications provide passing snapshots about what was known or had been measured up to date. In 2005, during the NSF phase of the project, a more complete characterization with regard to texture and some deep hydraulic property samples was conducted. With this new data, it becomes possible to construct a more complete geospatial model for the entire site than Wang et al. (2003) were able to do. As we will show, a better geospatial model of subsurface stratigraphy and texture also makes it possible to reanalyze the neutron calibration conducted by Yao et al. (2004) to produce unbiased estimates of subsurface water content dynamics. As a result of a better geospatial model and a more reliable neutron calibration, it will also become possible to conduct more sophisticated forward and inverse modeling that make it possible to answer important questions about what kind of (and how much) data is needed to characterize the site and to quantify the effects of the various sources of uncertainty on model results. The material presented in this chapter will be limited to: (a) brief description of the Maricopa infiltration site and the data collected, (b) characterization of the three-dimensional subsurface structure using geospatial techniques, (c) a selection of the most appropriate neutron thermalization calibration, and finally, (d) a brief evaluation of Experiment 3 in terms of mass recovery and moment analysis. Future work with regards to additional instrumental data and modeling will be based on the analysis methods and results reported here.

8.2 Materials and Methods

8.2.1 Site Description

The infiltration site is located at University of Arizona's Maricopa Agricultural Center (latitude 33.0695N, longitude 111.9737W, field F-115), between the cities of Phoenix and Tucson. The site is located in a broad alluvial valley with thick and generally horizontal deposits that vary between gravel and clay; the surface soil is characterized as a fine-loamy mixed, hyperthermic Typic Natrargid (Post et al. 1988; Young et al. 1999). The primary site itself is 60 by 60 m and aligned with the cardinal directions with a relative origin of $x = 0$, $y = 0$ at the southwestern point. As described by Young et al. (1999) a cover (0.8 mm Hypalon pond liner) was used to prevent evaporation from the surface. Notable other features in the surrounding area are two irrigation return canals to the south and east with adjacent access roads. Directly west, a service area of approximately $40 \times 60\,\mathrm{m}^2$ in size without cover was available for the duration of the experiments. To the north, a flood-irrigated alfalfa field was present that may occasionally have contributed water to the site by means of subsurface lateral drainage. Irrigation water was applied to the central $50 \times 50\,\mathrm{m}^2$ area of the site with 50 m long drip lines running under the cover in the west to east direction (starting at $x = 5$ m and ending at $x = 55$ m, thus allowing for a 5 m nonirrigated but covered border around the site). The 164 drip lines (Netafim Techline, Fresno, CA) were 30 cm apart and had emitters every 30 cm with a rated discharge of 2.27 l/h each. In this work we report on Experiment 3 which started on January 17, 2001 (day of year, DOY, 17), and ended on January 28, 2002 (DOY 393).

After an extensive 800-day drainage period since the previous experiment, irrigation for Experiment 3 started at noon, April 24, 2001 (DOY 114.5), and ended at noon, May 22 (DOY 142.5). Irrigation occurred ten times daily for periods of 6 min. A small amount of irrigation was applied in the weeks before the formal start of the irrigation phase (15 mm total) for system testing. A flow interruption occurred around DOY 119, making the infiltration deviate from a uniform target of 26.6 mm/day. The cumulative infiltration amount at DOY 142.5 was 764 mm, which is more than 3 times the mean annual rainfall in this region of Arizona. No formal accuracy is available for the total applied amount, but it is estimated to be 2% (cf. Young et al. 1999, p. 73). In the remainder of this work, it is assumed that water is applied uniformly in space even though Young et al. (1999, p. 55) show that it is possible that somewhat higher rates are present near the water distribution points on the western end of the site.

8.2.2 Instrumentation

The site features nine access wells intended for neutron thermalization (see Fig. 8.1). Throughout this chapter we maintain the historic well numbering (402, 403, 405, etc. in Fig. 8.1) to avoid confusion with future publications and the eventual release of the data. Each of the nine wells was 15 m deep and consisted of a 5 cm inner diameter PVC tube; shallower wells are also present at the site (see Young et al. 1999 for details), but these were not used in Experiment 3 and are not depicted in Fig. 8.1. Neutron thermalization counts (over 16-second periods) in 0.25 m increments were available for each well on 41 dates for Experiment 3.

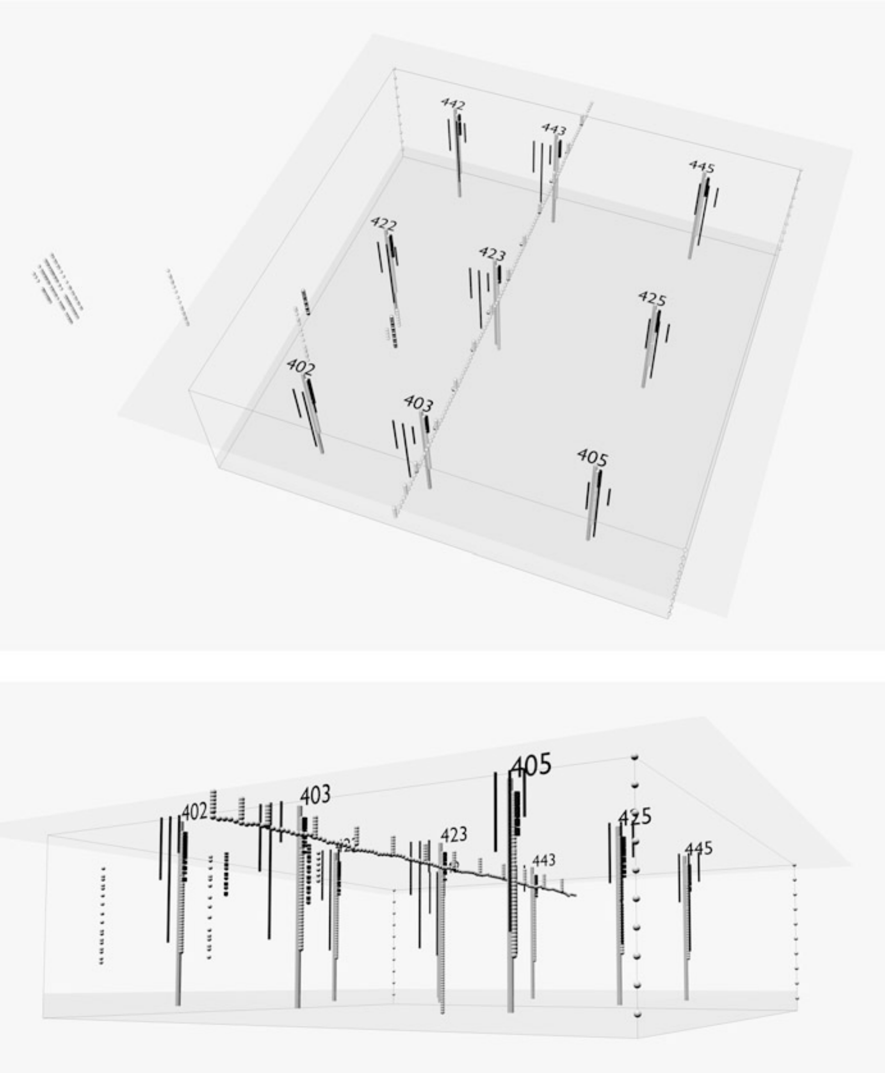

Fig. 8.1 Oblique views to the north–north west from 96 m above (*top*) and 12 m below the surface. The *square on top* is the 60 × 60 m impermeable cover with the 50 × 50 × 15 m cube underneath to delineate the flow domain (*drip lines on top* are not shown for clarity). *Wide vertical cylinders* depict the location of the nine neutron wells (numbered, 402, 403, etc.). *Adjacent narrower cylinders* indicate the position of the tensiometers (3, 5, and 10 m depth). *Spheres* indicate the position of the 1,042 samples for particle size; note that there are two groups of particle size samples outside the flow domain. *Short dark cylinders* (often overlapping) indicate the position of 250 samples for bulk density. The *gray area* near the bottom of the domain indicates the position of a perched groundwater table at 13 m. Individual objects are not sized to scale: all PSD and BD samples were drawn with a size of 0.4 m; the neutron wells were drawn with a diameter of 20 cm (5.08 cm diameter in reality); while the tensiometers were drawn with a diameter of 10 cm (2.54 cm in reality)

In total, 19,488 true measurements were performed, while 740 measurements were inferred because data were missing or unreliable due to neutron probe malfunction, operator error, or time constraints. The inferred measurements were generally derived by interpolation or extrapolation using data from observation dates before and/or after the missing date for the same well and depth. Most of the inferred data are present on DOY 17 and 47 when data for several wells are missing, and DOY 114.5 (start of irrigation) when no measurements were performed at depths greater than 5 m. No measurements were performed below the water table if present in the wells. The deepest recorded data were at depth $z = 14.25$ m (wells 405 and 425), and the shallowest well was 445 with a maximum measured depth of 13 m. In many cases observations deeper than 12.5 m are missing, and in order to consider a consistent depth range, we will therefore primarily focus on data from depths between 0 and 12.5 m. Anomalous neutron readings were found for large parts of well 405, presumably because of large air pockets around the PVC tube. Neutron count data for well 405 was therefore excluded from further analysis in this chapter. Four hundred usable neutron observations are available on each date (8 wells times 50 observation depths); the total number of useful neutron observations is 16,400 (41 dates times 400 observations). As described by Yao et al. (2004), the neutron data are available as count ratio (CR), which is the 16-second neutron count for each well and depth, normalized with a date-specific reference count.

In the following we will assume that each neutron measurement provides a volume average CR for depth increments of 0.25 m, which implicitly also defines our smallest scale of interest. This means that the neutron measurement at a nominal depth of 0.25 m senses moisture in a depth range between 0.125 and 0.375 m, while the measurement at 0.5 m senses moisture between 0.375 and 0.625 m, etc. It should be noted that while we assume a uniform depth weighting over each increment, measurements in reality are more sensitive to water near each nominal depth. In fact, the sensed thermalized volume becomes smaller at increased moisture contents. Guidelines given in Hignett and Evett (2002, p. 502) indicate that the sensed spherical radius was likely larger than 0.125 m under most conditions, indicating that consecutive neutron observations should exhibit some vertical correlation (and thus smoothing). In this work we did not take volume weighting nor spatial correlations of the neutron probe moisture observations into account. No observations are available for $z = 0$ for experimental, regulatory, and operator safety reasons; no moisture data are therefore available for the 0–0.125 m layer.

Visible in Fig. 8.1, but not analyzed in this work, are 27 deep tensiometers (see Young et al. 1999) adjacent to each well at depths of 3, 5, and 10 m. Future work will combine water contents derived from the neutron probe CR and the tensiometers into field moisture release curves. The tensiometers were located about 1 m to the south of each neutron well which ensures that the water present in these instruments does not interfere with the neutron thermalization measurements.

8.2.3 Particle Size and Bulk Density

During the course of the project, a large number of samples were collected to support measurements with specific instrumentation (cf. Young et al. 1999) or to characterize the subsurface stratigraphy. During Experiments 1 and 2, 520 samples for texture were available which were later used by Wang (2002) to conduct geospatial analysis. Some of the data were taken up to 25 m to the west of the site (Fig. 8.1). One hundred and twenty-nine bulk density samples were also available from this phase of the project. Many of these samples were taken in a narrow trench that runs north to south in the middle of the site (Fig. 8.1). Later in the project, Yao et al. (2004) collected an additional 124 core samples between $z = 0$ and 2.5 m near the neutron wells for neutron probe calibration; particle size and volumetric water contents were also determined. No reliable bulk density data is available below 5 m, as greater depths could only be accessed with destructive methods, such as split spoon sampling. In the spring of 2005, an NSF-funded effort was undertaken to characterize the site's texture down to a depth of 15 m. To this end, a total of 401 disturbed samples were collected with and measured in ten particle size classes (all previous samples were typically characterized with three classes: sand, silt, and clay percentages). All wells were typically sampled at 0.25 m increments down to approximately 10 m, except for well 423 in the middle of the site, which was sampled down to 15 m. The sampling was typically done within 1 m from each neutron well. Unfortunately, the exact position relative to each well was not recorded, leading to some positional uncertainty. Most vertical sample depths do not coincide with the nominal depth of the neutron probe observations but are offset by 0.125 m. Some kind of interpolation method is therefore needed to estimate the particle size and bulk density at each neutron well observation depth. After some quality checks, 1,042 and 250 samples remained for particle size and bulk density, respectively.

Figure 8.1 displays the locations of the particle size (spheres) and bulk density samples (cylinders) within the domain. To distinguish samples from the well tubes particle size samples taken at the neutron wells were offset 0.25 m to the east, and those for bulk density were offset by 0.5 m. It should be noted that some samples depicted in Fig. 8.1 appear to overlap and that most samples are located at shallow depth, especially for bulk density. This latter issue is also evident in Fig. 8.2 and will be revisited later on in this chapter.

8.2.4 Data Management and Analysis Software

The analysis conducted in this chapter makes extensive use of the open-source scriptable statistical package *R* (version 2.13.1, Ihaka and Gentleman 1996; R Development Core Team 2005) to perform most of the analysis and produce all graphs (with the exception of Fig. 8.1, which was constructed in Blender v. 2.62,

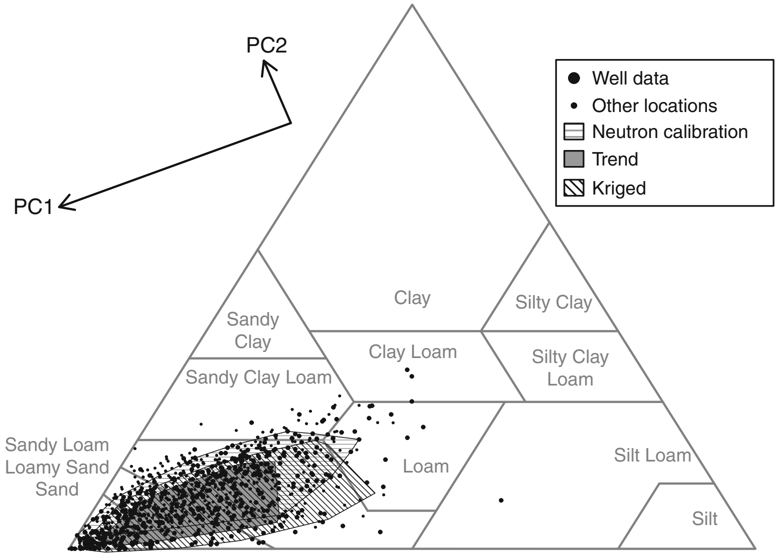

Fig. 8.2 Textural triangle for observed particle size data (*symbols*). *Large dots* indicate samples taken in the vicinity of the nine wells (used to derive the domain trends); *small dots* indicate samples taken elsewhere in the domain (cf. Fig. 8.1). The *three shaded areas* indicate the part of the distribution spanned by samples taken for neutron calibration, estimated vertical texture trend, and kriged values. Also shown (*top right*) are the direction and relative sizes of the first and second principal components offset from their origin, which is at the center of the triangle

www.blender.org). Of particular importance in the analysis with *R* was the package "gstat" (Pebesma 2004) which was used to perform the spatial analysis such as calculation of experimental variograms, variogram model fitting, and point kriging. The *R* function "loess" (Cleveland et al. 1992) was also widely used in this work to smooth noisy data, extract vertical trends in texture and bulk density, and for graphing purposes (Figs. 8.3 and 8.5). A particular advantage of "loess" and other geospatial or regression models in *R* is that they can be saved as objects and be used later to make estimates on new data or be distributed when the data of this project is released. The *R* scripts extracted and stored data using Standard Query Language (SQL) statements that queried a MySQL database. SQL statements were particularly useful for selecting, combining, and summarizing data, as well as outlier analysis for quality control. The effectiveness of *R* combined with an SQL-type database made it possible to quickly and effectively analyze the data, something not easily possible with other software systems such as spreadsheets. An extensive analysis was conducted and only a fraction of the results appear here. We attempted to keep the analysis and the models as simple as reasonable and we will state the assumptions needed to bring the analysis forward.

8.3 Data Analysis and Results

8.3.1 Textural Distribution and Its Principal Components

Figure 8.2 is the textural triangle of all 1042 particle size samples, illustrating that the subsurface consists primarily of sand, loamy sand, and sandy loam textural classes, with a minority in the loam, clay loam, sandy clay loam, and silt loam classes. From the clustered and elongated distribution of the samples, it is also clear that there is a rough correlation between sand and clay percentages, which is caused partly by the fact that sand, silt, and clay percentages for each sample must sum up to 100%, and partly by the alluvial sedimentary regime and subsequent soil formation. Correlated distributions are often found, even in the largest datasets; see, for example, Fig. 8.2 in Schaap et al. (2004) that shows a prominent linear clustering of samples extending from the sand through silty clay loam classes for a database of more than 47,000 samples. Rather than analyzing the particle size data in terms of sand, silt, and clay percentages, it is more effective and convenient to first transform the particle size data into their principal components. No information is lost in such a principal component analysis because this is just a rotation of the coordinate system such that the resulting variables are linearly independent.

The principal components were determined on a subset of the data: 520 samples that were collected in the later part of the project to more fully characterize the subsurface stratigraphy. These data were taken near each of the nine wells and have an almost uniform distribution with depth and do not have a substantial bias towards the surface. The *R* routine "princomp" was used to generate the principal component vectors. Table 8.1 shows that the first principal component, PC1, carries 92% of the variance in the textural triangle and is most sensitive to the sand fraction (see the vectors in Fig. 8.2 which are drawn with a length proportional to the square root of the variance). The clay fraction contributes most strongly to the principal component (PC2), which carries the remaining 8% of the variance. The third component (PC3) is essentially a constant that carries no information. In essence, PC1 measures the coarseness of the soil similar to that of sand, and PC2 represents the presence of fine material within the coarse matrix. PC1 and PC2 formally have percentage units, but because the origin of the new coordinate system is in the center of the triangle, both can have negative values.

Table 8.1 Normalized orthogonal vectors and cumulative variance for the three principal components of texture

	PC1	PC2	PC3
Sand	0.808	−0.119	−0.577
Silt	−0.507	−0.640	−0.577
Clay	−0.301	0.759	−0.577
Cumulative proportion of variance	0.920	1.000	1.000

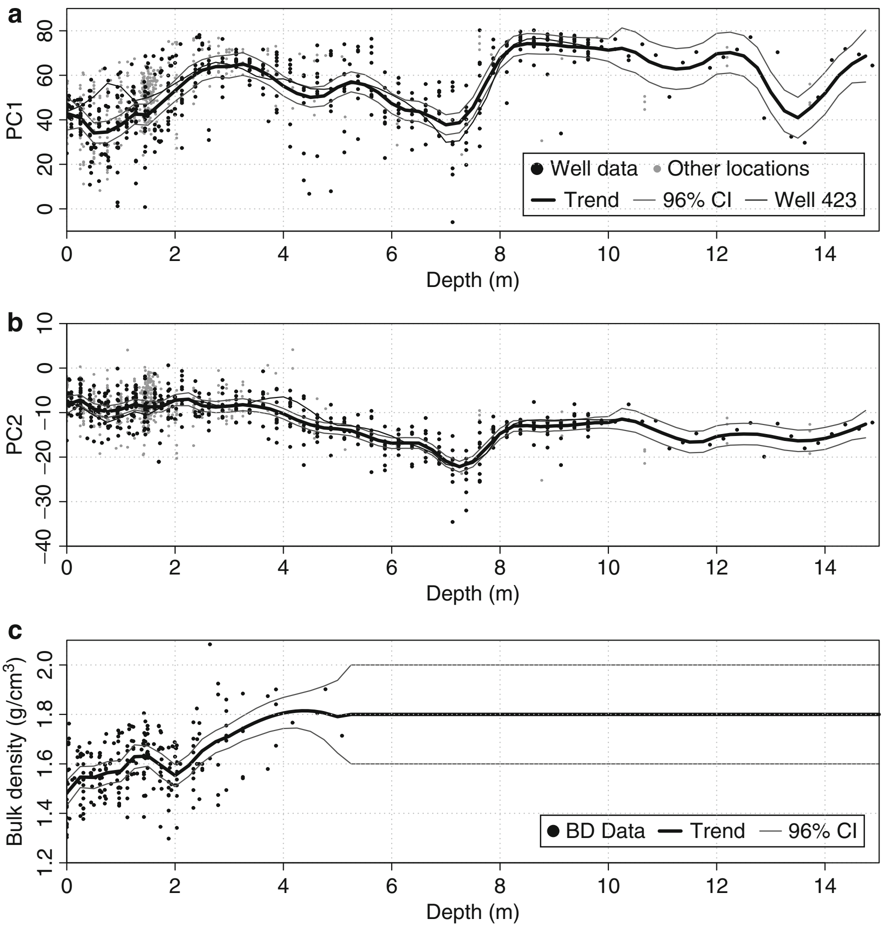

Fig. 8.3 Distribution principal components (**a**: PC1 and **b**: PC2) and bulk density (**c**) with depth. The estimated trends for all three variables are shown, as well as their 96% confidence intervals. The graphs for PC1 and PC2 also show the trend estimate using data for well 423 which was used for depths greater than 10 m for which other wells have scarce or no data (cf. Fig. 8.1). In the case of bulk density, no reliable data are available for depths greater than 5 m. For depths greater than 5 m, we assumed a uniform bulk density of $1.8\,\mathrm{g/cm^3}$ and a one standard error uncertainty of $0.1\,\mathrm{cm^3/cm^3}$

8.3.2 Stratigraphic Trends in Texture and Bulk Density

Figure 8.3a and b present the same data as Fig. 8.2, now expressed as PC1 and PC2 versus depth; Fig. 8.3c shows a similar graph for bulk density. From these graphs, it is clear that although all three data types exhibit considerable scatter with depth, they also exhibit individual trends that are indicative of the horizontal sedimentary layering that is consistent throughout the site. Despite the scatter in each of the

Table 8.2 Pearson correlation coefficients between domain trends and measured particle size ("domain") and kriged results and measured particle size ("kriged") for PC1 and PC2 at each of the nine wells

	PC1		PC2	
Well	Domain	Kriged	Domain	Kriged
402	0.75	0.90	0.69	0.77
403	0.79	0.90	0.85	0.90
405	0.74	0.85	0.82	0.92
422	0.87	0.94	0.81	0.88
423	0.72	0.91	0.84	0.90
425	0.72	0.92	0.65	0.70
442	0.60	0.87	0.79	0.85
443	0.79	0.89	0.86	0.89
445	0.59	0.88	0.84	0.87

datasets it is possible to extract common trends ("domain trends") of PC1, PC2, and bulk density versus depth. To this end we used the *R* function "loess" (Cleveland et al. 1992) which performs a local polynomial regression against depth and is able to provide a mean as well as a standard error for each depth. In the case of PC1 and PC2, we assumed Gaussian deviates from the trend and 24 degrees of freedom on the 520 uniformly distributed points (black data points and gray data points are the remaining 522 texture samples). The domain trends shown in Fig. 8.3a and b are actually a hybrid of two such loess models: one for all wells down to a depth of 10 m, and one for data from well 423 only, which was the only well that had data beyond 10 m. The 96% confidence intervals for the standard error of the trend lines are also shown. From the domain trends, it is evident that prominent coarse layers are present around 3 and 5 m and between 8 and 13 m. Fine textured layers are situated around 1, 4.5, 7, and 13.5 m.

Table 8.2 shows that individual well data exhibited correlation coefficients between 0.59 (well 442) and 0.87 (well 422) for the domain trend of PC1, the correlations for PC2 were between 0.65 (well 423) and 0.86 (well 443). These correlation coefficients and the loess interpolators for well 423 shown in Fig. 8.3a and b demonstrate that the domain trend is a reasonable characterization for the entire site, even though local departures from the overall trend occur (e.g., between 0.5 and 1.5 m for PC1 of well 423 in Fig. 8.3a). By evaluating the domain trend models for PC1 and PC2 for every depth with neutron probe observations and characterizing the resulting bivariate distribution as a convex hull ("chull" in *R*), we can demonstrate that while the domain trends capture a substantial part of the observed textural distribution (gray area in Fig. 8.2), they do not capture all variability present at the site. This is because the domain trends established here are only capturing dominant vertical variability (consistent layering) and not other, random, variability.

In the case of bulk density (Fig. 8.3c), the loess function was established for all available data and 12 degrees of freedom and considered valid until a depth of 5 m, beyond which we somewhat arbitrarily assumed a uniform bulk density of $1.8\,\mathrm{g/cm^3}$ because this value connects to the domain trend at 5 m depth; we assumed an associated one standard error uncertainty of $0.1\,\mathrm{g/cm^3}$. The bulk density increases with depth, but a local minimum appears to be present at 2 m. However, no clear reason was found for the presence of this minimum. We found that bulk density was poorly correlated with texture, and all attempts to extend it to greater depth with regression models failed (not shown).

8.3.3 Geospatial Model

Previously, Wang (2002) determined vertical and omnidirectional horizontal variograms using a subset of the data collected in the first phase of the project. Based on analysis of neutron probe data, Wang (2002) stratified the data 0.3 m thick layers between 0 and 1.8 m and fitted mostly spherical variograms for the horizontal direction with ranges generally between 20 and 25 m. Wang (2002) did not calculate horizontal variograms for deeper layers. Wang (2002) also calculated vertical variograms and concluded that the vertical correlation scale was about 2 m. Vertical variability was treated as random about a constant mean, and the analysis did not explicitly consider the consistent layering that is present in particle size data as well as neutron observations. Here we present a new spatial analysis using all currently available data and demonstrate that it is essential to carry out analysis on the residual variograms (i.e., variograms calculated on data with trend removed).

Figure 8.4a–f provides the omnidirectional horizontal and vertical semivariograms for PC1, PC2, and bulk density, experimental (lines with symbols) and fitted (thick lines) variograms are shown. Also shown are the number of point pairs (thin gray line in Fig. 8.4b, c, e, and f) and the number of samples per depth increment (0.25 m) versus depth in the vertical direction (dashed line in Fig. 8.4e and f). The lag distance bins used were 0.25 and 2.5 m for PC1 and PC2 in the vertical and horizontal directions, respectively, and 0.25 and 5 m for bulk density. The relatively large lag increments in the horizontal direction were used not only to create an appreciable number of samples per lag but also to mask the fact that there is considerable positional uncertainty ($\sim$1 m) in the horizontal direction.

The two experimental variograms in each graph show the effect of the removal of the vertical domain trend (i.e., the residual variogram). As expected, the domain trend correction has a much stronger effect in the vertical variograms (right-hand column) than in the horizontal variograms (left-hand column), simply because the trend caused by consistent layering is removed. The vertical variograms without trend correction in Fig. 8.4d and e show strong "hole effect" (Deutsch and Journel 1998) due to the presence of layering. Also notice that these effects are out of phase for PC1 and PC2. The effect of domain trend correction is minor for the horizontal directions and exists only in these graphs because we used a tolerance angle (see Pebesma 2004) of 3 degrees from horizontal to allow samples that were almost at the same depths to form pairs. However, even here it is evident that domain trend correction leads to a reduction in semivariance, especially at the longer lags.

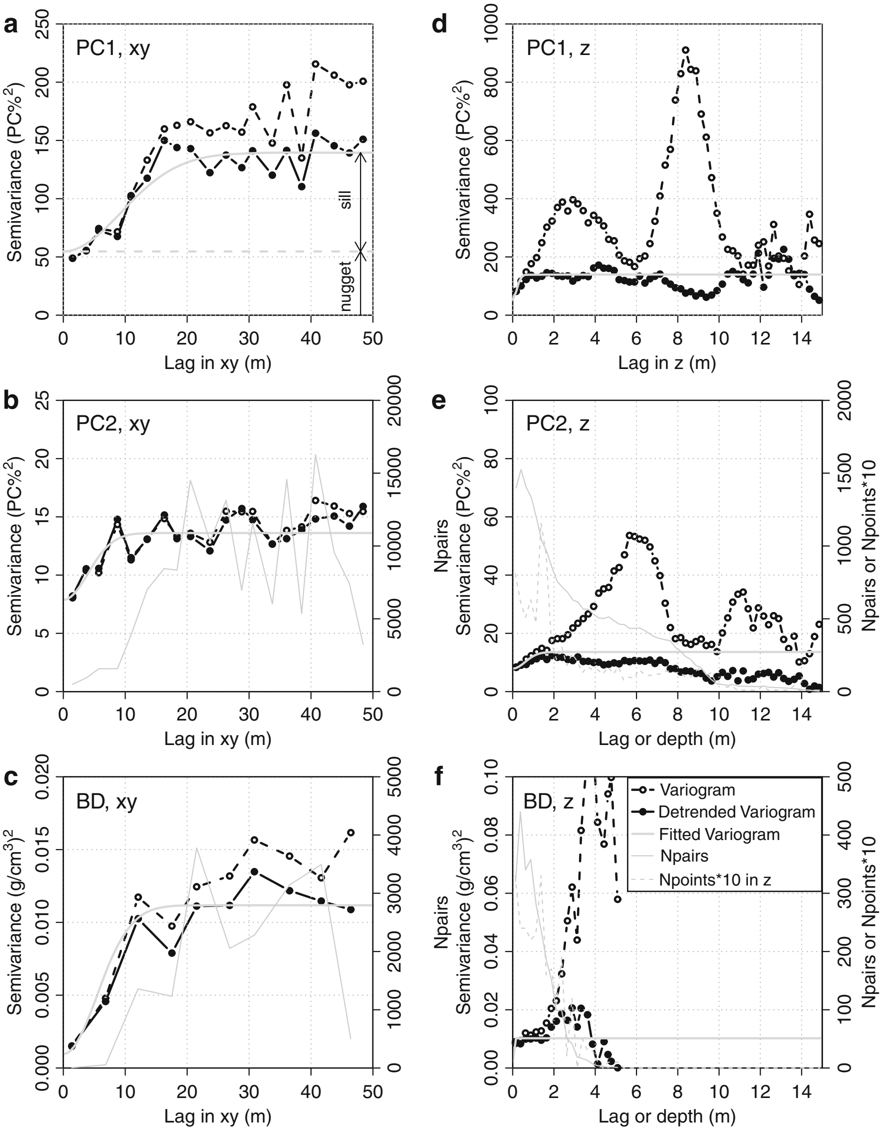

Fig. 8.4 Semi-variograms of PC1, PC2, and bulk density (BD). The left-hand column (a, b, and c) shows the experimental variograms (*dashed with points*) and residual variograms (*solid lines with points*) as well fitted variograms (*thick smooth gray line*) in the horizontal direction (xy). The right-hand column (d, e, and f) shows corresponding variograms for the vertical direction. The *thin gray line* in b, c, e, and f graphs show the number of pairs in each distance class; d and f also show the number of samples with depth (*gray dashed line*) which have been multiplied by 10 to conform to the right-hand axis. The *arrows* in the right-hand bottom corner in a show that our sill values do not include the nugget effect

Table 8.3 Fitted variogram models and their parameters. The long-range semivariance is equal to the nugget plus sill, the cross-validation error was computed as the square root of the mean cross-validation variance (see Pebesma 2004)

Variable	Model	Nugget	Sill	Range xy.(m)	Range z. (m)	Cross-validation error
PC1	Gaussian	$54.7\%^2$	$84.82\%^2$	13.1	0.28	10.66%
PC2	Gaussian	$7.87\%^2$	$5.74\%^2$	5.6	0.85	3.35%
Bulk density	Gaussian	9.61×10^{-4} $(\mathrm{g/cm^3})^2$	1.02×10^{-2} $(\mathrm{g/cm^3})^2$	7.7	0.02^*	$0.11\,\mathrm{g/cm^3}$

*assumed value, smaller than the scale of interest

A variety of analyses with regard to alternative lag distances as well as data stratification (top soil, subsurface) and anisotropy tests were carried out; however, none of these tests provided a more consistent spatial description. It was, therefore, assumed that the experimental residual variograms shown in Fig. 8.4 apply to the entire domain. However, it should be realized that since most samples are located near the top 2.5 m of the domain, the vertical variograms are potentially biased to the near surface. Similarly, few short distance sample pairs are available in the horizontal direction (especially for bulk density) and many of these are near the surface and predominantly in the central north-south trench (Fig. 8.1), making the horizontal variogram ranges uncertain and biased to the top of the domain. For reference, a uniform distribution of the 1,042 samples throughout the site would have required 100 wells (with a spacing of ~5 m) and samples taken every ~1.5 m depth increment (down to 15 m). The drilling costs associated with such a sampling scheme would have been prohibitive.

Table 8.3 provides the parameters of the variogram models that were fitted to the experimental residual variograms. The variograms were fitted using weights that varied with the number of samples divided by the squared distance (Pebesma 2004), thus making the model fits relatively insensitive to the longer lag distances. In the course of our geospatial analysis, we tested a number of different variogram models (linear, spherical, and exponential) and found by cross validation that the Gaussian model performed marginally better than the other models. Nuggets, sills, and ranges were fitted for the horizontal variograms (see also Fig. 8.3a on how we define nugget and sill). In the case of the vertical variograms, we only fitted the range and assumed that the horizontal nugget and sill applied to the vertical direction. The fitted variograms in Fig. 8.4 shows that these assumptions are reasonable. However, we should also note that the experimental residual variograms and fitted results are not completely independent from the domain trends. Choosing a different value for the degrees of freedom will lead to somewhat different domain trends and therefore somewhat different residual variograms. The chosen values (24 for PC1 and PC2) were determined after substantial analysis that showed that values between 16 and 30 yielded rather similar results. In addition, we should also mention that the local polynomial regression used by the “loess” function is unable to deal with discrete boundaries (i.e., sudden changes in texture). This may actually impart short-range spatial correlation that is not present. We are currently exploring alternative ways in dealing with drift, as published by Neuman and Jacobson (1984).

Table 8.3 shows the horizontal range for PC1 (13.1 m) is larger than that of PC2 (5.6 m). No acceptable variogram fits were obtained if a common range was attempted. Conversely, the vertical range of PC2 is longer (0.85 m) than that of PC1 (0.28 m). Because the results for PC1 and PC2 are based on the exact same 1,042 texture samples, we can ignore statistical sampling effects to explain these differences. Our best explanation is that PC1 (being a predominantly coarse component of texture) is determined mostly by the alluvial depositional regime, while PC2 is determined by subsequent soil formation with vertical clay transport that would increase the vertical range and possibly decrease the horizontal range if soil formation is horizontally heterogeneous. Further note that the sill of PC2 is smaller than the nugget, indicating that this variable is, in fact, mostly spatially uncorrelated.

The fitted horizontal range for bulk density was found to be 7.7 m, but this value is rather uncertain (not shown) because the lags shorter than this distance (nominally 2.5 and 7.5 m) contain very few sample pairs (5 and 55, respectively), relative to larger lags (>1,000; see also Fig. 8.4e). Because of the absence of a vertical correlation, no reliable vertical variogram model could be fitted for bulk density. We were unable to define a pure nugget effect in the vertical direction in the anisotropic variogram model, we therefore assumed a range of 0.02 m in this direction, which is smaller than a typical core sample and much smaller than our scale of interest (0.25 m or greater).

Cross-validation (R, gstat: krige.cv) errors shown in Table 8.3 were computed as the root mean square residuals and show considerable errors (10.66 and 3.35% for PC1 and PC2, respectively). The % units of the errors in Table 8.3 refer to the units of particle size and not to a fraction of the variable range. Finally, the convex hulls of the kriged PC1 and PC2 values for all wells are displayed in Fig. 8.2 as a cross-hatched area. This area expands upon that of the domain trends, demonstrating that the kriging procedure is capable of capturing more of the site textural variability. However, it is also clear that kriging is unable to honor all of the existing textural variability as evidenced by the points outside the convex hull for kriging. In this work we will be unable to answer whether this unresolved variability is indeed important to capture the site's hydrological dynamics.

8.3.4 Neutron Probe Calibration

Yao et al. (2004) carried out a neutron probe calibration and derived texture class-specific calibration equations for sand, loamy sand, sandy loam, and one for a textural boundary layer (based on a total of 106 samples taken from the top 2.5 m; see also Fig. 8.4 and Table 8.3 in Yao et al. 2004) that improved upon calibrations performed by Young et al. (1999) and Thomasson (2001). The calibration equations use a simple linear form:

$$\theta = a + b \cdot CR \tag{8.1}$$

where θ is the volumetric water content, CR is the count ratio, and a and b are regression parameters. Table 8.3 in Yao shows that the four equations exhibit rather different offsets and slopes, where the slope appears to become larger with finer textures and the intercepts smaller (more negative). Although these equations worked well for the purposes of Yao et al. (2004), resulting water contents are ambiguous if the textural distribution of a soil horizon is right at the boundary of two textural classes (i.e., two calibration equations apply). For example, a soil horizon with a count ratio of 1.2 and a particle size distribution that would place it right at the boundary between a sandy loam and loamy sand would have a water content of $0.198\,\mathrm{cm}^3/\mathrm{cm}^3$ if it was classified as a sandy loam ($a = -0.146$, $b = 0.287$) but a water content of only $0.145\,\mathrm{cm}^3/\mathrm{cm}^3$ if it were a loamy sand ($a = -0.095$, $b = 0.200$). Unphysical discrete jumps in water content will therefore result for minor variation in soil texture. Instead of stratifying the site according to textural classes, it is clear that the particle size distribution should be included as a continuous variable which we will do by using PC1 and PC2.

One more characteristic of the Yao et al. (2004) neutron calibration data set should be highlighted. In addition to the convex hulls for the domain trends and the kriging estimates for PC1 and PC2, Fig. 8.2 also shows the convex hull of the neutron calibration data set (horizontal hatching). This area only partly overlaps with that of the kriged results (diagonal hatching) we intend to use for our new calibration equations. A Kolmogorov–Smirnov test (*R*: "kstest") indeed confirms that the distributions of neutron calibration data and kriged data are different (at $p < 10^{-6}$). This implies that any neutron calibration including texture is potentially biased towards the characteristics of the top 2.5 m which may subsequently lead to incorrect estimates of water content at deeper layers. The solution to this problem is to correct the statistical distribution of the neutron calibration sample textures towards that of the kriging estimates. To this end, we established smoothed distributions (not shown here but using *R*'s "density" function with a bandwidth of 5.0) for both the neutron and kriged data and computed the ratio of these functions for each neutron calibration sample. This ratio was then used to weigh the data points in the regression while ensuring that the mean weight remained 1.0. Only PC1 was used for the calculation of weights because during the data analysis, it was evident that PC2 only had a minor effect on the calibration results. The minimum and maximum weights were 0.12 and 2.43, respectively.

Five neutron calibration model models (model 0 as a model without texture and *A* through *D* with terms that factor in texture) will be shown here, without and with weighting for the distribution of PC1 (a "w" subscript indicates weighting). Many more models were considered using stepwise regression with *R*'s "lm" and "step" functions and showed that bulk density was not a significant factor in any of the models, while higher-order terms with count ratio were routinely ruled out. Table 8.4 shows the model coefficients, significance codes of the regression

Table 8.4 Multiple linear regression model coefficients and statistics for the neutron calibration, without and with (with subscript “w”) distribution weighting. CR: count ratio; PC1, PC2: first and second principal component of texture; $PC1^2$: squared PC1; $PC1^*CR$: product of PC1 and count ratio; RMSE: root mean square error; R_{adj}: adjusted correlation coefficient; N_-: number of negative water contents generated when the model is applied to the count ratios observed during Experiment 3; M0: the difference in depth-integrated water content between DOY 67.5 and 142.5

Model	Intercept	CR	PC1	PC2	$PC1^2$	PC1*CR	RMSE	R_{adj}	N_-	M0 (m)
Yao								0.77–0.86	0	0.591
0	-0.351^{***}	0.426^{***}					0.0369	0.671	731	1.011
0_w	-0.354^{***}	0.419^{***}					0.0383	0.655	978	0.994
A	−0.067	0.280^{***}	-0.00172^{***}	0.00154			0.0314	0.761	258	0.664
A_w	0.046	0.234^{***}	−0.00261	0.00250^{*}			0.0284	0.810	50	0.555
B	−0.104	0.293^{***}	-0.00160^{***}				0.0317	0.757	233	0.695
B_w	−0.001	0.246^{***}	−0.00244				0.0291	0.800	50	0.584
C	-0.167^{**}	0.264^{***}	0.00326^{**}		$-5.220E\text{-}05^{***}$		0.0291	0.795	467	0.626
C_w	-0.090^{***}	0.222^{***}	0.00252		$-5.220E\text{-}05^{***}$		0.0277	0.820	205	0.526
D	-0.386^{*}	0.407^{***}	0.00861^{*}		$-6.912E\text{-}05^{***}$	−2.957e-03	0.0289	0.798	57	0.549
D_w	-0.544^{**}	0.520^{***}	0.0119^{**}		$-7.545E\text{-}05^{***}$	$-5.097e\text{-}03^{*}$	0.0270	0.829	0	0.516

*** /p/ $<$ 0.001; ** /p/ $<$ 0.01; * /p/ $<$ 0.05

coefficients, and some basic model statistics (root mean square error, RMSE, and adjusted correlation coefficients, R_{adj}). It is clear that some measure of texture must be factored into the equation: Model 0 and 0_w clearly perform worse than any of the other models. The model statistics are rather similar for all other the models: RMSE vary between 0.0270 (model D_w) and 0.0317 (model B) and R_{adj} range between 0.757 and 0.829. Weighted models appear to perform slightly better than models without weighting. Given these results, it cannot be immediately claimed that model D_w is truly superior. In fact, a case could be made to select either model A_w or B_w, which do not have the $\mathrm{PC1}^2$ or PC1*CR terms which seem to increase the fit of the models only in a minor way. At the same time, we note that all coefficients in D_w have a significance of $p < 0.05$, whereas this is not the case for the other models.

A further test of the models can be made by applying these to the field data and test for negative water contents: none of the models should yield such values. However, column N_{-} in Table 8.4 indicates that all models, except model D_w and the original Yao calibration, have a varying number of negative water contents for the observational period.

To illustrate how differently each model performs in terms of mass of water present in the subsurface, we computed the depth-integrated water contents for March 8 (DOY 67.5, drained state) and May 22 (DOY142.5, wet state) and calculated their differences (see also the section on moment analysis). The last column in Table 8.4 shows that model 0 and 0_w produce the largest amounts of water (∼1 m, which is much more than the applied irrigation amount, 0.764 m). All other models, including the Yao et al. (2004) calibration, provide much lower values between 0.516 and 0.695 m. Except for model D_w, each weighted model provided ∼0.1 m less water than the unweighted equivalent; D and D_w differed by only 0.03 m. The differences among the models are surprisingly large and it is clearly critical to select the correct neutron calibration model because mass balance errors would propagate throughout any subsequent analysis and bias results. Given the results in Table 8.4, and the stratified nature of the Yao et al. (2004) model as discussed before, it appears that model D_w is the most appropriate choice for further analysis.

8.3.5 Temporal Patterns of Moisture Content

Having chosen model D_w as the most suitable means to interpret count ratios and PC1 into moisture contents, it is now possible to investigate the temporal patterns of moisture content with depth. In the following, we will provide some results for the mean behavior of the site by determining the mean moisture content against depth and time:

$$\widehat{\theta}(t,z) = \frac{1}{8} \sum_{\forall w \in W} \theta_w(t,z) \tag{8.2}$$

where $\widehat{\theta}(t,z)$ is the mean site moisture content for observation date t and depth z and w is a well present in the set $W = \{402, 403, 422, 423, 425, 442, 443, 445\}$. An analogous equation is used for differential moisture contents ($\widehat{\theta}_d$), relative to the observations on DOY 67.5.

In order to visualize the resulting 2,050 values (50 depths and 41 irregularly spaced dates), we again apply *R*'s loess interpolating/smoothing function to the observations for each of the 50 depths (loess parameters: 15 degrees of freedom, second-order polynomial, Gaussian deviates). Instead of plotting the observations directly, we evaluate the 50 interpolators for each date between DOY 17 and DOY 393 (begin and end of Experiment 3) and represent the resulting moisture content (or moisture differentials) as a grayscale image, as well as with contour lines. The results can be found in Fig. 8.5a and b for water contents and water content differentials, respectively.

The moisture contents in Fig. 8.5a show the distinct effect of the site's stratigraphy (texture differences) in the dry period (prior to the vertical line at DOY 114.5) and the subsequent irrigation and drainage phase. To aid the eye with regard to stratigraphy, we also graphed the domain trend for PC1 on the left-hand side of the diagram with a separate partial horizontal axis on top. Minimum water contents at the site were slightly below $0.05\,\mathrm{cm}^3/\mathrm{cm}^3$ and correlate with high PC1 values, maximum water contents were slightly above $0.25\,\mathrm{cm}^3/\mathrm{cm}^3$ and correspond to low PC1 values.

The differential moisture contents in Fig. 8.5b provide a clearer picture of the actual infiltration and redistribution phase. The progression of the mean infiltration front is clearly visible after DOY 114.5 (the contours just prior to DOY 114.5 between $z = 0$ and 1 m are an artifact of the loess interpolation). The front appears to become more diffuse (wider spaced contours) around DOY 130 when the front reaches the coarse layer at $z = 8\,\mathrm{m}$; by the end of the irrigation period the mean front appears to reach the full depth (12.5 m). Water content differentials reach maximum values of slightly over $0.06\,\mathrm{cm}^3/\mathrm{cm}^3$ at $z = 5\,\mathrm{m}$ and $0.05\,\mathrm{cm}^3/\mathrm{cm}^3$ at $z = 7.5\,\mathrm{m}$. These maximums correlate with finer to coarser transitions with depth (again see PC1 graph on left-hand side) and may be a result of capillary barrier effects. Of note is that these particular maximums persist for a long time during the drainage phase. Other less extreme maximums in moisture content differentials are present at other depths. Slight negative differentials exist near the surface, especially after DOY 200, probably because of evaporation and loss or redistribution of water caused by transfer of heat from the black cover under the Arizona sun.

8.3.6 Moment Analysis

We further interpret the data in Fig. 8.5b with moment analysis (Freyberg 1986). In the following, we will calculate the discrete zeroth, first, and second moments to measure the total amount of water added to the site, the mean depth of the

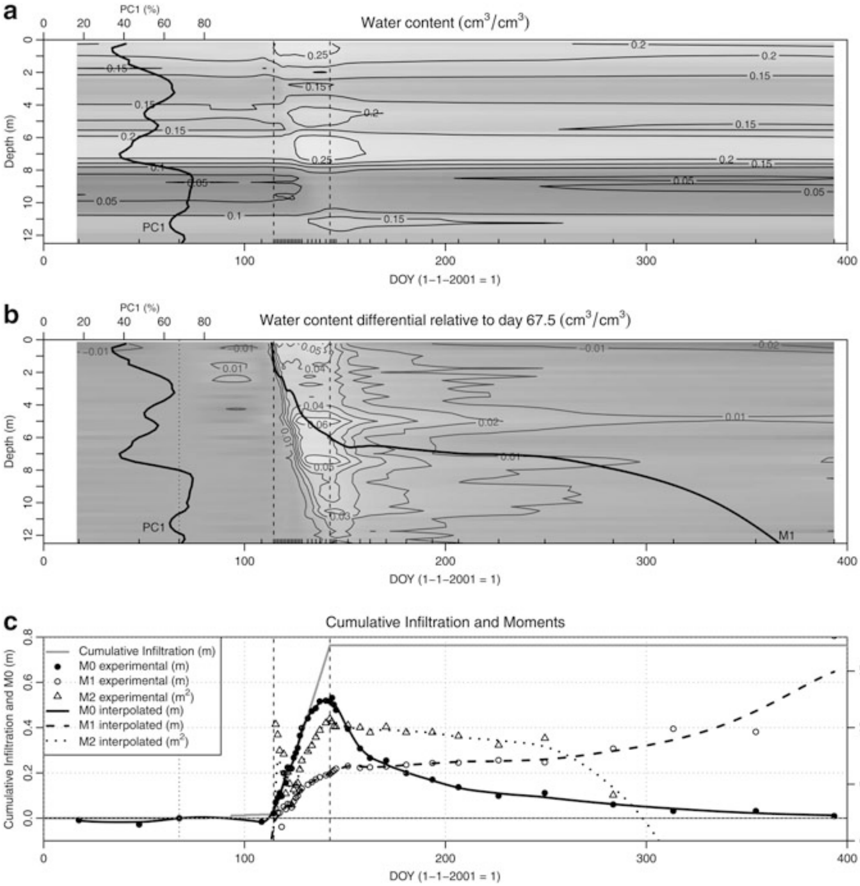

Fig. 8.5 (**a**) Water content versus time. *Contours and gray scale* indicate the volumetric water content in $\mathrm{cm}^3/\mathrm{cm}^3$ estimated with model D_w. *Vertical dashed lines* indicate the start and end of the infiltration period. *Thick line* on the left-hand side indicates the trend for PC1. High water contents are associated with lower values of PC1. (**b**) *Gray scale* and contours provide the change in water content relative to day 67.5 (noon on March 8, 2001). *Thick line* after day 100 indicates the evolution of M1 (depth of the center of mass). *Dotted line* indicates day 67.5 which was used as a reference water content. (**c**) The cumulative infiltration (*gray line*) and the three moments M0, M1, and M2. Symbols indicate the moments calculated using actual observation dates. The lines provide the moments for all days, using the loess interpolator based on the average domain water content differences (**b**). For clarity, the dashed line in c is identical to the *solid line* in b

added water, and the depth variance around the mean depth. The zeroth moment, M0, which gives the total volume increment in meters of water since DOY 67.5 is calculated as

$$\mathrm{M0}(t) = \sum_{z=0.25}^{12.5} \widehat{\theta}_d(t,z)\Delta z \tag{8.3}$$

where Δz is 0.25 m. Without vertical or horizontal drainage losses, M0 should closely track the cumulative amount of irrigation water.

The first moment gives the mean depth of the center of the infiltrated water in meters and is calculated as

$$\mathrm{M1}(t) = \frac{1}{\mathrm{M0}} \sum_{z=0.25}^{12.5} \widehat{\theta_d}(t,z) z \Delta z \tag{8.4}$$

M1 is especially meaningful if M0 is able to close the mass balance, i.e., when no drainage occurs. With drainage, M1 no longer provides the true center of mass of the infiltrating water, but rather the center of mass of the water remaining above 12.5 m. Irrespective of whether drainage occurs, M1 should increase (become deeper) over time, because of the dissipation of gravitational energy.

The second moment provides the variance around the center of mass and is calculated as follows:

$$\mathrm{M2}(t) = \frac{1}{\mathrm{M0}} \sum_{z=0.25}^{12.5} \widehat{\theta_d}(t,z) z^2 \Delta z - \mathrm{M1}^2 \tag{8.5}$$

Again, M2 can only readily be interpreted if M0 tracks the cumulative infiltration and M1 provides the actual center of mass; it should increase over time because of the diffusive-convective nature of the infiltration process. When drainage occurs at $z = 12.5$ m, M2 will decrease because the vertical distribution of θ_d is truncated beyond this depth.

Figure 8.5c shows M0 and cumulative infiltration (left-hand axis) and M1 and M2 (right-hand axis). The symbols denote the moments associated with the observed moisture content differentials (available for 41 observation dates), the lines correspond to the interpolated moisture content differentials, which are available for each day between DOY 17 and DOY 393. M0 tracks the cumulative infiltration well until about DOY 130, after which water is lost from the domain, most likely due to vertical drainage below 12.5 m. The M0 values before the reference date (DOY 67.5) are somewhat lower than 0, probably because these dates (DOY 17 and 47) had several missing wells each. The M0 value at DOY 108 (the last observation before the start of the irrigation) is also lower than zero, which could be due to some residual drainage occurring in the profile. However, some small amounts of irrigation were applied before this date that does not show up in the observations. We therefore treat the data collected at DOY 108 as suspect. The final M0 value at DOY 393.5 (0.01 m) is very close to 0, making it plausible that the drainage process has nearly completed (albeit that some residual moisture lingers at $z = 5$ m and the profile is drying out near the top; cf. Fig. 8.5b). The M0 values based on the interpolation procedure (line) track the observations very well, indicating that the interpolated results could be used for further analysis, for example, if equidistant values in time are needed.

M1 is plotted only for DOY $>$ 105 in Fig. 8.5c to remove some scattered data prior to this date. The symbols and line indicate that the mean center of mass progresses first rapidly to about 4 m around DOY 130 (when the mean front reaches 8m), after which the center of mass slows down to about DOY 144 when it appears to stall until DOY 170. Later the center of mass slowly moves down to greater depths. It is likely that moisture content maxima associated with the fine layers at 5 and 7.5 m limit the internal drainage of water deeper down into the profile. A complicating factor is that after DOY 130 drainage happens below 12.5 m, thus keeping M1 artificially shallow as the drained water is not factored into the calculation for M1. For comparison, M1 is also plotted in vertically inverted form in Fig. 8.5b, showing that M1 restarts its descent after DOY 170 when the maximum moisture differentials at 5 and 7.5 m are partially depleted by internal drainage.

After a noisy start during the first third of the infiltration period, M2 shows an almost linear increase during the remainder of the infiltration period, after which there is a gradual decrease in variance to about DOY 250. This pattern is caused by the spreading of moisture along the entire 12.5 m length of the profile at the end of the infiltration period. Internal drainage and subsequent flow out of the domain [and therefore out of scope for Eq. (8.5)] then cause a reduction in variance. M2 becomes negative after DOY 300 because M1 increases [see second term in Eq. (8.5)].

8.4 Summary and Conclusion

The present study is part of a larger effort to document and interpret the available data for Experiments 1–4 and make these available to the vadose zone research community. As such, the material presented here is only a fraction of the available moisture dynamics data (Experiment 3 only), and most of the analysis here was focused on establishing reliable geostatistical model that accounts for the subsurface structure of particle size and bulk density and an unbiased texture-dependent model for the neutron thermalization measurements. Because the work reported here had access to more data, the results presented here are substantially different than the geospatial analysis published by Wang (2002) and the neutron calibration presented by Yao et al. (2004).

In general, we find shorter horizontal correlation ranges than Wang (2002) who typically found values in between 20 and 25 m for gravel + sand, silt, and clay fractions. After applying principal component analysis to sand, silt, and clay fractions, we found a range of 13.1 m for PC1 and 5.6 m for PC2; Wang (2002) did not find shorter ranges for the clay fraction (which roughly corresponds to PC2). Our vertical variogram ranges were much smaller than those found by Wang (2002) because our analysis is based on a residual variogram (the estimated trend of texture with depth is subtracted from the data before variogram analysis), whereas the analysis of Wang (2002) is not. We believe that the current analysis provides a complimentary subsurface model for texture (essentially a depth trend with an added anisotropic spatially correlated component) upon other analyses can be based.

Even so, we should note that the model is probably more reliable towards the surface, simply because most of the texture and bulk density samples are located there (see Figs. 8.1 and 8.2). Cross-validation analysis showed that PC1 and PC2 can be estimated with an accuracy of 10.66 and 3.35%, respectively. These values roughly correspond to similar errors for the sand and clay fractions, indicating that substantial uncertainty exists in the actual texture at any point throughout the site, even with 1,042 texture samples.

The geospatial model was used to reinterpret the neutron probe calibration carried out by Yao et al. (2004). Instead of stratifying the neutron calibration data and the subsurface by textural class, we used PC1 as a regression variable. After investigating an extensive range of models with and without weighting for the distribution of PC1, we arrived at one model (D_w) which had the lowest root mean square error, produced no negative water contents when applied to neutron count observations, and was able to track the infiltration process more accurately than the other models investigated. Assuming that the (statistical) model D_w represents physical reality, substantial mass balance errors result if other calibration models were chosen. Such errors would propagate through any subsequent analyses and may lead to different conclusions about flow and transport dynamics.

Moment analysis (zeroth, first, and second moments) was used to interpret the infiltration and drainage process. Together with a graphical depiction of the depth-mean moisture content versus time, this analysis shows that several zones exist at the site that control the internal drainage of water. It took approximately 250 days of drainage (after 0.764 m of infiltration) to bring the site back to its initial state.

The analysis reported here will not only be instrumental in interpreting the other infiltration experiments but also greatly assist dynamical modeling of subsurface flow and transport. Important questions currently being addressed are the following: what is the effect of the various sources of uncertainty (geospatial uncertainty, neutron calibration parametric uncertainty) on model outcomes? How much data is truly needed to correctly parameterize the subsurface for flow modeling? Is the infiltration process fundamentally a 1D process (as assumed in Fig. 8.5), or are 2D or 3D approaches needed as found in an earlier study by Wang et al. (2003)? The availability of nine replicated wells (rather than the mean behavior presented here) will allow us to more completely understand the relation between subsurface variability and infiltration dynamics and allow us to make an assessment how well models and observations can represent deep vadose zone flow and transport dynamics.

Interested readers can contact the author for data and analysis code (in *R*, suitable for research and advanced educational use). After completion of the data analysis, the data and models will be made available free of charge on a publicly available website.

Acknowledgments The author thanks Professor S. P. Neuman and Y. Zhang, both at the University of Arizona for valuable discussions. Site construction and field observations were supported by the US Nuclear Regulatory Commission under contract number NRC-04–97–056 (1997–2002). The data collection for and the development of the geospatial model was supported in part by NSF-EAR grant 0737945 (2005–2009). The reanalysis of the neutron calibration data and moment analysis was supported in part through a contract between the University of Arizona and Vanderbilt University under the Consortium for Risk Evaluation with Stakeholder Participation (CRESP) III, funded by the US Department of Energy (2012).

References

Cleveland WS, Grosse E, Shyu WM (1992. Local regression models. In: Chambers JM, Hastie TJ (eds) Statistical models in S, Chap. . Wadsworth & Brooks/Cole, Pacific Grove, CA

Deng H, Ye M, Schaap MG, Khaleel R (2009) Quantification of uncertainty in pedotransfer function-based parameter estimation for unsaturated flow modeling. Water Resour Res 45: W04409, doi:10.1029/2008WR007477

Deutsch CV, Journel AG (1998) GSLIB-geostatistical software library and user's guide. Oxford University Press, New York

DOE (2002) DOE/EIS-0250, Final environmental impact statement for a geologic repository for the disposal of spent nuclear fuel and high-level radioactive waste at Yucca Mountain, Nye County, Nevada

DOE (2010) Long-range deep vadose zone program plan, DOE/RL-2010–89 Rev. 0, Richland Operations Office, Richland, WA 99352

Fang Z (2009) Using geostatistics, pedotransfer functions to generate 3d soil and hydraulic property distributions for deep vadose zone flow simulations. MS thesis The University of Arizona, Tucson

Fleming JB (2001) Applications of the inverse approach for estimating unsaturated hydraulic parameters from laboratory flow experiment. PhD dissertation, The University of Arizona, Tucson, AZ

Freyberg DL (1986) A natural gradient experiment on solute transport in a sand aquifer, 2, Spatial moments and the advection and dispersion of nonreactive tracers. Water Resour Res 22:2031–2046

Gee GW, Ward AL (2001) Vadose zone transport field study: status report, PNNL-13679, Pacific Northwest National Laboratory, Richland, WA

Gee GW, Oostrom M, Freshley MD, Rockhold ML, Zachara JM (2007) Hanford site vadose zone studies: an overview. Vadose Zone J 6(4):899–905

Graham AR (2004) In situ characterization of unsaturated soil hydraulic properties at the Maricopa Environmental Monitoring site. MS thesis The University of Arizona, Tucson

Hignett C, Evett SR (2002) Neutron thermalization. In: Dane JH, Topp GC (eds) Methods of soil analysis: physical methods. Soil Science Society of America, Madison, WI

Ihaka R, Gentleman R (1996) R: a language for data analysis and graphics. J Comput Graph Stat 5(3):299–314

Mattson ED, Magnuson SO, Ansley SL (2004) Interpreting INEEL vadose zone water movement on the basis of large-scale field tests and long-term vadose zone monitoring results. Vadose Zone J 3(1):35–46, doi: 10.2113/?3.1.35

Neuman SP, EA Jacobson (1984) Analysis of nonintrinsic spatial variability by residual kriging with application to regional groundwater levels. Math Geology 16(5):499–521

Pebesma EJ (2004) Multivariable geostatistics in S: the gstat package. Comput. Geosci. 30:683–691

Post DF, Mack C, Camp PD, Suliman AS (1988) Mapping and characterization of the soils on The University of Arizona Maricopa Agricultural Center In: Proceedings of the American Water Resources Association, Hydrology and Water Resources in Arizona and the Southwest, vol 18, pp 49–60

R Development Core Team (2005) R: a language and environment for statistical computing, ISBN: 3–900051–07–0, Vienna, Austria. http://www.R-project.org

Schaap MG, Nemes A, Van Genuchten MTh (2004) Comparison of models for indirect estimation of water retention and available water in surface soils. Vadose Zone J 3:1455–1463

Sisson JB, Lu AH (1984) Field calibration of computer models for application to buried liquid discharges: a status report, RHO-ST-46P, Rockwell Hanford Operations, Richland, WA

Thomasson MJ (2001) Hysteretic, variably saturated, transient flow and transport models with numerical inversion techniques to characterize a field soil in central Arizona. Ph.D dissertation The University of Arizona, Tucson

Thomasson MJ, PJ Wierenga (2003) Spatial variability of the effective retardation factor in an unsaturated field soil. J hydrol 272(1–4):213–225

Wang W (2002) Uncertainty analysis of ground water flow and in unsaturated-saturated porous medium: Maricopa case. Ph.D dissertation The University of Arizona, Tucson

Wang W, Neuman SP, Yao T, Wierenga PJ (2003) Simulation of large-scale field infiltration experiments using a hierarchy of models based on public, generic and site data. Vadose Zone J 2:297–312

Ward AL, Zhang ZF, Gee GW (2006) Upscaling unsaturated hydraulic parameters for flow through heterogeneous, anisotropic sediments Adv Water Resour 29(2):268–280

Wierenga PJ, Toorman AF, Hudson DB, Vinson J, Nash M, Hills RG (1989) Soil physical properties at the Las Cruces Trench Site, U.S. Nucl. Regul. Comm. Rep., NUREG/CR-5441

Wierenga PJ, Hudson DB, Hills RG, Porro I, Vinson J, Kirkland MR (1990) Flow and transport experiments at the Las Cruces Trench Site: Experiments 1 and 2, U.S. Nucl. Regul. Comm. Rep., NUREG/CR-5607

Yao T, Wierenga PJ, Graham AG, Neuman SP (2004) Neutron probe calibration in a vertically stratified vadose zone. Vadose Zone J 3:1400–1406

Ye M, Schaap MG, Khaleel R, Zhu J (2007) Simulation of field injection experiments in a layered formation using geostatistical methods and artificial neural network. Water Resour Res 43:W07413, doi:10.1029/2006WR005030

Young MH, Wierenga PJ, Warrick AW, Hofmann LL, Musil SA, Yao M, Mai CJ, Zou Z, Scanlon BR (1999) Results of field studies at the Maricopa Environmental Monitoring Site, Arizona. Rep. NUREG/CR-5694. US. Nuclear Regulatory Commission, Washington DC

Chapter 9
Unconfined Aquifer Flow Theory: From Dupuit to Present

Phoolendra K. Mishra and Kristopher L. Kuhlman

Abstract Analytic and semi-analytic solution are often used by researchers and practitioners to estimate aquifer parameters from unconfined aquifer pumping tests. The nonlinearities associated with unconfined (i.e., water table) aquifer tests make their analysis more complex than confined tests. Although analytical solutions for unconfined flow began in the mid-1800s with Dupuit, Thiem was possibly the first to use them to estimate aquifer parameters from pumping tests in the early 1900s. In the 1950s, Boulton developed the first transient well test solution specialized to unconfined flow. By the 1970s, Neuman had developed solutions considering both primary transient storage mechanisms (confined storage and delayed yield) without nonphysical fitting parameters. In the last decade, research into developing unconfined aquifer test solutions has mostly focused on explicitly coupling the aquifer with the linearized vadose zone. Despite the many advanced solution methods available, there still exists a need for realism to accurately simulate real-world aquifer tests.

9.1 Introduction

Pumping tests are widely used to obtain estimates of hydraulic parameters characterizing flow and transport processes in subsurface (e.g., Kruseman and de Ridder 1990; Batu 1998). Hydraulic parameter estimates are often used in planning or engineering applications to predict flow and design of aquifer extraction or

---

P.K. Mishra (✉)
Civil & Environmental Engineering California State University, Fullerton, CA 92831, USA
e-mail: pkmishra@fullerton.edu

K.L. Kuhlman
Repository Performance Department Sandia National Laboratories, 4100 National Parks Highway, Carlsbad, NM 88220, USA
e-mail: klkuhlm@sandia.gov

P.K. Mishra and K.L. Kuhlman (eds.), *Advances in Hydrogeology*,
DOI 10.1007/978-1-4614-6479-2_9,

© Springer Science+Business Media New York 2013

recharge systems. During a typical pumping test in a horizontally extensive aquifer, a well is pumped at constant volumetric flow rate, and head observations are made through time at one or more locations. Pumping test data are presented as time-drawdown or distance-drawdown curves, which are fitted to idealized models to estimate aquifer hydraulic properties. For unconfined aquifers, properties of interest include hydraulic conductivity, specific storage, specific yield, and possibly unsaturated flow parameters. When estimating aquifer properties using pumping test drawdown data, one can use a variety of analytical solutions involving different conceptualizations and simplifying assumptions. Analytical solutions are impacted by their simplifying assumptions, which limit their applicability to characterize certain types of unconfined aquifers. This chapter presents the historical evolution of the scientific and engineering thoughts concerning groundwater flow toward a pumping well in unconfined aquifers (also referred to variously as gravity, phreatic, or water table aquifers) from the steady-state solutions of Dupuit to the recent coupled transient saturated–unsaturated solutions. Although it is sometimes necessary to simulation using gridded numerical models in highly irregular or heterogeneous systems, here we limit our consideration to analytically derived solutions.

9.2 Early Well Test Solutions

9.2.1 Dupuit's Steady-State Finite-Domain Solutions

Dupuit (1857) considered steady-state radial flow to a well pumping at constant volumetric flow rate Q [L^3/T] in a horizontal homogeneous confined aquifer of thickness b [L]. He used Darcy's law (Darcy 1856) to express the velocity of groundwater flow u [L/T] in terms of radial hydraulic head gradient $(\partial h/\partial r)$ as

$$u = K\frac{\partial h}{\partial r}, \tag{9.1}$$

where $K = kg/\nu$ is hydraulic conductivity [L/T], k is formation permeability [L^2], g is the gravitational constant [L/T^2], ν is fluid kinematic viscosity [L^2/T], $h = \psi + z$ is hydraulic head [L], ψ is gage pressure head [L], and z is elevation above an arbitrary datum [L]. Darcy derived a form equivalent to (9.1) for one-dimensional flow through sand-packed pipes. Dupuit was the first to apply (9.1) converging flow by combining it with mass conservation $Q = (2\pi rb)u$ across a cylindrical shell concentric with the well, leading to

$$Q = K\left(2\pi rb\right)\frac{\partial h}{\partial r}. \tag{9.2}$$

Integrating (9.2) between two radial distances r_1 and r_2 from the pumping well, Dupuit evaluated the confined steady-state head difference between the two points as

$$h(r_2) - h(r_1) = \frac{Q}{2\pi Kb} \log\left(\frac{r_2}{r_1}\right). \tag{9.3}$$

This is the solution for flow to a well at the center of a circular island, where a constant head condition is applied at the edge of the island (r_2).

Dupuit (1857) also derived a radial flow solution for unconfined aquifers by neglecting the vertical flow component. Following a similar approach to confined aquifers, Dupuit (1857) estimated the steady-state head difference between two distances from the pumping well for unconfined aquifers as

$$h^2(r_2) - h^2(r_1) = \frac{Q}{\pi K} \log\left(\frac{r_2}{r_1}\right). \tag{9.4}$$

These two solutions are only strictly valid for finite domains; when applied to domains without a physical boundary at r_2, the outer radius essentially becomes a fitting parameter. The solutions are also used in radially infinite systems under pseudo-static conditions, when the shape of the water table does not change with time.

Equations (9.3) and (9.4) are equivalent when b in (9.3) is average head $(h(r_1) + h(r_2))/2$. In developing (9.4), Dupuit (1857) used the following assumptions (now commonly called the Dupuit assumptions) in context of unconfined aquifers:

- The aquifer bottom is a horizontal plane.
- Groundwater flow toward the pumping wells is horizontal with no vertical hydraulic gradient component.
- The horizontal component of the hydraulic gradient is constant with depth and equal to the water table slope.
- There is no seepage face at the borehole.

These assumptions are one of the main approaches to simplifying the unconfined flow problem and making it analytically tractable. In the unconfined flow problem, both the head and the location of the water table are unknowns; the Dupuit assumptions eliminate one of the unknowns.

9.2.2 Historical Developments After Dupuit

Narasimhan (1998) and de Vries (2007) give detailed historical accounts of groundwater hydrology and soil mechanics; only history relevant to well test analysis is given here. Forchheimer (1886) first recognized the Laplace equation $\nabla^2 h = 0$ governed two-dimensional steady confined groundwater flow (to which (9.3) is a solution), allowing analogies to be drawn between groundwater flow and steady-state heat conduction, including the first application of conformal mapping to solve a groundwater flow problem. Slichter (1898) also arrived at the Laplace equation for groundwater flow and was the first to account for a vertical flow component. Utilizing Dupuit's assumptions, Forchheimer (1898) developed the steady-state unconfined differential equation (to which (9.4) is a solution), $\nabla^2 h^2 = 0$. Boussinesq (1904) first gave the transient version of the confined groundwater flow equation $\alpha_s \nabla^2 h = \partial h / \partial t$ (where $\alpha_s = K/S_s$ is hydraulic diffusivity [L^2/T] and S_s is specific storage [1/L]), based upon analogy with transient heat conduction.

In Prague, Thiem (1906) was possibly the first to use (9.3) for estimating K from pumping tests with multiple observation wells (Simmons 2008). Equation (9.3) (commonly called the Thiem equation) was tested in the 1930s both in the field (Wenzel (1932) performed a 48-h pumping test with 80 observation wells in Grand Island, Nebraska) and in the laboratory (Wyckoff et al. (1932) developed a 15-degree unconfined wedge sand tank to simulate converging flow). Both found the steady-state solution lacking in ability to consistently estimate aquifer parameters. Wenzel (1942) developed several complex averaging approaches (e.g., the "limiting" and "gradient" formulas) to attempt to consistently estimate K using steady-state confined equations for a finite system from transient unconfined data. Muskat (1932) considered partial-penetration effects in steady-state flow to wells, discussing the nature of errors associated with assumption of uniform flux across the well screen in a partially penetrating well. Muskat's textbook on porous media flow (Muskat 1937) summarized much of what was known in hydrology and petroleum reservoir engineering around the time of the next major advance in well test solutions by Theis.

9.2.3 Confined Transient Flow

Theis (1935) utilized the analogy between transient groundwater flow and heat conduction to develop an analytical solution for confined transient flow to a pumping well (see Fig. 9.1). He initially applied his solution to unconfined flow, assuming instantaneous drainage due to water table movement. The analytical solution was based on a Green's function heat conduction solution in an infinite axisymmetric slab due to an instantaneous line heat source or sink (Carslaw 1921). With the aid of mathematician Clarence Lubin, Theis extended the heat conduction solution to a continuous source, motivated to better explain the results of pumping tests like the 1931 test in Grand Island. Theis (1935) gave an expression for drawdown due to pumping a well at rate Q in a homogeneous, isotropic confined aquifer of infinite radial extent as an exponential integral

$$s(r,t) = \frac{Q}{4\pi T} \int_{r^2/(4\alpha_s t)}^{\infty} \frac{\mathrm{e}^{-u}}{u} \, \mathrm{d}u, \tag{9.5}$$

Fig. 9.1 Unconfined well test diagram

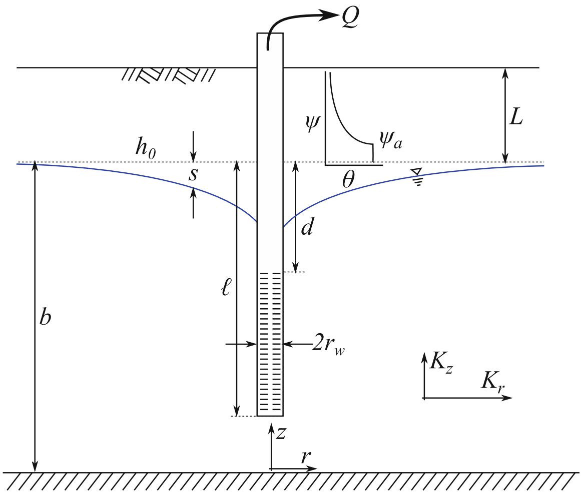

where $s = h_0(r) - h(t,r)$ is drawdown, h_0 is pretest hydraulic head, $T = Kb$ is transmissivity, and $S = S_s b$ is storativity. Equation (9.5) is a solution to the diffusion equation, with zero-drawdown initial and far-field conditions:

$$s(r,t=0) = s(r \to \infty, t) = 0. \tag{9.6}$$

The pumping well was approximated by a line sink (zero radius), and the source term assigned there was based upon (9.2):

$$\lim_{r \to 0} r \frac{\partial s}{\partial r} = -\frac{Q}{2\pi T}. \tag{9.7}$$

Although the transient governing equation was known through analogy with heat conduction, the transient storage mechanism (analogous to specific heat capacity) was not completely understood. Unconfined aquifer tests were known to experience slower drawdown than confined tests, due to water supplied by dewatering the zone near the water table, which is related to the formation specific yield (porosity less residual water). Muskat (1934) and Hurst (1934) derived solutions to confined transient radial flow problems for finite domains but attributed transient storage solely to fluid compressibility. Jacob (1940) derived the diffusion equation for groundwater flow in compressible elastic confined aquifers, using mass conservation and Darcy's law, without recourse to analogy with heat conduction. Terzaghi (1923) developed a one-dimensional consolidation theory which only considered the compressibility of the soil (in his case a clay), unknown at the time to most hydrologists (Batu 1998). Meinzer (1928) studied regional drawdown in North Dakota, proposing the modern storage mechanism related to both aquifer compaction and the compressibility of water. Jacob (1940) formally showed $S_s = \rho_w g(\beta_p + n\beta_w)$, where ρ_w and β_w are fluid density [M/L^3] and compressibility [LT^2/M], n is dimensionless porosity, and

β_p is formation bulk compressibility. The axisymmetric diffusion equation in radial coordinates is

$$\frac{\partial^2 s}{\partial r^2} + \frac{1}{r}\frac{\partial s}{\partial r} = \frac{1}{\alpha_s}\frac{\partial s}{\partial t}. \tag{9.8}$$

When deriving analytical expressions, the governing equation is commonly made dimensionless to simplify presentation of results. For flow to a pumping well, it is convenient to use $L_\mathrm{C} = b$ as a characteristic length, $T_\mathrm{C} = Sb^2/T$ as a characteristic time, and $H_\mathrm{C} = Q/(4\pi T)$ as a characteristic head. The dimensionless diffusion equation is

$$\frac{\partial^2 s_\mathrm{D}}{\partial r_\mathrm{D}^2} + \frac{1}{r_\mathrm{D}}\frac{\partial s_\mathrm{D}}{\partial r_\mathrm{D}} = \frac{\partial s_\mathrm{D}}{\partial t_\mathrm{D}}, \tag{9.9}$$

where $r_\mathrm{D} = r/L_\mathrm{C}$, $s_\mathrm{D} = s/H_c$ and $t_\mathrm{D} = t/T_\mathrm{C}$ are scaled by characteristic quantities.

The Theis (1935) solution was developed for field application to estimate aquifer hydraulic properties, but it saw limited use because at the time it was difficult to compute the exponential integral for arbitrary inputs. Wenzel (1942) proposed a type-curve method that enabled graphical application of the Theis (1935) solution to field data. Cooper and Jacob (1946) suggested for large values of t_D ($t_\mathrm{D} \geq 25$), the infinite integral in the Theis (1935) solution can be approximated as

$$s_\mathrm{D}(t_\mathrm{D}, r_\mathrm{D}) = \int_{r^2/(4\alpha_s t)}^{\infty} \frac{\mathrm{e}^{-u}}{u}\,\mathrm{d}u \approx \log_e\left(\frac{4Tt}{r^2 S}\right) - \gamma \tag{9.10}$$

where $\gamma \approx 0.57722$ is the Euler–Mascheroni constant. This leads to Jacob and Cooper's straight-line simplification

$$\Delta s \approx 2.3\frac{Q}{4\pi T} \tag{9.11}$$

where Δs is the drawdown over one log-cycle (base 10) of time. The intercept of the straight-line approximation is related to S through (9.10). This approximation made estimating hydraulic parameters much simpler at large t_D. Hantush (1961) later extended Theis' confined solution for partially penetrating wells.

9.2.4 Observed Time-Drawdown Curve

Before the time-dependent solution of Theis (1935), distance drawdown was the diagnostic plot for aquifer test data. Detailed distance-drawdown plots require many observation locations (e.g., the 80 observation wells of Wenzel 1936). Reanalyzing results of the unconfined pumping test in Grand Island, Wenzel (1942) noticed that the Theis (1935) solution gave inconsistent estimates of S_s and K, attributed to the delay in the yield of water from storage as the water table fell. The Theis (1935)

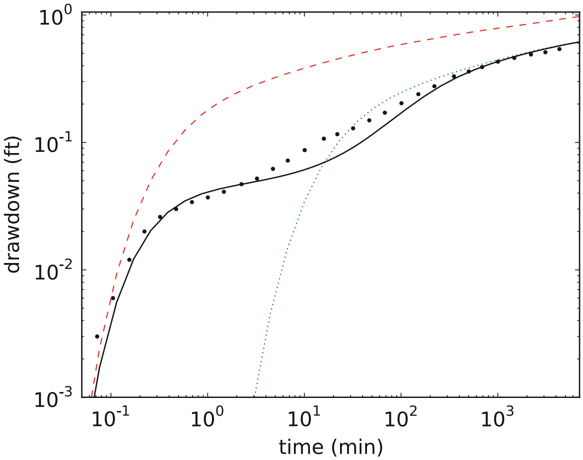

Fig. 9.2 Drawdown data from Cape Cod (Moench et al. 2001), observation well F377–037. *Upper dashed curve* is confined model of Hantush (1961) with $S = S_s b$, *lower dotted curve* is same with $S = S_s b + S_y$. *Solid curve* is unconfined model of Neuman (1974) using $S_y = 0.23$

solution corresponds to the Dupuit assumptions for unconfined flow and can only recreate the a portion of observed unconfined time-drawdown profiles (either late or early). The effect of the water table must be taken into account through a boundary condition or source term in the governing equation to reproduce observed behavior in unconfined pumping tests.

Walton (1960) recognized three distinct segments characterizing different release mechanisms on time-drawdown curve under water table conditions (see Fig. 9.2). A log–log time-drawdown plot in an unconfined aquifer has a characteristic shape consisting of a steep early-time segment, a flatter intermediate segment, and a steeper late-time segment. The early segment behaves like the Theis (1935) solution with $S = S_s b$ (water release due to bulk medium relaxation), the late segment behaves like the Theis (1935) solution with $S = S_s b + S_y$ (Gambolati 1976) (water release due to water table drop), and the intermediate segment represents a transition between the two. Distance-drawdown plots from unconfined aquifer tests do not show a similar inflection or change in slope and do not produce good estimates of storage parameters.

9.3 Early Unconfined Well Test Solutions

9.3.1 Moving Water Table Solutions Without Confine Storage

The Theis (1935) solution for confined aquifers can only reproduce either the early or late segments of the unconfined time-drawdown curve (see Fig. 9.2). Boulton (1954a) suggested it is theoretically unsound to use the Theis (1935) solution for unconfined flow because it does not account for vertical flow to the pumping well.

He proposed a new mechanism for flow toward a fully penetrating pumping well under unconfined conditions. His formulation assumed flow is governed by $\nabla^2 s = 0$, with transient effects incorporated through the water table boundary condition. He treated the water table (where $\psi = 0$, located at $z = \xi$ above the base of the aquifer) as a moving material boundary subject to the condition $h(r, z = \xi, t) = z$. He considered the water table without recharge to be comprised of a constant set of particles, leading to the kinematic boundary condition

$$\frac{\mathrm{D}}{\mathrm{D}t}(h - z) = 0 \tag{9.12}$$

which is a statement of conservation of mass for an incompressible fluid. Boulton (1954a) considered the Darcy velocity of the water table as $u_z = -\frac{K_z}{S_y}\frac{\partial h}{\partial z}$ and $u_r = -\frac{K_r}{S_y}\frac{\partial h}{\partial r}$ and expressed the total derivative as

$$\frac{\mathrm{D}}{\mathrm{D}t} = \frac{\partial}{\partial t} - \frac{K_r}{S_y}\frac{\partial h}{\partial r}\frac{\partial}{\partial r} - \frac{K_z}{S_y}\frac{\partial h}{\partial z}\frac{\partial}{\partial z}, \tag{9.13}$$

where K_r and K_z are radial and vertical hydraulic conductivity components. Using (9.13), the kinematic boundary condition (9.12) in terms of drawdown is

$$\frac{\partial s}{\partial t} - \frac{K_r}{S_y}\left(\frac{\partial s}{\partial r}\right)^2 - \frac{K_z}{S_y}\left(\frac{\partial s}{\partial z}\right)^2 = -\frac{K_z}{S_y}\frac{\partial s}{\partial z}. \tag{9.14}$$

Boulton (1954a) utilized the wellbore and far-field boundary conditions of Theis (1935). He also considered the aquifer rests on an impermeable flat horizontal boundary $\partial h/\partial z|_{z=0} = 0$; this was also inferred by Theis (1935) because of his two-dimensional radial flow assumption. Dagan (1967) extended Boulton's water table solution to the partially penetrating case by replacing the wellbore boundary condition with

$$\lim_{r\to 0} r\frac{\partial s}{\partial r} = \begin{cases} \frac{Q}{2\pi K(\ell - d)} & b - \ell < z < b - d \\ 0 & \text{otherwise} \end{cases}, \tag{9.15}$$

where ℓ and d are the upper and lower boundaries of the pumping well screen, as measured from the initial top of the aquifer (Fig. 9.1).

The two sources of nonlinearity in the unconfined problem are the following: (1) the boundary condition is applied at the water table, the location of which is unknown a priori, and (2) the boundary condition applied on the water table includes s^2 terms.

In order to solve this nonlinear problem, both Boulton and Dagan linearized it by disregarding second-order components in the free-surface boundary condition (9.14) and forcing the free surface to stay at its initial position, yielding

$$\frac{\partial s}{\partial t} = -\frac{K_z}{S_y}\frac{\partial s}{\partial z} \qquad z = h_0, \tag{9.16}$$

which now has no horizontal flux component after neglecting second-order terms. Equation (9.16) can be written in nondimensional form as

$$\frac{\partial s_{\mathrm{D}}}{\partial t_{\mathrm{D}}} = -K_{\mathrm{D}}\sigma^{*}\frac{\partial s_{\mathrm{D}}}{\partial z_{\mathrm{D}}} \qquad z_{\mathrm{D}} = 1, \tag{9.17}$$

where $K_{\mathrm{D}} = K_z/K_r$ is the dimensionless anisotropy ratio and $\sigma^{*} = S/S_y$ is the dimensionless storage ratio.

Both Boulton (1954a) and Dagan (1967) solutions reproduce the intermediate and late segments of the typical unconfined time-drawdown curve, but neither of them reproduces the early segment of the curve. Both are solutions to the Laplace equation and therefore disregard confined aquifer storage, causing pressure pulses to propagate instantaneously through the saturated zone. Both solutions exhibit an instantaneous step-like increase in drawdown when pumping starts.

9.3.2 Delayed Yield Unconfined Response

Boulton (1954b) extended Theis' transient confined theory to include the effect of delayed yield due to movement of the water table in unconfined aquifers. Boulton's proposed solutions (1954b; 1963) reproduce all three segments of the unconfined time-drawdown curve. In his formulation of delayed yield, he assumed as the water table falls, water is released from storage (through drainage) gradually, rather than instantaneously as in the free-surface solutions of Boulton (1954a) and Dagan (1967). This approach yielded an integrodifferential flow equation in terms of vertically averaged drawdown s^{*} as

$$\frac{\partial^2 s^{*}}{\partial r^2} + \frac{1}{r}\frac{\partial s^{*}}{\partial r} = \left[\frac{S}{T}\frac{\partial s^{*}}{\partial t}\right] + \left\{\alpha S_y \int_0^t \frac{\partial s^{*}}{\partial \tau}\mathrm{e}^{-\alpha(t-\tau)}\,\mathrm{d}\tau\right\} \tag{9.18}$$

which Boulton linearized by treating T as constant. The term in square brackets is instantaneous confined storage, and the term in braces is a convolution integral representing storage released gradually since pumping began, due to water table decline. Boulton (1963) showed the time when delayed yield effects become negligible is approximately equal to $\frac{1}{\alpha}$, leading to the term "delay index." Prickett (1965) used this concept, and through analysis of large amount of field drawdown data with Boulton (1963) solution, he established an empirical relationship between the delay index and physical aquifer properties. Prickett proposed a methodology for estimation of S, S_y, K, and α of unconfined aquifers by analyzing pumping tests with the Boulton (1963) solution.

Although Boulton's model was able to reproduce all three segment of the unconfined time-drawdown curve, it failed to explain the physical mechanism of the delayed yield process because of the nonphysical nature of the "delay index" in the Boulton (1963) solution.

Streltsova (1972a) developed an approximate solution for the decline of the water table and s^* in fully penetrating pumping and observation wells. Like Boulton (1954b), she treated the water table as a sharp material boundary, writing the two-dimensional depth-averaged flow equation as

$$\frac{\partial^2 s^*}{\partial r^2} + \frac{1}{r}\frac{\partial s^*}{\partial r} = \frac{S}{T}\left(\frac{\partial s^*}{\partial t} - \frac{\partial \xi}{\partial t}\right). \tag{9.19}$$

The rate of water table decline was assumed to be linearly proportional to the difference between the water table elevation ξ and the vertically averaged head $b - s^*$,

$$\frac{\partial \xi}{\partial t} = \frac{K_z}{S_y b_z}\left(s^* - b + \xi\right) \tag{9.20}$$

where $b_z = b/3$ is an effective aquifer thickness over which water table recharge is distributed into the deep aquifer. Equation (9.20) can be viewed as an approximation to the zero-order linearized free-surface boundary condition (9.16) of Boulton (1954a) and Dagan (1967). Streltsova considered the initial condition $\xi(r, t = 0) = b$ and used the same boundary condition at the pumping well and the outer boundary $(r \to \infty)$ used by Theis (1935) and Boulton (1963). Equation (9.19) has the solution (Streltsova 1972b)

$$\frac{\partial \xi}{\partial t} = -\alpha_T \int_0^t \mathrm{e}^{-\alpha_T (t-\tau)} \frac{\partial s^*}{\partial \tau}\, \mathrm{d}\tau \tag{9.21}$$

where $\alpha_T = K_z/(S_y b_z)$. Substituting (9.21) into (9.20) produces solution (9.18) of Boulton (1954b, 1963); the two solutions are equivalent. Boulton's delayed yield theory (like that of Streltsova) does not account for flow in unsaturated zone but instead treats water table as material boundary moving vertically downward under influence of gravity. Streltsova (1973) used field data collected by Meyer (1962) to demonstrate unsaturated flow had virtually no impact on the observed delayed process. Although Streltsova's solution related Boulton's delay index to physical aquifer properties, it was later found to be a function of r (Neuman 1975; Herrera et al. 1978). The delayed yield solutions of Boulton and Streltsova do not account for vertical flow within the unconfined aquifer through simplifying assumptions; they cannot be extended to account for partially penetrating pumping and observation wells.

Prickett's pumping test in the vicinity of Lawrenceville, Illinois (Prickett 1965), showed that specific storage in unconfined aquifers can be much greater than typically observed values in confined aquifers—possibly due to entrapped air bubbles or poorly consolidated shallow sediments. It is clear the elastic properties of unconfined aquifers are too important to be disregarded.

9.3.3 Delayed Water Table Unconfined Response

Boulton's (1954b; 1963) models encountered conceptual difficulty explaining the physical mechanism of water release from storage in unconfined aquifers. Neuman (1972) presented a physically based mathematical model that treated the unconfined aquifer as compressible (like Boulton 1954b, 1963 and Streltsova 1972a,b) and the water table as a moving material boundary (like Boulton 1954a and Dagan 1967). In Neuman's approach, aquifer delayed response was caused by physical water table movement, and he therefore proposed to replace the phrase "delayed yield" by "delayed water table response."

Neuman (1972) replaced the Laplace equation of Boulton (1954a) and Dagan (1967) by the diffusion equation; in dimensionless form, it is

$$\frac{\partial^2 s_{\mathrm{D}}}{\partial r_{\mathrm{D}}^2} + \frac{1}{r_{\mathrm{D}}}\frac{\partial s_{\mathrm{D}}}{\partial r_{\mathrm{D}}} + K_{\mathrm{D}}\frac{\partial^2 s_{\mathrm{D}}}{\partial z_{\mathrm{D}}^2} = \frac{\partial s_{\mathrm{D}}}{\partial t_{\mathrm{D}}}. \tag{9.22}$$

Like Boulton (1954a) and Dagan (1967), Neuman treated the water table as a moving material boundary, linearized it (using (9.17)), and treated the anisotropic aquifer as three-dimensional axisymmetric. Like Dagan (1967), Neuman (1974) accounted for partial penetration. By including confined storage in the governing equation (9.22), Neuman was able to reproduce all three parts of the observed unconfined time-drawdown curve and produce parameter estimates (including the ability to estimate K_z) very similar to the delayed yield models.

Compared to the delay index models, Neuman's solution produced similar fits to data (often underestimating S_y, though), but Neuman (1975, 1979) questioned the physical nature of Boulton's delay index. He performed a regression fit between the Boulton (1954b) and Neuman (1972) solutions, resulting in the relationship

$$\alpha = \frac{K_z}{S_y b}\left[3.063 - 0.567\log\left(\frac{K_{\mathrm{D}} r^2}{b^2}\right)\right] \tag{9.23}$$

demonstrating α decreases linearly with $\log r$ and is therefore not a characteristic aquifer constant. When ignoring the logarithmic term in (9.23), the relationship $\alpha = 3K_z/(S_y b)$ proposed by Streltsova (1972a) is approximately recovered.

After comparative analysis of various methods for determination of specific yield, Neuman (1987) concluded the water table response to pumping is a much faster phenomenon than drainage in the unsaturated zone above it.

Malama (2011) recently proposed an alternative linearization of (9.14), approximately including the effects of the neglected second-order terms, leading to the alternative water table boundary condition of

$$S_y\frac{\partial s}{\partial t} = -K_z\left(\frac{\partial s}{\partial z} + \beta\frac{\partial^2 s}{\partial z^2}\right) \qquad z = h_0 \tag{9.24}$$

where β is a linearization coefficient [L]. The parameter β provides additional adjustment of the shape of the intermediate portion of the time-drawdown curve (beyond adjustments possible with K_D and σ^* alone), leading to improved estimates of S_y. When $\beta = 0$, (9.24) simplifies to (9.16).

9.3.4 Hybrid Water Table Boundary Condition

The solution of Neuman (1972, 1974) was accepted by many hydrologists "as the preferred model ostensibly because it appears to make the fewest simplifying assumptions" (Moench et al. 2001). Despite acceptance, Nwankwor et al. (1984) and Moench (1995) pointed out that significant difference might exist between measured and model-predicted drawdowns, especially at locations near the water table, leading to significantly underestimated S_y using Neuman's models (e.g., see Fig. 9.2). Moench (1995) attributed the inability of Neuman's models to give reasonable estimates of S_y and capture this observed behavior near the water table due to the later's disregard of "gradual drainage." In an attempt to resolve this problem, Moench (1995) replaced the instantaneous moving water table boundary condition used by Neuman with one containing a Boulton (1954b) delayed yield convolution integral:

$$\int_0^t \frac{\partial s}{\partial \tau} \sum_{m=1}^{M} \alpha_m \mathrm{e}^{-\alpha_m (t-\tau)}\, \mathrm{d}\tau = -\frac{K_z}{S_y}\frac{\partial s}{\partial z} \tag{9.25}$$

This hybrid boundary condition ($M = 1$ in Moench (1995)) included the convolution source term Boulton (1954b, 1963) and Streltsova (1972a,b) used in their depth-averaged governing flow equations. In addition to this new boundary condition, Moench (1995) included a finite radius pumping well with wellbore storage, conceptually similar to how Papadopulos and Cooper Jr. (1967) modified the solution of Theis (1935). In all other respects, his definition of the problem was similar to Neuman (1974).

Moench's solution resulted in improved fits to experimental data and produced more realistic estimates of specific yield (Moench et al. 2001), including the use of multiple delay parameters α_m (Moench 2003). Moench et al. (2001) used (9.25) with $M = 3$ to estimate hydraulic parameters in the unconfined aquifer at Cape Cod. They showed that $M = 3$ enabled a better fit to the observed drawdown data than obtained by $M < 3$ or the model of Neuman (1974). Similar to the parameter α in Boulton's model, the physical meaning of α_m is not clear.

9.4 Unconfined Solutions Considering Unsaturated Flow

As an alternative to linearizing the water table condition of Boulton (1954a), the unsaturated zone can be explicitly included. The nonlinearity of unsaturated flow is substituted for the nonlinearity of (9.14). By considering the vadose zone, the water table is internal to the domain, rather than a boundary condition. The model-data misfit in Fig. 9.2 at "late intermediate" time is one of the motivations for considering the mechanisms of delayed yield and the effects of the unsaturated zone.

9.4.1 Unsaturated Flow Without Confined Aquifer Storage

Kroszynski and Dagan (1975) were the first to account analytically for the effect of the unsaturated zone on aquifer drawdown. They extended the solution of Dagan (1967) by accounting for unsaturated flow above the water table. They used Richards' equation for axisymmetric unsaturated flow in a vadose zone of thickness L

$$K_r \frac{1}{r}\frac{\partial}{\partial r}\left(k(\psi) r \frac{\partial \sigma}{\partial r}\right) + K_z \frac{\partial}{\partial z}\left(k(\psi)\frac{\partial \sigma}{\partial z}\right) = C(\psi)\frac{\partial \sigma}{\partial t} \qquad \xi < z < b + L \quad (9.26)$$

where $\sigma = b + \psi_a - h$ is unsaturated zone drawdown [L], ψ_a is air-entry pressure head [L], $0 \leq k(\psi) \leq 1$ is dimensionless relative hydraulic conductivity, $C(\psi) = \mathrm{d}\theta/\mathrm{d}\psi$ is the moisture retention curve [1/L], and θ is dimensionless volumetric water content (see inset in Fig. 9.1). They assumed flow in the underlying saturated zone was governed by the Laplace equation (like Dagan (1967)). The saturated and unsaturated flow equations were coupled through interface conditions at the water table expressing continuity of hydraulic heads and normal groundwater fluxes,

$$s = \sigma \qquad \nabla s \cdot \mathbf{n} = \nabla \sigma \cdot \mathbf{n} \qquad z = \xi \quad (9.27)$$

where $\mathbf{n}$ is the unit vector perpendicular to the water table.

To solve the unsaturated flow equation (9.26), Kroszynski and Dagan (1975) linearized (9.26) by adopting the Gardner (1958) exponential model for the relative hydraulic conductivity, $k(\psi) = \mathrm{e}^{\kappa_a(\psi - \psi_a)}$, where κ_a is the sorptive number [1/L] (related to pore size). They adopted the same exponential form for the moisture capacity model, $\theta(\psi) = \mathrm{e}^{\kappa_k(\psi - \psi_k)}$, where ψ_k is the pressure at which $k(\psi) = 1$, $\kappa_a = \kappa_k$, and $\psi_a = \psi_k$, leading to the simplified form $C(\psi) = S_y \kappa_a \mathrm{e}^{\kappa_a(\psi - \psi_a)}$. In the limit as $\kappa_k = \kappa_a \to \infty$, their solution reduces to that of Dagan (1967). The relationship between pressure head and water content is a step function. Kroszynski and Dagan (1975) took unsaturated flow above the water table into account but ignored the effects of confined aquifer storage, leading to early-time step-change behavior similar to Boulton (1954a) and Dagan (1967).

9.4.2 *Increasingly Realistic Saturated–Unsaturated Well Test Models*

Mathias and Butler (2006) combined the confined aquifer flow equation (9.22) with a one-dimensional linearized version of (9.26) for a vadose zone of finite thickness. Their water table was treated as a fixed boundary with known flow conditions, decoupling the unsaturated and saturated solutions at the water table. Although they only considered a one-dimensional unsaturated zone, they included the additional flexibility provided by different exponents $(\kappa_a \neq \kappa_k)$. Mathias and Butler (2006) did not consider a partially penetrating well, but they did note the possibility of accounting for it in principle by incorporating their uncoupled drainage function in the solution of Moench (1997), which considers a partially penetrating well of finite radius.

Tartakovsky and Neuman (2007) similarly combined the confined aquifer flow equation (9.22), but with the original axisymmetric form of (9.26) considered by Kroszynski and Dagan (1975). Also like Kroszynski and Dagan (1975), their unsaturated zone was characterized by a single exponent $\kappa_a = \kappa_k$ and reference pressure head $\psi_a = \psi_k$. Unlike Kroszynski and Dagan (1975) and Mathias and Butler (2006), Tartakovsky and Neuman (2007) assumed an infinitely thick unsaturated zone.

Tartakovsky and Neuman (2007) demonstrated flow in the unsaturated zone is not strictly vertical. Numerical simulations by Moench (2008) showed groundwater movement in the capillary fringe is more horizontal than vertical. Mathias and Butler (2006) and Moench (2008) showed using the same exponents and reference pressure heads for effective saturation and relative permeability decreases model flexibility and underestimates S_y. Moench (2008) predicted an extended form of Tartakovsky and Neuman (2007) with two separate exponents, a finite unsaturated zone, and wellbore storage would likely produce more physically realistic estimates of S_y.

Mishra and Neuman (2010) developed a new generalization of the solution of Tartakovsky and Neuman (2007) that characterized relative hydraulic conductivity and water content using $\kappa_a \neq \kappa_k$, $\psi_a \neq \psi_k$ and a finitely thick unsaturated zone. Mishra and Neuman (2010) validated their solution against numerical simulations of drawdown in a synthetic aquifer with unsaturated properties given by the model of van Genuchten (1980). They also estimated aquifer parameters from Cape Cod drawdown data (Moench et al. 2001), comparing estimated van Genuchten (1980) parameters with laboratory values (Mace et al. 1998).

Mishra and Neuman (2011) further extended their 2010 solution to include a finite-diameter pumping well with storage. Mishra and Neuman (2010, 2011) were the first to estimate non-exponential model unsaturated aquifer properties from pumping test data, by curve-fitting the exponential model to the van Genuchten (1980) model. Analyzing pumping test data of Moench et al. (2001) (Cape Cod, Massachusetts) and Nwankwor et al. (1984, 1992) (Borden, Canada), they estimated unsaturated flow parameters similar to laboratory-estimated values for the same soils.

9.5 Future Challenges

The conceptualization of groundwater flow during unconfined pumping tests has been a challenging task that has spurred substantial theoretical research in the field hydrogeology for decades. Unconfined flow to a well is nonlinear in multiple ways, and the application of analytical solutions has required utilization of advanced mathematical tools. There are still many additional challenges to be addressed related to unconfined aquifer pumping tests, including:

- Hysteretic effects of unsaturated flow. Different exponents and reference pressures are needed during drainage and recharge events, complicating simple superposition needed to handle multiple pumping wells, variable pumping rates, or analysis of recovery data.
- Collecting different data types. Validation of existing models and motivating development of more realistic ones depends on more than just saturated zone head data. Other data types include vadose zone water content (Meyer 1962) and hydrogeophysical data like microgravity (Damiata and Lee 2006) or streaming potentials (Malama et al. 2009).
- Moving water table position. All solutions since Boulton (1954a) assume the water table is fixed horizontal $\xi(r,t) = h_0$ during the entire test, even close to the pumping well where large drawdown is often observed. Iterative numerical solutions can accommodate this, but this has not been included in an analytical solution.
- Physically realistic partial penetration. Well test solutions suffer from the complication related to the unknown distribution of flux across the well screen. Commonly, the flux distribution is simply assumed constant, but it is known that flux will be higher near the ends of the screened interval that are not coincident with the aquifer boundaries.
- Dynamic water table boundary condition. A large increase in complexity comes from explicitly including unsaturated flow in unconfined solutions. The kinematic boundary condition expresses mass conservation due to water table decline. Including an analogous dynamic boundary condition based on a force balance (capillarity vs. gravity) may include sufficient effects of unsaturated flow, without the complexity associated with the complete unsaturated zone solution.
- Heterogeneity. In real-world tests, heterogeneity is present at multiple scales. Large-scale heterogeneity (e.g., faults or rivers) can sometimes be accounted in analytical solutions using the method of images or other types of superposition. A stochastic approach (Neuman et al. 2004) could alternatively be developed to estimate random unconfined aquifer parameter distribution parameters.

Despite advances in considering physically realistic unconfined flow, most real-world unconfined tests (e.g., Wenzel 1942, Nwankwor et al. 1984, 1992, or Moench et al. 2001) exhibit nonclassical behavior that deviates from the early–intermediate–late behavior predicted by the models summarized here. We must continue to strive to include physically relevant processes and representatively linearize nonlinear phenomena, to better understand, simulate, and predict unconfined flow processes.

Acknowledgements This research was partially funded by the Environmental Programs Directorate of the Los Alamos National Laboratory. Los Alamos National Laboratory is a multi-program laboratory managed and operated by Los Alamos National Security (LANS) Inc. for the US Department of Energy's National Nuclear Security Administration under contract DE-AC52-06NA25396.

Sandia National Laboratories is a multi-program laboratory managed and operated by Sandia Corporation, a wholly owned subsidiary of Lockheed Martin Corporation, for the US Department of Energy's National Nuclear Security Administration under contract DE-AC04-94AL85000.

References

Batu V (1998) Aquifer hydraulics: a comprehensive guide to hydrogeologic data analysis. Wiley-Interscience, New York

Boulton NS (1954a) The drawdown of the water-table under non-steady conditions near a pumped well in an unconfined formation. Proc Inst Civ Eng 3(4):564–579

Boulton NS (1954b) Unsteady radial flow to a pumped well allowing for delayed yield from storage. Assemblée Générale de Rome 1954, Publ. no. 37. Int Ass Sci Hydrol 472–477

Boulton NS (1963) Analysis of data from non-equilibrium pumping tests allowing for delayed yield from storage. Proc Inst Civ Eng 26(3):469–482

Boussinesq J (1904) Recherches théoriques sur l'écoulement des nappes d'eau infiltrées dans le sol et sur le débit des sources. J Mathématiques Pures Appliquées 10(5–78):363–394

Carslaw H (1921) Introduction to the mathematical theory of the conduction of heat in solids, 2nd edn., Macmillan and Company

Cooper H, Jacob C (1946) A generalized graphical method for evaluating formation constants and summarizing well field history. Trans Am Geophys Union 27(4):526–534

Dagan G (1967) A method of determining the permeability and effective porosity of unconfined anisotropic aquifers. Water Resour Res 3(4):1059–1071

Damiata BN, Lee TC (2006) Simulated gravitational response to hydraulic testing of unconfined aquifers. J Hydrol 318(1–4):348–359

Darcy H (1856) Les Fontaines Publiques de la ville de Dijon. Dalmont, Paris

Dupuit J (1857) Mouvement de l'eau a travers le terrains permeables. C R Hebd Seances Acad Sci 45:92–96

Forchheimer P (1886) Ueber die Ergiebigkeit von Brunnen-Analgen und Sickerschlitzen. Z Architekt Ing Ver Hannover 32:539–563

Forchheimer P (1898) Grundwasserspiegel bei brunnenanlagen. Z Osterreichhissheingenieur Architecten Ver 44:629–635

Gambolati G (1976) Transient free surface flow to a well: an analysis of theoretical solutions. Water Resour Res 12(1):27–39

Gardner W (1958) Some steady-state solutions of the unsaturated moisture flow equation with application to evaporation from a water table. Soil Sci 85(4):228

van Genuchten M (1980) A closed-form equation for predicting the hydraulic conductivity of unsaturated soils. Soil Sci Soc Am J 44:892–898

Hantush MS (1961) Drawdown around a partially penetrating well. J Hydraul Div Am Soc Civ Eng 87:83–98

Herrera I, Minzoni A, Flores EZ (1978) Theory of flow in unconfined aquifers by integrodifferential equations. Water Resour Res 14(2):291–297

Hurst W (1934) Unsteady flow of fluids in oil reservoirs. Physics 5(1):20–30

Jacob C (1940) On the flow of water in an elastic artesian aquifer. Trans Am Geophys Union 21(2):574–586

Kroszynski U, Dagan G (1975) Well pumping in unconfined aquifers: The influence of the unsaturated zone. Water Resour Res 421(3):479–490

Kruseman G, de Ridder N (1990) Analysis and evaluation of pumping test data, 2nd edn., vol 47, International Institute for Land Reclamation and Improvement, Wageningen, The Netherlands

Mace A, Rudolph D, Kachanoski R (1998) Suitability of parametric models to describe the hydraulic properties of an unsaturated coarse sand and gravel. Ground Water 36(3):465–475

Malama B (2011) Alternative linearization of water table kinematic condition for unconfined aquifer pumping test modeling and its implications for specific yield estimates. J Hydrol 399 (3–4):141–147

Malama B, Kuhlman KL, Revil A (2009) Theory of transient streaming potentials associated with axial-symmetric flow in unconfined aquifers. Geophys J Int 179(2):990–1003

Mathias S, Butler A (2006) Linearized Richards' equation approach to pumping test analysis in compressible aquifers. Water Resour Res 42(6):W06,408

Meinzer OE (1928) Compressibility and elasticity of artesian aquifers. Econ Geol 23:263–291

Meyer W (1962) Use of a neutron moisture probe to determine the storage coefficient of an unconfined aquifer. Professional Paper 174–176, US Geological Survey

Mishra PK, Neuman SP (2010) Improved forward and inverse analyses of saturated-unsaturated flow toward a well in a compressible unconfined aquifer. Water Resour Res 46(7):W07,508

Mishra PK, Neuman SP (2011) Saturated-unsaturated flow to a well with storage in a compressible unconfined aquifer. Water Resour Res 47(5):W05,553

Moench AF (1995) Combining the neuman and boulton models for flow to a well in an unconfined aquifer. Ground Water 33(3):378–384

Moench AF (1997) Flow to a well of finite diameter in a homogeneous, anisotropic water table aquifer. Water Resour Res 33(6):1397–1407

Moench AF (2003) Estimation of hectare-scale soil-moisture characteristics from aquifer-test data. J Hydrol 281(1–2):82–95

Moench AF (2008) Analytical and numerical analyses of an unconfined aquifer test considering unsaturated zone characteristics. Water Resour Res 44(6):W06,409

Moench AF, Garabedian SP, LeBlanc D (2001) Estimation of hydraulic parameters from an unconfined aquifer test conducted in a glacial outwash deposit, Cape Cod, Massachusetts. Professional Paper 1629, US Geological Survey

Muskat M (1932) Potential distributions in large cylindrical disks with partially penetrating electrodes. Physics 2(5):329–364

Muskat M (1934) The flow of compressible fluids through porous media and some problems in heat conduction. Physics 5(3):71–94

Muskat M (1937) The flow of homogeneous fluids through porous media. McGraw-Hill, New York

Narasimhan T (1998) Hydraulic characterization of aquifers, reservoir rocks, and soils: A history of ideas. Water Resour Res 34(1):33–46

Neuman S, Guadagnini A, Riva M (2004) Type-curve estimation of statistical heterogeneity. Water Resour Res 40(4):W04,201

Neuman SP (1972) Theory of flow in unconfined aquifers considering delayed response of the water table. Water Resour Res 8(4):1031–1045

Neuman SP (1974) Effect of partial penetration on flow in unconfined aquifers considering delayed gravity response. Water Resour Res 10(2):303–312

Neuman SP (1975) Analysis of pumping test data from anisotropic unconfined aquifers considering delayed gravity response. Water Resour Res 11(2):329–342

Neuman SP (1979) Perspective on delayed yield. Water Resour Res 15(4)

Neuman SP (1987) On methods of determining specific yield. Ground Water 25(6):679–684

Nwankwor G, Cherry J, Gillham R (1984) A comparative study of specific yield determinations for a shallow sand aquifer. Ground Water 22(6):764–772

Nwankwor G, Gillham R, Kamp G, Akindunni F (1992) Unsaturated and saturated flow in response to pumping of an unconfined aquifer: Field evidence of delayed drainage. Ground Water 30(5):690–700

Papadopulos IS, Cooper Jr HH (1967) Drawdown in a well of large diameter. Water Resour Res 3(1):241–244

Prickett T (1965) Type-curve solution to aquifer tests under water-table conditions. Ground Water 3(3):5–14

Simmons CT (2008) Henry darcy (1803–1858): Immortalized by his scientific legacy. Hydrogeology J 16:1023–1038

Slichter C (1898) 19th Annual Report: Part II - Papers Chiefly of a Theoretic Nature, US Geological Survey, chap Theoretical Investigations of the Motion of Ground Waters, pp 295–384

Streltsova T (1972a) Unconfined aquifer and slow drainage. J Hydrol 16(2):117–134

Streltsova T (1972b) Unsteady radial flow in an unconfined aquifer. Water Resour Res 8(4):1059–1066

Streltsova T (1973) Flow near a pumped well in an unconfined aquifer under nonsteady conditions. Water Resour Res 9(1):227–235

Tartakovsky GD, Neuman SP (2007) Three-dimensional saturated-unsaturated flow with axial symmetry to a partially penetrating well in a compressible unconfined aquifer. Water Resour Res 43(1):W01,410

Terzaghi K (1923) Die berechnung der durchlassigkeitsziffer des tones aus dem verlauf der hydrodynamischen spannungserscheinungen. Sitzungsberichte der Akademie der Wissenschaften in Wien, Mathematisch-Naturwissenschaftliche Klasse, Abteilung IIa 132:125–138

Theis CV (1935) The relation between the lowering of the piezometric surface and the rate and duration of discharge of a well using groundwater storage. Trans Am Geophys Union 16(1):519–524

Thiem G (1906) Hydrologische Methoden. Leipzig, Gebhardt

de Vries JJ (2007) The handbook of groundwater engineering, 2nd edn. CRC Press, Boca Raton. chap History of Groundwater Hydrology

Walton W (1960) Application and limitation of methods used to analyze pumping test data. Water Well Journal 15(2–3):22–56

Wenzel LK (1932) Recent investigations of Thiem's method for determining permeability of water-bearing materials. Trans Am Geophys Union 13(1):313–317

Wenzel LK (1936) The Thiem method for determining permeability of water-bearing materials and its application to the determination of specific yield. Water Supply Paper 679-A, US Geological Survey

Wenzel LK (1942) Methods for determining permeability of water-bearing materials, with special reference to discharging well methods. Water Supply Paper 887, US Geological Survey

Wyckoff R, Botset H, Muskat M (1932) Flow of liquids through porous media under the action of gravity. Physics 3(2):90–113

Index

A
Aquifer properties. *See also* Confined aquifer pumping tests; Unconfined aquifer flow theory
  geologic continuity identification, 86–87
  and leaky layers, 98
  learned sparse geologic dictionaries, 85–86
  preconstructed (generic) sparsifying transforms
    discrete cosine transform, 83
    wavelet transform, 83–85
Archie's law
  electrical current problem, 117
  electrical resistivity log, 115–116
  as empirical law, 116
  governing equation, 117–118
  macroscopic diffusion coefficient, 117
  pure diffusion, 117
  pure diffusion and electrical current problems, 117–118
  tortuosity
    and porosity, 121–125
    porous medium, 116, 117
    quantification, 118–121

C
Cellular automata (CA) models
  definition, 58
  event clusters, 61
  fluid pressure evolution, 59
  key components, 58–59
  plastic deformation/fluid source, 60
  toggle-switch permeability model, 60
Compressed sensing, 92. *See also* Sparse reconstruction
Compressible multiple-phase flow model. *See* Multiphase flow model
Confined aquifer pumping tests, 133–135
Constitutive laws
  Parker et al.'s model
    relative permeability *vs.* saturation, 34
    saturation *vs.* capillary pressure, 32–33
  Tsai and Yeh's model, L-phase fluids, 34
    relative permeability *vs.* saturation, 35–36
    saturation *vs.* capillary pressure, 35

D
Darcy's law, 75, 98, 100, 186, 189
Discrete cosine transform (DCT), 76, 83, 84
Dupuit's approximation, 96, 97

E
Earth and environmental variables
  sub-Gaussian random fields
    apparent multifractality, 19–20
    extended power-law scaling, 7–13
    generation of, 13–18
  truncated fractional Brownian motion, 6–7
Electrokinetic theory and groundwater flow
  electric double layer (EDL), 131, 132
  electric field, 131
  mass continuity equation, 132
  three-layered conceptual model, 133
Extended power-law scaling (ESS) expression
  curves, 11
  linear/near-linear variation, 3
  log-log plot, 8–10, 12
  permeability profile, 9
  power-law scaling, 3

P.K. Mishra and K.L. Kuhlman (eds.), *Advances in Hydrogeology*,
DOI 10.1007/978-1-4614-6479-2,
© Springer Science+Business Media New York 2013

Extended power-law scaling (ESS) expression (*cont.*)
  spatial and/or temporal increments, 4
  Topopah Spring tuff data, 12

F
Finite element methods (FEM)
  Galerkin, 29
  numerical discretizations, 29, 51–55
Fluid pressure redistribution events
  calculations, 62
  CA models (*see* Cellular automata (CA) models)
  cluster size, 66, 67
  complete spatial randomness (CSR), 68
  correlation length, 63
  domain-spanning clusters, 62–65
  parameter estimation, 67
  percolation cluster, 66
  permeability, failure patterns, 69
  spatial correlation, 61–62
  toggle-switch permeability model, 58
Fractional Brownian motion (tfBm). *See* Sub-Gaussian random fields

G
Gaussian random fields. *See* Sub-Gaussian random fields
Geospatial model
  cross-validation errors, 173
  fitted variograms, 172
  hole effect, 170
  lag distance bins, 170
  semi-variograms, 171
  vertical variability, 170
Greedy algorithms (GA), 79
Groundwater model calibration. *See also* Sparse reconstruction
  data limitation, 74
  flow equations and inverse modeling formulation
    capillary pressure, 75
    Darcy's law, 75
    fluid displacement pattern prediction, 74
    objective function, 75
    physical saturation constraint, 75
    regularization, 76
  nonlinear model calibration, sparse reconstruction, 88
  parameterization, 76
  regularization, 77
  sparse model calibration formulation, 87
  sparse reconstruction applications
    groundwater flow model calibration, 90–91
    travel-time tomography, 88–90
  sparsity-promoting
    aquifer properties, 82–85
    geologic continuity identification, 86–87
    learned sparse geologic dictionaries, 85–86

H
Hanford site, 160
Hankel-Laplace transform, 154
Hankel transform, 134, 136, 138, 139

I
Incompressible three-phase flow problems. *See* Multiphase flow model
Infiltration experiment. *See* Semiarid deep vadose zone

L
Laboratory pumping test simulations
  experimental procedure, 143–144
  experimental setup and materials, 142–143
  model application to data, 146–149
  results and observations, 144–146
Laplace transform, 97
  confined aquifer solution, 133
  flow between aquifer layers, 99–100
  inverse, 104
  mathematical model, 98–99
  multilayer wells and line-sinks, 102–103

M
Maricopa project, 160
Mass conservation equation, 29–30
Matching pursuit (MP), 79
Material property correlation impact. *See* Fluid pressure redistribution events
Moisture content temporal patterns, 176–177
Moment analysis, 177–180
Multi-aquifer system, 107–108
Multilayer flow systems. *See* Transient multilayer flow systems
Multiphase flow model
  compressibility, three fluid phases, 32
  constitutive laws
    Parker et al.'s model, 32–34

        - Tsai and Yeh's model, L-phase fluids, 34–36
    - fractional flow-based approach, 28
    - mass conservation equation, 29–30
    - numerical results
        - NAPL infiltration problem, 40–48
        - water infiltration problem, 36–40
    - total pressure equation, 30–31
    - transport equations, 31–32

N

- Neutron probe calibration
    - calibration equation, 173–174
    - multiple linear regression model coefficients, 175
    - neutron calibration data set, 174
    - water contents, 176
- Neutron thermalization, 162–163
- Nonaqueous phase liquid (NAPL) infiltration problem
    - boundary conditions, 40
    - degrees of saturation, 45–48
    - description and relevant parameters, 44
    - saturation phases, 40
    - water distributions, 43

P

- Parameterization, 76
- Parker et al.'s model
    - relative permeability *vs.* saturation, 34
    - saturation *vs.* capillary pressure, 32–33
- Particle size and bulk density, 165
- Power-law scaling, 2–5, 7–13
- Preconstructed compression transforms. *See* Discrete cosine transform (DCT)
- Pursuit algorithms, 79

R

- Regularization, 77

S

- Semiarid deep vadose zone
    - data management and analysis software, 165–166
    - geospatial model
        - bulk density, 173
        - cross-validation errors, 173
        - fitted variograms, 172
        - hole effect, 170
        - lag distance bins, 170
        - semi-variograms, 171
        - vertical variability, 170
    - Hanford site, 160
    - instrumentation
        - measurement, 164
        - neutron thermalization, 162–163
        - tensiometers, 164
    - Maricopa project, 160
    - moisture content temporal patterns, 176–177
    - moment analysis, 177–180
    - neutron probe calibration
        - calibration equation, 173–174
        - multiple linear regression model coefficients, 175
        - neutron calibration data set, 174
        - water contents, 176
    - particle size and bulk density, 165
    - Sisson and Lu infiltration site, 160
    - site description
        - drainage period, 162
        - irrigation, 162
        - location, 161
    - textural distribution, 167–168
    - texture and bulk density, stratigraphic trends
        - correlation coefficients, 169
        - loess function, 169–170
        - scatter, 168–169
- Sisson and Lu infiltration site, 160
- Sparse reconstruction
    - advantage, 80
    - applications
        - groundwater flow model calibration, 90–91
        - travel-time tomography, 88–90
    - commutative distribution function (CDF), 81
    - and compressed sensing, 79–81
    - convex relaxation techniques, 79
    - greedy algorithms, 79
    - matching pursuit, 79
    - nonzero components, 78
    - pursuit algorithms, 79
    - solution sparsity, 77–78
    - underdetermined linear system, 80–81
- Streaming potentials measurement
    - Boise Hydrogeophysical Research Site (BHRS), 130
    - coupled flow and SP, equations, 151–154
    - electrokinetic theory and groundwater flow
        - electric double layer (EDL), 131, 132
        - electric field, 131
        - mass continuity equation, 132
        - three-layered conceptual model, 133
    - geophysics *vs.* hydrology, 128

Streaming potentials measurement (*cont.*)
    and head data, 129
    laboratory pumping test simulations
        experimental procedure, 143–144
        experimental setup and materials, 142–143
        model application to data, 146–149
        results and observations, 144–146
    petrophysical transform approach, 129
    SP solutions, 154–155
    transient theory
        application to field data, 136–138
        confined aquifer solution, 133–135
        finite cylindrical domain, 138–142
        unconfined aquifer solution, 135–136
Sub-Gaussian random fields
    subordinated to tfBm
        apparent multifractality, 19–20
        extended power-law scaling, 7–13
        generation of, 13–18
    truncated fractional Brownian motion, 6–7
Subsurface flow model calibration inverse problems
    groundwater model calibration (*see also* Groundwater model calibration)
        flow equations and inverse modeling formulation, 74–76
        parameterization and regularization, 76–77
    sparse reconstruction and compressed sensing (*see also* Sparse reconstruction)
        advantage, 80
        convex relaxation techniques, 79
        greedy algorithms, 79
        matching pursuit, 79
        nonzero components, 78
        pursuit algorithms, 79
        solution sparsity, 77–78

T
Thiem equation, 188
Three-phase flow problems. *See* Multiphase flow model
Tortuosity, Archie's law
    vs. porosity
        anisotropic porous medium, 122, 123, 124
        COMSOL, 122
        dependency, 122, 123
        dimensionless bulk electrical conductivity change, 123, 124
        and electrical conductivity, 121
        geometric profile, 122
    property, porous medium, 116, 117
    quantification
        bulk electrical conductivity, 119
        defined, 118
        fluid velocity, 118
        pore throat effect, 120
        in tubes, 119, 120
Total pressure equation, 30–31
Transient multilayer flow systems
    analytic approach application, 95–96
    analytic element solution, 103–105
    benchmarking, 105
    differential equations, system, 101–102
    drawdown and stream depletion
        contour plots, 110, 111
        layers, 109
        near meandering river, 108
        stream depletion, 111–112
    flow between aquifer layers
        leaky layer, 99–100
        vertical flux, 101
    Laplace transform, multilayer wells and line-sinks, 102–103
    layers, 96
    mathematical model
        aquifer layers and leaky layers, 98
        Darcy's law, 98
        discharge vector, 98
        Laplace transformation, 98–99
        three-dimensional Dupuit flow, 97
    periodic pumping, multi-aquifer system, 107–108
    pumping well, unconfined aquifer, 105–106
Transient theory
    application to field data, 136–138
    confined aquifer solution, 133–135
    finite cylindrical domain, 138–142
    unconfined aquifer solution, 135–136
Transport equations, 31–32
Tsai and Yeh's model, L-phase fluids, 34
    relative permeability *vs.* saturation, 35–36
    saturation *vs.* capillary pressure, 35

U
Unconfined aquifer flow theory
    benchmark against pumping well, 105–106
    delayed water table unconfined response, 195–196
    delayed yield unconfined response, 193–194
    hybrid water table boundary condition, 196
    hydraulic parameters, 185–186

- moving water table solutions without confine storage, 191–193
- pumping tests, 135–136
- unsaturated flow, solution for
  - saturated-unsaturated well test models, 198
  - without confined aquifer storage, 197
- well test solutions
  - confined transient flow, 188–190
  - Dupuit's steady-state finite-domain solutions, 186–187
  - historical developments after Dupuit, 187–188
  - time-drawdown curve observation, 190–191

W

- Water infiltration problem
  - air density variation, 38, 39
  - boundary pressure distributions, 40
  - degrees of saturation distribution, 38, 42
  - description and relevant parameters, 37
  - Parker's constitutive law, 39
  - Parker's model, 40
  - plausible solutions, 40
  - variable-switch algorithm, 39
- Wavelet transform, 83–85

Z

- Zeroth moment, 178